UAB

Universitat Autònoma de Barcelona

2   3

Synthesis and Characterization of ε-Fe₂O₃ Nanoparticles and Thin Films

Zheng Ma

Thesis submitted for the degree of Doctor of Philosophy

PhD programme in Materials Science

Supervisor: Dr. Martí Gich Garcia

Institut de Ciència de Materials de Barcelona
(ICMAB-CSIC)

January 2021

Memòria presentada per aspirar al Grau de Doctor per:

ZHENG MA

Vist i plau directors:

………………………
Dr. Martí Gich Garcia
Supervisor
Group of Nanoparticles and Nanocomposites,
Institut de Ciència de Materials de Barcelona (ICMAB-CSIC),
Campus UAB, 08193 Bellaterra, Barcelona, Spain

Bellaterra, January 2021

Reality leaves a lot to the
imagination

John Lennon

Preface

When I arrived at ICMAB to start my PhD in October 2016 the initial plans were to put the research focus on the ferroelectric and multiferroic properties of ε-Fe_2O_3 films. However, our interest gradually shifted to the understanding of magnetic anisotropy in ε-Fe_2O_3 and its stabilization as epitaxial thin films, which have finally the core of the work presented herein. My work has opened other research avenues, some of which giving interesting results and others failing or resulting in more complicated than initially expected. In the interest of thematic coherence and because in most cases the results are too preliminary and incomplete all this work has been left aside.

The thesis starts with a general introduction to contextualize the research topic and motivation for establishing the main objectives of our research. Chapter 2 covers the experimental techniques used in this work. The main body of the thesis has been organized into two parts: Part I is devoted to the research done on nanoparticles (Chapters 3 and 4) while Part II reports the work on epitaxial thin films (Chapters 5, 6 and 7). Chapter 8 summarizes the main findings and conclusions of the thesis and gives an outlook on future work. Let us finally mention that more specific introductions have been included with Part I and II, as well as at the beginning of each chapter. The references are given at the end of each chapter.

Acknowledgments

They say this part is often the chapter that is most read. I hope I manage to do justice to all those who have contributed to the body of work for my doctoral thesis and who have helped and supported me greatly during the processes.

I would first like to thank Dr. Martí Gich, my research supervisor, for introducing me into this amazing project and providing me with regular assistance, patient guidance, and constant encouragement throughout the production of this thesis. I am especially grateful for the opportunities he has given to pursue my own ideas within the scope of the intended research focus. I also greatly appreciate the enormous effort he has put into helping me advance with the thesis during these difficult times of the pandemic. It was a huge privilege and honor to conduct this most exciting research under his guidance.

Within this line of research, collaborative efforts from a number of colleagues have been harnessed, which are essential for the completion of the thesis project. I stand to also gain from the numerous inspiring interactions and exchange of ideas with our collaborators, to whom I am incredibly grateful. In particular, a big and sincere THANK YOU:

To Dr. Nico Dix, who has helped me greatly with the production of the thesis during the last few months, especially for your spending time reviewing Chapter 2 and Chapters 6-8 of the thesis, for the valuable input and the many "aha moments" on the thin film study. To Prof. Jose Luis Garcia-Muñoz for introducing me to the research facilities and for providing me with expert advice and solving my many puzzles on the nanoparticle study. To Prof. Vassil Skumryev from UAB for the fruitful discussion about magnetism, for your kind assistance on the magnetic measurements, and for many both enlightening and entertaining off-the-topic discussions. To Dr. Jaume Gazquez, for the support with the (S)TEM studies on the films and valuable discussions. To Dr. Jesús López Sánchez from ICMM-CSIC, for the Raman study and the fruitful discussions. To Arnau Romaguera for showing me structural Refinement with patience and for the explanations on the synchrotron and neutron data analysis. To Dr. Javier Herrero-Martín from ALBA synchrotron for the collaborative work of XAS/XMCD study and the

feel at home in the group.

Outside of work, I thank my many other friends, with special mention to Pengmei, Saúl, Cica, Ziliang, Hailin, Xiaodong, Mikko, Qiao, Adrian, Artur, Alejandro, Songbai, Jike, Pamela, Mengdi, Huan, Yunwei Liang, and Zhaobin, for making my day brighter and fill it with so much joy.

Last but not the least, my deepest gratitude goes to my family for their incredible support, their sacrifice, and their love. I hope I have made you proud.

Abstract

In the course of the last two decades, the ferric oxide polymorph ε-Fe_2O_3 has transitioned from being a scientific rarity to attracting increasing attention for its multiferroic character and huge coercive field at room temperature. Such uncommon properties bring out fundamental aspects related to its complex magnetic phase diagram and also make ε-Fe_2O_3 appealing for applications in information technologies or photocatalysis. In spite of this rising interest, the synthesis and characterization of ε-$(Fe_{1-x}M_x)_2O_3$ in which Fe^{3+} is substituted by other metallic cations remains largely unexplored. Moreover, the mechanisms governing the stabilization of ε-Fe_2O_3 in form of thin films, the form preferred for most applications, are still poorly understood. This Thesis aims at advancing knowledge in this particular area by exploring the synthesis and characterization of ε-$(Fe_{1-x}M_x)_2O_3$ nanoparticles substituted with magnetic transition metals (M= Cr, Mn, Co, Ru). It also focuses on the stabilization mechanisms of ε-Fe_2O_3 epitaxial thin films and the characterization of their structural and magnetic properties.

The research on nanoparticles has brought new insights on the high and low temperature phase transitions of pure ε-Fe_2O_3, revealing its sensitivity to magnetic fields and strain state. It has been found that Cr^{3+} preferentially substitutes Fe^{3+} in the regular octahedral environment of ε-$(Fe_{1-x}Cr_x)_2O_3$, drastically reducing the magnetic anisotropy and saturation magnetization of the nanoparticles. The Fe^{3+} replacement by Cr^{3+} was studied up $x=0.25$ without the appearance of other secondary phases but strong evidence of structural evolution was observed for $x>0.10$. The Mn substitution was studied up to $x=0.20$ and did not induce the appearance of additional secondary phases but above $x=0.10$ a structural change was also observed. In connection with this, low Mn substitution has the effect of enhancing the magnetic anisotropy which rapidly falls for $x>0.05$ while the magnetization is strongly increased. In contrast to Cr and Mn, the Co substitution was found to be limited to 3 at. % with secondary phases appearing above this limit. Even such small substitutions resulted in significant changes of the lattice parameters with the effect of stretching a and compressing b and c, most likely as a consequence of magnetoelastic effects related to the unquenched orbital moment of Co^{2+}. The latter seems to strongly influence the

high temperature magnetic transition of $\varepsilon\text{-Fe}_2\text{O}_3$ by magnetically stabilizing the regular octahedral and tetrahedral sublattices of Fe^{3+}. The synthesis of stoichiometric Ru substituted $\varepsilon\text{-Fe}_2\text{O}_3$ was challenging due to the volatility of this metal and the magnetic characteristics of the Ru-doped nanoparticles presented reproducibility issues among different batches, indicating that experimental improvements are still needed.

Regarding the research on $\varepsilon\text{-Fe}_2\text{O}_3$ thin films, the Thesis has investigated the epitaxial growth and the structural characteristics of $Sc_{0.2}Al_{0.4}Fe_{1.4}O_3$ on different substrates, finding that it yields high-quality epitaxial films on LSAT (111), STO (111), Fluorophlogopite Mica (001) and YSZ (001) substrates. This has allowed us to stabilize epitaxial $\varepsilon\text{-Fe}_2\text{O}_3$ films on flexible Mica substrates using $Sc_{0.2}Al_{0.4}Fe_{1.4}O_3$ films as a buffer layer. The magnetic characterization of the $\varepsilon\text{-Fe}_2\text{O}_3$ films on Mica revealed the existence of a low temperature magnetic transition which reminds that of $\varepsilon\text{-Fe}_2\text{O}_3$ nanoparticles, but which had not been previously reported in films. The stabilization of epitaxial $\varepsilon\text{-Fe}_2\text{O}_3$ films on Fe_3O_4 (111) spinel buffer layers or directly on $MgAl_2O_4$ (111) (MAO (111)) substrates was also investigated and it was found that impurities are prone to appear when Fe_3O_4 (111) layers are used. The low temperature magnetic transition was also found on the $\varepsilon\text{-Fe}_2\text{O}_3$ films directly grown on MAO (111). We show that Raman spectroscopy is a powerful tool to probe both the high and low temperature magnetostructural transformations in this system.

Resum de la Tesi

Al llarg de les dues darreres decades, el polimorf d'òxid de ferro(III) ε-Fe_2O_3 ha passat de ser una raresa científica a estar a centre d'una intensa activitat de recerca a causa del seves propietats multiferroiques elevada coercivitat a temperatura ambient. Aquestes propietats tan poc habituals posen de relleu aspectes fonamentals relacionats amb la complexitat del seu diagrama de fases magnètic i susciten interès per les seves aplicacions potencials en tecnologies de la informació o fotocatàlisi. Tot i aquest interés creixent, la síntesi i caracterització de materials de tipus ε-$(Fe_{1-x}M_x)_2O_3$ en què el Fe^{3+} es substitueix per altres cations metàl·lics encara ha estat poc estudiada. Així mateix, tampoc s'acaben d'entendre els mecanismes que controlen l'estabilització de l'ε-Fe_2O_3 en capes primes que son molt rellevants en les aplicacions d'interès per aquest material. Aquesta tesi pretén contribuir a fer avançar el coneixement en els aspects que s'acaben d'esmentar, concretament explorant la síntesi i caracterització de nanopartícules ε-$(Fe_{1-x}M_x)_2O_3$ dopades amb metalls de transició magnètics (M= Cr, Mn, Co, Ru). També s'ha centrat en els mecanismes d'estabilització de les capes epitaxials d' ε-Fe_2O_3, tot fent-ne la caracterització estructural i de les seves propietats.

La recerca en nanopartícules ha permés aprofundir el coneixement de les transicions de fase de l' ε-Fe_2O_3 i ha posat de manifest la seva sensibilitat a la deformació i als camps magnètics. S'ha vist que el Cr^{3+} substituix preferencialment el Fe^{3+} en els entorns octaèdrics regulars de l'ε-$(Fe_{1-x}Cr_x)_2O_3$, i que redueix de forma dràstica l'anisotropia magnètica i la magnetització de saturació de les nanopartícules. La substitució del Fe^{3+} per Cr^{3+} s'ha pogut estudiar fins a $x=0.25$ sense observer-se l'aparició d'altres fases secundàries, tot i que per a $x>0.10$ s'han obtingut clars indicis de canvis estructurals. La substitució amb Mn s'ha estudiat fins a $x=0.20$ sense que tampoc en aquest cas s'observés l'aparició de fases secundàries a l'augmentar el contingut de Mn. Tanmateix, per sobre de $x=0.10$ també s'han observat canvis estructurals. En relació amb això, per baixos nivells de substitució l'efecte del Mn és fer augmenter l'anisotropia magnètica tot i que aquesta disminueixi ràpidament per a $x>0.05$ coincidint amb un fort increment de la magnetització. A diferència del que passa amb el Cr i el Mn, la substitució

amb Co no pot anar més enllà del 3 % atomic sense que apareguin fases secundàries. Però fins i tot aquests nivells tan baixos de substitució tenen l'efecte de fer augmentar a i al mateix temps comprimir b i c, molt probablement com a conseqüència d'efectes magnetoelàstics relacionats amb el moment orbital del Co^{2+}. Aquests efectes magnetoelàstics semblen tenir una forta influència sobre la transició magnètica de l'ε-Fe_2O_3 a alta temperatura tot estabilitzant les subxarxes magnètiques dels ferros en entorns octaèdrics regulars i tetraèdrics. Pel que fa a la substitució amb Ru, cal dir que ha estat complicada a causa de la volatilitat d'aquest metall i que els resultats de la caracterització magnètica de diferents síntesis no ha resultat reproduïbles, fet que indica que aquestes s'han de millorar.

Pel que fa a la recerca sobre capes primes d'ε-Fe_2O_3, en aquesta Tesi s'ha investigat el creixement de $Sc_{0.2}Al_{0.4}Fe_{1.4}O_3$ sobre diferents substrats i s'ha vist que se'n poden obtenir capes epitaxials de molt bona qualitat sobre substrats LSAT (111), STO (111), Mica Fluoroflogopita (001) i YSZ (001). Això ha permès estabilitzar capes primes epitaxials d'ε-Fe_2O_3 sobre substrats flexibles com la Mica fent servir l'$Sc_{0.2}Al_{0.4}Fe_{1.4}O_3$ com a capa tampó. La caracterització magnètica de les capes d'ε-Fe_2O_3 sobre Mica ha posat de manifest l'existència d'una transició magnètica a baixa temperatura de característiques similars a les de la que s'observa en el cas de les nanopartícules d'ε-Fe_2O_3, però que fins ara encara no s'havia vist en capes primes. També s'ha investigat l'estabilització de capes epitaxials d'ε-Fe_2O_3 sobe l'espinel·la Fe_3O_4 (111) com a capa tampó o bé directament sobre substrats $MgAl_2O_4$ (111) (MAO(111)) i s'ha trobat una tendència a que apareguin impureses d'hematita en els creixements sobre Fe_3O_4 (111). La transició a baixa temperatura també s'ha observat en el cas de les capes d'ε-Fe_2O_3 crescudes directament sobre MAO(111) i s'ha estudiat de forma detallada amb espectroscòpia Raman.

Resumen de la Tesis

A lo largo de las dos últimas décadas, el polimorfo de óxido de hierro(III) ε-Fe$_2$O$_3$ ha pasado de ser una rareza científica a estar en el centro de una intensa actividad de investigación debido a sus propiedades multiferroicas y su elevada coercividad a temperatura ambiente. Estas propiedades ponen de relieve aspectos fundamentales relacionados con la complejidad de su diagrama de fases magnético y suscitan interés por sus aplicaciones potenciales en tecnologías de la información o fotocatálisis. A pesar de este interés creciente, la síntesis y caracterización de materiales de tipo ε-(Fe$_{1-x}$M$_x$)$_2$O$_3$ en que el Fe^{3+} se sustituye por otros cationes metálicos ha sido poco estudiada. Asimismo, tampoco se acaban de entender los mecanismos que controlan la estabilización de la ε-Fe$_2$O$_3$ en capas delgadas, muy relevantes en las aplicaciones de interés para este material. Esta tesis pretende contribuir a hacer avanzar el conocimiento en los aspectos que se acaban de mencionar, concretamente explorando la síntesis y caracterización de nanopartículas ε-(Fe$_{1-x}$M$_x$)$_2$O$_3$ dopadas con metales de transición magnéticos (M = Cr, Mn, Co , Ru). También se ha centrado en los mecanismos de estabilización de capas epitaxiales de ε-Fe$_2$O$_3$, caracterizando su estructura y propiedades.

La investigación en nanopartículas ha permitido profundizar en el conocimiento de las transiciones de fase del sistema ε-Fe$_2$O$_3$ y ha puesto de manifiesto su sensibilidad a la deformación y los campos magnéticos. Se ha visto que el Cr^{3+} sustituye preferencialmente el Fe^{3+} en los entornos octaédricos regulares del ε-(Fe$_{1-x}$Cr$_x$)$_2$O$_3$, y que reduce de forma drástica la anisotropía magnética y la magnetización de saturación de las nanopartículas. La sustitución del Fe^{3+} por   Cr^{3+} se ha podido estudiar hasta x=0.25 sin observarse la aparición de otras fases secundarias, aunque para x>0.1 se han obtenido claros indicios de cambios estructurales. La sustitución con Mn se ha estudiado hasta x=0.20 sin que tampoco en este caso se observara la aparición de fases secundarias en aumentar el contenido de Mn. Sin embargo, por encima de x>0.1 también se han observado cambios estructurales. Para bajos niveles de sustitución el efecto del Mn es aumentar la anisotropía magnética aunque esta disminuya rápidamente para x>0.05, coincidiendo con un fuerte incremento de la magnetización. A diferencia de

lo que ocurre con el Cr y el Mn, la sustitución con Co no puede ir más allá del 3% atómico sin que aparezcan fases secundarias. Pero incluso estos niveles tan bajos de sustitución tienen el efecto de aumentar a y al mismo tiempo comprimir b y c, muy probablemente como consecuencia de fenómenos magnetoelásticos relacionados con el momento orbital del Co^{2+}. Estos efectos magnetoelásticos parecen tener una fuerte influencia sobre la transición magnética del sistema ε-Fe_2O_3 a alta temperatura, en particular estabilizando las subredes magnéticas de los hierros en entornos octaédricos regulares y tetraédricos. Respecto a la sustitución con Ru, cabe decir que ha sido complicada debido a la volatilidad de este metal y que los resultados de la caracterización magnética de diferentes síntesis no han resultado reproducibles, lo que indica que estas deben mejorarse.

En cuanto a la investigación sobre capas delgadas de ε-Fe_2O_3, en esta Tesis se ha investigado el crecimiento de $Sc_{0.2}Al_{0.4}Fe_{1.4}O_3$ sobre diferentes sustratos y se ha visto que se pueden obtener capas epitaxiales de buena calidad sobre sustratos LSAT (111), STO (111), Mica Fluoroflogopita (001) y YSZ (001). Esto ha permitido estabilizar capas delgadas epitaxiales de ε-Fe_2O_3 sobre sustratos flexibles como la Mica con $Sc_{0.2}Al_{0.4}Fe_{1.4}O_3$ como capa tampón. La caracterización magnética de las capas de ε-Fe_2O_3 sobre Mica ha puesto de manifiesto la existencia de una transición magnética a baja temperatura de características similares a las de la que se observa en el caso de las nanopartículas de ε-Fe_2O_3, pero que aún no se había visto en capas delgadas. También se ha investigado la estabilización de capas epitaxiales de ε-Fe_2O_3 sobe la espinela Fe_3O_4 (111) como capa tampón o bien directamente sobre sustratos MgAl2O4 (111) (MAO (111)) y se ha detectado una tendencia a que aparezcan impurezas de hematita al hacer crecimientos sobre Fe_3O_4 (111). La transición a baja temperatura también se ha observado en el caso de las capas de ε-Fe_2O_3 crecidas directamente sobre MAO (111) y se ha estudiado de forma detallada con espectroscopia Raman.

Table of Contents

Chapter 1

Introduction and Objectives

1.1 The complex physics of transition metal oxides

Transition metal oxides present a broad range of physical properties epitomized by intricate phase diagrams. Such a rich physics results from the diversity of electronic states allowed to outer electrons in partially filled d orbitals in a complex competition between different interactions involving the electronic spin, charge and orbital degrees of freedom and the crystal lattice [1–4].

In this context, understanding the magnetic orders, crystal structures and transition temperatures of the simplest cubic single transition metal oxides is still challenging from the theoretical point of view. A paradigmatic example of this is illustrated by the huge research devoted to understanding the phase transitions of MnO, NiO and CoO, with a cubic rock-salt structure in their paramagnetic state, as they become antiferromagnetically ordered (see [5] and references therein).

1.2 Iron Oxides

An equally stimulating playground for the advancement of condensed matter physics is offered by iron oxides which, in contrast, exist in a rich variety of crystal forms but tend to preserve their space group symmetry through magnetic orders they undergo at different temperatures. At ambient pressure, there are six known crystalline structures of iron oxides which are presented in

Figure 1.1.: wüstite (FeO), magnetite (Fe_3O_4) and the four iron oxide polymorphs hematite (α-Fe_2O_3), β-Fe_2O_3, maghemite (γ-Fe_2O_3), and ε-Fe_2O_3; each compound is based on a close-packed anion lattice, with a different distribution and oxidation state of the Fe cations in interstitial sites. The details about the different crystal structures, their properties and polymorphic transformations have been well covered in the book by Schwertmann and Cornell [6] and article reviews [7,8].

This thesis is centered on the ε-Fe_2O_3 polymorph and its magnetic transitions with special emphasis on the influence of iron substitutions by different magnetic transition metals.
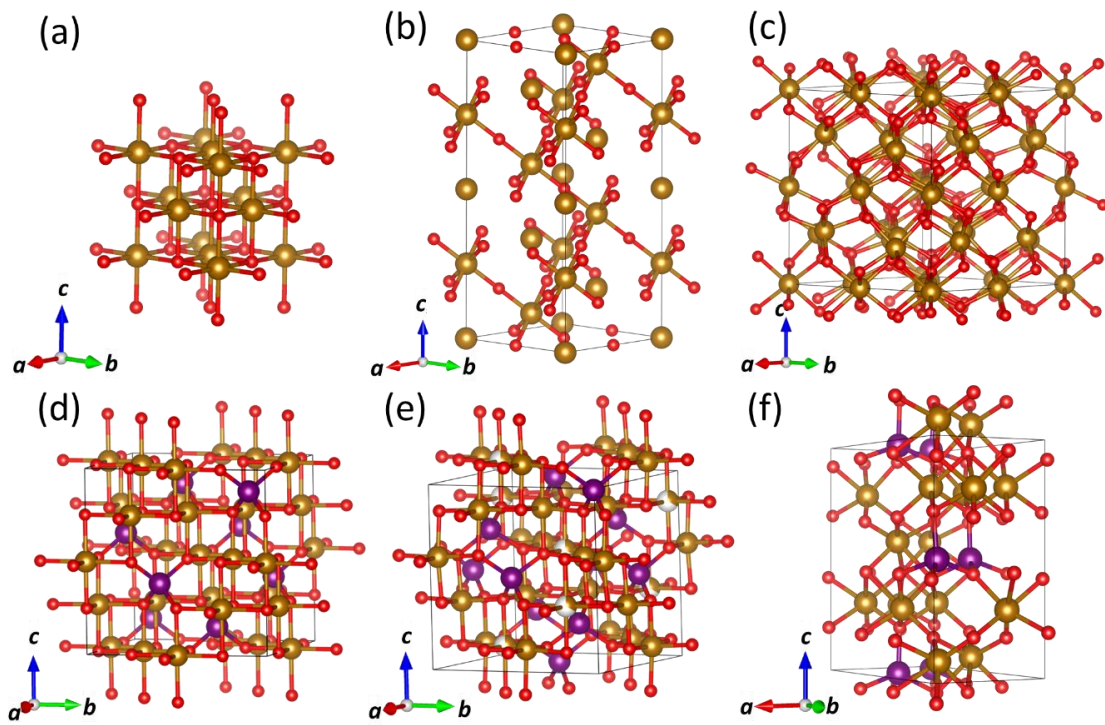
Figure 1.1 Schematic representations of the crystal structures of Fe_2O_3: (a) FeO, (b) α-Fe_2O_3, (c) β-Fe_2O_3, (d) Fe_3O_4, (e) γ-Fe_2O_3, and (f) ε-Fe_2O_3. The iron cations are represented by the brown (octahedrons) and violet (tetrahedra) balls, whereas the red balls refer to oxygen anions. The crystal structures were produced with the VESTA program [9].

1.3 ε-Fe₂O₃

The different aspects of ε-Fe_2O_3 have been specifically reviewed [10,11] and in the following we will briefly present its basic structural characteristics and properties relevant to contextualize the objectives of this work, with some emphasis on certain recent advances.

Among the different iron oxides, the ε-polymorph of Fe_2O_3 stands out for its non-centrosymmetric structure (orthorhombic, space group $Pna2_1$) with cell parameters a=5.098 Å, b=8.785 Å and c=9.468 Å at room temperature. In the structure of ε-Fe_2O_3, four distinct Fe^{3+} cation positions

exist: three are coordinated in edge-sharing octahedra and one in corner-sharing tetrahedron, having GaFeO$_3$ as the prototype (see Figure 1.2).

From the viewpoint of thermal phase transformation and crystal structures, ε-Fe$_2$O$_3$ is considered as an intermediate phase that occurs, under certain circumstances, during thermal conversion from γ-Fe$_2$O$_3$ to α-Fe$_2$O$_3$ [12], [13], [14]. Although ε-Fe$_2$O$_3$ is a metastable phase and is generally synthesized in laboratory with nanometer-sized dimensions or in the form of epitaxial thin films, the natural occurrence of this oxide in different environments has recently been reported [15], [16], [17], [18].
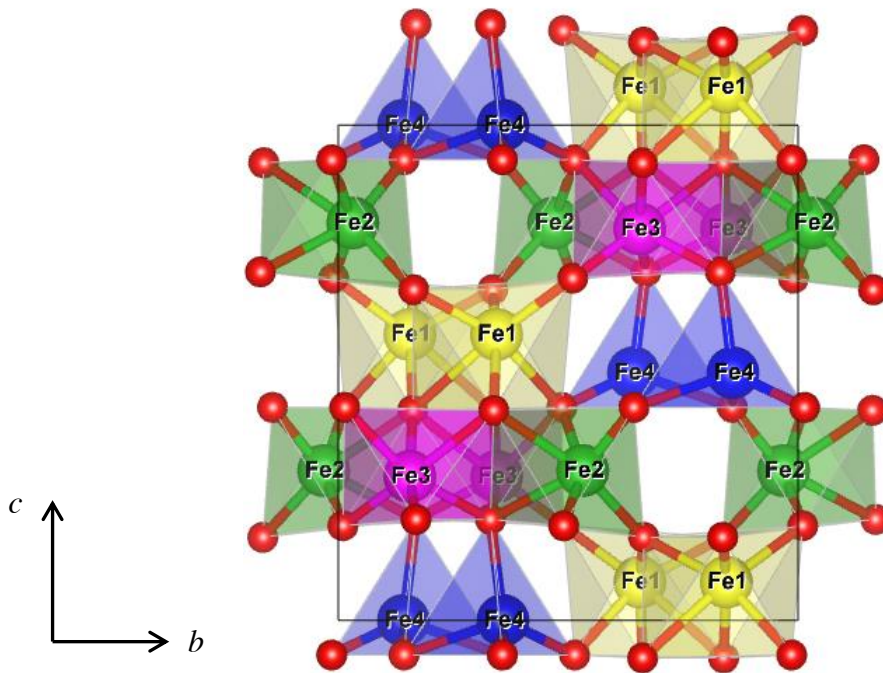
Figure 1.2 Orthorhombic structure of ε-Fe$_2$O$_3$. The four independent Fe sites of the cell are represented in different colors: distorted octahedral Fe1 and Fe2 in yellow and green, respectively; regular octahedral Fe3, pink; tetrahedral Fe4, blue. Oxygen atoms are manifested in red.

ε-Fe$_2$O$_3$ presents uncommon magnetic properties, including a giant coercive field at room temperature (H_C~ 2 T) related to a large magnetocrystalline anisotropy [19] with a high Curie temperature T_C of approximately 850 K [20], a remarkable non-linear magneto-optical effect in the range of millimeter waves [21] and coupled magnetoelectric features [22,23]. Moreover, it is also one of the few room-temperature multiferroics [24] although with a very small coupling between the ferroic orders and the ferroelectric switching mechanism is still not well understood [25,26]. More recently it has been reported that oxides based in ε-Fe$_2$O$_3$ can exhibit THz-assisted magnetic recording [27] and the interest of this oxide in the next generation magnetic recording reviewed [28]. Overall, ε-Fe$_2$O$_3$ has attracted increasing attention since it was prepared in pure form thanks to sol-gel chemistry methods the late 90's [29] and it is currently the object of more

than 30 publications and about 900 citations every year and according to Web of Science (search done with Topic= epsilon-Fe2O3).

1.3.1 Temperature dependent magnetic phase diagram of ε-Fe$_2$O$_3$

Between 4 K and 900 K ε-Fe$_2$O$_3$ presents five different magnetic structures (see Figure 1.3): two incommensurate magnetic orders (IM2 and IM1), below 150 K, and 2 collinear ferrimagnetic orders (FM2 and FM1) between 150 and the Curie temperature at 850 K above which it is paramagnetic. The contrasting magnetic properties between the different phases are illustrated by changes in the magnetization and the coercive field. The latter is quite remarkable, with a huge increase on cooling from FM1 to FM2 and a large decrease in the FM2 to IM1 transition. Those changes in the coercivity, are due to dramatic changes in the magnetocrystalline anisotropy and in particular to the existence of a significant spin-orbit coupling [30] which arises with the FM2 magnetic order below 500 K and then vanishes when the FM2 is transformed below 150 K.
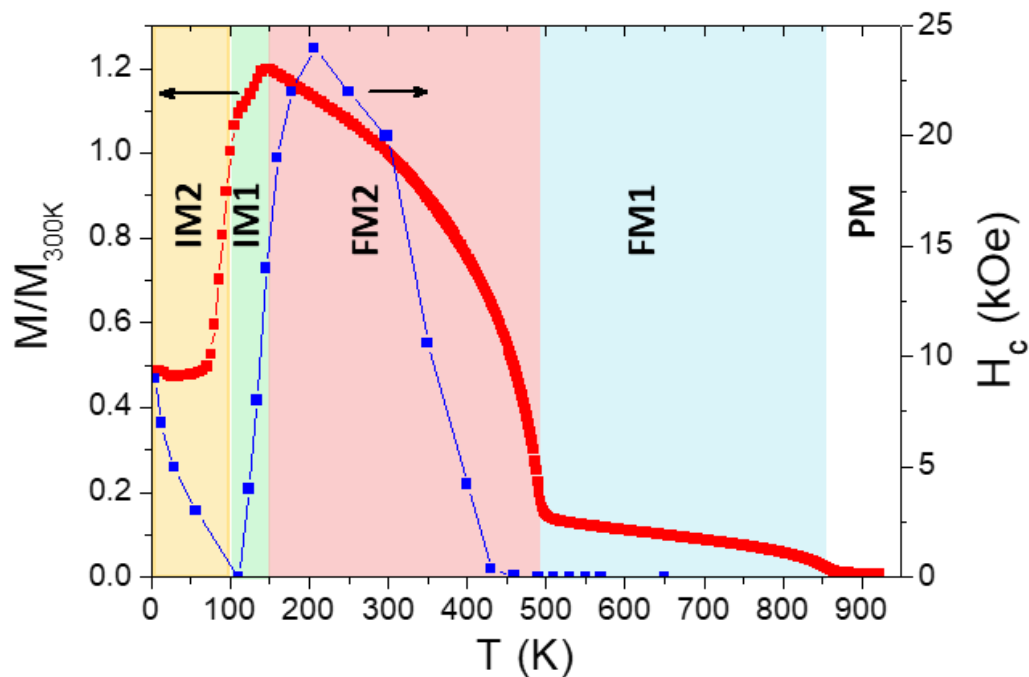
Figure 1.3: Magnetic phase diagram of ε-Fe$_2$O$_3$. The different magnetic structures are well correlated with important changes in the magnetization (left axis, in red) and coercive field (right axis, in blue).

However, according to Hund's rules, spin-orbit coupling and orbital magnetic moment are not to be expected from the Fe^{3+} cations of ε-Fe$_2$O$_3$ (half-filled 3d^5 orbitals produce an angular momentum L=0). By breaking these rules, even if a recent study reports a significantly lower orbital moment [31], one can argue that the unique structural features of ε-Fe$_2$O$_3$ make it particularly sensitive to spin-orbit interaction. Indeed, our recent study of the ε-Fe$_2$O$_3$ structure

around the emergence of large magnetocrystalline anisotropy on cooling below 500 K offers important clues to further understanding of this system [20]. Firstly, the transition is not only magnetic but also structural with a remarkable relative change of the unit cell volume in the order of 10^{-3} (Figure 1.4). This evidences a huge spontaneous magnetostriction which is comparable to those found for rare-earth iron alloys. Moreover, this figure suggests that since the onset of magnetocrystalline anisotropy is accompanied by a significant strain of the structure one could expect that conversely it would be possible to control the magnetic anisotropy through strain.
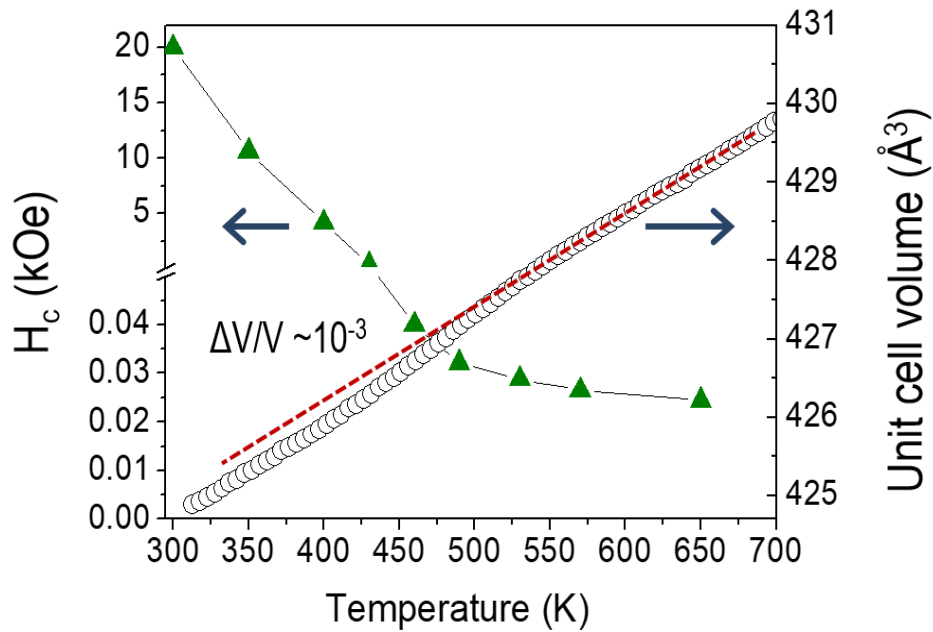
Figure 1.4 Temperature dependence of unit cell volume along the transition from low anisotropy FM1 phase to the high coercivity FM2 on cooling below 500 K.

1.3.2 Interest of investigating the influence of chemical substitutions in ε-Fe$_2$O$_3$

The group of Prof. Ohkoshi in Japan has shown that the large magnetocrystalline anisotropy of ε-Fe$_2$O$_3$ sets its ferromagnetic resonance (FMR) in zero-applied fields above 180 GHz, more than doubling the FMR of BaFe$_{12}$O$_{19}$ [32]. This stresses the soundness of ε-Fe$_2$O$_3$ as a reference structure to develop new functional ferrites for prospective non-reciprocal mm-wave devices for the upcoming 5G and beyond wireless communications. With several dopants, the zero-field FMR of ε-Fe$_2$O$_3$ ranges between 22 GHz and 220 GHz [21,32], and display different degree of losses which have not been characterized. The huge possibilities of developing ε-Fe$_2$O$_3$–based ferrites remain thus largely unexplored. Namely, the relevant substitution of Fe^{3+} by strongly magnetic cations has not been studied. Undertaking a systematic and rational approach to explore the possibilities of these novel ferrites at high-frequencies is thus particularly timely.

Our recent synchrotron X-ray diffraction study of ε-Fe$_2$O$_3$ at high pressure revealed a remarkable stability up to 27 GPa. [33] (see Figure 1.5). This indicates that this phase can sustain large chemical and mechanical pressures and thus extensive chemical doping, strain engineering in epitaxial films and use of high pressures are promising directions to expand the family of ε-Fe$_2$O$_3$– based materials.
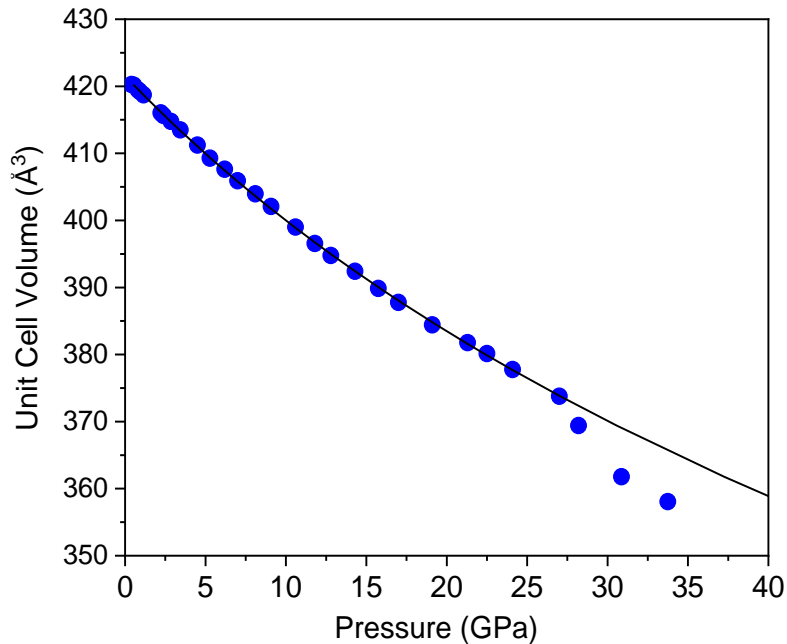
Figure 1.5 High pressure dependence of the unit cell volume of ε-Fe$_2$O$_3$. The structure is stable up to above 27 GPa [33].

The most appealing substitutions of ε-Fe$_2$O$_3$ are strongly magnetic 3d cations which have not been studied so far and more specifically Cr^{3+} and Mn^{3+}, which can be readily stabilized in trivalent state and Co^{2+}, for its unquenched orbital moment. Another important aspect in the choice of Mn^{3+} is that it induces strong spontaneous lattice distortions (Jahn-Teller effect [34]), which are not related to spin-orbit interaction. On the other hand, Cr^{3+} is known to induce non-collinear magnetic orders in spinels [35], which are structurally related to ε-Fe$_2$O$_3$. In particular, the emergence of these orders is related to the antisymmetric exchange interaction [36] which can be an important asset to balance the significant spin-orbit effect in ε-Fe$_2$O$_3$.

1.3.3 Thin epitaxial films of ε-Fe$_2$O$_3$

For most potential applications of ε-Fe$_2$O$_3$ in information technologies, the use of epitaxial thin films is a must. In spite of the fact that we already demonstrated the epitaxial growth of ε-Fe$_2$O$_3$ by pulsed laser deposition (PLD) relatively long time ago, there have been relatively few advances to improve the microstructures of these type of films, which tend grow 3D and result in large

roughness. Quite recently the ultrathin epitaxial ε-Fe$_2$O$_3$ films were prepared on mica substrates by chemical vapour deposition from the decomposition of FeCl$_3$ at high temperature [37]. In contrast to the films grown by PLD in this case ε-Fe$_2$O$_3$ growing laterally in a 2D mode. This work motivated us to undertake the PLD growth of ε-Fe$_2$O$_3$ on mica also inspired by the possibility of exploiting the ε-Fe$_2$O$_3$ films grown on this flexible substrate as a testbed for strain-dependent magnetic properties of this oxide. In parallel, a significant number of studies on GaFeO$_3$-type epitaxial films grown by PLD have appeared in recent years. An analysis of all this literature (see the introduction to Part II) makes one consider the relative importance of lattice mismatch with the substrate compared to the thermodynamics for the stabilization of GaFeO$_3$-type films. Namely, the growth of ultra-flat GaFeO$_3$ by significantly increasing the substrate temperature [38] and the crystallinity improvements achieved with the Sc$_{0.2}$Ga$_{0.4}$Fe$_{1.4}$O$_3$ films [39] in which there is an increased entropy of mixing strongly suggests this possibility. This motivated us to employ quaternary buffer oxide layers to improve the quality of ε-Fe$_2$O$_3$ films and expand the diversity of substrates in which it can be grown.

1.4 Objectives of the thesis

The two basic objectives of the present thesis are:

1- Contributing to understand the underlying mechanisms of the magnetic properties of ε-Fe$_2$O$_3$.

2- Understanding the stabilization of ε-Fe$_2$O$_3$ in form of epitaxial thin films to improve its quality and diversify the substrates in which it can be grown.

To address the first objective, we investigated the magnetic transitions of pure ε-Fe$_2$O$_3$ nanoparticles (Chapter 3) and thin films (Chapter 6) and we studied the effect of Cr, Mn and Co substitutions (Chapter 4). The second objective is addressed in Chapters 5, 6 and 7.

References

[1]   C.N.R. Rao, Transition Metal Oxides, Annu. Rev. Phys. Chem. 40 (1989) 291–326. https://doi.org/10.1146/annurev.pc.40.100189.001451.

[2]   J.M.D. Coey, M. Venkatesan, H. Xu, Introduction to Magnetic Oxides, Funct. Met. Oxides. (2013) 1–49. https://doi.org/https://doi.org/10.1002/9783527654864.ch1.

[3]   E. Dagotto, Complexity in Strongly Correlated Electronic Systems, Science (80-.). 309 (2005) 257 LP – 262. https://doi.org/10.1126/science.1107559.

[4]   Y. Tokura, N. Nagaosa, Orbital Physics in Transition-Metal Oxides, Science (80-.). 288 (2000) 462–468.

[5]   S. Lee, Y. Ishikawa, P. Miao, S. Torii, T. Ishigaki, T. Kamiyama, Magnetoelastic coupling forbidden by time-reversal symmetry: Spin-direction-dependent magnetoelastic coupling on MnO, CoO, and NiO, Phys. Rev. B. 93 (2016) 1–12. https://doi.org/10.1103/PhysRevB.93.064429.

[6]   R.M. Cornell, U. Schwertmann, Applications, in: Iron Oxides, Wiley-VCH Verlag GmbH & Co. KGaA, 2004: pp. 509–524. https://doi.org/10.1002/3527602097.ch19.

[7]   R. Zboril, M. Mashlan, D. Petridis, Iron(III) oxides from thermal processes-synthesis, structural and magnetic properties, Mossbauer spectroscopy characterization, and applications, Chem. Mater. 14 (2002) 969–982. https://doi.org/10.1021/cm0111074.

[8]   L. MacHala, J. Tuček, R. Zbořil, Polymorphous transformations of nanometric iron(III) oxide: A review, Chem. Mater. 23 (2011) 3255–3272. https://doi.org/10.1021/cm200397g.

[9]   K. Momma, F. Izumi, VESTA: A three-dimensional visualization system for electronic and structural analysis, J. Appl. Crystallogr. 41 (2008) 653–658. https://doi.org/10.1107/S0021889808012016.

[10]   J. Tucek, R. Zboril, A. Namai, S. Ohkoshi, epsilon-Fe2O3: An Advanced Nanomaterial Exhibiting Giant Coercive Field, Millimeter-Wave Ferromagnetic Resonance, and Magnetoelectric Coupling, Chem. Mater. 22 (2010) 6483–6505. https://doi.org/10.1021/cm101967h.

[11]   S.-I. Ohkoshi, H. Tokoro, Hard Magnetic Ferrite: ε -Fe 2 O 3, Bull. Chem. Soc. Jpn. 86 (2013) 897–907. https://doi.org/10.1246/bcsj.20130120.

[12]   C. Chanéac, E. Tronc, J.P. Jolivet, Thermal behavior of spinel iron oxide-silica composites, Nanostructured Mater. 6 (1995) 715–718. https://doi.org/10.1016/0965-9773(95)00158-1.

[13]   M. Popovici, M. Gich, D. Nižňanský, A. Roig, C. Savii, L. Casas, E. Molins, K. Zaveta, C. Enache, J. Sort, S. De Brion, G. Chouteau, J. Nogués, Optimized synthesis of the elusive ∈-Fe2O3 phase via sol-gel chemistry, Chem. Mater. 16 (2004) 5542–5548. https://doi.org/10.1021/cm048628m.

[14]   E. Tronc, C. Chanéac, J.P. Jolivet, Structural and Magnetic Characterization ofε-Fe2O3, J. Solid State Chem. 139 (1998) 93–104. https://doi.org/10.1006/jssc.1998.7817.

[15]   R.G. McClean, M.A. Schofield, W.F. Kean, C. V. Sommer, D.P. Robertson, D. Toth, M. Gajdardziska-Josifovska, Botanical iron minerals: correlation between nanocrystal structure and modes of biological self-assembly, Eur. J. Mineral. 13 (2001) 1235–1242. https://doi.org/10.1127/0935-1221/2001/0013-1235.

[16]   C. Dejoie, P. Sciau, W. Li, L. Noé, A. Mehta, K. Chen, H. Luo, M. Kunz, N. Tamura, Z. Liu, Learning from the past: Rare ε-Fe2O3 in the ancient black-glazed Jian (Tenmoku) wares, Sci. Rep. 4 (2014) 1–9. https://doi.org/10.1038/srep04941.

[17]   H. Xu, S. Lee, H. Xu, Luogufengite: A new nano-mineral of Fe2O3 polymorph with giant coercive field, Am. Mineral. 102 (2017) 711–719. https://doi.org/10.2138/am-2017-5849.

[18]   T. Wen, Y. Zhang, Y. Geng, J. Liu, A. Basit, J. Tian, Y. Li, J. Li, J. Ju, W. Jiang, Epsilon-Fe2O3 is a novel intermediate for magnetite biosynthesis in magnetotactic bacteria, Biomater. Res. 23 (2019) 13. https://doi.org/10.1186/s40824-019-0162-1.

[19] M. Gich, A. Roig, C. Frontera, E. Molins, J. Sort, M. Popovici, G. Chouteau, D. Martín y Marero, J. Nogús, Large coercivity and low-temperature magnetic reorientation in ε-Fe 2O 3 nanoparticles, J. Appl. Phys. 98 (2005) 044307. https://doi.org/10.1063/1.1997297.

[20] J.L. García-Muñoz, A. Romaguera, F. Fauth, J. Nogués, M. Gich, Unveiling a New High-Temperature Ordered Magnetic Phase in ε-Fe2O3, Chem. Mater. 29 (2017) 9705–9713. https://doi.org/10.1021/acs.chemmater.7b03417.

[21] A. Namai, M. Yoshikiyo, K. Yamada, S. Sakurai, T. Goto, T. Yoshida, T. Miyazaki, M. Nakajima, T. Suemoto, H. Tokoro, S.I. Ohkoshi, Hard magnetic ferrite with a gigantic coercivity and high frequency millimetre wave rotation, Nat. Commun. 3 (2012). https://doi.org/10.1038/ncomms2038.

[22] M. Gich, C. Frontera, A. Roig, J. Fontcuberta, E. Molins, N. Bellido, C. Simon, C. Fleta, Magnetoelectric coupling in ε-Fe$_2$O$_3$ nanoparticles, Nanotechnology. 17 (2006). https://doi.org/10.1088/0957-4484/17/3/012.

[23] C. Kadlec, F. Kadlec, V. Goian, M. Gich, M. Kempa, S. Rols, M. Savinov, J. Prokleska, M. Orlita, S. Kamba, Electromagnon in ferrimagnetic epsilon-Fe2O3 nanograin ceramics, Phys. Rev. B. 88 (2013). https://doi.org/10.1103/PhysRevB.88.104301.

[24] M. Gich, I. Fina, A. Morelli, F. Sánchez, M. Alexe, J. Gàzquez, J. Fontcuberta, A. Roig, Multiferroic iron oxide thin films at room temperature, Adv. Mater. 26 (2014). https://doi.org/10.1002/adma.201400990.

[25] X. Guan, L. Yao, K.Z. Rushchanskii, S. Inkinen, R. Yu, M. Ležaic, F. Sánchez, M. Gich, S. Van Dijken, Unconventional ferroelectric switching via local domain wall motion in multiferroic ε-fe2o3 films, ArXiv. (2019).

[26] B.N. Rao, S. Yasui, T. Katayama, A. Taguchi, H. Moriwake, Y. Hamasaki, M. Itoh, Investigation of ferrimagnetism and ferroelectricity in AlxFe2-xO3 thin films, J. Mater. Chem. C. 8 (2020) 706–714. https://doi.org/10.1039/c9tc05390e.

[27] S. Ohkoshi, M. Yoshikiyo, K. Imoto, K. Nakagawa, A. Namai, H. Tokoro, Y. Yahagi, K. Takeuchi, F. Jia, S. Miyashita, M. Nakajima, H. Qiu, K. Kato, T. Yamaoka, M. Shirata, K. Naoi, K. Yagishita, H. Doshita, Magnetic-Pole Flip by Millimeter Wave, Adv. Mater. 2004897 (2020) 1–7. https://doi.org/10.1002/adma.202004897.

[28] H. Tokoro, A. Namai, S. Ohkoshi, Advances in magnetic films of epsilon-iron oxide toward next-generation high-density recording media, Dalt. Trans. (2021). https://doi.org/10.1039/d0dt03460f.

[29] E. Tronc, C. Chaneac, J.P. Jolivet, Structural and magnetic characterization of epsilon-Fe2O3, J. Solid State Chem. 139 (1998) 93–104. https://doi.org/10.1006/jssc.1998.7817.

[30] Y.-C. Tseng, N.M. Souza-Neto, D. Haskel, M. Gich, C. Frontera, A. Roig, M. Van Veenendaal, J. Nogués, Nonzero orbital moment in high coercivity ε-Fe$_2$O $_3$ and low-temperature collapse of the magnetocrystalline anisotropy, Phys. Rev. B - Condens. Matter Mater. Phys. 79 (2009). https://doi.org/10.1103/PhysRevB.79.094404.

[31] R. Jones, R. Nickel, P.K. Manna, J. Hilman, J. Van Lierop, Temperature and field evolution of site-dependent magnetism in ε−Fe2O3 nanoparticles, Phys. Rev. B. 100 (2019). https://doi.org/10.1103/physrevb.100.094425.

[32] A. Namai, S. Sakurai, M. Nakajima, T. Suemoto, K. Matsumoto, M. Goto, S. Sasaki, S. Ohkoshi, Synthesis of an Electromagnetic Wave Absorber for High-Speed Wireless Communication, J. Am. Chem. Soc. 131 (2009) 1170–1173. https://doi.org/10.1021/ja807943v.

[33] J.A. Sans, V. Monteseguro, G. Garbarino, M. Gich, V. Cerantola, V. Cuartero, M. Monte, T. Irifune, A. Muñoz, C. Popescu, Stability and nature of the volume collapse of ε-Fe2O3 under extreme conditions, Nat. Commun. 9 (2018). https://doi.org/10.1038/s41467-018-06966-9.

[34] G.F. Dionne, Magnetic Ions in Oxides BT - Magnetic Oxides, in: G.F. Dionne (Ed.), Springer US, Boston, MA, 2009: pp. 37–106. https://doi.org/10.1007/978-1-4419-0054-8_2.

[35] Y. Yamasaki, S. Miyasaka, Y. Kaneko, J.-P. He, T. Arima, Y. Tokura, Magnetic Reversal of the Ferroelectric Polarization in a Multiferroic Spinel Oxide, Phys. Rev. Lett. 96 (2006) 207204.

https://doi.org/10.1103/PhysRevLett.96.207204.

[36]   H. Katsura, N. Nagaosa, A. V Balatsky, Spin Current and Magnetoelectric Effect in Noncollinear Magnets, Phys. Rev. Lett. 95 (2005) 57205. https://doi.org/10.1103/PhysRevLett.95.057205.

[37]   J. Yuan, A. Balk, H. Guo, Q. Fang, S. Patel, X. Zhao, T. Terlier, D. Natelson, S. Crooker, J. Lou, Room-Temperature Magnetic Order in Air-Stable Ultrathin Iron Oxide, Nano Lett. 19 (2019) 3777–3781. https://doi.org/10.1021/acs.nanolett.9b00905.

[38]   S. Homkar, D. Preziosi, X. Devaux, C. Bouillet, J. Nordlander, M. Trassin, F. Roulland, C. Lefèvre, G. Versini, S. Barre, C. Leuvrey, M. Lenertz, M. Fiebig, G. Pourroy, N. Viart, Ultrathin regime growth of atomically flat multiferroic gallium ferrite films with perpendicular magnetic anisotropy, Phys. Rev. Mater. 3 (2019) 1–10. https://doi.org/10.1103/PhysRevMaterials.3.124416.

[39]   T. Katayama, S. Yasui, Y. Hamasaki, T. Osakabe, M. Itoh, Chemical tuning of roomerature ferrimagnetism and ferroelectricity in ϵ-Fe2O3-type multiferroic oxide thin films, J. Mater. Chem. C. 5 (2017) 12597–12601. https://doi.org/10.1039/c7tc04363e.

Chapter 2

Sample Preparation and Characterization Techniques

In this chapter, we will provide a quick, concise overview of the main experimental methodologies and techniques used in this thesis. We begin with a general discussion of the synthesis methods for ε-Fe$_2$O$_3$ nanoparticles and thin films. Then we will focus on the key characterization techniques from which some valuable insights have been gained, attempting to give a brief description on some important concepts and basic principles underpinning the use of these techniques. Some practical information on the main implemented instruments (either the laboratory instrumentation or those from large facilities) may also be covered. More detailed sample synthesis approaches to ε-Fe$_2$O$_3$ (or metal-substituted ε-Fe$_2$O$_3$) nanoparticles and thin films are deferred the subsequent chapters.

2.1 Synthesis methods

Despite the particularly rich physics in ε-Fe$_2$O$_3$, it has been a proven challenge to synthesize this thermodynamically metastable polymorph without intrusion of other phases. To facilitate the study of its fascinating properties and the exploration of its technological application potentials, it is highly desirable to establish appropriate synthesis routes. In this regards, this Thesis mainly concerns sol-gel based wet chemical method and pulsed laser deposition. A short overview of these synthesis methods is presented below.

2.1.1 Sol-gel chemistry

All the nanoparticles presented in this thesis were produced by sol-gel chemical process. Sol-gel method is one of the most well-established synthetic approaches to prepare a wide range of functional metal oxide nanoparticles and nanocomposites. The sol-gel method offers some significant advantages compared to many other chemical or solid-state reactions, such as its low synthesis temperature, low cost and short synthesis time, its versatility to preparing multicomponent nanostructures, the fine control of the product's chemical composition and good chemical homogeneity enabled by the atomic mixing of reagents, its great ability to control over particle morphology and size.

Sol-gel chemistry in general involves the sol (colloidal suspension) synthesis, subsequent gel formation, aging and drying to form xerogel, and the removal of surface hydroxyl groups through calcination whenever necessary [1]. The gel is composed of three-dimensional cross-linked networks containing a liquid phase. It is worth pointing out that the calcination treatment of xerogel may become beneficial to obtain well-controlled structure in terms of high crystallinity and even morphologic and phase selectivity in some cases.

Sol-gel chemistry is sensitive to many process factors. In particular, parameters such as the types and molar ratios of the employed salt precursors/solvents, hydrolysis and condensation rates, pH, relative humidity of the synthesis atmosphere, agitation, gelation temperature, sintering protocols, etc.. can strongly influence the kinetics of growth reactions and nucleation/crystallization process, and consequently, the composition, structure and properties of the final product.
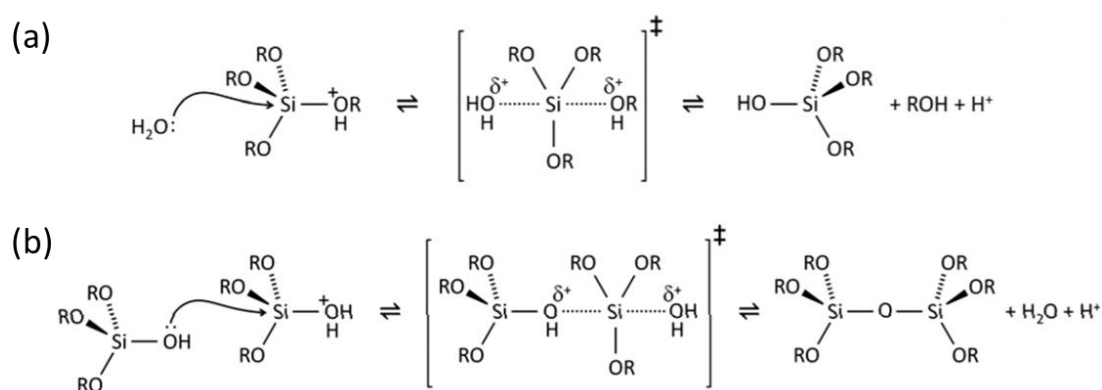
Figure 2.1 Illustration of acid catalyzed (a) hydrolysis and (b) condensation of silicon alkoxides. Depending on the synthesis conditions, the hydrolysis may continue to completion. The condensation results in the formation of a network of siloxane bonds. Note that the progression of condensation depends on the degree of the prior hydrolysis. If hydrolysis is complete before the first condensation step (Equation 2.1 in the text), the resulting product $(OH)_3Si-O-Si(OH)_3$ has 6 sites for subsequent condensation steps. A widely used alcoxide in the sol-gel chemistry of silica is tetraethylorthosilicate (TEOS) where the alkyl group $R=C_2H_5$. Figures taken from Reference [1].

The most common precursors used in the preparation of the sol are water-sensitive alkoxides ($M(OR)_x$, where M= metal or metalloid, R= alkyl group), which are hydrolyzed in either acidic or alkali conditions and subsequently undergo a condensation of the hydrolysis products forming a polymeric network or a gel. As an example of this, the hydrolysis and condensation of silicon alkoxides, $Si(OR)_4$, which are widely used for the sol-gel chemistry of silica, are depicted in Figure 2.1. Hydrolysis results in a hydroxyl attached to the silicon atom by replacement of an alkoxy group in the alkoxide. Depending on the Si/H_2O ratio and the catalyst present, the hydrolysis may continue to completion, so that

$$Si(OR)_4 + 4H_2O \rightarrow Si(OH)_4 + 4 \text{ R-OH} \tag{2.1}$$

The hydrolyzed molecules can link together via multiple condensation reactions to form a network of siloxane bonds (Si-O-Si). Condensation often occurs on terminal silanols (Si-OH), and its progression depends on the degree of hydrolysis that has occurred. In acidic conditions, where the first hydrolysis step is typically the fastest, condensation begins before hydrolysis is complete [1]. In the present thesis, iron oxide nanoparticles inside a silica matrix have been prepared by adding iron nitrate and TEOS into a hydroethanolic solution from which gels were obtained (see more details in Chapter 3).

2.1.2 Pulsed layer deposition

Pulsed layer deposition (PLD) is a widely used physical vapor deposition technique for the growth of complex oxide thin films. A typical set-up for PLD is schematically shown is Figure 2.2(a). A pulsed KrF excimer laser (λ= 248 nm) is focused by an optical lens system onto a scanning ceramic target placed in a vacuum chamber. The absorption of short (25 ns) high power laser pulses focused on the small target area (about 1 x 3 mm^2) locally heat and vaporize the target material, resulting in the emission of a plasma plume. Note that the ablation process is far from the thermodynamical equilibrium. The plasma plume is very directional and a heater (T_{max} = 850 °C) with the mounted substrate (glued with silver paint for good thermal contact) is located about 47 mm away from the target, where the ablated material condenses. Several experimental parameters such as laser energy and frequency, substrate temperature, cooling procedure and chamber pressure, can affect the film deposition. Careful tuning of these parameters can allow the stabilization of different polymorphs , even metastable phases may be stabilized under specific growth conditions.

13
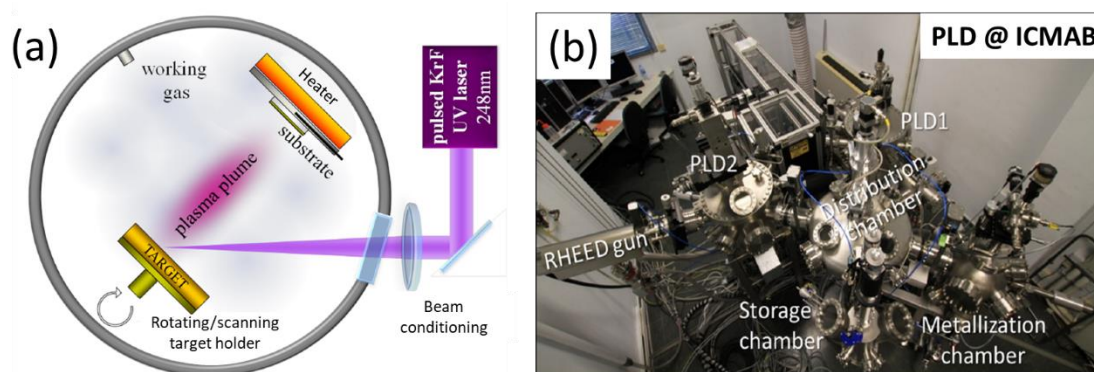
Figure 2.2 (a) Schematic illustration of a typical PLD set-up. Prior to the laser beam is steered into the vacuum chamber, beam conditioning is realized by an optical lens system. A plasma plume is generated after laser ablation of a target that is exposed to the PLD laser. The thin film growth occurs when the plume arrives on the surface of the substrate. (b) A picture of the PLD set-up at ICMAB. Courtesy of Dr. Nico Dix, ICMAB.

The PLD technique allows stoichiometric transfer of the target material to the substrate and one can achieve relatively high growth rates (0.001 – 0.5A/pls) within a homogeneous area of 5x10 mm^2. The growth chamber is maintained in ultrahigh vacuum (UHV) and thus allows for precise control of background gases such as oxygen during the deposition. This has allowed the fabrication of complex oxide thin films such as $BaTiO_3$, $SrRuO_3$, $LaNiO_3$, Yttria-stabilized zirconia (YSZ), spinel iron oxides, YBCO, etc.

In the current work, the investigated thin films had been grown using PLD by the technical staff (Raúl Solanas and Dr. Mengdi Qian) of the Thin Film Laboratory Service at ICMAB, with the support from Dr. Florencio Sánchez. A picture of the PLD set-up installed at ICMAB is shown in Figure 2.2(b). In this set-up, one of the system (PLD1) is connected to a sputtering unit, while the other system (PLD2) is equipped with a reflection high energy electron diffraction (RHEED) set-up, enabling to monitor *in-situ* the growth of epitaxial films. The deposition chambers are accessed via load-locks to transfer target and sample holders to the main chamber, which allows to maintain a constant high vacuum in the main chambers.

A prior polishing of the target surface is carried out before the deposition to ensure a similar and clean target surface for each deposition. Additionally, to achieve the same initial conditions for all depositions a selected area is pre-ablated. A shutter is placed between substrate and target to avoid deposition on the substrate during pre-ablation. During the deposition, the focused laser beam is rastered across a region with size, depending on the applied pulse number (typically a few hundred up to 10 k pulses) on the target in order to ensure uniformity in the film thickness and composition. More description on the thin film depositions is dealt with in detail in Chapter 5, 6, and 7.

2.2 X-ray Techniques

Various X-ray-based experimental techniques are used in this dissertation to study the details of the structure, electronic, magnetic or chemical properties of the synthesized samples. With this section, we provide a brief introduction to these techniques, concentrating on the basic principles of X-ray powder diffraction (both laboratory and synchrotron based), X-ray diffraction (XRD) of thin films, X-ray reflectivity (XRR), X-ray absorption (XAS), as well as X-ray magnetic circular magnetic dichroism (XMCD). A short description of the beamline instrumentation will be presented. The knowledge we have gained here will provide the basis that assists in understanding not only these experimental methodologies but also the data therefrom.

2.2.1 X-ray diffraction

X-ray diffraction (XRD) is a widely used non-destructive technique by materials science community for determining the crystalline structure of crystals. They can be produced in a laboratory system by bombarding a metal (typically Cu) with electrons in an evacuated tube, and monochromatic X-rays are usually selected. When the monochromatic X-ray beam impinges on a crystal, it is primarily scattered by the crystal's electrons. The periodicity of electron density is defined explicitly in the crystal where periodic arrangement of atoms constitutes lattice planes. Due to such regularity, the scattered X-rays add up constructively to generate diffraction maxima via interference in certain directions, and cancel each other in other directions. The diffraction of X-rays from a crystal is described by the Bragg's law as shown in Figure 2.3:

$$2d_{hkl} \sin \theta = n\lambda \qquad\qquad (2.2)$$

whereby d_{hkl} is the interplanar spacing of the lattice planes with Miller indices *(hkl)*, the Bragg angle θ is one-half the angle between the incident and scattered X-ray beams, *n* is an integer denoting the order of the reflection, and λ is the X-ray wavelength. Consequently, a family of lattice planes {*hkl*} produces a diffraction peak only at a specific diffraction angle θ. By definition, the scattering vector $s= k_{out} - k_{in}$, where k_{in} and k_{out} are respectively the incident and diffracted beam vectors. Note that the scattering vector *s* lies perpendicular to the scattering planes when the Bragg's law is satisfied.
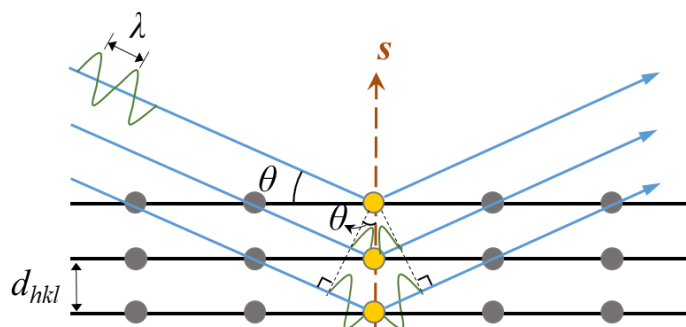
Figure 2.3 The Bragg´s law describes interference between diffracted X-rays of successive atomic planes with interplanar spacing of d_{hkl}. When the optical path difference (shown here in green) between adjacent X-rays is an integer multiple n of a known X-ray wavelength λ, interference is constructive, and hence a diffraction maximum appears at that specific angle. The scattering vector s is perpendicular to the scattering planes.

For a polycrystalline (powder) sample, in which crystallites are oriented randomly, the diffraction pattern forms a series of diffraction cones (Debye rings). Typically, the geometry for X-ray powder diffraction (XRPD) is such that the sample rotates in the path of the incident X-ray beam at a Bragg angle θ, while the X-ray detector and rotates at an angle of 2θ collecting the diffracted X-rays. This geometry is commonly known as *Bragg-Brentano geometry* and the scan mode is called θ-2θ scan. In the present work, the X-ray powder diffraction (as well as the below-mentioned neutron powder diffraction) data have been analyzed using the Rietveld method implemented in the Fullprof Suite program [2]. This method is based on minimizing the weighted sum of squared difference between the observed data and the calculated pattern using an approximate structural model.

XRD can be exploited for phase identification and for the examination of the crystallinity, texture, epitaxial relationships and lattice parameters of thin films. In a typical 4-circle diffractometer (angles ω, 2θ, χ, ϕ), as shown schematically in Figure 2.4, there are different rotation axes and angles, enabling various X-ray measurement geometries that are applicable to thin films, some of which are briefly discussed below:

ω-2θ scan: It is normally realized when the sample is rotated by ω, the angle at which the incident beam meets the sample surface, and the detector is rotated by 2θ. The angle χ (sometimes referred to as ψ in the literature) is the plane tilt angle in the diffraction plane, namely, the angle between the sample normal and the scattering vector s. If $\omega=\theta$ and there is no χ offset, the Bragg-Brentano geometry is thus satisfied, i.e., the s vector is parallel to the sample normal, this is a symmetrical scan (θ-2θ scan), while an asymmetric geometry is characterized by $2\theta \neq 2\omega$ and $\chi \neq 0$.

ω-scan (rocking curve), the incident angle ω is varied at a specific out-of-plane Bragg peak, the ω-scan measurement reveals broadening of the diffraction peaks, enabling the evaluation

of the crystalline quality crystals (very high quality single crystalline substrates can have a FWHM of the rocking curves below 0.002º).

Pole figure and *ϕ scan*: In this scan mode, a specific family of lattice planes is selected by setting a Bragg reflection (ω-2θ) and a tilt angle χ, and the sample is rotated around the sample normal axis. The distribution of the selected diffraction peak along ϕ angle can be used to determine the in-plane epitaxial relationship.
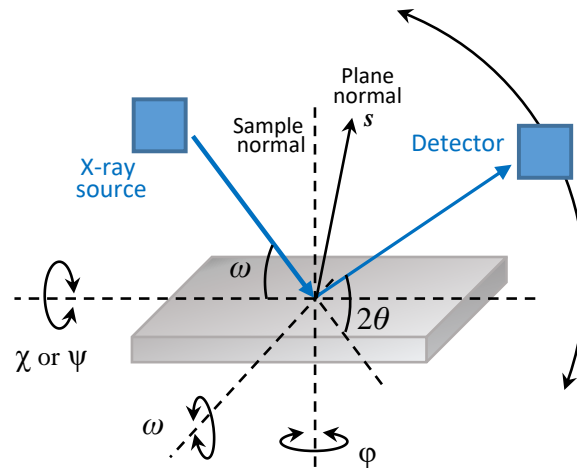
Figure 2.4 (a) Illustration of sample axes of rotation and rotation angles determining various scan types in a thin film XRD measurement. Here ω represents the angle between the incoming X-ray beam and its projection on the sample surface. The sample rotation around this projection axis determines angle χ, while ϕ can be altered by the sample rotation around its normal. 2θ refers to the angle between the incident and diffracted beams.

Systems with a two-dimensional (2D) detector (area detector) simultaneously measure the whole or a large portion of the diffraction rings. The captured diffraction ring profile (commonly referred to as a frame) can be considered as the intensity distribution of the diffracted X-rays as a function of both 2θ and χ angles [3]. Therefore, much more information and faster measurements are possible in a 2D X-ray diffraction system. In particular, thin film textures are readily assessed from a 2D XRD since all the texture data and background values appear simultaneously in 2D frames for multiple poles and multiple directions. Figure 2.5 depicts a schematic of a typical 2D diffractometer configuration. Pole figure can also be measured at very fine steps in ϕ angle for sharp textures thanks to the high measurement speed. For the present work, a Bruker D8 Advance diffractometer and a General Area Detector Diffraction System (GADDS) equipped with VANTEC-500 area detector have been used for 2D XRD studies.
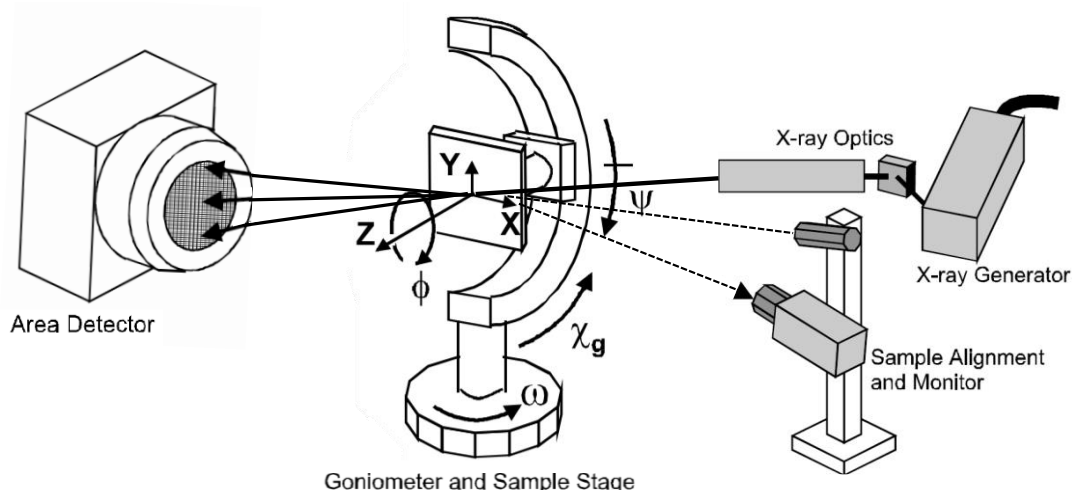
Figure 2.5 Illustration of a 2D XRD system, showing the five major components, i.e., an area detector, an x-ray generator, x-ray optics (monochromator and collimator), goniometer and sample stage, and sample alignment and monitoring (laser/video) system, together with the sample orientation axes (ω, χ_g, ψ, ϕ) and translation axes XYZ in the laboratory system. The angle ω is the base rotation, ψ and χ_g (goniometer chi) have the same horizontal rotation axis but different starting positions and rotation directions. The ϕ rotation axis is always on the Z axis, which is typically normal to the sample surface in reflection mode diffraction. Figure adapted from Bob B. He's manual book [4].

2.2.2 Diffraction using synchrotron radiation

Having covered the XRD techniques that can be readily obtained from conventional laboratory diffractometers, we now introduce into synchrotron radiation (SR), attempting to convey the most important aspects relevant to the current study. For a better understanding of SR theory, the reader is referred to the work of Willmott [5].

Briefly, the typical synchrotron source consists of a linear electron accelerator that produces and pre-accelerates electrons, a booster ring where the projected electrons are further accelerated, an evacuated storage ring. Within the storage ring, the high-energy electrons circulate on a closed path at highly relativistic velocities, and the synchrotron light (electromagnetic radiation) is produced by different types of *sources* which include bending magnets and insertion devices such as wigglers or undulators. The radiation is then normally focused and/or monochromatized using X-ray optics at the *beamlines* positioned tangential to the storage ring, where experiments are performed with the selected radiation.

The tunability and high brilliance of synchrotron X-rays offers greater possibilities compared to conventional X-ray sources. One of the most important advantages of SR is its high *brilliance*, a term which takes into account several variables: the photon flux, the collimation of the beam (i.e., how the beam diverges as it propagates), as well as the size of the source. Such highly intense radiation permits high resolution X-ray analysis and rapid acquisition of

data from small volumes of samples. Furthermore, some experiments may require special measurement conditions, such as *in situ*, and controlled ambient setups including cryogenic coolers, high-temperature furnaces, and high-pressure anvil cells, which are accessible at most synchrotron-based diffraction stations, yet generally cannot be implemented in a conventional laboratory-based diffractometer.

Synchrotron X-ray powder diffraction (SXPD) involved in this thesis were collected at the BL04-MSPD beamline of the ALBA Synchrotron Light Facility (Barcelona, Spain). The samples under study were loaded into borosilicate glass capillaries (diameter of 0.5 mm) and then mounted on an ALBA designed 4-capillary holder. The samples kept spinning during data acquisition using an X-ray wavelength λ= 0.412 84(6) Å. The value of λ was calibrated using standard silicon. Most of the patterns were collected at 300 K using a MYTHEN position sensitive detector, while the temperature dependent SXPD measurement for selected samples were performed with either a Dynaflow liquid He cryostat (10-300 K) or an Oxford Cryostream (80-450 K) or a FMB Oxford hot air blower (above 300 K). Rietveld XRD refinements were carried out using the FULLPROF program.

The high-temperature high-pressure SXPD measurements were collected at the High Pressure endstation located at the same beamline. The powder sample to be investigated was mounted into a resistively heated membrane diamond anvil cell (DAC) consisting two diamonds faced one to each other. Between them, we used a gasket with a hole in the middle, which defines the pressure cavity where the sample is placed. The pressure inside the cavity is obtained by measuring the fluorescence signal of the calibrant ($Sm:SrB_4O_7$) inserted into the pressure cavity [6]. The applied pressure P is controlled by the membrane of the DAC which is inflated applying force to the mobile anvil whereas the other diamond is fixed and the pressure is monitored by the calibrant.

2.2.3 X-ray reflectivity

Aside from the above-mentioned X-ray scattering, refraction and absorption of X-rays are also important phenomena involved in the interaction of X-ray with matter. It is known that for X-rays impinging on a smooth surface at an angle below a certain critical angle θ_c (typically in the range of 0.1-0.5 °), *total external reflection* will occur. In the X-ray reflectivity (XRR) measurement, the reflected X-ray intensity is recorded at very low incident angles, close to the critical θ_c, e.g., 2θ= 0.5° to 6° typically used in this thesis. As shown in Figure 2.6(a), the incoming X-rays will be partially reflected from the upper layer surface at the same angle, and some of them may transmit through the film and get reflected at the interface between the layer and substrate. The interference of X-rays reflected from the top and the bottom of the thin film

occurs as the detector position is changed. This causes oscillations of the reflected intensity, the so-called "Kiessig fringes", in the reflectivity profile. As a surface-sensitive technique, XRR essentially probes contrast in the average electron density, therefore offers a non-destructive tool to access the thickness, surface roughness and density of thin films and multilayers.
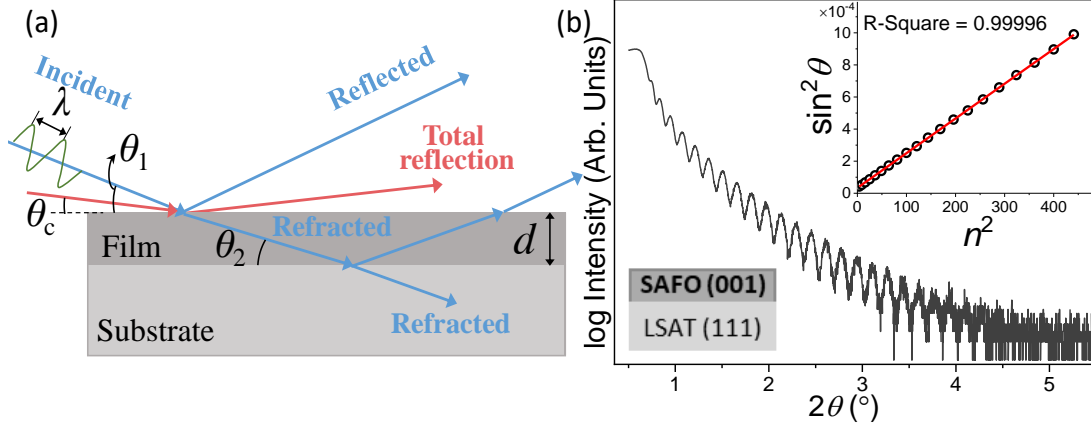
Figure 2.6 (a) Illustration of X-ray reflection when an incident X-ray beam impinges on a homogeneous thin layer of thickness d grown on a flat substrate. The red lines with arrow indicate total reflection at the critical angle θ_c. θ_1 and θ_2 are the incident and transmitted angles, respectively. The interference between X-ay beams reflected at the top and bottom surfaces of the film gives rise to so-called "Kiessig fringes" as the detector position changes. Note that the angles denoted here do not reflect the real cases. (b) A representative XRR profile of a Sc and Al codoped ε-Fe_2O_3 thin film grown on LSAT substrate (see Chapter 5). The inset shows the $sin^2\theta_n$ versus n^2 plot used for determining the film thickness.

As an example, Figure 2.6(b) shows the XRR profile acquired on a Sc and Al codoped $Sc_{0.2}Al_{0.4}Fe_{1.4}O_3$ (001) epitaxial thin film grown on $(LaAlO_3)_{0.3}$-$(Sr_2AlTaO_6)_{0.7}$ (111) [LSAT(111)] substrate (see Chapter 5 for further details). The peak positions of the Kiessig fringes are determined according to the following expression:

$$sin^2(\theta_n) = sin^2(\theta_c) + n^2\left(\frac{\lambda}{2d}\right)^2 \quad (2.3)$$

where θ_c is the critical angle, θ_n represents the peak positions, n is the order of the peak, λ is the wavelength and d is the thickness of the layer. Thus the d can be determined from the slop of the fitted $sin^2\theta_n$ versus n^2 plot. The obtained thickness of the $Sc_{0.2}Al_{0.4}Fe_{1.4}O_3$ (001) thin film is 58 nm (see the inset of Figure 2.6(b)).

2.2.4 X-ray absorption spectroscopy

We now introduce into X-ray absorption and X-ray absorption spectroscopy (XAS), which constitute the basis for X-ray magnetic circular dichroism (XMCD) that we will address in some detail afterwards. In order to perform these experiments, SR sources are generally required to provide highly intense and tunable X-ray beams (in terms of both photon energy

and polarization). The XAS and XMCD experiments were carried out at the BL29-BOREAS beamline at the ALBA Synchrotron Light Facility (Barcelona, Spain) in close collaboration with Dr. Javier Herrero-M\artín from ALBA Synchrotron.

In an X-ray absorption event, we are mainly concerned with absorption coefficient μ, which is governed by the Beer-Lambert law for linear absorption which takes the form

$$I = I_0 e^{-\mu d} \tag{2.4}$$

where I_0, d, and I are the intensity of incident X-rays, sample thickness, and transmitted intensity through the sample, respectively. In general, μ strongly depends on the X-ray photon energy E, and varies approximately as

$$\mu(E) \approx \frac{\varrho Z^4}{A E^3} \tag{2.5}$$

where ϱ denotes the sample density while Z and A are the atomic number and the molar mass, respectively. Hence, μ is not only material specific but also decreases with increasing photon energy E. However, if this energy is in the region of the so-called absorption edges of a certain element, where it matches the binding energies of core electrons, a new absorption channel is available in which the photon is annihilated thereby creating a photoelectron and a core-hole. As a result, an abrupt increase of X-ray absorption takes place, as can be seen from the X-ray absorption spectrum for Pb in Figure 2.7(a). The absorption edges are named according to the principal quantum number n of the electron that is excited: K-, L- and M-edges corresponds to n=1, 2, 3 inner-shell electrons, respectively. Each absorption edge represents a different core-electron binding energy in the atom. A closer look at the L-edge (see the inset of Figure 2.7(a)), however, reveals that the L-edge presents three distinct closely lying "sub-edges", namely, L_1, L_2, and L_3 in order of decreasing energy. The L_1 is from the excitation of a 2s electron, while the 2p excitation is split into two edges, L_2 and L_3, as a result of the spin-orbit coupling energy of the 2p^5 configuration that is created when a core-shell 2p electron is excited. The higher energy of the 2p^5 excited states is the 2$p_{1/2}$ term; This gives rise to the L_2 edge. At lower energy is the L_3 edge, corresponding to the 2$p_{3/2}$ excited state.

Subsequent to the excitation of the core electron, the core-hole is filled up by an electron from a higher energy state. The corresponding energy difference is released mainly via characteristic fluorescence X-ray or Auger electron emission. Both the two decay channels can be exploited as the basis for absorption measurement, which we will discuss later.
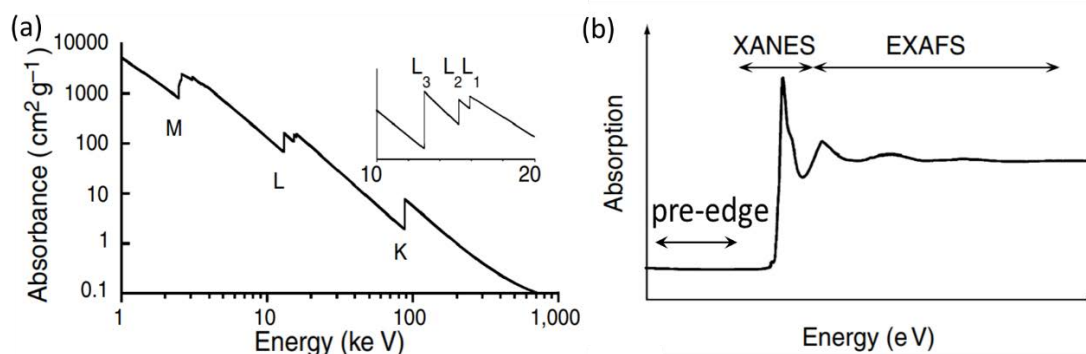
Figure 2.7 (a) Low-resolution X-ray absorption spectrum for Pb across its *K*-, *L*- and *M*-edges, corresponding to excitation of an electron from *n*= 1, 2 and 3 shells, respectively. At higher resolution (inset) both the *L* and the *M* edges are split. (b) Schematic illustration of an X-ray absorption spectrum around a core-electron absorption edge, showing the important regions. The pre-edge region is due to the transitions of core electrons to empty bound states. X-ray absorption near-edge structure (XANES) lies in the region around the absorption edge, while the extended X-ray absorption fine structure (EXAFS) manifesting a series of oscillations is located at energies ranging from about 50 eV above the edge to as high as 1000 eV. (Figures taken from Reference [7].

X-ray absorption spectroscopy (XAS) involves the measurement of X-ray absorption cross-section at energies near and above the binding energy of core-level electrons of an element. Figure 2.7(b) depicts schematically a typical X-ray absorption spectrum around an absorption edge. The important regions with different features can be observed. The pre-edge region lies below the edge and is due to the transition of a core electron to empty bound state. The other two important regions are referred to as X-ray absorption near-edge structure (XANES) and extended X-ray absorption fine structure (EXAFS). XANES covers the range in the vicinity of the edge, while EXAFS, which is featured by continuous oscillations, extends from 50 eV above the edge to 1,000 eV or more [1]. Moreover, unlike the XANES region, which is sensitive to the oxidization state and electronic structure of the detected atom, the EXAFS region reflects the radial distribution of electron density around the absorbing atom and is used for quantitative determination of bond length and coordination number [7].

In terms of the measurement of XAS, the simplest method is the so-called transmission mode, where the intensities of the incident and the transmitted X-ray beams are measured. This approach is normally applied for XAS involving hard X-rays (*E*> 3keV) due to the larger mean free path of photons. In the soft X-ray range (E< 1 keV), on the other hand, the transmission scheme can be tricky owing to the thickness effect (variation in thickness or pinhole) and the short attenuation length, requiring the sample under study to be homogeneous and extremely thin. To circumvent the above-mentioned, XAS spectra are frequently measured in the fluorescence mode, in which the intensities of the incident beam and the fluorescence X-rays

---

[1] The dividing energy between XANES and EXAFS is not universally defined, as the transition between ''near-edge'' and ''extended'' structure is gradual.

emitted from the element of interest are detected. Providing the sample is diluted or thin, the intensity of the fluorescence X-rays is proportional to the X-ray absorption cross-section. Although it is more complicated to detect the fluorescence signal than measuring the transmitted intensity, the big advantage of the fluorescence yield (FY) scheme is its ability to study highly dilute and non-homogeneous samples, which is impossible in the transmission mode. Instead of detecting the fluorescent X-rays, one can also measure the electrons emitted from the sample such as the ejected photoelectrons, secondary electrons and Auger electrons, which is known as total electron yield (TEY) mode. The most distinct feature of the electron yield mode is its surface sensitive nature (probing depth is approximately 3-10 nm for TEY, depending on the element), ascribed to the relatively shorter mean free path of the electrons. Electron yield detection of XAS is particularly beneficial for measuring absorption in the soft X-ray regime where the filling of the core-hole is accompanied mainly by Auger electron emission and only to a much lesser extent by fluorescence X-ray emission.

In this thesis we are concerned with the XAS spectra of the magnetic $3d$ transition-metal L-edges (in particular the Fe $L_{2,3}$-edge), probing the transitions of $2p^6$ core electrons into $3d$ valence holes ($2p^63d^n \rightarrow 2p^53d^{n+1}$). Similar to the Pb L-edge, the Fe L_2-edge is due to the $2p_{1/2}$ and the L_3-edge is due to the $2p_{3/2}$ core level. They can be found in the energy range from 700 eV to 740 eV, which can be easily accessed by soft X-rays (E< 1 keV).

2.2.5 X-ray magnetic circular dichroism

X-ray magnetic circular dichroism (XMCD) is a spectroscopic X-ray technique that probes the difference in X-ray absorption of the right- and left- handed circularly polarized X-rays by a magnetic material. This difference is strongly enhanced near the absorption edges of core levels, therefore element specificity can be guaranteed by tuning the X-ray energy to the characteristic absorption edges of magnetic elements.

Compared to classical magnetometry techniques (see Section 2.5), XMCD spectroscopy is particularly useful for extracting detailed information on the local magnetic state by distinguishing between the spin and orbital magnetic moments of an atom. Taking the $3d$ transition metals as an example, such magnetic dichroism can be seen as a result of the spin-dependent electronic excitation from $2p$ to unoccupied $3d$ states, whose spin asymmetry is closely linked to the ferromagnetism of the magnetic ions. The photon transfers its angular momentum to the core electron in the absorption process. In the case of the spin-orbit split $2p$ level, such as the L_2 and the L_3 edge of $3d$ transition metals, the angular momentum of the electron will be partially transferred to its spin through the spin-orbit coupling. Left-handed (right-handed) circularly polarized photons excite more spin-up (spin-down) electrons from the

$2p_{3/2}$ level (L_3 edge), whereas the opposite is true for the $2p_{1/2}$ level (L_2 edge) due to the opposite spin-orbit coupling. In other words, the spin-polarized photoelectrons are excited to an empty $3d$ valance band which can act as a detector of their angular momenta. Finally, from the difference of XAS spectra recorded with X-rays of opposite helicities (i.e., the XMCD spectrum), the spin and orbital magnetic moments can be obtained separately using the *sum rules* developed by Thole and coworkers [8],[9].

For the XMCD experiments conducted in this Thesis, the magnitude of the applied magnetic field was 6 T provided by a superconducting magnet. The sample was irradiated with circularly polarized photons, using a cryostat allowing sample temperatures down to ~ 2 K. The spectra were recorded in the Total Electron Yield (TEY) mode by measuring the drain current of the electrically isolated sample.

2.3 Neutron powder diffraction

Complementary to X-ray scattering, neutron scattering has been a primary tool for the microscopic characterization of the structural and magnetic properties of matter. Especially, for the study of multiferroics, neutron diffraction plays a unique role, since it probes both magnetic ordering and the subtle atomic displacement associated with ferroelectricity. We will introduce into this technique in this section, focusing on powder diffraction.

2.3.1 Neutron vs X-rays

Neutron scattering is a powerful tool to study the structure and dynamics of condensed matter. Although both carrying no electrical charge, in contrast to X-rays (electromagnetic waves or photons), neutrons are subatomic particles. Unlike X-rays, which are primarily scattered at the electrons of atomic shells via electromagnetic interaction, neutrons interact with atomic nuclei via very short-range strong nuclear interaction (nuclear scattering). Neutrons are therefore able to penetrate deeply into bulk matter without being scattered or absorbed. Another distinct aspect of neutrons is that they carry a magnetic moment with spin 1/2 that will interact directly with the unpaired spin and orbital magnetic moments of atoms via magnetic dipole interactions (magnetic scattering), which makes neutrons a sensitive probe for studying microscopic magnetic properties of solids.

The measure of the strength of the neutron-nucleus interaction is represented by neutron scattering length, which depends sensitively on the details of the nuclear interaction, and thus on the nuclear properties (isotopes, nuclear spin, energy levels, etc.) of every particular type of

nucleus (i.e., element and isotope). As a result, the neutron scattering length varies seemingly irregularly across the periodic table. This can be seen from Figure 2.8 showing the neutron scattering length of elements [1]. For comparison, the almost linear evolution of X-ray scattering length, which is a measure of X-ray scattering power of an atom, with atomic number Z at photon energy of 10 keV is also plotted. The irregular variation of neutron scattering length means that, in contrast to X-rays, neutrons are uniquely sensitive to some light elements, such as hydrogen and oxygen. Further, in many cases, elements having similar Z values in the periodic table can have vastly different neutron scattering lengths from one another. Because of this differing atomic sensitivities with X-rays, together with its unique magnetic sensitivity, neutron is often regarded as a complementary probe to photon-based methods. In particular, in the current study this concerns the excellent contrast in the scattering length of Fe with that of its adjacent Mn and Co, as well as with Cr, Ru, or In (see Figure 2.8). Therefore, neutron scattering is ideally suited for exploring the atomic and/or magnetic structures of metal-substituted $\varepsilon\text{-}(Fe_{1-x}M_x)_2O_3$ (M= Cr, Mn, Co, Ru, and In) nanoparticles.
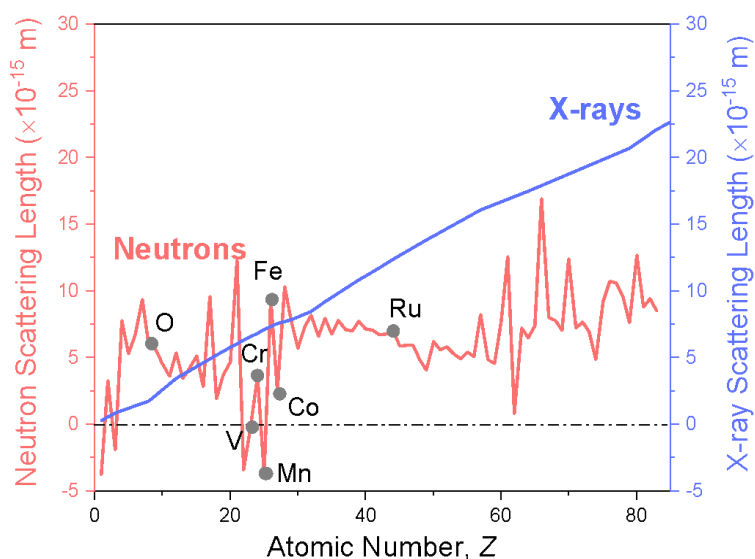
Figure 2.8 Complementarity of neutrons and X-rays. Neutron scattering length of elements, where the negative sign means that the scattered neutrons wavefunction is out of phase with respect to the incident neutrons wavefunction. X-ray scattering length at photon energy of 10 keV is also plotted for comparison. While scattering power of X-rays generally scales systematically with electron density and therefore with the atomic number Z of an atom, neutron scattering power from atoms is rather random, due to complicated short-range nuclear interaction between neutron and nuclei.

2.3.2 Neutron powder diffraction

Neutron diffraction is based on elastic scattering, where the scattered neutron energy is the same as the energy of the incident neutron beam, and is arguably the most straightforward among all neutron scattering techniques. In the current project, we used neutron powder

diffraction (NPD) as a nondestructive tool to probe the nuclear and magnetic structures of our powdered samples. From a neutron powder diffraction experiment, one can extract crystal structure information such as crystal lattice symmetry and the unit cell parameters. In addition, the fractional coordinates and occupation factors, as well as the chemical nature of the component atoms within the unit cell can also be derived with very high precision, thereby providing reliable information on the interatomic bond distances, angles and thermal displacements of the atoms. Finally, the magnetic structures, such as magnetic space group, moments and propagation vector, can also be determined.

2.3.3 Neutron diffraction instruments

The involved NPD experiments were performed at the two-axis diffractometers located at the D20 and D2B beamlines of the Institut Laue-Langevin (ILL) in Grenoble, France, in close collaboration with Prof. Jose Luis García-Muñoz and Arnau Romaguera from ICMAB. The ILL facility is based on a reactor neutron source where fission reactions take place in the nuclear reactor. The produced high-energy neutron beam then will be modulated into three types of neutrons classified by their energy, i.e., cold neutrons (energy $E < 10$ meV or wavelength $\lambda > 2.9$ Å), thermal neutrons (10 meV $< E < 100$ meV or 0.9 Å $< \lambda < 2.9$ Å), hot neutrons (100 meV $< E < 500$ meV or 0.4 Å $< \lambda < 0.9$ Å). Both the D20 and D2B beamlines utilize the H11 thermal beam tube. For clarity, a schematic of the high-flux D20 instrument layout is shown in Figure 2.9(a). The thermal beam then reaches one of its four monochromators that are employed to select the energy of interest from the incident neutron beam. The monochromatic beam leaves the monochromator shielding by one of its five take-off ports, each offering a different instrument resolution. It then reaches the fine powder sample that diffracts it in different directions. The samples are sealed in a vanadium metal cylindrical can (very low neutron scattering length, see Figure 2.8), which is placed in a cryostat or furnace. The diffracted beams are simultaneously counted by the large ^{3}He based microstrip position sensitive detector (PSD), as shown in Figure 2.9(a). The counts are accumulated during a certain time to give a powder diffraction pattern with a suitable intensity. For the NPD experiments at D20, we have utilized the thermal neutron flux with a selected wavelength of either $\lambda = 2.4$ Å (pyrolytic graphite HOPG (002) monochromator at take-off angle of 42°) or $\lambda = 1.54$ Å (germanium (113) monochromator at take-off angle of 90°). The experiments were conducted at both low and high temperatures.
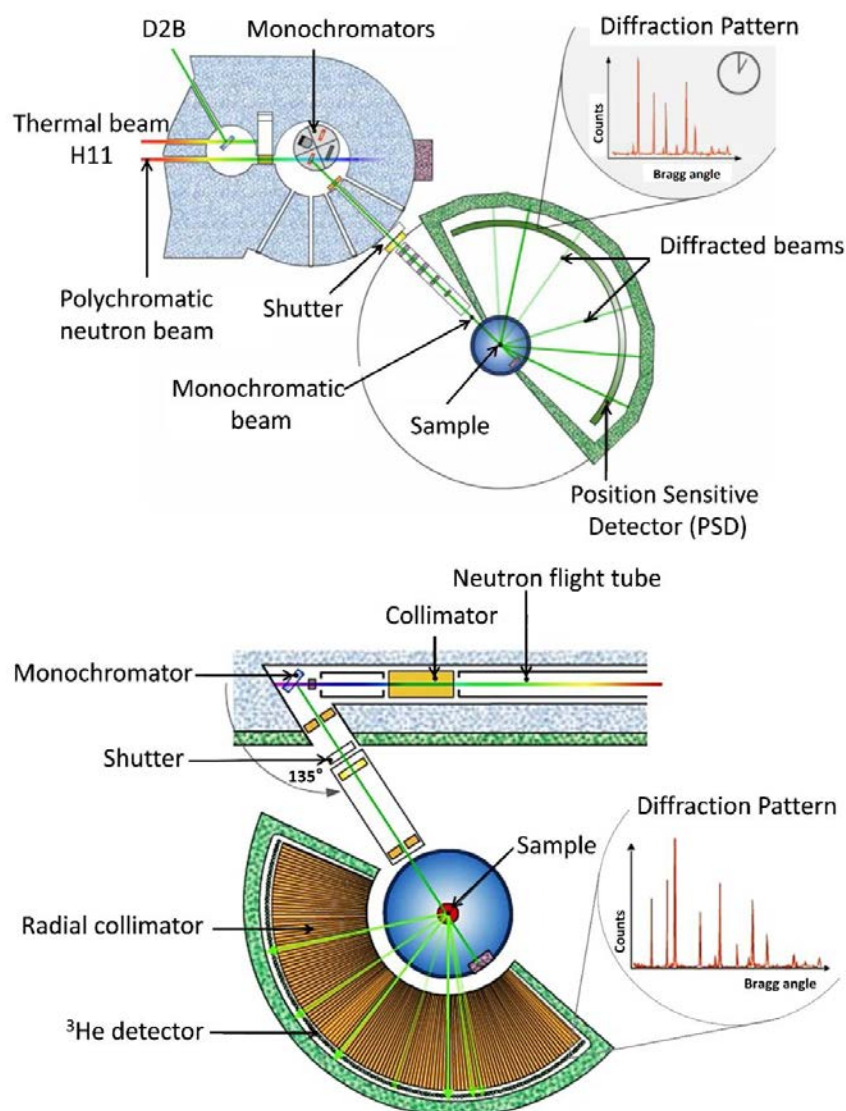
Figure 2.9 Schematics of the instrument layout for the (a) D20 and (b) D2B beamlines (ILL, Grenoble). Figures adapted from the ILL D20 (https://www.ill.eu/users/instruments/instruments-list/d20/description/instrument-layout/) and D2B (https://www.ill.eu/users/instruments/instruments-list/d2b/how-it-works/simulated-experiment/) instrument pages.

On the other hand, the D2B diffractometer is a high-resolution two-axis diffractometer, characterized by a very large monochromator take-off angle of 135°. Figure 2.9(b) depicts the layout the high-resolution D2B instrument at ILL, Grenoble. The large value of the monochromator angle together with the use of radial collimators, placed in front of the ^{3}He detector to select the trajectory of the diffracted neutrons, make it possible to obtain well-defined Bragg peaks at high scattering angles. The polycrystalline powder samples were loaded inside cylinder vanadium cans. The diffraction measurements were carried out at room temperature.

2.4 Electron microscopy and spectroscopy

Distinct from X-rays and neutrons, electrons are negatively charged particles and can thus interact with matter through electrostatic interactions. A wide range of signals can be produced from electron-matter interactions, some of which are summarized in Figure 2.10. Electron microscopy concerns the imaging of a specimen based on the various emitted signals induced by accelerating focused electron beams in a vacuum towards the specimen.

The theoretical resolution, R, of an optical system is given approximately by Abbe's equation

$$R = \frac{0.61\,\lambda}{\mu \sin \theta} \tag{2.6}$$

where λ is the wavelength of the radiation, μ the refractive index of the viewing medium, and θ the semi-angle of collection of the magnifying lens. Thanks to the utilization of electron beams as the probe, which generally have much shorter wavelengths than visible light (note the particle-wave duality of electrons), the resolving power of electron microscopy is greatly improved compared to light microscopy. In an electron microscope, electrons that are accelerated in a potential, V, have a quantifiable wavelength λ given by (see, for example, Reference [10])

$$\lambda = \frac{h}{\left[2m_0 eV \left(1 + \frac{eV}{2m_0 c^2} \right) \right]^{\frac{1}{2}}} \tag{2.7}$$

In this equation $m_0 = 9.109 \times 10^{-31}$ kg is the electron mass, $e = 1.602 \times 10^{-19}$ C is the electron charge and c the speed of light in vacuum (2.998×10^{-8} m/s). To put it into perspective, for example, electrons accelerated at 100 kV have a wavelength of 0.037 Å (Eq. 2.16). This is significantly shorter than the wavelengths of normally used Cu $K\alpha$ X-ray radiation source (1.54 Å). Further, the above equation indicates the inverse relationship between electron wavelength λ and the accelerating voltage V of the electron microscope.
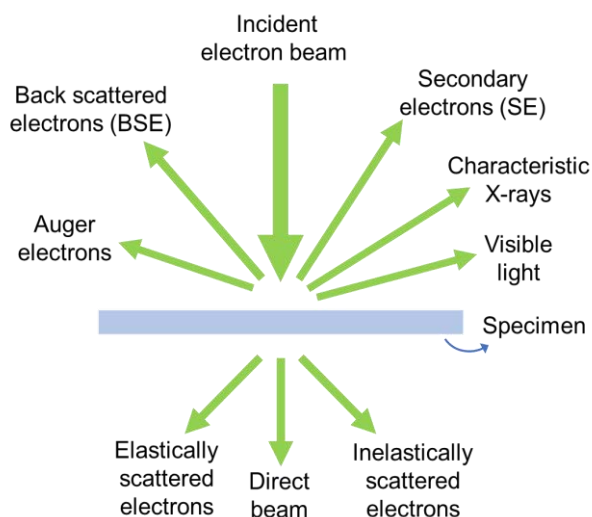
Figure 2.10 Scheme of signals generated from electron-matter interactions when a high-energy electron beam interacts with a thin specimen. The directions shown for each signal do not represent the physical direction of the signal. The signal below the specimen is only abundant if the specimen is ultrathin.

Nowadays, electron microscopy and its various associated spectroscopic methods represent indispensable tools to gain insights into the structure, morphology and composition of a specimen, together with its chemical and electronic information. In this section we cover the basic principles of scanning electron microscopy (SEM) and transmission electron microscopy (TEM). As the core spectroscopic methodologies available in SEM and TEM, the working principles of energy dispersive X-ray spectroscopy (EDX) and electron energy loss spectroscopy (EELS) are described in some detail. In addition, an overview of the TEM specimen preparation techniques that adapted in the current study is present, since they play a very important role in TEM analysis.

2.4.1 Scanning electron microscopy and energy dispersive X-ray spectroscopy

The scanning electron microscope (SEM) is a type of electron microscope that images the sample surface by scanning it with a beam of high-energy electrons. Figure 2.11(a) sketches the major components of an SEM, including electron source, accelerating anode, electromagnetic lenses to focus the electrons, a vacuum chamber housing the specimen stage, and a selection of detectors to collect the signals emitted from the specimen. The electron source is usually either thermionic source (a filament of tungsten or lanthanum hexaboride LaB_6 crystals) or a field emission gun (FEG). Among the signals arising from the electron-matter interactions in SEM, two types of signals are usually used for imaging, namely, the backscattered electrons (BSE) and the secondary electrons (SE) (see Figure 2.10); they can reflect the surface topography and compositional distribution, respectively.

Energy dispersive X-ray spectroscopy (EDX) is spectroscopic technique commonly used in conjunction with SEM. This technique is based on the measurement of the energy of characteristic X-rays emitted from a specimens under study. These characteristic X-rays are recorded by an energy dispersive spectrometer to produce an EDX spectrum, from which one can extract compositional information of a sample.

In this Thesis, a QUANTA FEI 200 FEG-ESEM model SEM microscope was employed for most of the SEM-EDX analysis. It is equipped with a field emission gun (FEG) for optimal spatial resolution and an EDX detector for chemical analysis. Unless otherwise stated, the microscope was operated high vacuum (HV) condition with 10-mm working distance and an accelerating voltage of 30 kV.
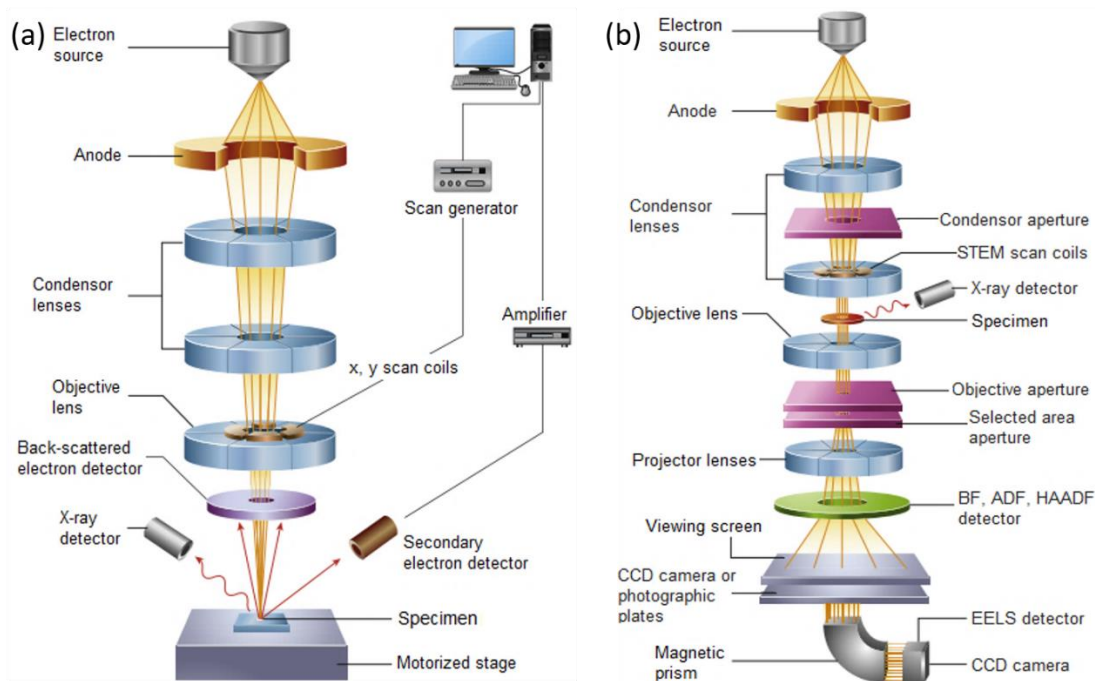
Figure 2.11 Schematic diagram of the major components of (a) SEM and (b) TEM microscopes. Figure adapted from Reference [11].

2.4.2 Transmission electron microscopy and electron energy loss spectroscopy

By virtue of its versatility and extremely high spatial resolution, transmission electron microscope (TEM) has been implemented in the study of samples of both nanoparticle and thin film. The higher spatial resolution of TEM is due to the shorter electron beam wavelength ascribed to larger accelerating voltages, and to the electromagnetic lenses used to converge the electron beams.

Figure 2.11(b) shows some of the major components of a TEM microscope. The electron beam generated by the electron source is accelerated by an anode, focused and guided by the condenser lenses as traveling through the vacuum column of the microscope. The monochromatic electron beam then in part transmits through the ultrathin specimen under study and in part scatters with it. The transmitted electron beam carrying information about the specimen is focused by the objective lens system to form images and diffraction patterns. Compared to SEM, TEM has another additional lens— the projector lens, which is used to magnify the image/diffraction patterns on the viewing screen, or on a layer of imaging plate, or to be detected by a CCD camera.

In the traditional TEM operation mode, the first two condenser lenses before the specimen are adjusted to illuminate the specimen with a parallel beam of electrons. This parallel-beam operation mode is used primarily for TEM imaging and selected-area diffraction (SAD). On the other hand, by a modification on the electron optics, one can use the convergent beam to illuminate the specimen and collect data by raster scanning over the area of interest. This mode is used mainly for scanning TEM (STEM) imaging, analysis via X-ray and electron spectrometry, etc.

One key advantage of STEM is the possibility of using multiple detectors to obtain simultaneous information from different beam-matter interactions. Figure 2.12 shows the positions of the various electron detectors that can be installed in a STEM system. Depending on the scattering angle of the transmitted electrons being detected, the STEM images formed can be called bright-field (BF) image, annular dark-field (ADF) or high-angle annular dark-field (HAADF) image. The ADF detector is annularly shaped to maximize the collection efficiency. Compared to ADF, the annular HAADF detector detects electrons that are scattered to higher angles and almost only incoherent Rutherford scattering contributes to the image. Thereby, Z contrast (atomic number) might dominate the dark-field image. Especially, with the advent of aberration correction technology, the HAADF imaging can provide atomic-resolution images, enabling Z-contrast on the atomic scale.
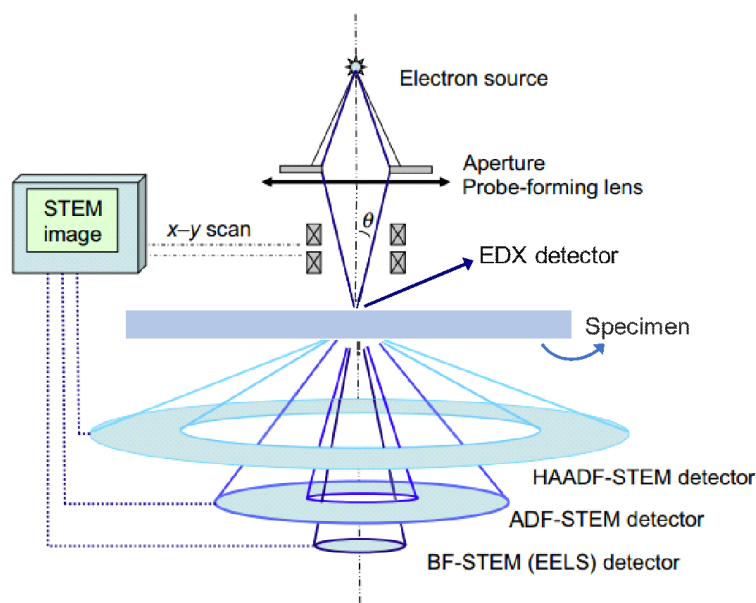
Figure 2.12 Schematics of the arrangement of the various electron detectors for the STEM mode operation in a TEM, showing the BF, ADF and HAADF detectors. Figure adapted from Reference [12].

Chemical analysis is also possible in TEM through addition of peripheral equipment with EDX capability or an electron spectrometer for electron energy-loss spectroscopy (EELS), as seen from Figure 2.12. It is known that inelastic electron scattering from electron-matter interactions causes the primary electrons to lose energy, which can be detected by passing the transmitted electrons through a magnetic prism to disperse the electrons according to their energy losses (see Figure 2.11(b)). Finally, the energy distribution of electrons can be counted to form an EELS spectrum. Such spectra reflect the local sample composition with atomic resolution through the detection of the absorption edges of the different elements as in XAS (Section 2.2.4) and thus are also sensitive to local electronic structure and chemical bonding.

Thus far, we have provided a brief description of TEM, the reader is direct to the specialized books by Williams and Carter for more comprehensive discussion of this topic [10]. In the following, we will turn our focus to TEM sample preparation.

Specimen preparation is an important part of TEM analysis. To be analyzed by a TEM, the specimen should be thin enough (typically less than 100 nm in thickness) to be electron transparent. On the other hand, the specimen to be investigated should be mechanically robust for handling. So, TEM specimens are usually either self-supported or mounted on a grid for analysis. For nanoparticle samples, we used standard procedures consist of drop-casting and drying a particle suspension on a TEM Cu grid. To avoid the formation of nanoparticle aggregates, the particle suspension was subject to bath-ultrasonication for several minutes prior to the drop-casting.
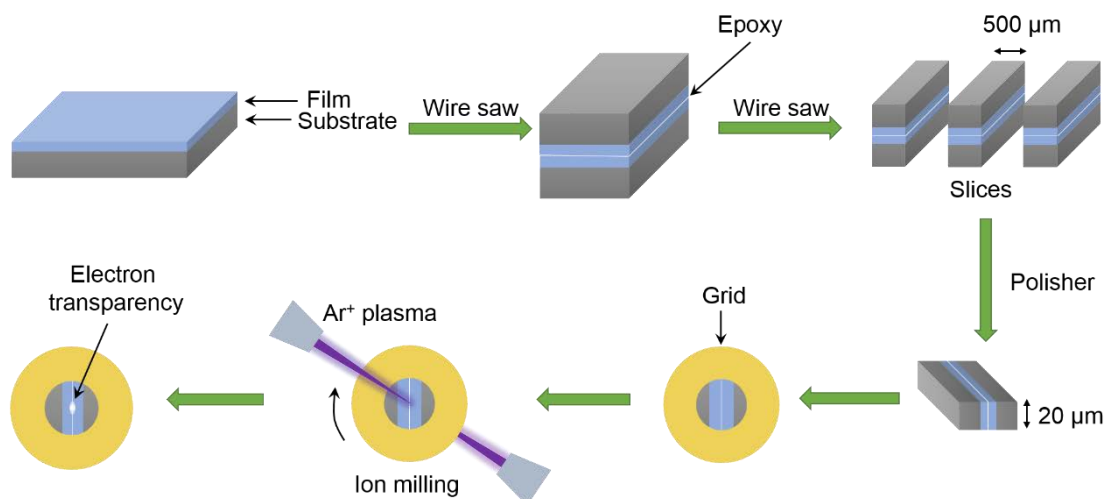
Figure 2.13 The schematic diagram of the main procedures for producing a cross-section TEM specimen. A variety of specimen support grids of different mesh size and shape are commercially available. For simplicity, a typical 3-mm-diameter TEM grid with a single circular slot was represented in the sketch. The final ion thinning is achieved with the specimen rotating and until a small hole is opened at the center of the specimen, guaranteeing an electron-transparency region

For the thin film samples, it involves the TEM sample preparation in both cross-sectional and plane-view configurations. Most of the cross-section specimens have been prepared by a conventional specimen preparation procedure that involves cutting, polishing and ion milling, as shown in Figure 2.13. The basic principles can be detailed as follow: First, the sample to be viewed by TEM is cut using vertical diamond wire cutter (Precision Diamond Wire Saw 3242, Well Diamond Wire Saws Inc.), and then glued together to produce a sandwich-like structure with the film layers contacted face-to-face with epoxy glue. In order to make the epoxy thin enough, the sample is pressed during heat treatment at 130 °C for around 3 hours. One can then cut the glued sections into slices with each having a thickness of about 500 µm using a wire saw. Next, the chosen slice can be thinned mechanically to a thickness of less than 20 µm using a MultiPrep^{TM} precision polishing system. Subsequently, the thin specimen is glued on suitable TEM Cu support grid. Finally, the specimen is thinned down to electron transparency using a precision ion polishing system (Gatan model 691) with two ion guns of Ar^+ beams at an angle of 7 °. During the ion milling, the specimen is kept rotating, and an initial accelerating voltage of 5 keV is used, which is then gradually reduced to a final beam energy of 2 keV during the milling process in order to minimize ion implantation, which could lead to chemical modifications and amorphization in the near-surface region.

For the ε-Fe_2O_3 thin films grown on cleavable mica substrate, special care was taken to prepare a plane-view TEM specimen. More specifically, instead of using the mechanical polishing, the substrate was thinned to tens of micrometers by firstly cleaving the mica using a sharp blade and then exfoliating it with scotch tape, before it was mounted on a TEM grid. Moreover, unlike

for the cross-sectional preparation, where both the top and bottom sides were ion milled (see Figure 2.13), the dual ion sources are focused at the bottom side of the substrate in this case. The other side of the film is covered with a piece of glass to avoid any contamination by redeposition from the sputtered backside.

The focused ion beam (FIB) method was used for preparing a TEM cross-section sampling of ε-Fe_2O_3 thin films grown on mica substrate, to which the above-mentioned preparation method cannot be easily applied due to the difficulty in handling the very thin (less than $0.2\,\mu m$) layered mica substrate. Although operating in a similar fashion to a SEM, FIB technique uses a finely focused gallium ion beam that can be used for ion milling. The combination of FIB with a SEM allows site specific sputtering or ion milling of specimen with high resolution imaging. In a FIB-SEM dual-beam instrument, a thin slab of the sample is cut from the area of interest and mechanically polished as thin as possible. The extracted thin lamella is then mounded on a special holder and further thinned by the use of charged ions.

2.5 Magnetic characterization

Complementary to the above-mentioned magnetic neutron diffraction (see Section 2.3) and (XMCD) technique (see Subsection 2.2.5), macroscopic magnetic measurements have been carried out to probe the magnetic responses of the powder or thin film samples to temperature and external magnetic field. The measurements were performed using a superconducting quantum interference device (SQUID) magnetometer and/or a vibrating sample magnetometer (VSM) both from Quantum Design. The basic principles of these methodologies are covered in the following subsections, along with a description of most relevant sample preparation procedures.

2.5.1 Superconducting quantum interference device magnetometry

SQUID magnetometers have an extremely high sensitivity (in the order of 10^{-7} emu, 1 emu= 10^{-3} A$\cdot$m^2) and are thus commonly used experimental tools to study the magnetic properties of a range of magnetic materials including nanoparticles and thin films. The SQUID measurements in the present work were carried out in a commercial magnetic property measurement system MPMS-XL (Quantum Design Inc.) magnetometer from the Low Temperature and Magnetic Service of ICMAB.
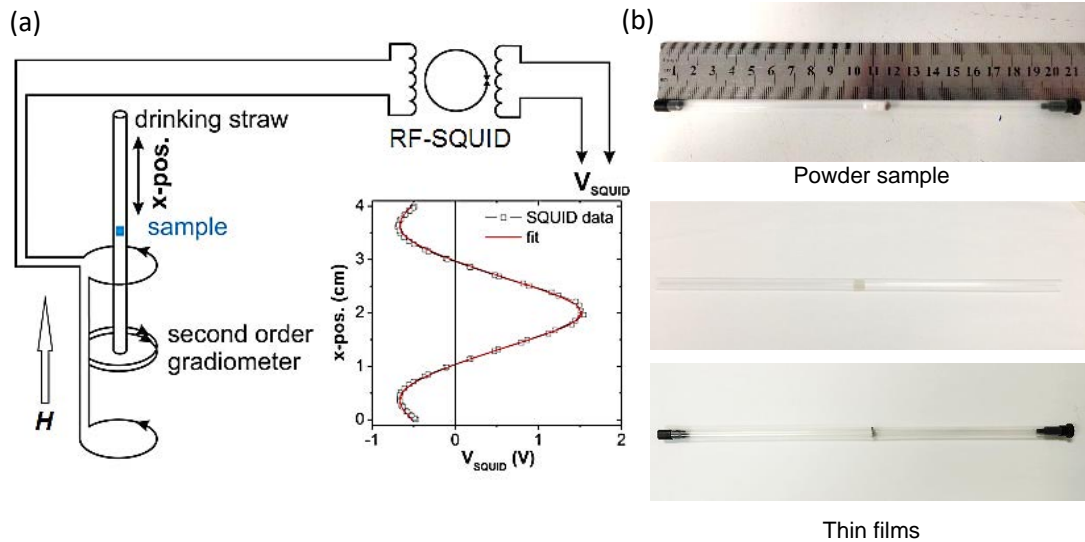
2.14 (a) Schematic setup of a SQUID magnetometer with an RF-SQUID and a second-order gradiometer. The inset shows the SQUID response V_{SQUID} versus sample position (x-pos.) from a single SQUID scan. Figure adapted from reference [13]. (b) A photo of a powder sample mounted inside a capsule holder for subsequent SQUID magnetic measurements (top). Film-on-substrate samples in straw sample holders with the in-plane (middle) and out-of-plane (bottom) geometries are also shown.

A basic schematic of a SQUID magnetometer used in Quantum Design MPMS is shown in Figure 2.14. One important component of the SQUID magnetometer is the second-order gradiometer, comprising four single-turn superconducting pickup coils. In order to suppress the influence of external magnetic interference, the four pickup coils are connected, with the currents in the two central coils circulating clockwise while in the more external ones the current sense is anticlockwise. The second-order gradiometer is electrically connected to a radio frequency type RF-SQUID device, the basic element of the magnetometer (see Figure 2.14). In practice, the RF-SQUID is a ring of superconducting metal separated by a small insulating barrier (forming the so-called Josephson junction), allowing one to precisely probe the magnetic flux variations passing through the ring by recording directly the resulting voltage V_{SQUID} across the SQUID.

The basic principle is as follows: the sample inside a sample holder (e.g., a drinking straw) is vertically oscillated inside the four pickup coils, creating magnetic flux variations. The resulting changes of flux are coupled into the SQUID loop and consecutively converted to measurable V_{SQUID} using the RF-SQUID device. Therefore, the voltage V_{SQUID} can be measured as a function of sample position, denoted as the x direction (x-pos.). The inset of Figure 2.14(a) shows an example of a voltage versus position (V_{SQUID}-x-pos.) curve from single SQUID scan, where the maximum of V_{SQUID} at x-pos. of 2 cm corresponds to the sample directly positioned in-between the double coil of the pickup gradiometer. Subsequently, the collected raw voltage versus x position (V_{SQUID}-x-pos.) curve is automatically fit to a model using a complex algorithm to determine the magnetic moment of the sample under study.

The extreme sensitivity of SQUID magnetometry requires proper attention to background noise and sample geometries (such as shape and dimensions) ion order to avoid experimental artefacts. In terms of background noise, sample preparation and mounting prior to data acquisition can be important. This is especially true when measuring nanometer-sized objects with small magnetic moment. So, we now turn to the description of the main preparation procedures that were adopted throughout our SQUID measurement. For the fine powder samples, gelatin capsules were used as sample holders. The powder sample of a known weight was firstly mounted in the center of the capsule, then a certain amount of white cotton fibers was put in the capsule to prevent sample movement within the capsule during the measurement. The capsule was then mounted in a transparent drinking straw. After adjusting the sample position within the straw for an easier sample centering, the straw can be mounted to a SQUID platform. A typical picture of a mounted powder sample ready for measurement is shown in the top panel of Figure 2.14(b).

On the other hand, the studied thin film samples with a typical size of ~5×5 mm^2 were mounted in the drinking straw, where the sample is held in place by no other means than clamping it in-between the walls of the straw. For the magnetic measurements on textured thin films, magnetic field configurations must be specified. In most cases the external magnetic field are applied either parallel (i.e., in-plane geometry, see the middle panel of Figure 2.14(b)) or perpendicular (i.e., out-of-plane geometry, see the bottom panel of Figure 2.14(b)) to the thin film plane.

2.5.2 Vibrating sample magnetometry

In parallel, the vibrating sample magnetometer (VSM) option of a physical property measurement system (PPMS) from Quantum Design has been used to measure magnetic Responses at high temperatures (T ≥ 300 K). The AC measurement system (ACMS) option was also adopted for identifying the low-temperature transition features of the powders. These measurements have been done with the support from the Low Temperature and Magnetic Service of ICMAB.
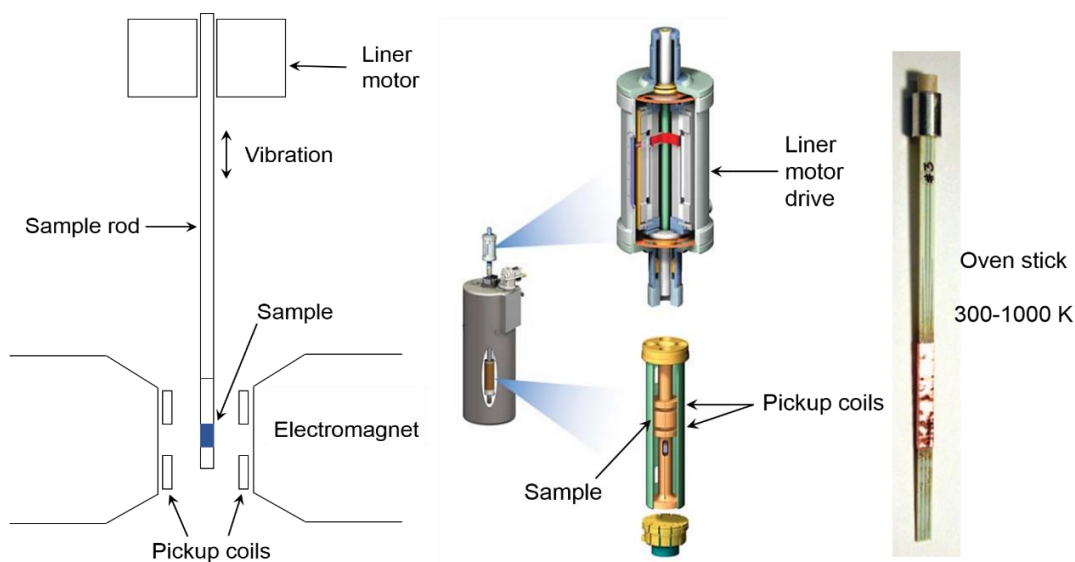
Figure 2.15 (a) A simplified schematic setup of a VSM magnetometer operated using an electromagnet. (b) A PPMS-VSM working in a superconducting solenoid. The oscillating sample motion is provided by a linear motor. Courtesy of Quantum Design, Inc. The rightmost figure shows a VSM oven heater stick sample holder, allowing the operation temperature range up to 1000 K.

The VSM is a fast and sensitive (10^{-6} emu) magnetometer for the determination of the DC magnetization of a material. A simplified schematic setup of VSM is given in Figure 2.15(a). The Figure on the right shows the device configuration of a PPMS-VSM (Quantum Design, Inc.), highlighting the liner motor drive and the pickup coils. In the VSM, the sample loaded on the end of a sample rod is centred between the poles of two electromagnetic pieces, which are used to generate the measuring field H. When the sample is driven sinusoidally along the vertical direction by a linear motor unit extended on the sample rod, an alternating emf (electromotive force) will be generated as a response of the change in magnetic flux linking the coils (Faraday's law). The magnitude of the emf signal is proportional to the magnetic moment of the sample. With appropriate manipulation, one can deduce precisely the magnetic moment of the sample from the output emf.

Equipped with an oven auxiliary, the VSM can make sensitive DC magnetometry measurements at controlled temperatures up to around 1000 K. Prior to the measurement, the powder sample was mounted onto the heater stick (see the rightmost figure of Figure 2.15(b)) using high-temperature Zircar cement as an adhesive. Heating of the sample is realized by applying current to a resistive heating element lithographically patterned onto the heater stick. Meanwhile, the sample temperature is measured by a thermocouple embedded on the back side of the stick. After mounting the powders/cement mixture, they are wrapped using a copper-foil shield with the heater stick to retain the heat and minimize thermal gradients between the sample and the stick.

The AC susceptibility measurements were carried out using the AC measurement system

(ACMS) options of the Quantum Design PPMS. With this option, PPMS can be used as a DC magnetometer or an AC susceptometer. To perform this kind of measurement, powder samples were usually loaded in capsules using cotton to avoid sample motion, as show in the top photograph of Figure 2.14(b).

2.6 Atomic force microscopy

Atomic force microscopy (AFM) is a microscopic technique to measure the surface topography of samples at micro to atomic resolutions. It is based on the attractive and repulsive interaction forces between the tip on a cantilever and a sample, as sketched in Figure 2.16. The flexible cantilever with a small tip at the end raster scans across the sample surface using a piezoelectric tube controlled by a computer.

Two basic measurement modes have been commonly used for surface morphology study: contact mode and non-contact mode. In contact mode, the AFM tip is in direct contact with the sample surface so that the cantilever is bent due to repulsive forces. Non-contact mode is also called dynamic mode or tapping mode, thereby the cantilever is excited into oscillations at resonance frequency so that the tip slightly "taps" on the sample surface and the interaction forces between tip and sample modify the oscillation frequency and amplitude. In both operation modes the position of the cantilever is monitored by a laser signal which is reflected from the cantilever and measured by a position sensitive photodiode (see Figure 2.16). A feedback loop is employed to maintain a constant oscillation amplitude or a constant bending of the cantilever while scanning over the sample surface. The movement of the tip and/or sample in the x, y and z directions is normally applied through piezoelectric actuators. The feedback signal of the necessary adjustment is stored for each position of the sample and is used to generate the image of the surface topography.
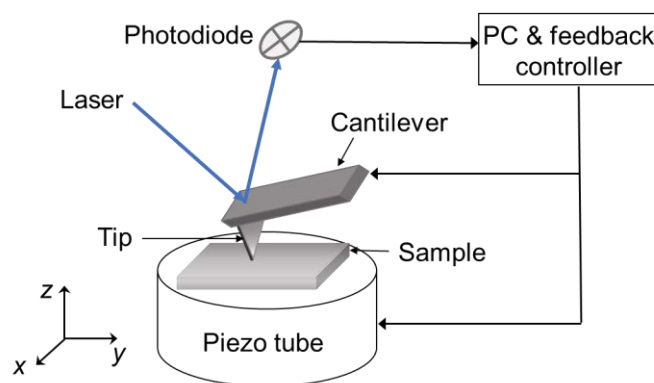
Figure 2.16 Schematic diagram of the working principle of an AFM microscope. The cantilever-tip assembly that raster scans across the sample surface using a piezoelectric tube controlled by a computer. The deflection of the cantilever is monitored using an optical detection system in the form of a laser that reflects off the back of the cantilever and onto a four quadrant photodiode. A feedback loop is employed to continuously adjust the tip-to-sample distance in the z-axis based on the chosen operation mode.

2.7 Raman spectroscopy

This section briefly describes Raman spectroscopy. We begin by touching upon the basic principles of Raman scattering. When a sample is irradiated monochromatic light (electromagnetic radiation) of frequency υ_0, the photons that make up the light may be absorbed or scattered. As depicted in Figure 2.17, the scattered light consists of two types: the Rayleigh scattering and Raman scattering; for both of which, the incident photon is momentarily absorbed by a transition into a "virtual state" and a new photon is created and scattered by a transition from this virtual state into a vibrational energy state. While Rayleigh scattering is elastic and the scattered photon has the same frequency as the incident beam (υ_0), Raman scattering process is far less probable and inelastic, and the energy of the scattered photon is different from that of the incident photon by one vibrational unit. On the basis of the classical arguments of Raman effect (see, for example, Reference [14]]), the associated frequency for Raman scattering is $\upsilon_0 - \upsilon_m$ or $\upsilon_0 + \upsilon_m$ (υ_m being the vibrational frequency of a molecule), which correspond to the *Stokes* and *anti-Stokes* Raman scattering, respectively (see Figure 2.17). According to the Maxwell-Boltzmann distribution law, the Stokes lines are stronger than the anti-Stokes lines under ambient conditions. Raman scattering is, therefore, usually recorded only on the low-energy side to give Stokes scattering.
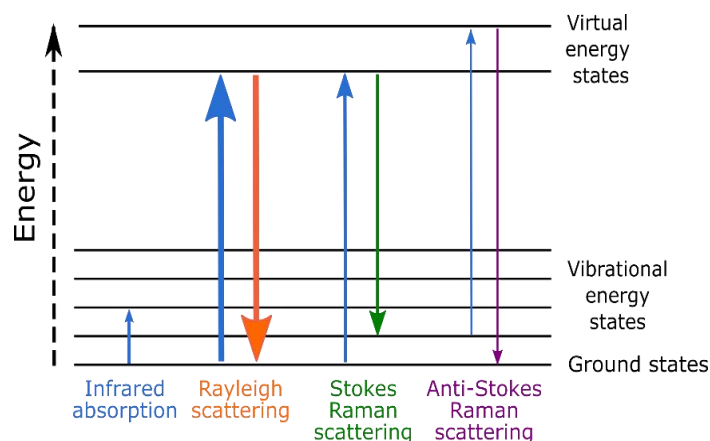
Figure 2.17 Energy-level diagram showing transitions of energy for absorption as well as different scattering events. The horizontal lines from the bottom upwards represents respectively ground electronic state, excited electronic states, and virtual states. The frequency of the scattered photon (downward arrows) is unchanged in Rayleigh scattering, but is of either lower or higher frequency in Raman scattering. Under ambient conditions, the Stokes scattered radiation is more intense than the anti-Stokes scattered radiation.

Raman spectroscopy is such a spectroscopic technique that relies upon the Raman scattering of light with low frequency modes, e.g., vibrational or rotational modes, in a system of atoms or within molecules. For general Raman spectroscopy, a monochromatic laser typically in the visible, near infrared, or near ultraviolet range is used as excitation light source. After light-mater interaction, the radiation emitted from the sample is collected, the laser wavelength is filtered out (e.g., by a notch or bandpass filter), and the resulting light is sent through a diffraction grating which separates the different frequencies of Raman scattering, the radiation is then collected by a CCD detector, where the Raman spectra will be processed and displayed graphically using software.

Raman spectroscopy is widely used for determining the chemical and crystal structures from the characteristic spectral patterns ('fingerprinting'). It is a non-destructive technique with the merits of the ease of sample handling and preparation and the ability to examine samples in a whole range of physical states (for example, as solids, liquids or vapours, in bulk, as microscopic particles, or as surface layers). In addition, in the case of Raman micro-spectroscopy the light passes through a microscope before reaching the sample, enabling to detect Raman scattering from regions in the micro scale. This allows accurate mapping of a sample, or confocal microscopy in order to probe the local structure of a sample.

Within this thesis, the Raman study of the thin films has been done by Dr. Jesús López-Sánchez at Universidad Complutense de Madrid via collaboration.

References

[1]   A.E. Danks, S.R. Hall, Z. Schnepp, The evolution of "sol-gel" chemistry as a technique for materials synthesis, Mater. Horizons. 3 (2016) 91–112. https://doi.org/10.1039/c5mh00260e.

[2]   J. Rodríguez-Carvajal, Recent advances in magnetic structure determination by neutron powder diffraction, Phys. B Phys. Condens. Matter. 192 (1993) 55–69. https://doi.org/10.1016/0921-4526(93)90108-I.

[3]   B.B. He, U. Preckwinkel, K.L. Smith, Fundamentals of two-dimensional X-ray diffraction (XRD2), in: Adv. X-Ray Anal. Vol. 43, 1999. the 48th Annual Denver X-ray Conference, Steamboat Springs, CO.

[4]   B.B. He, Geometry and Fundamentals, in: Two-Dimensional X-Ray Diffraction, John Wiley & Sons, Inc., Hoboken, NJ, USA, 2018: pp. 29–55. https://doi.org/10.1002/9781119356080.ch2.

[5]   P. Willmott, An introduction to synchrotron radiation: Techniques and applications, 2011. https://doi.org/10.1002/9781119970958.

[6]   S. V. Rashchenko, A. Kurnosov, L. Dubrovinsky, K.D. Litasov, Revised calibration of the Sm:SrB4O7 pressure sensor using the Sm-doped yttrium-aluminum garnet primary pressure scale, J. Appl. Phys. 117 (2015) 145902. https://doi.org/10.1063/1.4918304.

[7]   J.E. Penner-Hahn, X-ray Absorption Spectroscopy, in: Encycl. Life Sci., John Wiley & Sons, Ltd, Chichester, UK, 2005. https://doi.org/10.1038/npg.els.0002984.

[8]   P. Carra, B.T. Thole, M. Altarelli, X. Wang, X-ray circular dichroism and local magnetic fields, Phys. Rev. Lett. 70 (1993) 694–697. https://doi.org/10.1103/PhysRevLett.70.694.

[9]   B.T. Thole, P. Carra, F. Sette, G. Van Der Laan, X-ray circular dichroism as a probe of orbital magnetization, Phys. Rev. Lett. 68 (1992) 1943–1946. https://doi.org/10.1103/PhysRevLett.68.1943.

[10]   D.B. Williams, C.B. Carter, Transmission electron microscopy: A textbook for materials science, Springer US, 2009. https://doi.org/10.1007/978-0-387-76501-3.

[11]   B.J. Inkson, Scanning Electron Microscopy (SEM) and Transmission Electron Microscopy (TEM) for Materials Characterization, in: Mater. Charact. Using Nondestruct. Eval. Methods, Elsevier Inc., 2016: pp. 17–43. https://doi.org/10.1016/B978-0-08-100040-3.00002-X.

[12]   Z. Li, Scanning transmission electron microscopy studies of mono- and bimetallic nanoclusters, in: Front. Nanosci., Elsevier Ltd, 2012: pp. 213–247. https://doi.org/10.1016/B978-0-08-096357-0.00002-9.

[13]   M. Buchner, K. Höfler, B. Henne, V. Ney, A. Ney, Tutorial: Basic principles, limits of detection, and pitfalls of highly sensitive SQUID magnetometry for nanomagnetism and spintronics, J. Appl. Phys. 124 (2018) 161101. https://doi.org/10.1063/1.5045299.

[14]   J.R. Ferraro, K. Nakamoto, C.W. Brown, Introductory Raman Spectroscopy: Second Edition, Elsevier Inc., 2003. https://doi.org/10.1016/B978-0-12-254105-6.X5000-8.

Part I

ε-Fe$_2$O$_3$ nanoparticles

Chapter 3

New Insights on The High- and Low- Temperature Magnetic Transitions of ε-Fe₂O₃ Nanoparticles

3.1 Introduction

Perhaps the most salient feature of ε-Fe$_2$O$_3$ is a large magnetocrystalline anisotropy of about $5 \cdot 10$ J/m^3 at room temperature [1]. This high anisotropy is related to a collinear ferromagnetic structure (FM2) which exists, as indicated in Figure 3.1, between 150 K and 490 K. In the FM2 structure, two of the four Fe^{3+} sublattices, the ones corresponding to distorted octahedral environments (yellow and green in the figure), are practically compensated and the net magnetization comes from the unbalance of the two remaining ones, with regular octahedral and tetrahedral environments (pink and blue in Figure 3.1). Below 150 K, ε-Fe$_2$O$_3$ undergoes a magnetic softening driven by a structural and magnetic phase transition to two consecutive incommensurate magnetic orders (IM1 and IM2) which are still not well understood [2]. A progressive magnetic softening is also observed above room temperature, connected to another magnetic and structural phase transition characterized by the disruption of the magnetic order of the two uncompensated sublattices of FM2 structure [3].

The contrasting magnetic properties between the different phases are illustrated by remarkable changes in the magnetization and the coercive field (see the blue curve in Figure 3.1). Those dramatic changes in the coercivity have been related to a significant spin-orbit coupling the existence of an orbital magnetic moment which would arise with the FM2 order below 500 K and disappears when the FM2 is transformed below 150 K [4]. However, recent experimental and theoretical works point that the orbital moment would be much lower [5,6] than previously reported with opposite signs of spin and orbital moments.
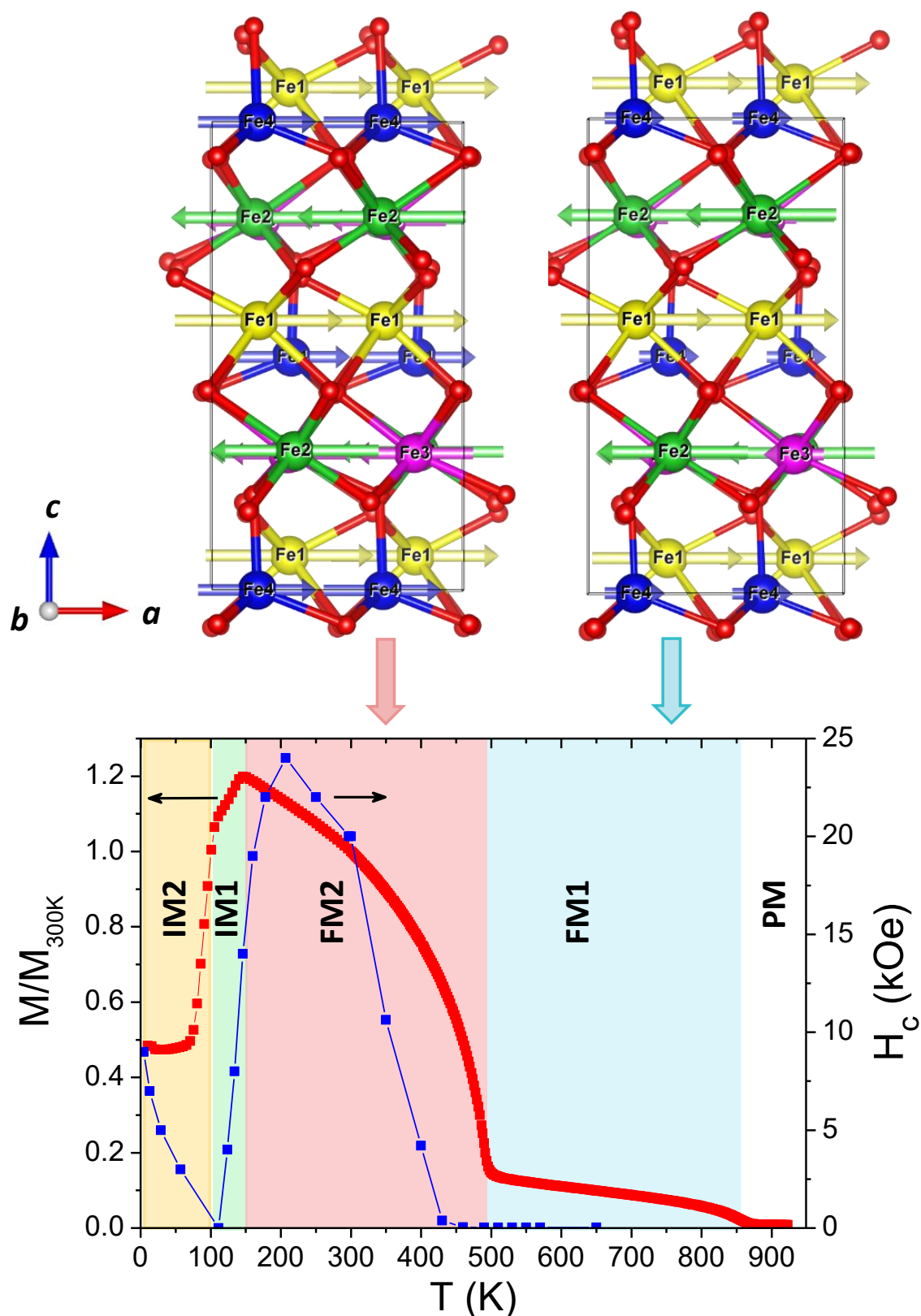
Figure 3.1 Magnetic phase diagram of ε-Fe₂O₃. The distinct magnetic phases are reflected from the temperature dependence of normalized magnetization ($M/M_{300 K}$) and coercive field (H_C). The top panels from left to right depict the magnetic structures for the ferrimagnetic FM2 and FM1 phases, respectively [7]. The four independent Fe sites of the cell are represented in different colors: distorted octahedral Fe1 and Fe2 in yellow and green, respectively; regular octahedral Fe3, pink; tetrahedral Fe4, blue. Oxygen atoms are manifested in red.

The FM2→FM1 and FM2→IM1 phase transitions are highly relevant to understand the unusually high magnetic anisotropy of ε-Fe$_2$O$_3$. The actual mechanisms controlling the surge and fall of high anisotropy at different temperature scales are related to the interplay of different magnetic interactions, spin orbit coupling, and crystalline electric fields. Thus, monitoring the structural and magnetic changes along those phase transitions can give clues to explain the origin of large magnetic anisotropy in this transition metal oxide. In these regards, the ε-Fe$_2$O$_3$ samples prepared during my PhD have been studied in several experiments at the ALBA synchrotron (High resolution X-ray powder diffraction and XAS-XMCD) the Advanced Light Source synchrotron (XAS-XMCD at high temperature) and the Institut Laue Langevin (Neutron Powder diffraction) in collaboration with Jose Luis Garcia-Muñoz, Arnau Romaguera and Javier Herrero. Most of these results are still being analyzed and one can foresee that will result in one or several publications. This chapter provides additional experimental insights into the magnetic transitions which limit the high magnetic anisotropy state above and below room temperature.

3.2 Sol-gel synthesis of ε-Fe₂O₃ nanoparticles

Sol-gel method is one of the well-established and efficient synthetic approaches to prepare high-quality ε-Fe$_2$O$_3$ nanoparticles with minimal intrusion of secondary phases. Single crystalline ε-Fe$_2$O$_3$ nanoparticles embedded in silica matrix were prepared using sol-gel based method. Hydrated iron (III) nitrate Fe(NO$_3$)$_3$·9H$_2$O (Aldrich) was used as the Fe precursor and Tetraethyl orthosilicate (TEOS, Si(OC$_2$H$_5$)$_4$) (Aldrich) was the metal-organic precursor for the formation of a SiO$_2$ matrix. The silica support limits the growth of ε-Fe$_2$O$_3$ particles preventing its transformation to α-Fe$_2$O$_3$ [8], and also keeps particles isolated avoiding agglomeration. The iron oxide content with respect to silica was fixed to 24 % wt., while the molar ratios of TEOS, ethanol, and water were 1:6:6. In the following, we will describe the synthesis processes in more detail.

Firstly, 8.61 g of iron (III) nitrate nonahydrate was dissolved in appropriately mixed Milli-Q water (6.23 mL) and ethanol (31.42 mL) solution under stirring. The resultant solution has a pH of ~ 0.35. Subsequently, 20 mL of TEOS was pipetted dropwise into the solution while stirring continuously. The stirring was maintained for ~15 minutes after the addition of TEOS in order to obtain a stable, clear, and homogeneous solution (see Figure 3.2(a)). The final sol was then distributed into four Petri dishes of 9 cm in diameter, which were covered and placed inside a plastic box in a chemical hood for around two weeks for the gelation (Figure 3.2(b)). The gels were crushed in a ceramic mortar and then were further air-dried at 60 ºC for 24 hours (Figure 3.2(c)). Next, the dried xerogels were ground thoroughly. The resulting powders were placed in an alumina boat and were subsequently subjected to a thermal treatment in a tubular furnace (Figure 3.2(d)). The annealing was done in air atmosphere, heating at 200 °C/h to 450 °C and then to a maximum temperature of 1100 °C at 80 °C/h. The sample was held for

two hours at 1100 °C before being cooled to room temperature at 350 °C/h. Eventually, single-crystalline ε-Fe$_2$O$_3$ NPs supported on silica matrix were stabilized.

In order to remove the silica support in the sample, ~3 g of the above-obtained sample was further ground into fine powders and added into concentrated NaOH aqueous solution (12 M) in a round-bottomed flask, immersed in an oil bath at 80 °C. The mixture was subjected to vigorous stirring for 48 hours while the water vapour was refluxed using a water-refrigerated condenser (Figure 3.2(e)). The products were collected by centrifugation at 6000 rpm and the supernatant was discarded. The collected solid was redispersed in distilled water. The centrifugation and washing were repeated twice. The final precipitates were then air-dried at 60 °C for 24 hours. Finally, we can get nanometric ε-Fe$_2$O$_3$ particles which are highly stable upon heating in air up to 940 K (no phase transitions were detected at such temperature from synchrotron X-ray diffraction data).
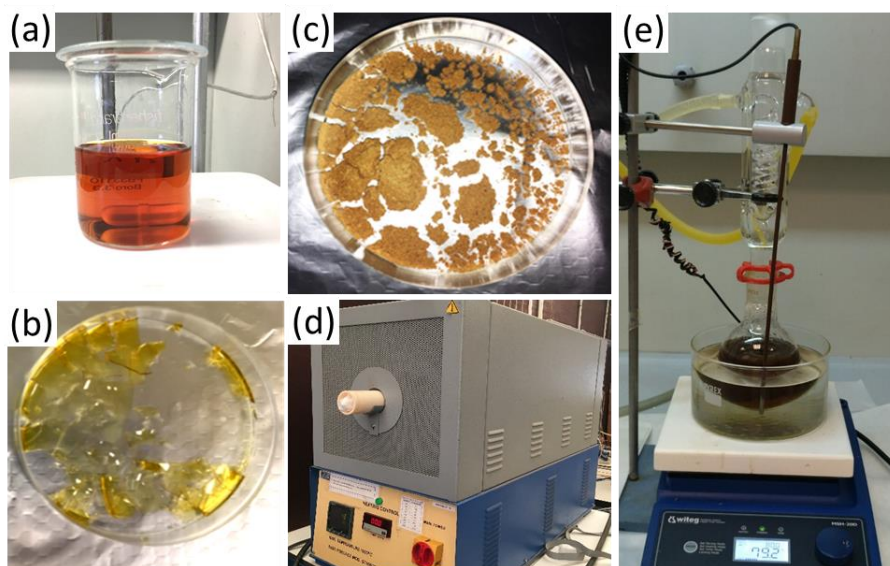
Figure 3.2 Sol-gel synthesis process for the production of ε-Fe$_2$O$_3$ nanoparticles. (a) Sol formation: TEOS:H$_2$O:EtOH = 1:6:6 molar, with iron (III) nitrate nonahydrate used as the iron precursor. (b) Condensation and aging, which ultimately produces a solid jelly-like gel. (c) Drying and (d) thermal treatment at proper temperatures to form ε-Fe$_2$O$_3$ NPs confined in SiO$_2$ matrix. Finally, (e) the silica matrix can be removed by immersing in concentrated NaOH solution.

3.3 Structural characterization of ε-Fe₂O₃ nanoparticles at room temperature

Both the non-etched and etched ε-Fe₂O₃ nanoparticles (i.e., before and after the removal of the SiO₂ matrix, respectively) have been examined by synchrotron x-ray powder diffraction (SXRPD) at the BL04-MSPD beamline of the ALBA Synchrotron Light Facility (Barcelona, Spain). The samples were loaded into borosilicate glass capillaries (diameter of 0.5 mm) and kept spinning during data acquisition, performed using a wavelength of $\lambda = 0.412\,84(6)$ Å. The value of λ was calibrated using a silicon standard. The patterns (see Figure 3.3(a, b)) were collected under the same conditions at 300 K using a MYTHEN position sensitive detector. The broad bump at a 2θ angle slightly above 5° in the diffraction pattern of the non-etched particles corresponds to the scattering of amorphous SiO₂ matrix, whose content is significantly reduced in the etched sample. No extra diffraction peaks are observed from the pattern of the etched sample compared to that of its non-etched counterpart. One interesting observation is that after the silica removal the 2θ peak positions shifted towards slightly larger angles with respect to those recorded before etching (see Figure 3.3(c)) and this is reflected by a decrease of the lattice parameters upon silica removal (see Table 3.1). This may indicate that the silica matrix imposes a tensile strain to ε-Fe₂O₃ nanoparticles and could also be relevant to the stabilization of this polymorph. Rietveld XRD refinements were carried out on both patterns using the FULLPROF program [9], and the results are shown in the red solid lines. The top row of vertical bars (in magenta) corresponds to Bragg reflection positions from the *Pna2₁* structure of ε-Fe₂O₃, while the bottom vertical bars (in violet) correspond to a minor hematite impurity. The contribution to the patterns from the amorphous silica was treated as background points of the patterns during the refinement. The lattice parameters (*a*, *b*, and *c*) and the atomic coordinates of ε-Fe₂O₃ obtained from the refinement are summarized in Table 3.1. The weight percentage of α-Fe₂O₃ is ~ 3 wt.% according to our best fits of both patterns. No other impurities were detected in both the etched and non-etched samples. The inset of Figure 3.3(c) displays the resulting crystal structure of ε-Fe₂O₃ visualized by VESTA program [10]. Among the four crystallographic non-equivalent Fe sites, the octahedrally coordinated Fe1O₆ and Fe2O₆ are largely distorted, Fe3O₆ is a regular octahedron, and Fe4O₄ is the tetrahedron.
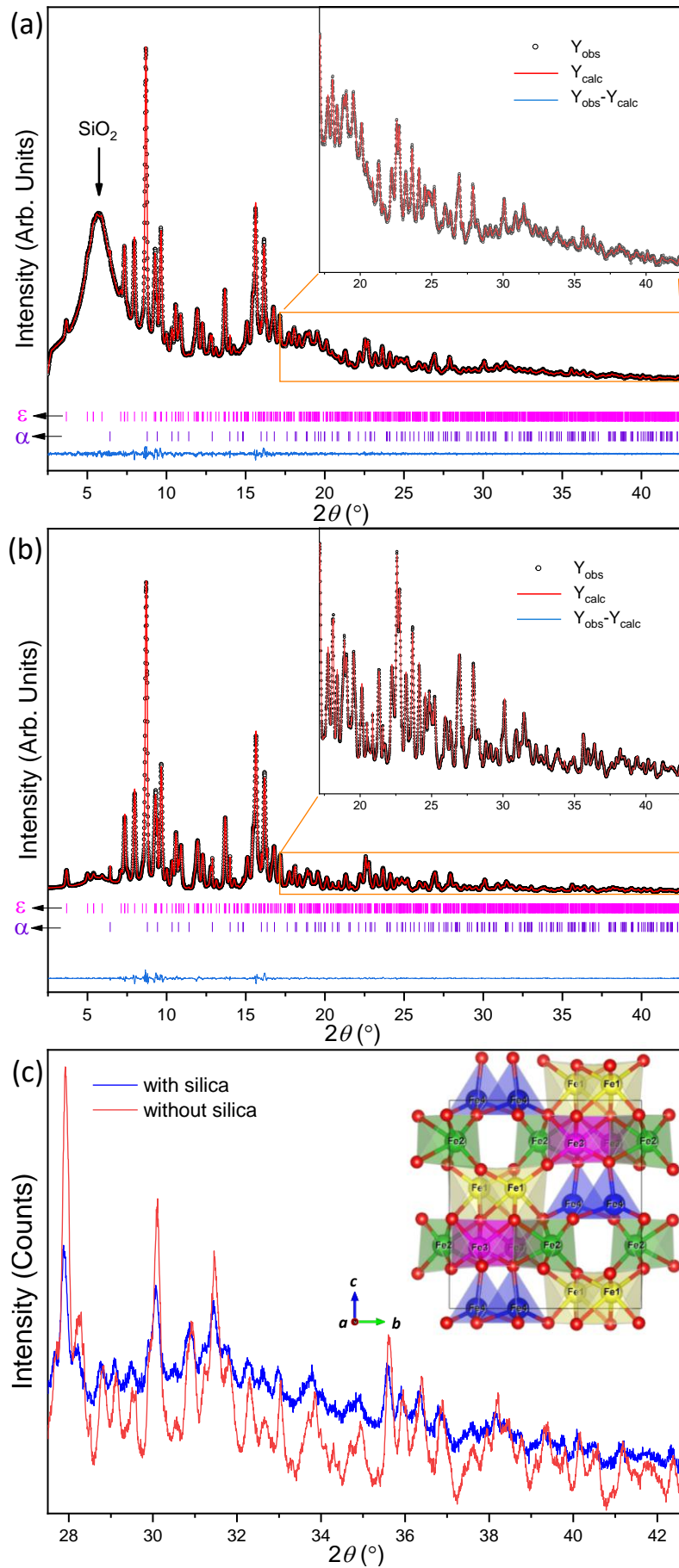
(*Caption appears on following page*)

Figure 3.3 (a) Rietveld refinement of the Synchrotron X-ray powder diffraction patterns collected at 300 K for both the (a) non-etched (with SiO₂) and etched (without SiO₂) ε-Fe₂O₃ nanoparticles. The black circles and the red lines represent the observed and calculated intensities, respectively. The bottom blue line is their difference. The top row of vertical bars (in magenta) corresponds to Bragg reflection positions from the *Pna2₁* SG of ε-Fe₂O₃, while the bottom vertical bars (in violet) are from α-Fe₂O₃ minor impurity, accounting for ~ 3 wt.% in both cases. The insets of Panels (a) and (b) show an enlarged view of the corresponding high-angle regions. (c) An enlarged region of the patterns of non-etched (in blue) and etched (in red) samples, showing a slight peak shift between them. The inset of Panel (c) depicts the crystallographic projection of ε-Fe₂O₃ along the *a*-axis. The four crystallographically independent Fe sites are shown with different colors in the structure: Fe1, yellow; Fe2, green; Fe3, pink; Fe4, blue). O atoms are represented in red.

Figure 3.4(a) and (b) show respectively the representative TEM images for the non-etched and etched samples. A well-defined roughly spherical shape of the particles can be appreciated in the images. Probability distributions of nanoparticle diameters, which were obtained by measuring more than 300 particles using the ImageJ software [11], are presented in Panels (c) and (d) below the corresponding TEM images.
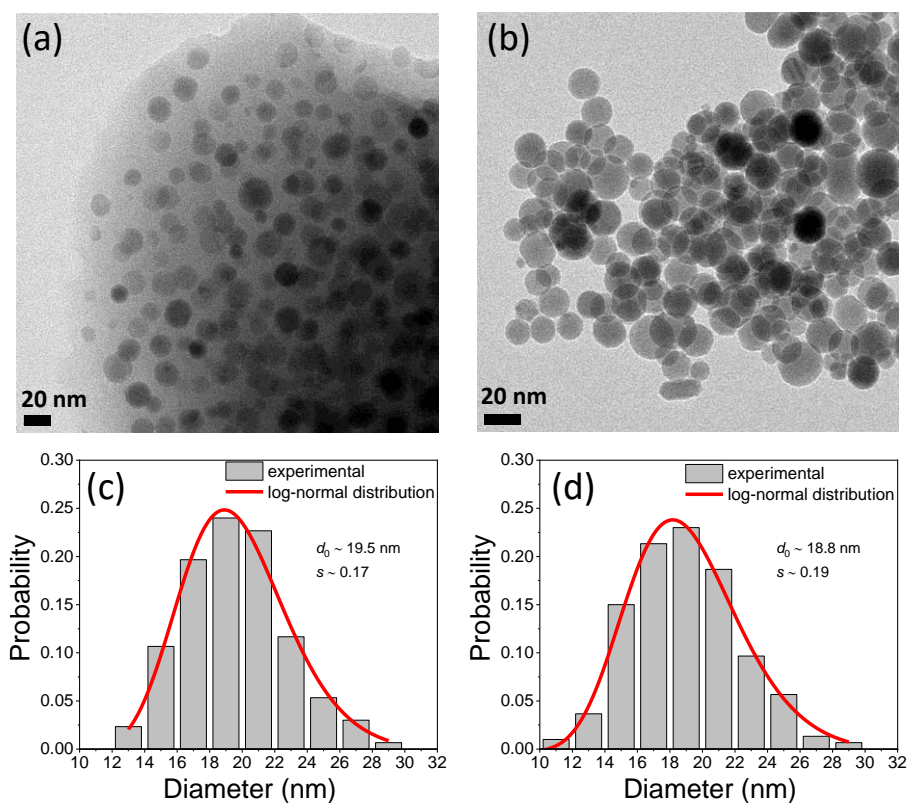
Figure 3.4 Representative TEM images of the (a) non-etched and (b) etched ε-Fe₂O₃ nanoparticles. The Panels (c) and (d) present the particle size distributions along with the fitting to the log-normal distribution (red solid lines).

The obtained mean particle sizes are 19.6(3) nm and 19.0(3) nm for the non-etched and etched samples, respectively, indicates that within the error there is no significant difference between the sizes of the etched and nonetched samples. The diameter distributions of the NPs were fitted to the log-normal distribution function [12],[13]:

$$f(x) = \frac{1}{\sqrt{2\pi}\sigma x}\ \exp\left(-\frac{\ln^2(x/d_0)}{2\sigma^2}\right) \tag{3.1}$$

$$s = \sqrt{\exp(\sigma^2) - 1} \tag{3.2}$$

where d_0 represents the median of particle diameters, σ is the standard deviation of the log of the distribution, and dimensionless s the coefficient of variation (a measure of the dispersion of the log-normal probability distribution). The resulting fitting yields a median d_0 of 19.5(4) nm and an s index of 0.17(2) for the non-etched sample, and d_0= 18.8(3) nm and s= 0.19(2) for the etched one (see Figure 3.4(c-d)). Compared to the previously reported broad particle size distributions of ε-Fe$_2$O$_3$ [14],[15],[16], the obtained particle size distributions are relatively narrow.

Table 3.1 Summary of the unit-cell parameters and atomic coordinates of ε-Fe$_2$O$_3$ obtained from the SXRPD on etched ε-Fe$_2$O$_3$ particles (without silica) at T= 300 K. The lattice parameters for nonetched particles (with silica) are also shown for comparison. Among the four distinct Fe sites, Fe1 and Fe2 are the largely distorted octahedral coordination, Fe3 and Fe4 atomic labels refer to the regular octahedron and the tetrahedron, respectively. The agreement factors of the structural refinement for etched (nonetched) particles are: R_B = 0.8 % (1.1 %), R_f = 0.6 % (0.6 %), χ^2 = 3.9 (0.7).

	Atomic coordinates		
	x	y	z
Fe1	0.1952(3)	0.1519(2)	0.5813(1)
Fe2	0.6811(2)	0.0322(1)	0.7932(2)
Fe3	0.8089(2)	0.1590(2)	0.3065(1)
Fe4	0.1826(3)	0.1516(2)	0.0000
O1	0.9789(10)	0.3256(5)	0.4318(5)
O2	0.5136(10)	0.4911(6)	0.4234(9)
O3	0.65512(10)	0.9982(5)	0.1935(4)
O4	0.1586(9)	0.1630(6)	0.1972(2)
O5	0.8452(11)	0.1657(6)	0.6717(3)
O6	0.5295(10)	0.1634(7)	0.9361(5)
Cell parameters	a= 5.0897(1) Å, b= 8.7833(2) Å, c= 9.4629(2) Å, V= 423.04(1) Å^3 (without silica)		
Cell parameters	a= 5.0984(1) Å, b= 8.7947(1) Å, c= 9.4700(2) Å, V= 424.63(1) Å^3 (with silica)		

3.4 Revisiting magnetostructural transition of ε-Fe₂O₃ nanoparticles at high temperatures

In this section, we will proceed with the temperature-dependent magnetic characterizations of ε-Fe$_2$O$_3$ nanoparticles, primarily focusing on the magnetometry (both dc and ac) and neutron scattering studies.

3.4.1 Magnetometry study of ε-Fe₂O₃ nanoparticles above room temperature

In order to avoid any structural transformations in a high-temperature high-vacuum environment, the magnetic properties of the ε-Fe$_2$O$_3$ nanoparticles in the high-temperature (HT) regime have been measured using a VSM magnetometer on the non-etched ε-Fe$_2$O$_3$ nanoparticles (with SiO$_2$). For this purpose, the ε-Fe$_2$O$_3$/SiO$_2$ composite was first mixed with high-temperature alumina cement adhesive (Zircar) before it was mounted onto the VSM heater stick. The temperature dependence of the zero-field cooling (ZFC) and field-cooling (FC) magnetic moments (m-T) of the ε-Fe$_2$O$_3$ nanoparticles embedded in SiO$_2$ is presented in Figure 3.5(a). The magnetic moment undergoes a sharp decrease at ~ 490 K, accompanied by a continuous and mild drop until ~ 850 K before it finally goes to zero.

The local minima of the derivative of moment versus temperature (dm/dT) curve corroborate the presence of different magnetic phases (see inset of Figure 3.5(a)). This observation is consistent with the recent work by García-Muñoz et al. [7], where the two rather different magnetic behaviors above and below T_{N2}~ 490 K are attributed to two distinct ferrimagnetic phases (FM1 and FM2, respectively). The magnetic hysteresis loops collected with a maximum magnetic field of 70 kOe at various temperatures are shown in Figure 3.5(b) and (c), from which the temperature dependence of coercivity (H_C) and maximum magnetic moment ($m_{\_7T}$) can be obtained (see Figure 3.5(d)). It is seen that the large H_C, which is characteristic of the FM2 phase, sharply drops upon heating until it collapses at T_{N2}~ 490 K. Nevertheless, although the H_C shrinks by more than a factor of ten from H_C~ 13.9 kOe at room temperature, it does not vanish in the ferrimagnetic FM1 state in which it is still of a few hundreds of Oersteds. Moreover, upon heating, the maximum moment $m_{\_7T}$ experiences a Brillouin-type monotonic decrease up to ~ 530 K, above which it slowly drops down with a further increase of temperature. Hence, in agreement with the report by García-Muñoz et al. [7], the critical temperature of the magnetic order-disorder transition for our ε-Fe$_2$O$_3$ nanoparticles is around $T_{N1} \sim 850$ K. The room temperature hard ferrimagnetic state FM2 is followed by a different ferrimagnetic state FM1 with a much smaller ferromagnetic component and coercivity in a 490-850 K temperature range.
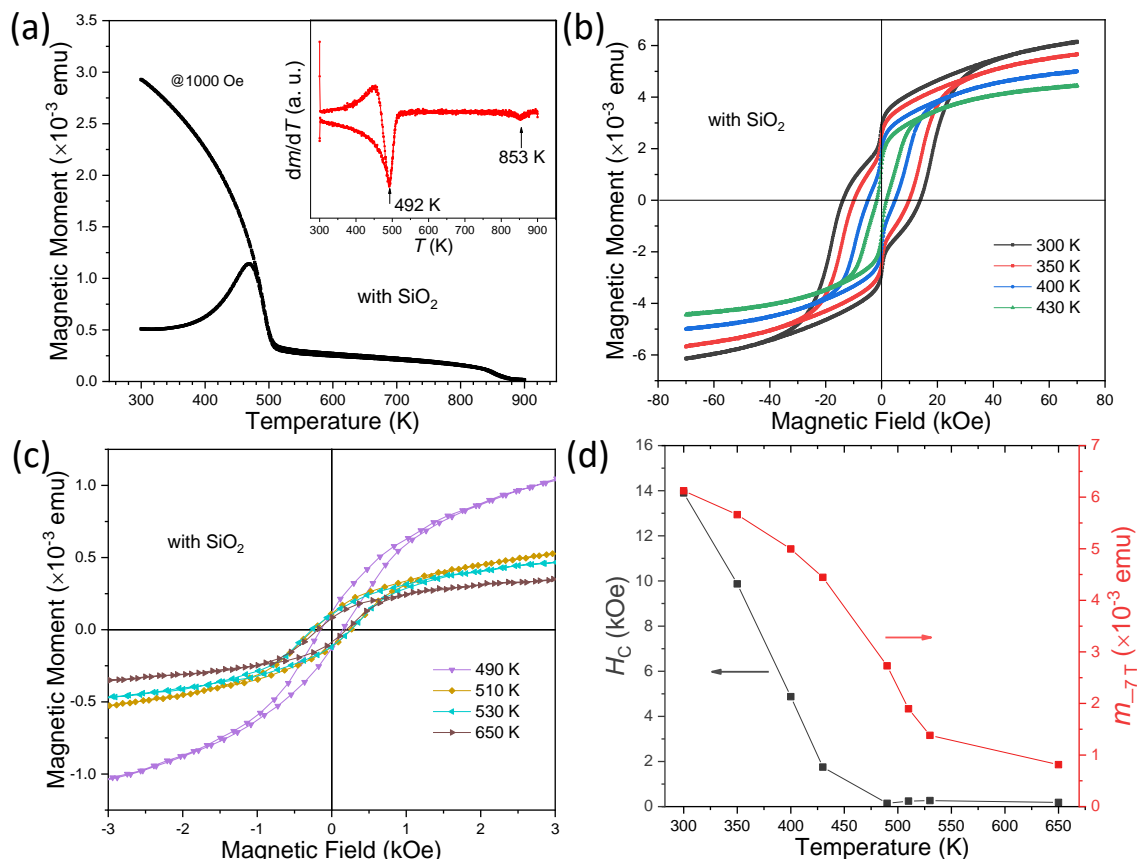
Figure 3.5 (a) HT magnetic moment versus temperature curves acquired under both ZFC (lower branch) and FC (upper branch) conditions for the non-etched ε-Fe₂O₃ nanoparticles (H= 1000 Oe). The inset depicts the temperature evolution of the first-order derivative of the moment with respect to temperature. (b) and (c) show the magnetic hysteresis loops recorded at various temperatures (note the different x- and y-scales in the figures). (d) Magnetic coercivity and the moment at H_{max}= 70 kOe as a function of temperature derived from the hysteresis loops.

While no visible irreversibility is observed above 490 K, below this temperature the FC and ZFC curves of Figure 3.5(a) present a thermomagnetic irreversibility and the ZFC magnetization shows a maximum below T_{N2}. This behavior has been known for a long time as the Hopkinson effect [17], and results from the combination of the decreasing magnetocrystalline anisotropy as T increases and the diminution of magnetization close to T_{N2}. Upon heating, at a certain T below T_{N2}, the applied field in ZFC measurement is above the coercive field and the magnetization sharply increases but then declines as T_{N2} is approached. Indeed, when larger fields are applied in the ZFC measurement (see Figure 3.6) the peak shifts to lower temperatures and broadens in agreement with what is found in such as the ferromagnetic SrRuO₃, as is discussed in detail in the studies by Date and co-workers [18,19].
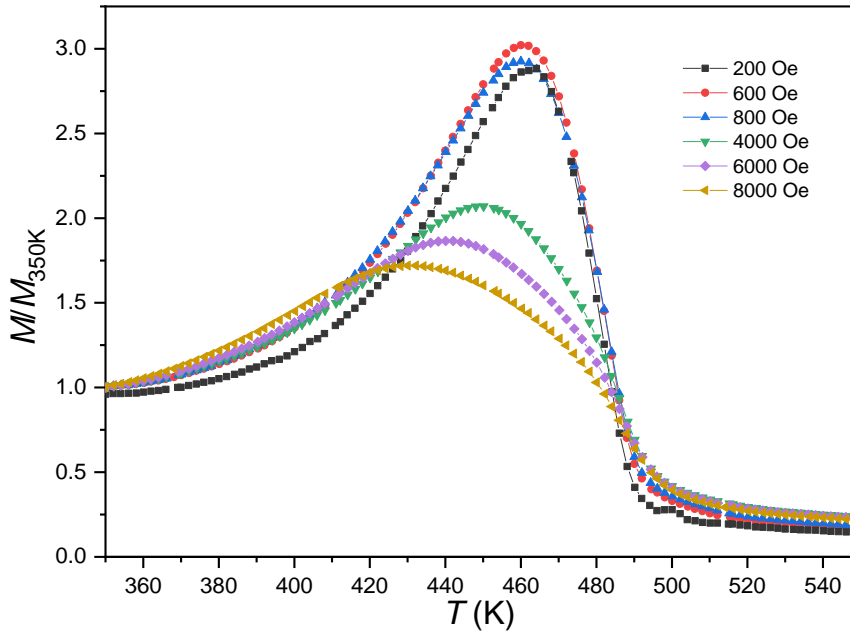
Figure 3.6. ZFC magnetization measured on non-etched ε-Fe$_2$O$_3$ nanoparticles under different applied fields with a heating rate of 2 K/min. Note that the magnetization has been normalized to the 350 K value.

Such peaks in the ZFC magnetization are observed in spin glasses and ferromagnetic cluster glasses altogether with other magnetic features such as the absence of magnetic saturation even at large fields and relaxation effects. It is interesting to note that ε-Fe$_2$O$_3$ presents other additional characteristics of spin-glasses. The non-saturating magnetization is evident in Figure 3.5(b) up to 70 kOe, and it is worth noting that the lack of saturation has also been observed by applying static fields as large as 230 kOe [20]. Regarding relaxation effects, preliminary time-dependent measurements indicate that the temperature dependence of the relaxation scales with T/T_p. Figure 3.7 shows time-dependent measurements of the magnetization under an applied field of 100 Oe at different temperatures. The magnetization increases with time displaying a logarithmic dependence and the increase is more pronounced as the ZFC peak temperature at about 460 K is approached. These effects can be attributed to thermally activated transitions following an Arrhenius law in combination with a distribution of barrier heights stemming from the relatively broad distribution of particle sizes (see Figure 3.4(c, d)).
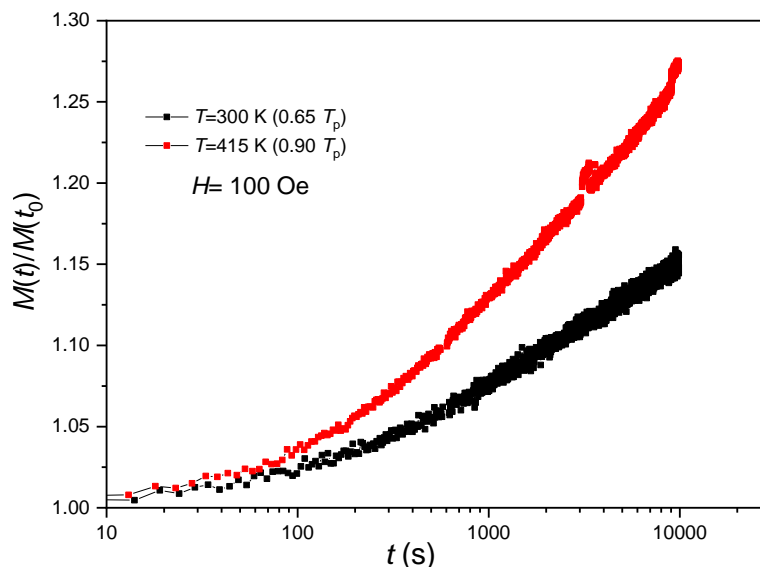
Figure 3.7. Time-dependent magnetization of an initially demagnetized ε-Fe$_2$O$_3$ under an applied field of 100 Oe at different temperatures. The measurements were conducted on particles embedded in silica matrix.

3.4.2 High-temperature neutron powder diffraction

Figure 3.8(a) presents the Rietveld refinement profile of the room temperature NPD data for the etched ε-Fe$_2$O$_3$ particles performed at the D20 high-flux powder diffractometer (ILL, Grenoble) at a selected wavelength of 2.41 Å. The pattern was refined using the nuclear (*Pna2$_1$*) and magnetic (*Pna'2$_1$'*) structures for ε-Fe$_2$O$_3$ phase [7], and the nuclear (*R-3c*) and magnetic (*P*1) structures for the minor α-Fe$_2$O$_3$ phase [21]. The refined magnetic moments for the distorted octahedral Fe1 and Fe2, regular octahedral Fe3 and tetrahedral Fe4 are 3.6(1) μ_B/Fe, -3.6(1) μ_B/Fe, -2.5(1) μ_B/Fe and 2.7(3) μ_B/Fe, respectively (all lie along the crystallographic *a*-axis), in agreement with the previous report [7]. A crystallographic representation of ε-Fe$_2$O$_3$ structure derived from the refinement, together with the arrangement of magnetic moments, are illustrated in Figure 3.8(b). Furthermore, we obtained a 2.8(4) % in weight of hematite as an impurity phase in our particles. No diffraction peaks associated with other phases are detected.
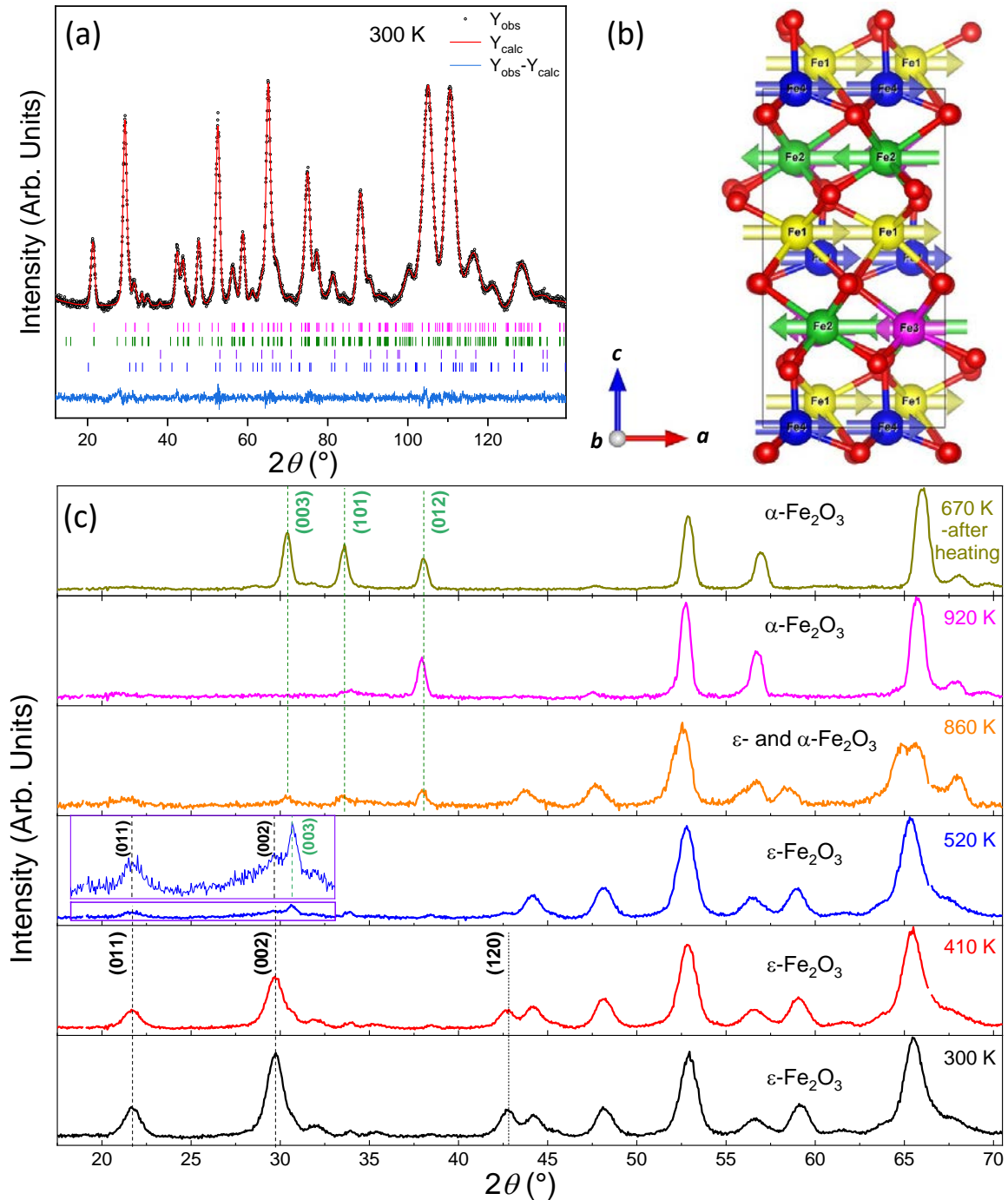
Figure 3.8 (a) Rietveld refinement (red solid line) of the neutron powder diffraction (NPD) of ε-Fe$_2$O$_3$ particles collected at 300 K (black circles, experimental points; bottom blue line, difference). The top row (in magenta) and the second row (in olive) of vertical bars correspond respectively to the nuclear (*Pna2$_1$*) and magnetic (*Pna'2$_1$'*) structures of ε-Fe$_2$O$_3$. The third row (in violet) and the last row (in blue) of vertical bars indicate the Bragg positions from the nuclear (*R-3c*) and magnetic (*P1*) structures of α-Fe$_2$O$_3$. The fit gives 2.8(4) wt.% of hematite in the particles. Goodness factors: R_B = 0.4 %, R_f = 0.3 %, R_{Mag} = 1.9 %, χ^2 = 1.5. (b) Crystallographic projection of ε-Fe$_2$O$_3$ along the b-axis. The four crystallographically independent Fe sites are shown with different colors in the structure, O atoms are represented in red. The arrows indicate the relative alignments of atomic magnetic moments of the Fe atoms. (c) The temperature evolution of the NPD patterns collected upon heating up to 920 K. A final pattern was recorded at 670 K after the heating process. The dashed lines indicate the (011), (002) and (012) magnetic peaks of ε-Fe$_2$O$_3$ (in black), as well as the (003) and (101) peaks (magnetic) and (012) peak (both structural and magnetic) of α-Fe$_2$O$_3$ phase (in green). An enlarged region of the 520 K pattern is shown in the inset.

Figure 3.8(c) shows the thermal evolution of the NPD patterns collected at temperatures T= 300, 410, 520, 860 and 920 K (on heating). A final pattern was recorded at 670 K afterwards (see the top panel). Several observations and conclusions can be made: First, the diffraction peaks shift to lower Bragg positions with the increment of temperature due to thermal expansion. Moreover, the *Pna2$_1$* structure of epsilon phase persists up to ~ 860 K under the present investigation condition (note that the pressure was in the order of 10^{-4} mbar at the time), where the (012) peak of hematite located at 2θ~ 38° starts to appear. The (012) peak becomes much more pronounced at 920 K. Meanwhile, the characteristic peaks of ε-Fe$_2$O$_3$ phase are almost invisible, indicating the phase transformation of ε-Fe$_2$O$_3$ to α-Fe$_2$O$_3$. When the sample cooled to 670 K, the (003) and (101) magnetic peaks of α-Fe$_2$O$_3$ phase showed up. Another pertinent observation is that the magnetic reflections associated with the ferrimagnetic FM2 phase, e.g., the (011), (002) and (120) peaks indicated by the black dashed lines, become weaker in intensity with increasing temperature but persist at 520 K, which is well above the critical temperature T_{N2}~ 490 K. The finite intensity of the magnetic peaks at temperatures above T_{N2} is in accordance with the HT magnetometry results. It is, therefore, confirmed the presence of the HT magnetic phase characterized by a magnetic order-disorder critical temperature of T_{N1}~ 850 K in our nanoparticles. In fact, a *Pna'2$_1$'* (33.147) magnetic model, as suggested in Reference [7], was fitted to the 520 K pattern, and a very good agreement between experimental and refined data was found (not shown). It is thus concluded that both magnetic orders adopt the same magnetic space group, the transformation of the hard-softer FM2-FM1 is accompanied by the disruption of the magnetic order associated with the Fe3 and Fe4 magnetic atoms [7].

3.4.3 Magnetocaloric response of ε-Fe$_2$O$_3$ nanoparticles

The magnetocaloric effect (MCE) is the reversible temperature change of a magnetic material upon the application or removal of a magnetic field. Adiabatic demagnetization has been employed with paramagnetic salts for achieving sub-Kelvin temperatures for decades, and its use led to the Nobel Prize in Chemistry being awarded to Giauque in 1949. Nowadays, there is a great deal of interest in using the MCE as an energy-efficient and environment-friendly alternative technology for refrigeration, from room temperature to the liquefaction temperatures of hydrogen and helium (∼20-4.2 K).

The MCE is intrinsic to all magnetic materials and is measured as adiabatic temperature change (ΔT_{ad}) or isothermal entropy change (ΔS_M) induced by a changing magnetic field. The quantity ΔS_M is easy to determine from magnetization measurement and therefore is the most commonly used parameter in the study of MCE. In this case, the magnetic field is applied isothermally (i.e., temperature remains constant), and the ΔS_M can be deduced from the Maxwell relation as

$$\Delta S_M(H, T) = \mu_0 \int_0^{H_{max}} \left(\frac{\partial M}{\partial T}\right)_H dH \tag{3.3}$$

where the μ_0 is the permeability of free space and H_{max} is the maximum applied field. This equation indicates that the ΔS_M is proportional to the derivative of the magnetization with respect to temperature (dM/dT) at a constant magnetic field. Therefore, it is expected that the largest ΔS_M takes place when its magnetization is changing rapidly with temperature, i.e., in the vicinity of a spontaneous magnetic-ordering temperature. For a thorough discussion of magnetocaloric effect and the principles of magnetic refrigeration, we refer to the excellent reviews by Gschneidner [22] and Franco [23].

Apart from the above-mentioned application prospects, the MCE was also studied to gain insight into the characteristics of phase transitions such as information about the critical exponents of a material or the order of the phase transition, even in cases for which standard techniques do not give accurate results (see, for example, reference [23]).

Herein we report on the magnetocaloric response of ε-Fe₂O₃ nanoparticles near the ferrimagnetic FM1-FM2 transition. It has been demonstrated that the magnetic FM1-FM2 transition at $T_{N2} \sim 490$ K in ε-Fe₂O₃ NPs involves the ordering transition from only one of the two pairs of magnetic sublattices, i.e., the regular Fe3 octahedron and the Fe4 tetrahedron [7]. Furthermore, the presence of a significant structural anomaly with an abrupt contraction (≈ -0.1 %) is accompanied by this magnetic hard-soft phase transition. This means that mechanocaloric (barocaloric or elastocaloric) effects may be achieved in this system depending on the external stimulus (uniaxial stress or hydrostatic pressure). It is, therefore, possible to exploit the different degrees of freedom such as spin and lattice and cross-coupling effects between them within this Fe₂O₃, in order to stimulate larger entropy changes via the so-called multicaloric effects [24],[25]. The structural evolution of ε-Fe₂O₃ nanoparticles across the FM1-FM2 transition under high pressure will be accessed in some detail in the next section. Finally, it is important to note here that properties of this transition are susceptible to considerable modulation by proper chemical substitutions, e.g., the critical transition temperature T_{N2} can be largely tuned by metal-substitution (as discussed later in the following chapter), and it can even be reduced to near room temperature via In-doping (preliminary results, unpublished).

In order to avoid any possible structural transformations, the non-etched ε-Fe₂O₃ NPs have been used as the subject for the magnetic characterization involved in this section. The measurement was carried out using a VSM option of a PPMS from Quantum Design Inc. As mentioned earlier, prior to the powder sample mounting, the ε-Fe₂O₃/SiO₂ composite was glued to a heater stick using Zircar cement, making it difficult to assess the effective weight of ε-Fe₂O₃ for the measurement. To overcome this, we first recorded a room temperature magnetic hysteresis loop on the ε-Fe₂O₃/SiO₂ composite (see Figure 3.9(a)), where one can obtain a remanent moment of 6.4×10^{-3} emu. According to a similar measurement on the etched sample via SQUID magnetometer (see Figure 3.14(a) below), the remanence is 7.69 emu/g. Therefore, the contained ε-Fe₂O₃ is approximately 0.83 mg [$= 10^3 \times (6.4 \times 10^{-3}$ emu$)/(7.69$ emu/g$)$] in weight. The sample was then demagnetized and was used for the subsequent low-field *M-T* and

isothermal *M-H* measurements, as shown in Figure 3.9 (b) and (c-d), respectively. The FC magnetization versus temperature curve was measured under a constant field of 300 Oe during heating from 300 to 560 K. The typical HT magnetic behavior of ε-Fe₂O₃ can be seen from the *M-T* curve. The *dM/dT* versus *T* curve in the inset of Figure 3.9(b) shows a local minimum at a critical temperature $T_{N2}=$ 487 K, which is the FM1-FM2 transition temperature. Figure 3.9(c, d) presents the *M-H* isotherms at different temperatures with the temperature intervals of $\Delta T = 2$ and 4 K for the 450-520 K and 520-560 K ranges, respectively. To reset the thermal and magnetic states of the particles, the following isothermal magnetization measurement protocol was adapted [26]: For every initial *M-H* curve, the sample was first heated to 560 K in zero field, then brought to a stable temperature under an applied field of 300 Oe and then the isothermal magnetization was finally recorded while the magnetic field increased up to 50 kOe. Typical ferro- or ferri-magnetic behaviors are found even for the *M-H* curves recorded at temperatures above T_{N2}.
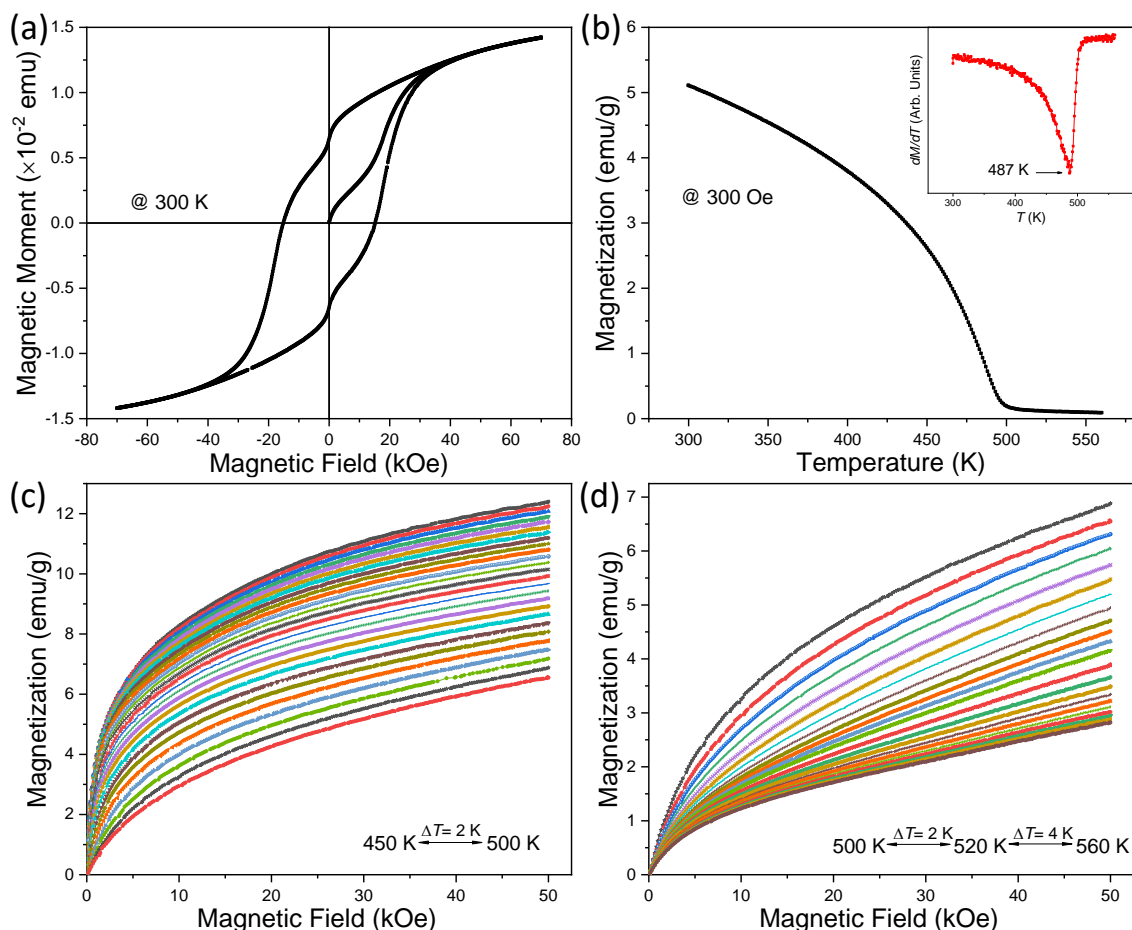
Figure 3.9 (a) Room temperature hysteresis loops collected on the ε-Fe₂O₃/SiO₂ composites mixed with VSM Zircar cement adhesive. (b) Temperature dependence of the FC magnetization curve (*M-T*) under a 300 Oe magnetic field for the same sample. The inset depicts the derived *dM/dT* versus *T* curve. (c) Isothermal magnetization curves measured with rising fields up to 50 kOe in the temperature range of (c) 450-500 K and (d) 498-560 K.

From the isothermal magnetization curves, the temperature dependence of magnetic entropy change, ΔS_M, calculated using Equation 3.3 is shown in Figure 3.10. It can be seen that the $-\Delta S_M$ peaks at 493 K, around which it decreases steadily. This behavior is commonly associated with a second-order magnetic phase transition. The maximum $-\Delta S_M$ is 0.9 J/kgK under a magnetic field change of 50 kOe. This value compares favorably to manganite of similar particle size (17 nm) [27]. The refrigeration capacity or relative cooling power (*RCP*) is a measure of the amount of heat transfer between the cold to the hot end of a refrigerator in one ideal thermodynamic cycle. The -ΔS_M The *RCP* can be evaluated as the product of the maximum -ΔS_M and the full-width at half maximum (*FWHM*) of the -ΔS_M versus *T* curve. When the applied field was changed from 0 to 50 kOe, a *RCP* of around 40 J/kg is obtained for our 20 nm nanoparticles, thanks to a large *FWHM* spanning a temperature range of 45 K.
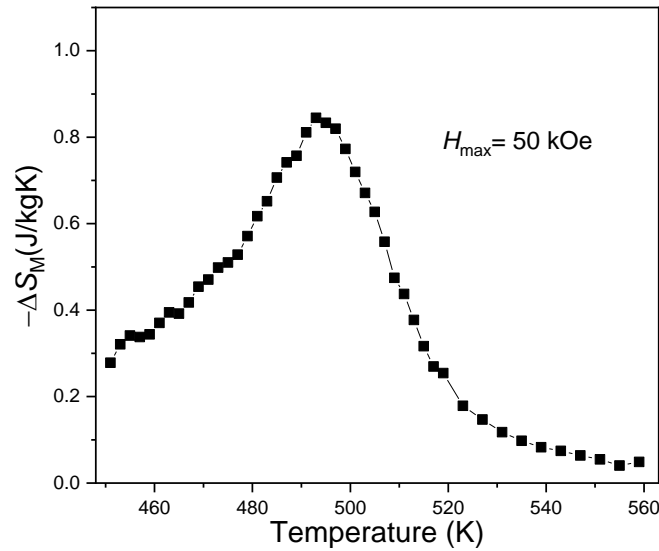
Figure 3.10 Temperature dependence of the magnetic entropy change, ΔS_M, under a maximum applied field of 50 kOe for ε-Fe₂O₃. Solid line is a guide to eye.

3.4.4 Effect of pressure on the high-temperature magnetostructural transition in ε-Fe₂O₃

Accompanying the magnetic soft-hard transition in ε-Fe₂O₃ at T_{N2}, there is a significant decrease of the unite cell volume of $\Delta V/V \sim 10^{-3}$ upon cooling. This magnetostructural transition offers a unique playground for studying the competition between different energy terms, such as spin-orbit, coulombic interactions and crystal electric field, in this $3d$ electron system. To complement previous measurements of the magnetocaloric response (Figure 3.10), we investigated the effect of pressure on the structural evolution of the *Pna2₁* epsilon phase by performing high-pressure SXRPD across this hard-soft magnetic transition. In particular, we intended to study the pressure dependence of this volume change by performing temperature dependent X-ray diffraction measurements at different pressures. This would will allow us to measure, through barocaloric effect, the isothermal barocaloric entropy change under a pressure change [28] as indicated in equation 3.4:

$$\Delta S(p_1 \to p_2) = -\frac{1}{m}\int_{p1}^{p2}\left(\frac{\partial V}{\partial T}\right)_{p'} dp' \tag{3.4}$$

On the other hand, the effect of increasing pressures on the transition temperature and the associated $\Delta V/V$ can be relevant to predict the effects of chemical pressure obtained by chemical doping ε-Fe₂O₃.
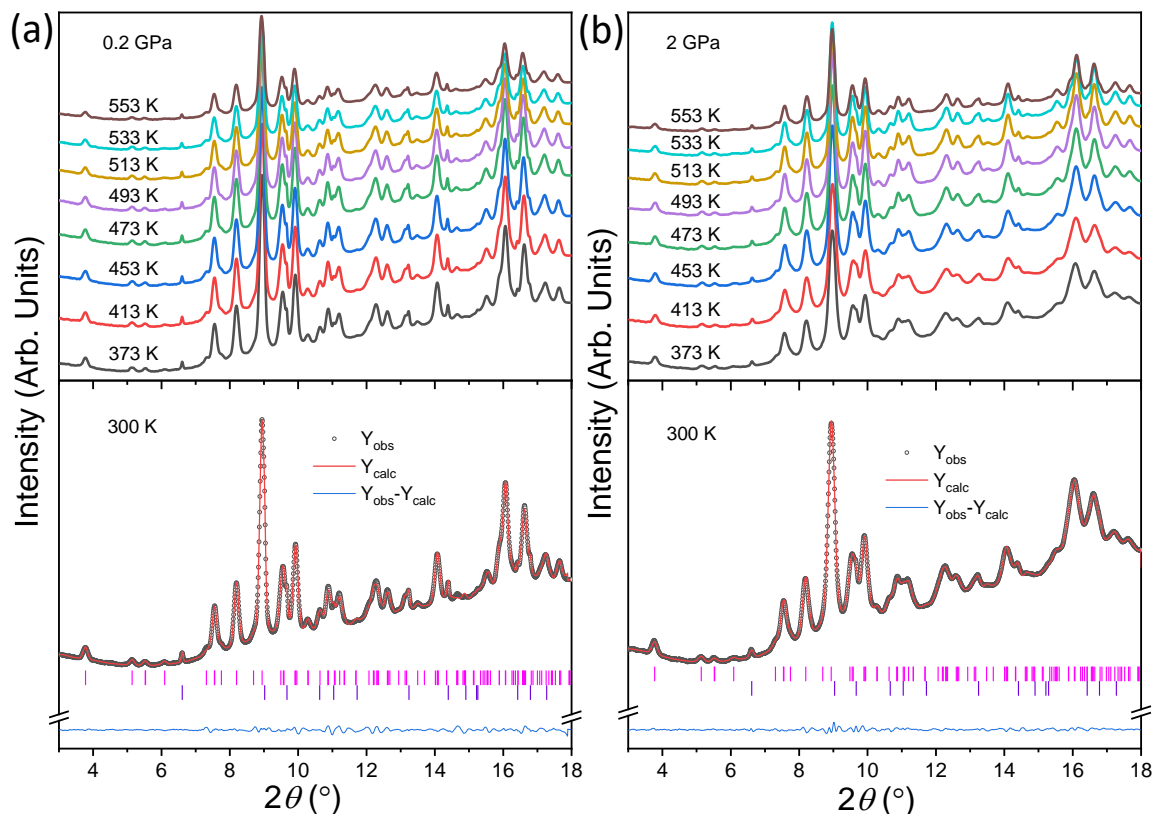
Figure 3.11 Temperature evolution of the SXPD patterns recorded under pressures of (a) 0.2 GPa and (b) 2 GPa for etched ε-Fe₂O₃ powder sample. The bottom Panels depict the corresponding Rietveld refinement (red curve) for the diffraction patterns considering both ε-Fe₂O₃ (in magenta) and minor α-Fe₂O₃ (in violet) phases. The bottom blue line in each Panel is the difference between observed and calculated diffraction patterns.

The experiment was carried out at the High Pressure endstation of the BL04-MSPD beamline at ALBA Synchrotron. For this experiment, the etched ε-Fe₂O₃ powder sample was loaded into a resistively heated membrane diamond anvil cell (DAC) consisting two diamonds faced one to each other. Between them, we used a gasket with a hole in the middle, which defines the pressure cavity where the sample is placed. The pressure inside the cavity is obtained by measuring the fluorescence signal of the calibrant (Sm:SrB₄O₇) inserted into the pressure cavity [29]. The applied pressure P is controlled by the membrane of the DAC which is inflated applying force to the mobile anvil whereas the other diamond is fixed and the pressure is monitored by the calibrant. The sample-detector distance was 240 mm and the wavelength λ= 0.4246 Å. The measurements were conducted during heating in the 300-553 K range at desired pressures. Rietveld structural refinements of the data sets collected under a certain pressure

were carried out using FULLPROF program in the "sequential mode" after refining the diffraction pattern at 300 K separately. Figure 3.11(a) and (b) show the temperature evolution of SXPD patterns acquired at pressure P= 0.2 and 2 GPa, respectively. The panels below manifest the corresponding Rietveld fitting of the room temperature patterns.
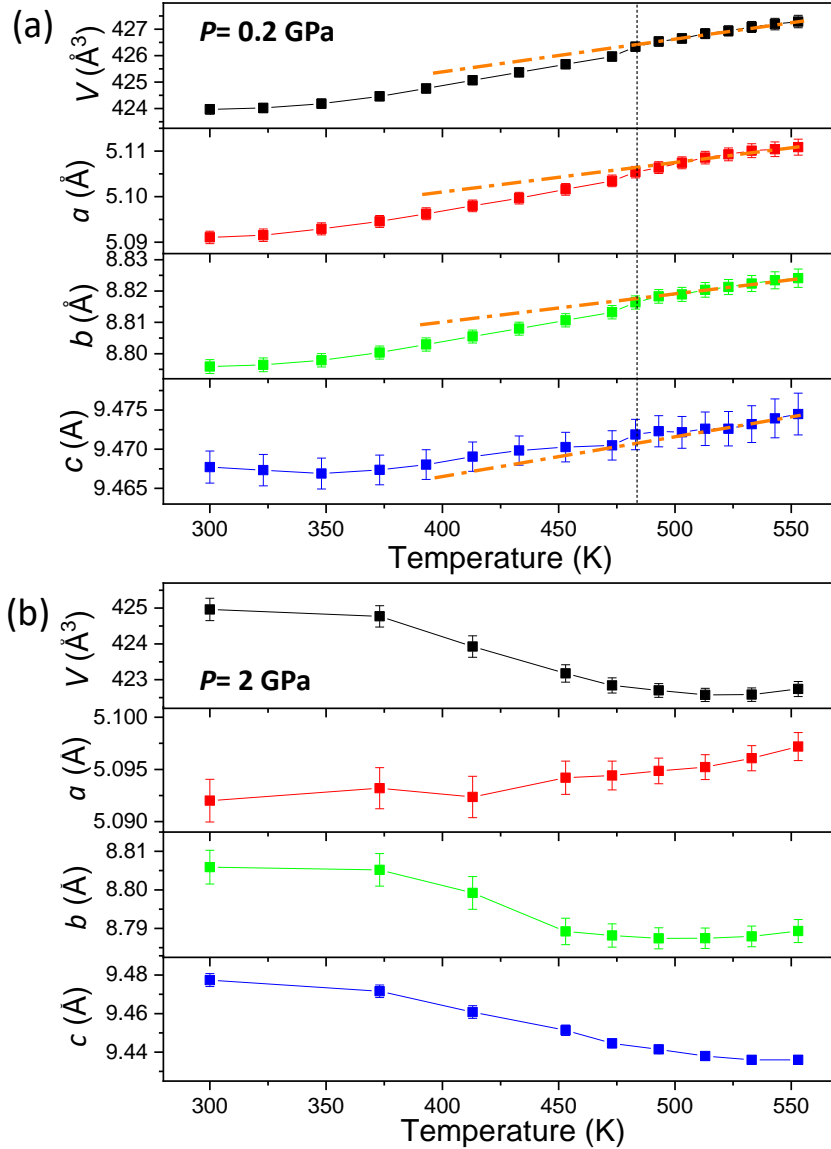
Figure 3.12 Temperature dependence of the unit-cell parameters of ε-Fe₂O₃ powders derived from the SXPD data collected under (a) 0.2 GPa and (b) 2 GPa pressure. The orange dashed lines in Panel (a) were obtained from linearly extrapolating the regions above the critical temperature T_{N2} (black dashed line). Contrary to the trend shown in Panel (a), when P= 2 GPa, the V, b, and c parameters decrease as the sample temperature increases.

Figure 3.12(a) and (b) show the temperature evolution of the lattice parameters of ε-Fe₂O₃ for P= 0.2 and 2 GPa, respectively. As can be seen from Figure 3.12(a), for P = 0.2 GPa a structural anomaly takes place at around T_{N2}, below which the unit-cell volume, V, and the orthorhombic a and b lattice constants abruptly contract, but the c parameter expands. This behavior is similar to that observed for the SXPD

at ambient pressure [7]. On the other hand, at 2 GPa, quite unexpectedly, the *V*, *b*, and *c* parameters tend to decrease with increasing temperature. In particular, the unit cell contracts quite suddenly over the 373-473 K range, i.e., it presents a volumetric negative thermal expansion above 350 K. The unit-cell contraction is also reflected by the peak shift to larger 2θ positions upon heating in the high-angle regions of the diffraction patterns (not shown).
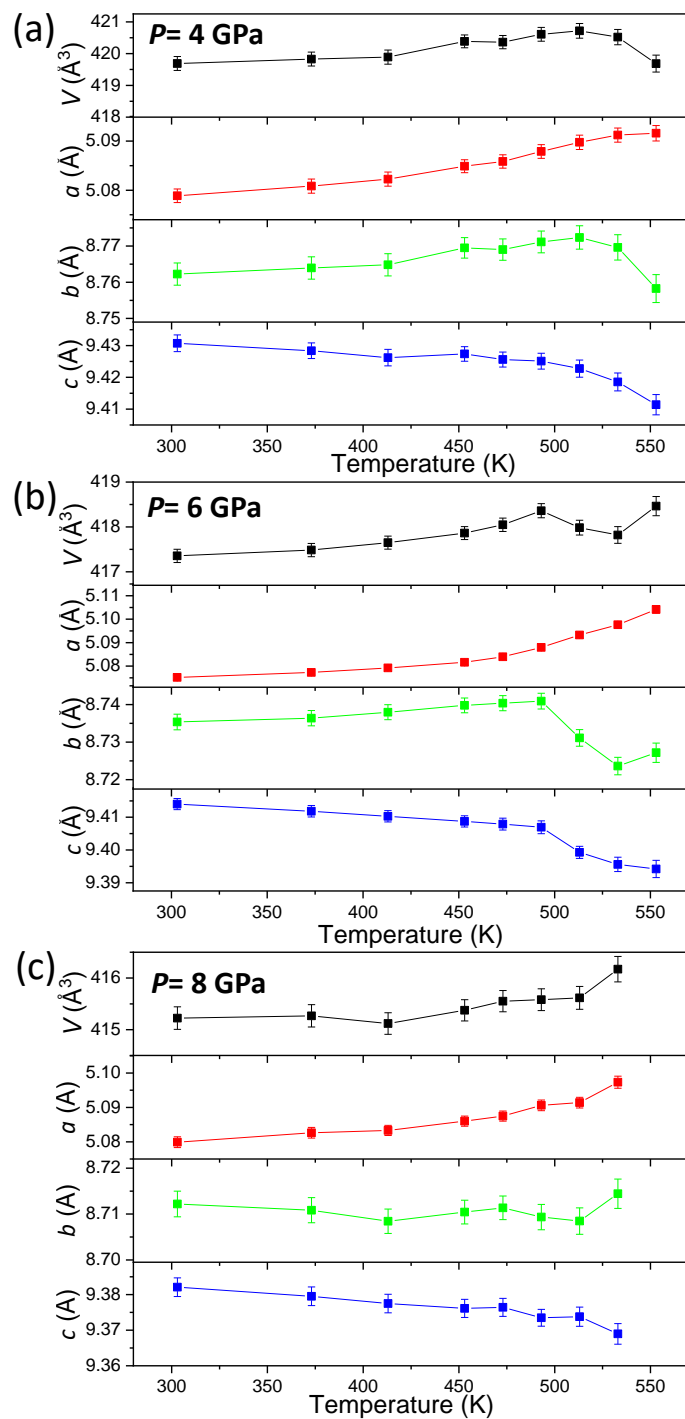
Figure 3.13 Temperature evolution of the unit-cell parameters of ε-Fe$_2$O$_3$ powders under (a) 4 GPa, (b) 6 GPa and (c) 8 GPa pressure.

The temperature dependencies of the lattice parameters at 4 GPa, 6 GPa and 8 GPa are shown in Figure 3.13(a-c). One can also observe the negative thermal expansion for $P=$ 4 and 6 GPa, but the onset of this behavior occurs at higher temperatures, above ~ 500 K, implying that such structural singularity is pressure dependent and one can note that at 6 GPa, a positive thermal expansion is again observed between 530 and 550 K. In contrast, at 8 GPa, the positive thermal expansion is observed, within the errors, throughout all the studied temperature range. Observing the thermal expansions along the different lattice parameters, a and c display opposite behaviors. At all the studied pressures there is a positive thermal expansion along a, which corresponds to the magnetic easy axis. In contrast, a negative thermal expansion is measured along c, which is the polar axis, for pressures between 2 GPa and 8 GPa at all temperatures between 300 K and 550 K. The negative thermal expansion near phase transition temperatures has been observed in many other magnetic or ferroelectric oxides, such as LaMnO$_3$ [30],[31], BaTiO$_3$ [32], and Pb(Mg$_{1/3}$Nb$_{2/3}$)O$_3$ [33], and is generally viewed as a consequence of a complex interplay among the lattice, phonons, and electrons.

No structural transformation of ε-Fe$_2$O$_3$ to hematite was found to be induced by high pressure, confirming the structural stability of *Pna2$_1$* epsilon phase. This is what one would expect since the volume collapse of ε-Fe$_2$O$_3$ at room temperature reportedly only occurs above 27 GPa [34], well above the maximum pressure examined in our investigation (i.e., 8 GPa). However, despite that within the 300-553 K range, the orthorhombic *Pna2$_1$* structure of epsilon phase seems to be preserved at all the pressures examined. We found that for increasing pressures, namely at 6 and 8 GPa, the fits after refining the structures were not as good as at lower pressures and the resulting structure is significantly distorted. Moreover, meaningless negative isotropic temperature factors were obtained and it was necessary to consider a (011) texture to improve the fits at 8 GPa which even though are less good than at lower pressures. The possibility of achieving better refinements of the data considering supergroups of *Pna2$_1$* has also been considered but *Pna2$_1$* seems to be the one that yields the best results. However, the possibility of the existence of a partial transformation cannot be excluded. A deeper analysis of the evolution of the interatomic distances and the distortion of the four non-equivalent Fe polyhedral units under compression is undergoing. Further experiments using neutron diffraction and/or Mössbauer spectroscopy under pressure would be necessary to clarify the magnetic behavior at high pressures and temperatures.

3.5 Revisiting low-temperature magnetostructural transition of ε-Fe$_2$O$_3$ nanoparticles

3.5.1 Magnetometry study of ε-Fe$_2$O$_3$ nanoparticles at low temperatures

For the low-temperature (LT) magnetic property characterization, dc magnetometry was firstly carried out using a Quantum Design SQUID magnetometer on the etched ε-Fe$_2$O$_3$ NPs (unless otherwise specified). Figure 3.14(a) shows the isothermal magnetization versus magnetic field (*M-H*) curves

recorded at various temperatures from a maximum field H= 70 kOe for the etched particles. The hard magnetic feature is evident especially for the curves at 200 and 300 K. From the hysteresis loops, the temperature evolution of the coercive field (H_C) and the ratio of remanence to the maximum magnetization at 70 kOe (M_R/M_{7T}) can be obtained (see Figure 3.14(b)). Here, the room temperature H_C is found to be 13.6 kOe. The H_C undergoes a gradual rise with decreasing temperature, reaching a local maximum at ~ 200 K, to decrease abruptly upon further cooling. The minimum H_C occurs at 100 K (H_C= 1.3 kOe), then increasing at lower temperatures. A similar trend has been observed in the M_R/M_{7T} versus T curve, but the changes of M_R/M_{7T} are observed at relatively lower temperatures. The above observations are in line with previous reports [35], which relate these magnetic changes to commensurate-incommensurate (FM2-IM1) phase transitions.
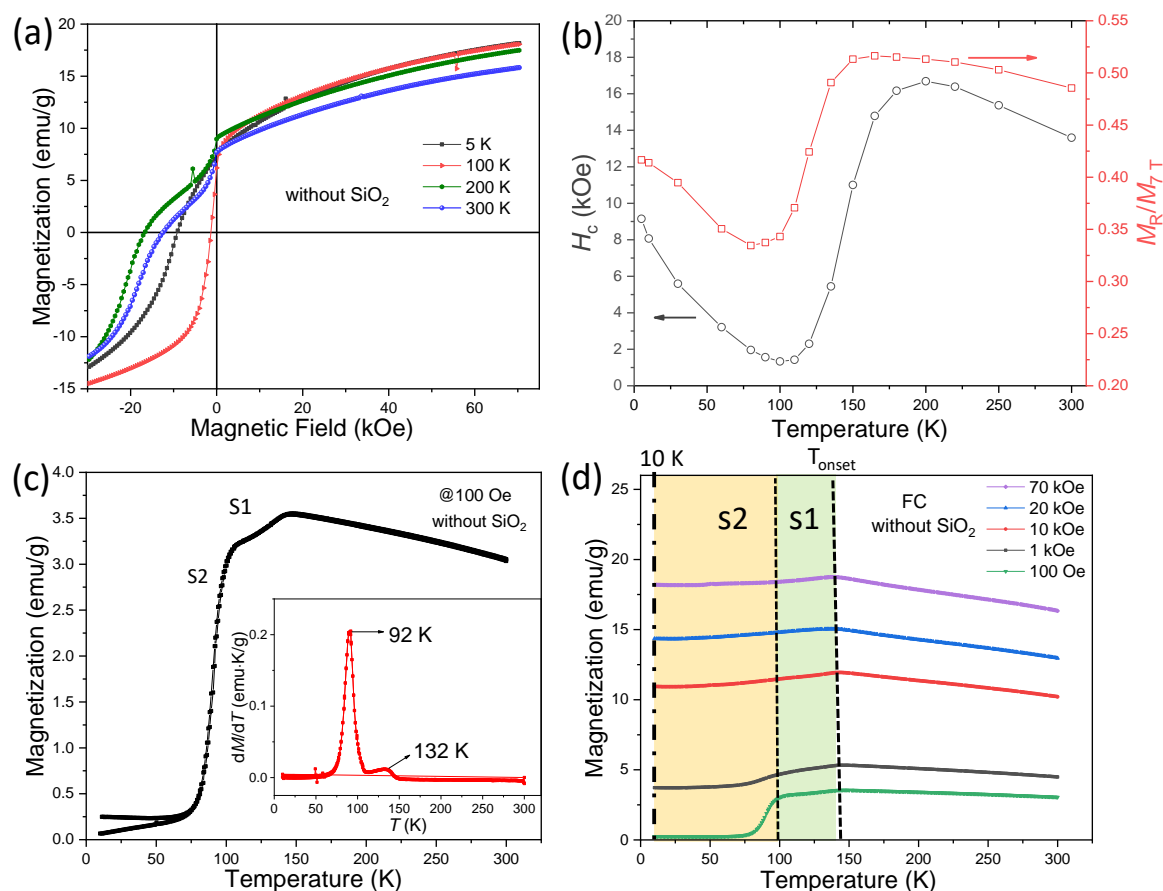
Figure 3.14 (a) Representative LT magnetization versus magnetic field curves collected on the etched ε-Fe$_2$O$_3$ nanoparticles. (b) Temperature dependence of coercivity H_C (left axis) and the ratio of remanence to the maximum magnetization at 70 kOe (M_R/M_{7T}, right axis). (c) LT magnetization versus temperature (M-T) curve acquired under both ZFC (lower branch) and FC (upper branch) conditions for the etched nanoparticles (H= 100 Oe). The inset depicts the dM/dT versus T curve. (d) The FC M-T curves acquired under various dc magnetic fields, showing the different field dependence of the **s1** and **s2** transitions. Note that the FC M-T curves are recorded during heating at 2 K/min.

Next, we focus on the LT commensurate-incommensurate (FM2-IM1) phase transitions. Figure 3.14(c) shows the temperature dependence of ZFC and FC magnetization (M-T) collected under a dc field of 100 Oe. For the measurements, a virgin sample was firstly cooled down to 10 K without field, we then

measured the magnetic moment upon heating the sample in 100 Oe field to 300 K (ZFC). Subsequently, the sample was cooled down to 10 K under the same field, the moment was finally recorded upon heating again to 300 K without removal of the field (FC). Below ~ 85 K, an irreversible thermomagnetic behavior is observed in the difference between the ZFC and FC curves. Upon heating, the rapid growth of M develops at ~ 85 K and spans to 100 K. Subsequently, the M presents a further relatively slow increase with the temperature approaching ~ 150 K, before it gradually drops as temperature increases up to 300 K. In other words, the increase of M between 85 and 150 K takes place in two stages: 85-100 K (hereafter referred to as **s2**) and 100-150 K (hereafter referred to as **s1**). This is in agreement with the derivative of magnetization versus temperature (dM/dT) curve (see inset of Figure 3.14(c)), where the two local minimums, 132 and 92 K, are found to locate respectively in the **s1** and **s2** regimes. It is interesting to note that a three-stage increase of M has been reported in the previous work of Gich et al. [2], where a third stage of M variation with a distinct slope was found in an 85-95 K range in the M-T curve under the same applied field. These differences between ε-Fe$_2$O$_3$ nanoparticles prepared following the same method are striking but are also reflected in the neutron powder diffraction (see previous discussion in Section 3.4.2).

Table 3.2 Summary of the onset temperatures of the IM1-FM2 transition and the relevant magnetization values at different magnetic fields.

H (kOe)	T_{onset} (K)	$M_{10\,K}$ (emu/g)	M_{T_onset} (emu/g)	M_{10K}/M_{T_onset}
0.1	146	0.25	3.55	0.07
1	146	3.72	5.33	0.70
10	143	10.94	11.94	0.92
20	139	14.35	15.04	0.95
70	138	18.20	18.75	0.97

The field-dependence of the magnetization in the **s1** and **s2** regions is quite different, as can be seen from the FC measurements of the M-T curves in various applied fields (Figure 3.14(d)). The onset temperature of the IM1-FM2 transition (T_{onset}), i.e., the temperature where the M starts to decrease upon heating near 150 K, the magnetizations at 10 K and T_{onset} (referred to as M_{10K} and M_{T_onset}, respectively), as well as the ratio M_{10K}/M_{T_onset}, for each applied field are summarized in Table 3.2. It can be observed that, whereas the magnetic character of the **s1** basically remains unchanged, the **s2** is rather sensitive to the field strength, and M is almost leveled-off under high dc fields in this temperature range. It is noteworthy that the M_{10K}/M_{T_onset} soars from 0.70 to 0.92 as the field strength changes from 1 to 10 kOe, giving rise to a practically continuous and steady increase of M upon heating from 10 to 150 K for $H \geq$ 10 kOe.
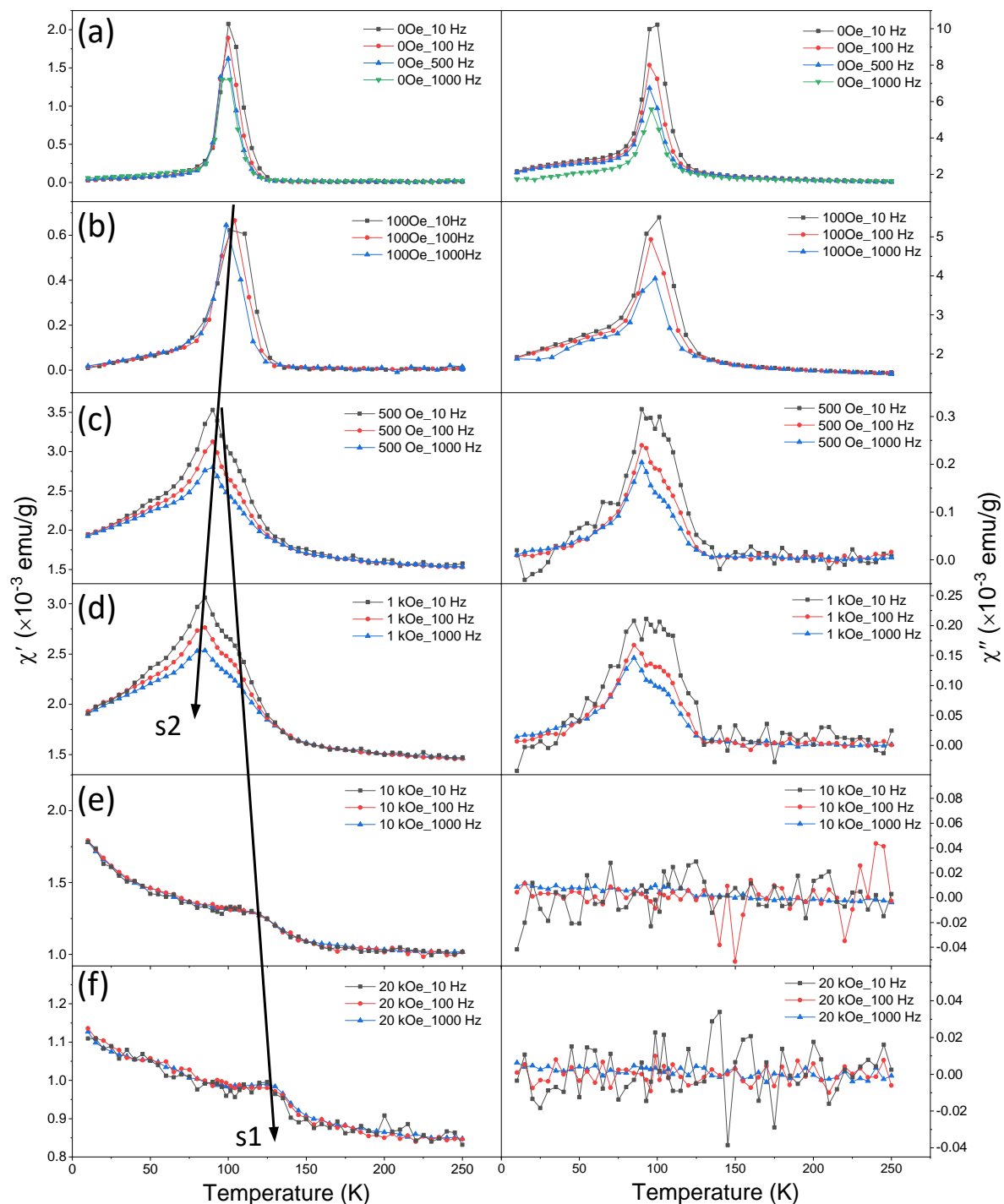
Figure 3.15 Temperature and frequency dependence of the in-phase component (χ') of the ac susceptibility for etched ε-Fe$_2$O$_3$ nanoparticles under dc field bias of (a) 0 Oe, (b) 100 Oe, (c) 500 Oe, (d) 1 kOe, (e) 10 kOe and (f) 20 kOe. The corresponding out-of-phase component (χ'') versus temperature curves are shown in their right-side Panels. The measurements were carried out during heating from 10 to 250 K at 1.5 K/min. Note that the nearly vanishing peaks in (e) and (f), as well as the magnetic signal becomes almost null for the χ'' at high dc fields (close to or beyond the detection limit of our magnetometer).

This magnetic anomaly implies the presence of a metamagnetic transition with a critical field between 1 and 10 kOe. This metamagnetic transition has also been identified in Kurmoo's work, where the nanoparticles of ε-Fe$_2$O$_3$ were synthesized by vacuum heat treatment of yttrium iron garnet (YIG) [36]. However, presumably due to the rather high content of impurities (such as YIG, yttrium silicate and yttrium oxide), the authors observed a further upturn of M below 20 K in high fields that is not seen in the current study.

Macroscopic magnetic measurements via ac magnetometry were also carried out to probe the LT magnetic transition. Figure 3.15 illustrates the temperature and frequency dependent in-phase (χ') and out-of-phase (χ'') components of the ac susceptibility, χ_{ac}, for the etched ε-Fe$_2$O$_3$ nanoparticles under various dc magnetic field strength H_{dc}. Interestingly, instead of having two well-separated peaks, both the χ' and χ'' exhibit only one sharp peak at $\sim$ 100 K when no dc field bias was applied (see Figure 3.15(a) and its right Panel). The peaks become broader with increasing dc field strength. The appearance of a shoulder on the high-temperature side of the central sharper χ' peak under H_{dc}= 500 Oe and 1 kOe (see respectively Figure 3.15(c) and (d)) indicates the existence of a secondary broad peak in the curves, which coincides with the **s1**. The two-peak feature is more well-defined in the χ'' versus T curves shown in the right panel of Figure 3.15(d). Finally, distinct responses of the χ' peaks to H_{dc} are seen from the χ' versus T curves. The sharp peak, corresponding to the above-mentioned **s1** transition region, shifts to lower temperatures as the H_{dc} increases up to 1 kOe, and disappears at high H_{dc} (see Figure 3.15(e) and (f)). This is also seen in the χ'' versus T curves. On the other hand, the **s1** progressively peaks at higher temperatures in response to an enhanced dc field, and persists under the field up to H_{dc}= 20 kOe (the maximum field examined). These observations agree well with the previous discussion. Sharp peaks in the same temperature range are also found in the χ' and χ'' of the ε-Fe$_2$O$_3$ nanoparticles embedded in silica matrix (see Figure 3.16), excluding the possible effect of silica etching on the LT magnetic phase transitions.
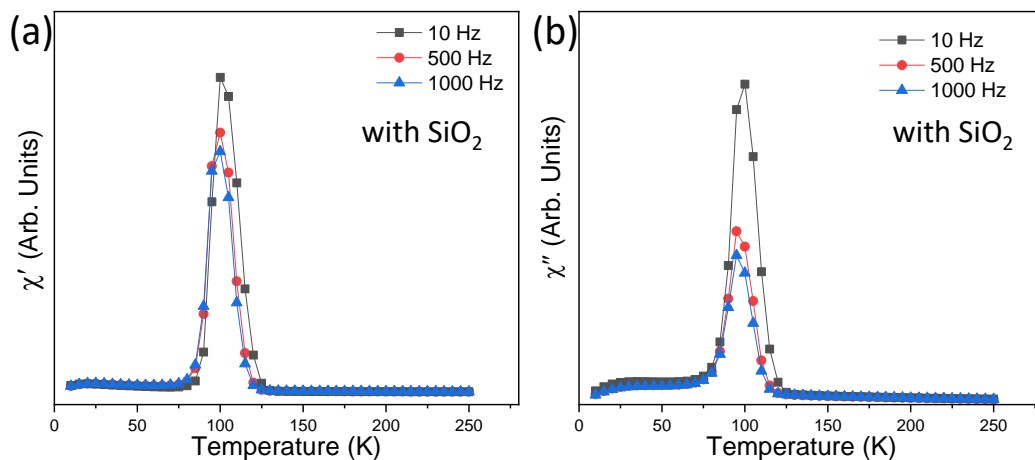
Figure 3.16 Temperature and frequency dependence of the (a) in-phase (χ') and (b) out-of-phase (χ'') components of the ac susceptibility for the non-etched ε-Fe$_2$O$_3$ nanoparticles without dc field bias. The curves are measured during heating from 10 to 250 K at 1.5 K/min.

3.5.2 Low-temperature neutron powder diffraction

The NPD patterns of the etched ε-Fe$_2$O$_3$ NPs recorded at 300 K and 10 K are shown in Figure 3.17(a). A change of the magnetic structure is evidenced from the reduced intensity of the (011) and (120) magnetic reflections under decreasing temperature, and the concurrent development of satellites on both low- and high-angle sides of these peaks. The latter is attributed to the occurrence of the incommensurate magnetic Bragg reflections at LT. This phase transition is more clearly illustrated in the temperature evolution of the intensity of the (120) commensurate magnetic peak and its satellite reflections (see Figure 3.17(b)). As temperature decreases from ~ 150 K, the (120) peak gets weaker and weaker, whereas the IM1 satellites creep and get progressively stronger afterwards. It is noteworthy that, in contrast to previously observed the disappearance of the commensurate magnetic peaks at low temperatures [2], they are preserved with quite large intensity at temperatures as low as 10-20 K. In other words, here the (120) reflection partially splits into the two IM1 satellite peaks, implying the existence of phase competition between the collinear ferrimagnetic FM2 phase and the IM1 phase at low temperatures in our particles.
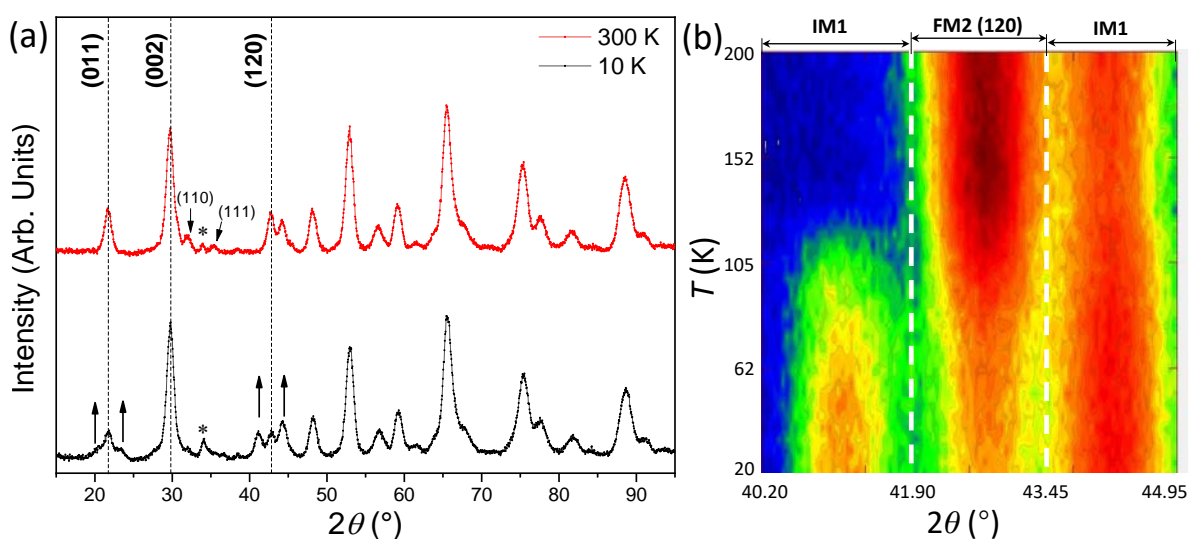
Figure 3.17 (a) Neutron diffraction patterns acquired at 10 K and 300 K for the etched ε-Fe$_2$O$_3$ nanoparticles (λ= 2.41 Å), showing the LT and HT phases of ε-Fe$_2$O$_3$. The dashed lines mark the characteristic magnetic reflections of the ferrimagnetic phase at room temperature. The up arrows in the 10 K pattern indicate the satellites emerging in the LT phase. The asterisks refer to the (101) magnetic reflection of hematite. (b) Temperature evolution of the powder neutron diffraction intensity of the (120) magnetic reflection and the associated IM reflections in the temperature range of 20-200 K. Note that the satellite on the right shoulder coincides with one of the nuclear diffraction peaks of ε-Fe$_2$O$_3$.
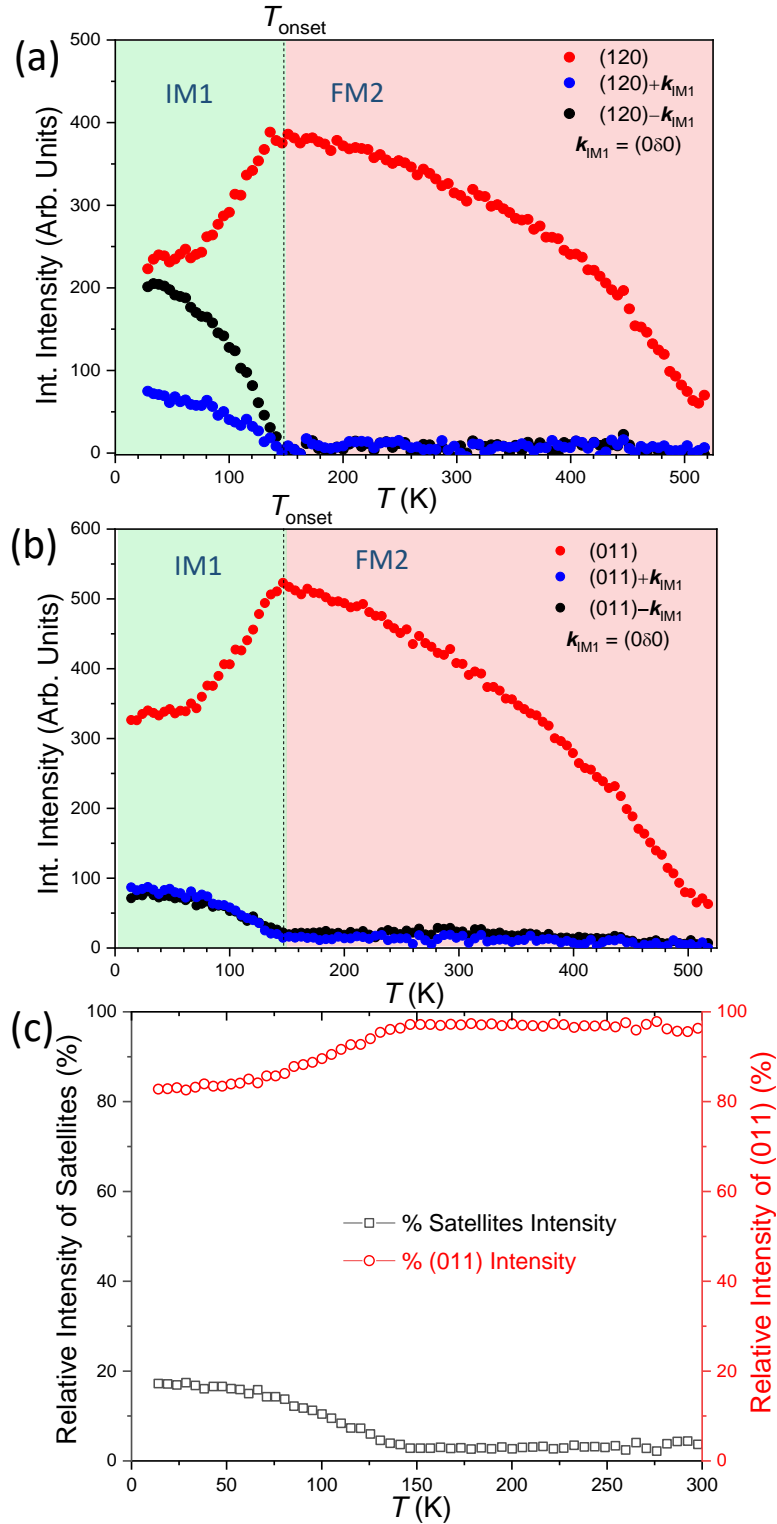
Figure 3.18 (a) Temperature dependence of the integrated peak intensity for the (120) Bragg peak and its incommensurate satellites showing the FM2-IM1 magnetic transition. Note that the contribution from the nuclear reflection intensity for the (120)+k_{IM1} satellite has been offset by compensating the integrated intensity obtained above 150 K. (b) Integrated peak intensity of the FM2 (011) Bragg peak and the associated satellite reflections. T_{onset} refers to the onset of the IM magnetic order. The propagation vector is k_{IM1}= (0, 0.07, 0) for the IM1 magnetic phase.

From the thermal evolution of the NPD patterns, the plots of integrated peak intensity can be obtained, as shown in Figure 3.18(a, b) for the (120) and (011) reflections and their associated IM1 reflections. The intensity of the FM2 phase tends to increase down to the temperature $T_{onset} \sim 150$ K, below which it starts to decrease, and meanwhile the two IM1 satellite peaks gradually develop upon further cooling down. Here T_{onset} refers to the temperature where the maximum intensity of the commensurate magnetic reflection is reached and then starts to decrease as the reflection partially splits into the two IM1 satellite peaks. This tendency is in line with the observations made from the contour map of the neutron intensity in Figure 3.17(b). The incommensurate propagation vector is $k_{IM1} = (0, 0.07, 0)$ for the IM1 magnetic phase. In addition, the intensity of the FM2 peak is quite sizeable at LT, corroborating the competition between the FM2 and IM1 phases at such temperatures. Furthermore, the broad and continuous variation of the IM1 peak intensity from $T_{onset} \sim 150$ K indicates there is only one observable magnetic transition at LT, consistent with the LT magnetometry result under zero dc magnetic field. The relative intensities of the satellite peaks and the (011) reflection as a function of temperature, derived from Figure 3.18(b), are shown in Figure 3.18(c). It can be observed that less than 20 % of the FM2 intensity is transformed into the incommensurate modulated orders.

It is interesting to compare these neutron powder diffraction results with those obtained for other batches of ε-Fe$_2$O$_3$ NPs prepared previously, also using the D20 diffractometer at ILL [2]. In that case two consecutive incommensurate phases were observed: IM1 (between 140 K and 110 K) and IM2 (below 110 K). Figure 3.19(a) shows the (011) magnetic reflections and the satellites which appear associated with the incommensurate phases at different temperatures. Figure 3.19(b) shows the 2θ position of the satellites as a function of temperature and Figure 3.19(c) gives the relative intensities of the (011) magnetic reflection and the satellites. As can be seen in Figure 3.19(b, c), the first incommensurate order on cooling (IM1) presents satellites of significantly lower intensity and appears closer to the (011) reflection as compared to those of the second incommensurate order (IM2).
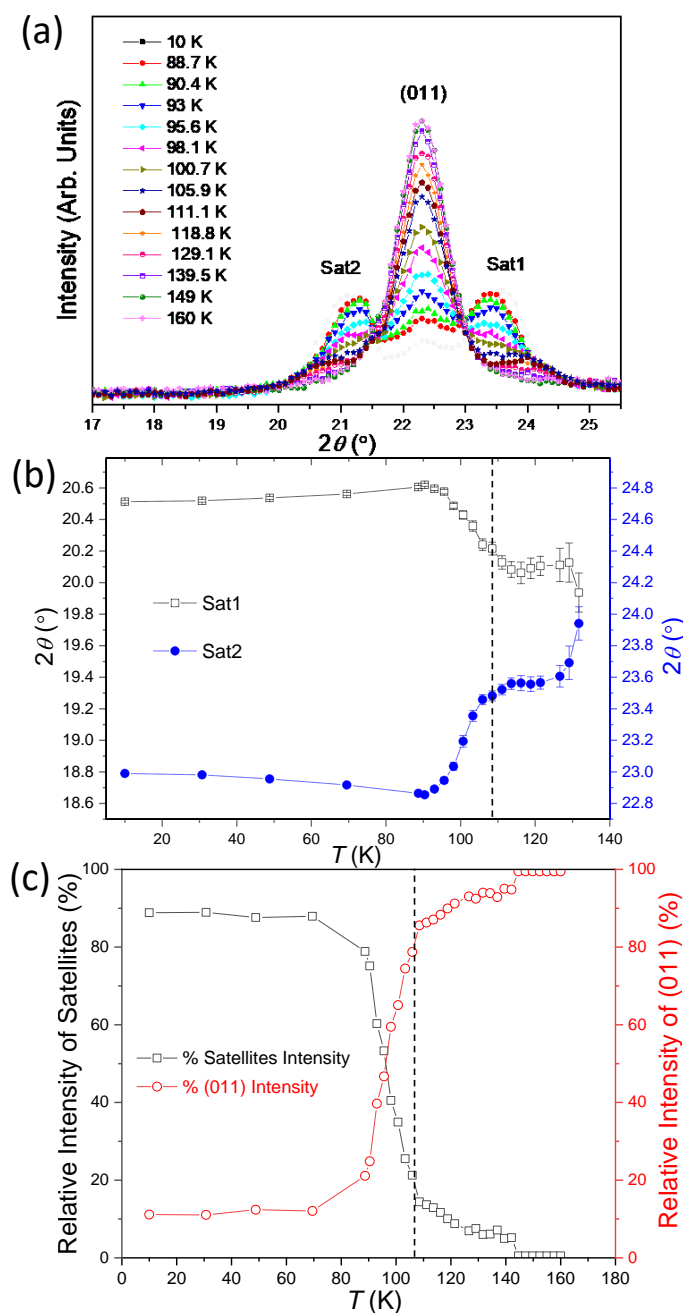
Figure 3.19 (a) Enlarged neutron diffraction patterns showing the (011) magnetic reflections and the satellites which appear associated with the incommensurate phases at different temperatures. Panel (b) shows the 2θ position of the satellites as a function of temperature. Note that the peak positions have been compensated by the 2θ zero shift. (c) Relative intensities of the (011) magnetic reflection and the satellites. The two consecutive regions separated by the dashed lines in Panel (b) and (c) are correlated to the ICM1 (140-110 K) and ICM2 (below 110 K) incommensurate phases. Note that the results are collected on other batches of ε-Fe₂O₃ NPs [2].

We can see that the relative intensities of the (011) satellites at low temperatures in Figure 3.18(c) are very similar to these of the IM1 (140-110 K) in Figure 3.19(c), and their positions also coincide. This clearly indicates that in the last NPD experiments the IM1 phase has been stabilized but contrary to what was previously observed, the second IM2 phase did not appear and IM1 could be observed down to the lowest temperatures. Since the synthesis method of the nanoparticles and their sizes are comparable, this can indicate that transitions to incommensurate magnetic orders at low temperatures

can be very sensitive to parameters affecting the sample conditioning for measurement, such as the degree of compaction. In particular, the strain state of the nanoparticles seems to be quite relevant here. Indeed, previous results obtained in the group on neutron diffraction experiments on ε-Fe$_2$O$_3$ nanoparticles doped with non-magnetic metals (see Figure 3.20) show that an incommensurate order akin to IM2 can be readily stabilized by substituting Fe^{3+} with In^{3+} which due to its significantly larger diameter compared to Fe^{3+}, increases the strain state of the nanoparticles. In contrast, doping with smaller cations such as Al^{3+} and Ga^{3+} tends to suppress the incommensurate orders.
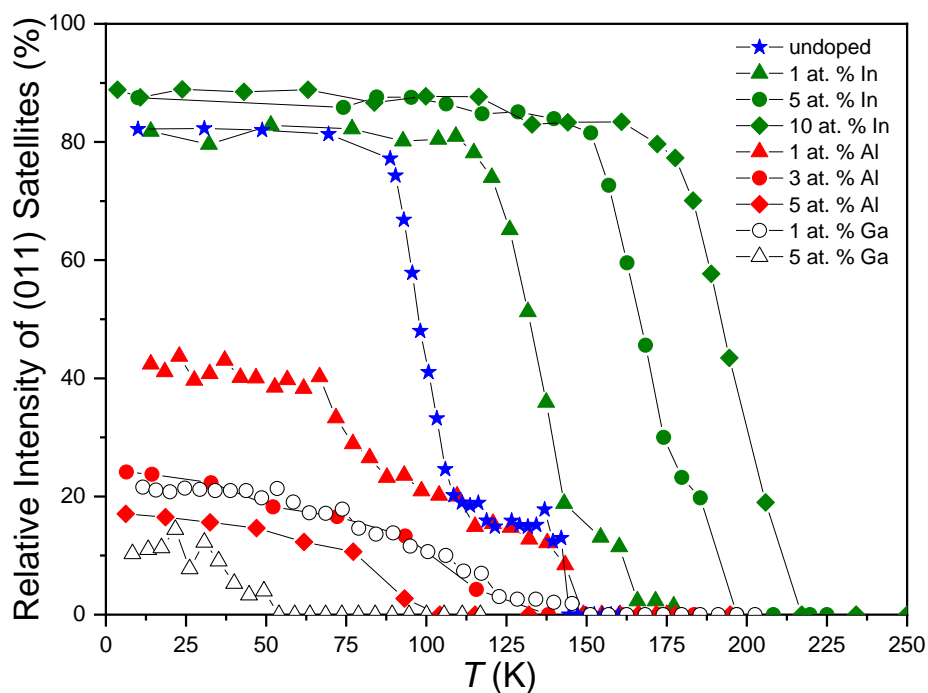
Figure 3.20 Integrated intensities of (011) satellites of doped ε-Fe$_2$O$_3$ nanoparticles from neutron powder diffraction experiments, showing the different effects of metal-substitution on the incommensurate orders.

3.6 Summary

To sum up, herein we presented the sol-gel synthesis of ε-Fe_2O_3 nanoparticles and the characterization of their structural and magnetic properties. The 20-nm particles exhibit a coercive field (H_C) of 14 kOe at room temperature. Above 300 K, a magnetic transition FM2-FM1 takes place at $T_{N2} \sim 490$ K and the H_C collapse near T_{N2}. The magnetocaloric properties associated with this magnetostructural transition have been evaluated. Preliminary high-pressure synchrotron X-ray diffraction experiments reveal the existence of anomalous thermal expansion under pressure near this transition. Below 300 K, the presence of incommensurate IM1 phase was evidenced by both magnetometry and neutron diffraction studies in our particles. Our study reveals the important roles of magnetic field and strain on the stabilization of the low-temperature incommensurate orders.

References

[1]   M. Gich, A. Roig, C. Frontera, E. Molins, J. Sort, M. Popovici, G. Chouteau, D. Martín y Marero, J. Nogús, Large coercivity and low-temperature magnetic reorientation in ε-Fe$_2$O$_3$ nanoparticles, J. Appl. Phys. 98 (2005). https://doi.org/10.1063/1.1997297.

[2]   M. Gich, C. Frontera, A. Roig, E. Taboada, E. Molins, H.R. Rechenberg, J.D. Ardisson, W.A.A. Macedo, C. Ritter, V. Hardy, J. Sort, V. Skumryev, J. Nogués, High- and low-temperature crystal and magnetic structures of ε-Fe$_2$O$_3$ and their correlation to its magnetic properties, Chem. Mater. 18 (2006) 3889–3897. https://doi.org/10.1021/cm060993l.

[3]   J.L. García-Muñoz, A. Romaguera, F. Fauth, J. Nogués, M. Gich, Unveiling a New High-Temperature Ordered Magnetic Phase in ϵ-Fe$_2$O$_3$, Chem. Mater. 29 (2017) 9705–9713. https://doi.org/10.1021/acs.chemmater.7b03417.

[4]   Y.C. Tseng, N.M. Souza-Neto, D. Haskel, M. Gich, C. Frontera, A. Roig, M. van Veenendaal, J. Nogues, Nonzero orbital moment in high coercivity epsilon-Fe$_2$O$_3$ and low-temperature collapse of the magnetocrystalline anisotropy, Phys. Rev. B. 79 (2009). https://doi.org/10.1103/PhysRevB.79.094404.

[5]   R. Jones, R. Nickel, P.K. Manna, J. Hilman, J. Van Lierop, Temperature and field evolution of site-dependent magnetism in ε−Fe$_2$O$_3$ nanoparticles, Phys. Rev. B. 100 (2019). https://doi.org/10.1103/physrevb.100.094425.

[6]   K. Xu, J.S. Feng, Z.P. Liu, H.J. Xiang, Origin of Ferrimagnetism and Ferroelectricity in Room-Temperature Multiferroic ϵ−Fe$_2$O$_3$, Phys. Rev. Appl. 9 (2018). https://doi.org/10.1103/PhysRevApplied.9.044011.

[7]   J.L. García-Muñoz, A. Romaguera, F. Fauth, J. Nogués, M. Gich, Unveiling a New High-Temperature Ordered Magnetic Phase in ϵ-Fe$_2$O$_3$, Chem. Mater. 29 (2017) 9705–9713. https://doi.org/10.1021/acs.chemmater.7b03417.

[8]   M. Gich, A. Roig, E. Taboada, E. Molins, C. Bonafos, E. Snoeck, Stabilization of metastable phases in spatially restricted fields: The case of the Fe$_2$O$_3$ polymorphs, Faraday Discuss. 136 (2007) 345–354. https://doi.org/10.1039/b616097b.

[9]   J. Rodríguez-Carvajal, Recent advances in magnetic structure determination by neutron powder diffraction, Phys. B Phys. Condens. Matter. 192 (1993) 55–69. https://doi.org/10.1016/0921-4526(93)90108-I.

[10]   K. Momma, F. Izumi, VESTA: A three-dimensional visualization system for electronic and structural analysis, J. Appl. Crystallogr. 41 (2008) 653–658. https://doi.org/10.1107/S0021889808012016.

[11]   C.A. Schneider, W.S. Rasband, K.W. Eliceiri, NIH Image to ImageJ: 25 years of image analysis, Nat. Methods. 9 (2012) 671–675. https://doi.org/10.1038/nmeth.2089.

[12]   R.B. Bergmann, A. Bill, On the origin of logarithmic-normal distributions: An analytical derivation, and its application to nucleation and growth processes, J. Cryst. Growth. 310 (2008) 3135–3138. https://doi.org/10.1016/j.jcrysgro.2008.03.034.

[13]   E. Limpert, W.A. Stahel, M. Abbt, Log-normal distributions across the sciences: Keys and clues, Bioscience. 51 (2001) 341–352. https://doi.org/10.1641/0006-3568(2001)051[0341:LNDATS]2.0.CO;2.

[14]   D. Kubániová, P. Brázda, K. Závěta, T. Kmječ, M. Klementová, J. Kohout, Identification of ferric oxide polymorphs in nanoparticles prepared by sol-gel method and maximization of ε-Fe2O3 content, J. Magn. Magn. Mater. 472 (2019) 96–103. https://doi.org/10.1016/j.jmmm.2018.09.107.

[15]   L. Kubíčková, P. Brázda, M. Veverka, O. Kaman, V. Herynek, M. Vosmanská, P. Dvořák, K. Bernášek, J. Kohout, Nanomagnets for ultra-high field MRI: Magnetic properties and transverse relaxivity of silica-coated ε-Fe$_2$O$_3$, J. Magn. Magn. Mater. 480 (2019) 154–163. https://doi.org/10.1016/j.jmmm.2019.02.067.

[16]   A.A. Dubrovskiy, D.A. Balaev, K.A. Shaykhutdinov, O.A. Bayukov, O.N. Pletnev, S.S. Yakushkin, G.A. Bukhtiyarova, O.N. Martyanov, Size effects in the magnetic properties of ε-Fe2O3 nanoparticles, J. Appl.

Phys. 118 (2015) 213901. https://doi.org/10.1063/1.4936838.

[17] O. Popov, M. Mikhov, Thermal activation and the Hopkinson effect, J. Magn. Magn. Mater. 82 (1989) 29–32. https://doi.org/https://doi.org/10.1016/0304-8853(89)90058-9.

[18] P.S.A. Kumar, P.A. Joy, S.K. Date, On the irreversible magnetic behavior of the anisotropic ferromagnetic system SrRuO3, Phys. B Condens. Matter. 269 (1999) 356–361. https://doi.org/https://doi.org/10.1016/S0921-4526(99)00126-X.

[19] P.A. Joy, P.S.A. Kumar, S.K. Date, The relationship between field-cooled and zero-field-cooled susceptibilities of some ordered magnetic systems, J. Phys. Condens. Matter. 10 (1998) 11049–11054. https://doi.org/10.1088/0953-8984/10/48/024.

[20] M. Gich, A. Roig, C. Frontera, E. Molins, J. Sort, M. Popovici, G. Chouteau, D.M.Y. Marero, J. Nogues, Large coercivity and low-temperature magnetic reorientation in epsilon-Fe2O3 nanoparticles, J. Appl. Phys. 98 (2005). https://doi.org/10.1063/1.1997297.

[21] A.H. Hill, F. Jiao, P.G. Bruce, A. Harrison, W. Kockelmann, C. Ritter, Neutron diffraction study of mesoporous and bulk hematite, α-Fe$_2$O$_3$, Chem. Mater. 20 (2008) 4891–4899. https://doi.org/10.1021/cm800009s.

[22] K.A. Gschneidner, V.K. Pecharsky, Magnetocaloric Materials, Annu. Rev. Mater. Sci. 30 (2000) 387–429. https://doi.org/10.1146/annurev.matsci.30.1.387.

[23] V. Franco, J.S. Blázquez, B. Ingale, A. Conde, The Magnetocaloric Effect and Magnetic Refrigeration Near Room Temperature: Materials and Models, Annu. Rev. Mater. Res. 42 (2012) 305–342. https://doi.org/10.1146/annurev-matsci-062910-100356.

[24] Y. Liu, L.C. Phillips, R. Mattana, M. Bibes, A. Barthélémy, B. Dkhil, Large reversible caloric effect in FeRh thin films via a dual-stimulus multicaloric cycle, Nat. Commun. 7 (2016) 1–6. https://doi.org/10.1038/ncomms11614.

[25] E. Stern-Taulats, T. Castán, L. Mañosa, A. Planes, N.D. Mathur, X. Moya, Multicaloric materials and effects, MRS Bull. 43 (2018) 295–299. https://doi.org/10.1557/mrs.2018.72.

[26] J.H. Chen, A. Us Saleheen, P.W. Adams, D.P. Young, N. Ali, S. Stadler, On entropy determination from magnetic and calorimetric experiments in conventional giant magnetocaloric materials, J. Appl. Phys. 123 (2018) 145101. https://doi.org/10.1063/1.5016858.

[27] S. Xi, W. Lu, Y. Sun, Magnetic properties and magnetocaloric effect of La$_{0.8}$Ca$_{0.2}$MnO$_3$ nanoparticles tuned by particle size, J. Appl. Phys. 111 (2012) 63922. https://doi.org/10.1063/1.3699037.

[28] P. Lloveras, M. Barrio, J. Tamarit, S. Crossley, W. Li, V. Pomjakushin, N.D. Mathur, X. Moya, A. Planes, L. Man, Giant barocaloric effects at low pressure in ferrielectric ammonium sulphate, (2015). https://doi.org/10.1038/ncomms9801.

[29] S. V. Rashchenko, A. Kurnosov, L. Dubrovinsky, K.D. Litasov, Revised calibration of the Sm:SrB$_4$O$_7$ pressure sensor using the Sm-doped yttrium-aluminum garnet primary pressure scale, J. Appl. Phys. 117 (2015) 145902. https://doi.org/10.1063/1.4918304.

[30] J.L. García-Muñoz, M. Suaaidi, C. Ritter, Magnetostructural effects in insulating and metallic La$_{0.85-x}$Y$_{0.15}$Ca$_x$MnO$_3$ (x < 0.50), Phys. B Condens. Matter. 234–236 (1997) 854–855. https://doi.org/10.1016/S0921-4526(96)01126-X.

[31] T. Chatterji, F. Fauth, B. Ouladdiaf, P. Mandal, B. Ghosh, Volume collapse in LaMnO$_3$ caused by an orbital order-disorder transition, Phys. Rev. B - Condens. Matter Mater. Phys. 68 (2003) 052406. https://doi.org/10.1103/PhysRevB.68.052406.

[32] V. Mueller, L. Jäger, H. Beige, H.P. Abicht, T. Müller, Thermal expansion in the Burns-phase of barium titanate stannate, Solid State Commun. 129 (2004) 757–760. https://doi.org/10.1016/j.ssc.2003.12.035.

[33] P. Bonneau, P. Garnier, G. Calvarin, E. Husson, J.R. Gavarri, A.W. Hewat, A. Morell, X-ray and neutron diffraction studies of the diffuse phase transition in PbMg$_{1/3}$Nb$_{2/3}$O$_3$ ceramics, J. Solid State Chem. 91 (1991) 350–361. https://doi.org/10.1016/0022-4596(91)90090-5.

[34] J.A. Sans, V. Monteseguro, G. Garbarino, M. Gich, V. Cerantola, V. Cuartero, M. Monte, T. Irifune, A.

Muñoz, C. Popescu, Stability and nature of the volume collapse of ε-Fe$_2$O$_3$ under extreme conditions, Nat. Commun. 9 (2018). https://doi.org/10.1038/s41467-018-06966-9.

[35]   M. Gich, A. Roig, C. Frontera, E. Molins, J. Sort, M. Popovici, G. Chouteau, D. Martín y Marero, J. Nogús, Large coercivity and low-temperature magnetic reorientation in ε-Fe 2O 3 nanoparticles, J. Appl. Phys. 98 (2005) 044307. https://doi.org/10.1063/1.1997297.

[36]   M. Kurmoo, J.L. Rehspringer, A. Hutlova, C. D'Orléans, S. Vilminot, C. Estournès, D. Niznansky, Formation of nanoparticles of ε-Fe$_2$O$_3$ from yttrium iron garnet in a silica matrix: An unusually hard magnet with a Morin-like transition below 150 K, Chem. Mater. 17 (2005) 1106–1114. https://doi.org/10.1021/cm0482838.

Chapter 4

Effect of Transition-Metal Substitutions on the Properties of ε-Fe$_2$O$_3$ Nanoparticles

While exhibiting intriguing properties and great application potentials, relatively little systematic research has been conducted on doped ε-Fe$_2$O$_3$. In this work we synthesized various transition-metal-substituted ε-Fe$_2$O$_3$ nanoparticles via sol-gel chemistry. This chapter studies the effects of chemical doping with magnetic transition metals on the structural and magnetic properties of ε-Fe$_2$O$_3$. The changes caused by doping ε-Fe$_2$O$_3$ nanoparticles provide insights into the complex magnetic ground states and the unusual interplays between different degrees of freedom. Furthermore, metal-substitution allows us to tune the magnetic properties of ε-Fe$_2$O$_3$, opening up further applications for this oxide.

4.1 Introduction

In the study of ε-Fe_2O_3, the relevance of metal-substitution is evident. For example, the structural stability of this phase can be improved through chemical doping by Ga, leading to a thermodynamically stable $GaFeO_3$ which has been reportedly grown as bulk single-crystals [1],[2]. Moreover, the substitution of Fe by other transition metals offers many possibilities of tuning the functional properties and modifying the complex phase diagram of ε-Fe_2O_3, expanding further its potential applications. To illustrate this, thanks to the gigantic room-temperature coercivity of ε-Fe_2O_3 and its tunability upon chemical doping, metal-substituted ε-$M_xFe_{2-x}O_3$ (M= In [3], Ga [4], Al [5], et al.) nanomagnets have been studied by Ohkoshi and co-workers aiming at their potential use as millimeter-wave absorption devices. Furthermore, it is anticipated that the selective occupancy of dopant(s) in certain crystallographic Fe cation(s) can provide valuable information on the characteristics and/or roles of the Fe^{3+} in parent ε-Fe_2O_3. Thus, metal-substitution, especially, the substitutions by 3d transition metal cations bearing a net magnetic moment due to unpaired spins, offers an alternative pathway to understand aspects of the physics of ε-Fe_2O_3 which are still not well understood such as the large magnetocrystalline anisotropy and the subtle interplay between charge, orbital and lattice degrees of freedom which are responsible for the complex phenomena in this oxide. Yet, little systematic work has been conducted on metal-doped ε-Fe_2O_3 in this respect.

In this chapter, we report on the effect of metal-substitution on the evolution of its structural and magnetic properties. The primary focus is devoted to the study of Cr-doped ε-$(Fe_{1-x}Cr_x)_2O_3$ nanoparticles; however, some preliminary results of other metal-doped ε-$M_xFe_{2-x}O_3$ (M= Mn, Co and Ru) are also presented.

4.2 Synthesis and characterization of Cr-substituted ε-Fe₂O₃ nanoparticles

4.2.1 Sol-gel synthesis of ε-(Fe₁₋ₓCrₓ)₂O₃ nanoparticles

The single-crystalline ε-$(Fe_{1-x}Cr_x)_2O_3$ (x= 0.01, 0.03, 0.05, 0.075, 0.10, 0.15, 0.20, 0.25) nanoparticles (NPs) embedded in silica matrix were prepared using sol–gel based method. The above compositions correspond to 1 at.%, 3 at.%, 5 at.%, 7.5 at.%, 10 at.%, 15 at.%, 20 at.% and 25 at.% Cr-substituted ε-Fe_2O_3, respectively. In addition to (III) nitrate (Aldrich) and TEOS (Aldrich) as the precursors for Fe cation and SiO_2 matrix, which were also used for the synthesis of ε-Fe_2O_3 particles, here hydrated chromium (III) nitrate $Cr(NO_3)_3 \cdot 9H_2O$ (Aldrich) was the Cr cation precursor. The weight percentage of metal oxide with respect to silica was 20 %. The molar ratio of TEOS, ethanol, and water was fixed to 1:6:6. Compared to the detailed description of the synthesis given in Chapter 3, the only relevant

difference for the synthesis of Cr-doped particles is that it is necessary to dissolve the appropriate amounts of Cr(NO$_3$)$_3$·9H$_2$O before adding iron nitrate. The resultant xerogels were placed in an alumina boat and treated in a tubular furnace in air atmosphere at 200 °C/h to 450 °C and then to 1100 °C at 80 °C/h, and were held for 3 h at this temperature before being cooled to room temperature at 350 °C/h. After thermal treatment, single-crystalline ε-(Fe$_{1-x}$Cr$_x$)$_2$O$_3$ NPs supported on silica matrix can be obtained. Finally, following the same procedure described in Chapter 3, the silica matrix was removed by immersing the particles in a concentrated NaOH aqueous solution for each composition.

A list of the synthesized samples is given in Table 4.1, together with the chemical compositions obtained from energy-dispersive X-ray spectroscopy (EDX) analysis. Within the error expected in EDX analysis, these results are in very good agreement with the targeted stoichiometric ratios.

Table 4.1 Summary of the Cr-doped ε-(Fe$_{1-x}$Cr$_x$)$_2$O$_3$ (x= 0.01, 0.03, 0.05, 0.075, 0.10, 0.15, 0.20, 0.25) nanoparticles under study. Both the theoretical atomic percentages (at.%) of Cr and the chemical compositions of the compounds obtained from SEM-EDX technique are given. The EDX spectra were collected from a number of distinct areas for all the examined samples, and the numbers in parentheses are the standard deviations of the last digit.

x	at.% Cr	EDX Analysis	
		Fe (at.%)	Cr (at.%)
0.01	1	98.5	1.5(3)
0.03	3	96.8	3.2(5)
0.05	5	94.5	5.8(3)
0.075	7.5	92.1	7.8(9)
0.10	10	89.9	10.1(4)
0.15	15	85.0	15.0(7)
0.20	20	78.9	21.1(7)
0.25	25	75.3	24.7(5)

4.2.2 Effect of Cr substitutions on the structural and magnetic properties of ε-Fe$_2$O$_3$ nanoparticles

Synchrotron X-ray diffraction and X-ray absorption study

Figure 4.1(a) presents the synchrotron X-ray powder diffraction (SXRPD) patterns of the etched ε-Fe$_2$O$_3$ and Cr-doped ε-(Fe$_{1-x}$Cr$_x$)$_2$O$_3$ NPs. It can be seen that for $x \leq 0.10$ (i.e 10 at. % Cr), all the nanoparticles maintain the ε-Fe$_2$O$_3$ $Pna2_1$ structure with small amounts of hematite impurity. An enlarged portion of the synchrotron X-ray patterns (right panel (c)) shows that for the samples with increased Cr content there is a slight shift of the diffraction peaks towards higher angular positions. The diffraction peak shifts are due to shrinkage of the $Pna2_1$ orthorhombic cell as a result of the increase in

the proportion of Fe^{3+} ions substituted by isovalent Cr^{3+} ions (see below). Cr^{3+} has an ionic radius of 0.615 Å in the VI-shell, very similar and only slightly smaller than Fe^{3+} ions (0.645 Å) [6].
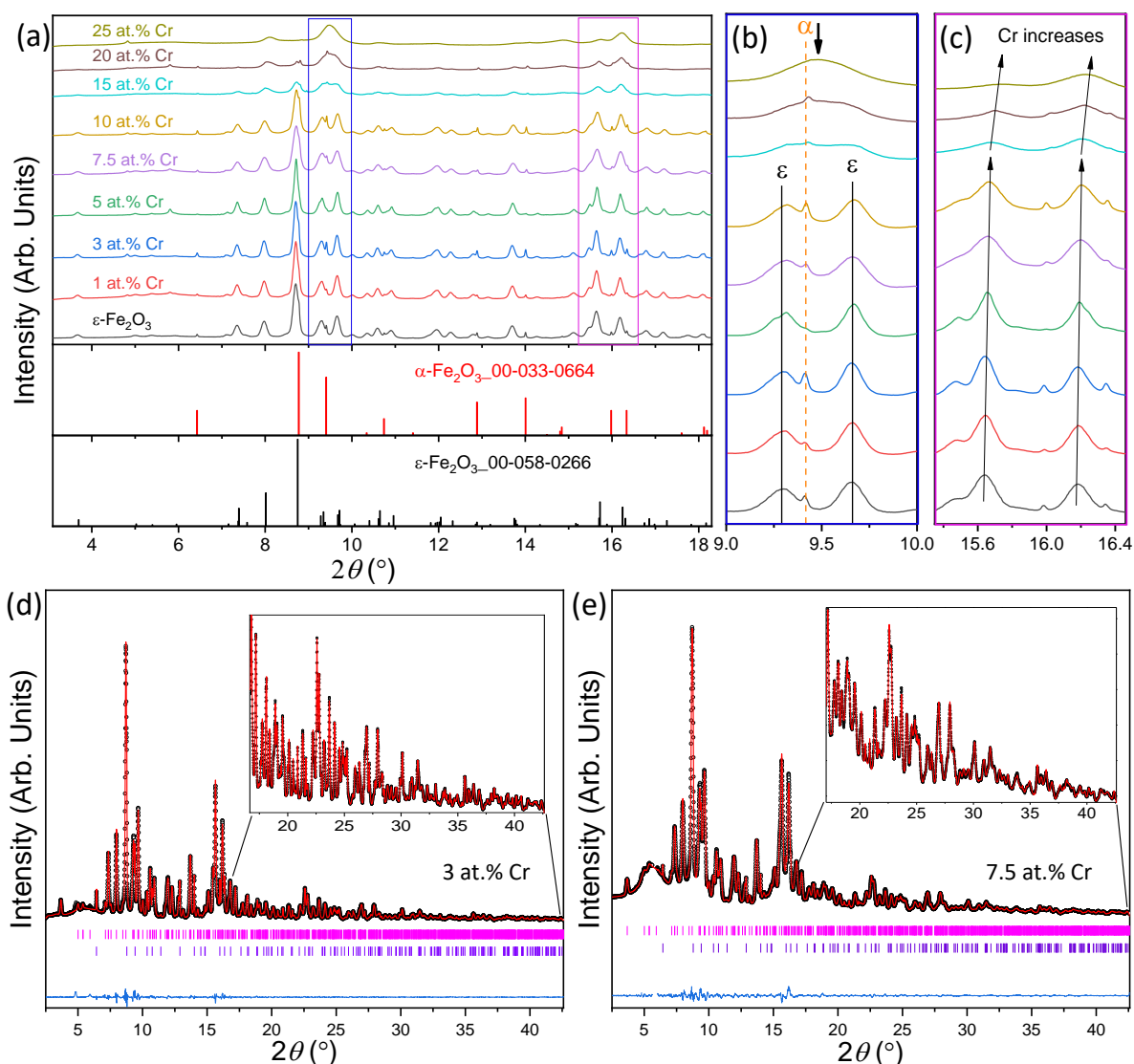
Figure 4.1 (a) Room-temperature synchrotron X-ray diffraction patterns for the etched ε-$(Fe_{1-x}Cr_x)_2O_3$ ($0 \leq x \leq 0.25$) nanoparticles. The wavelength λ= 0.412 84(6) Å. The panels below depict the diffraction peaks of α-Fe₂O₃ (ICSD 00-033-0664, in red) and ε-Fe₂O₃ (ICSD 00-058-0266, in black). The delimited high-angle regions of the patterns are shown in the (b) and (c) Panels. Note that the spectra are vertically offset for clarity. (d) and (e) show the Rietveld refinement for the 3 at.% Cr and 7.5 at.% Cr patterns, respectively. The bottom blue line is the difference between observed and calculated diffraction patterns. The top row of vertical bars (in magenta) corresponds to Bragg reflection positions from the *Pna2₁* SG of ε-Fe₂O₃, while the bottom vertical bars (in violet) are from hematite minor impurity (α-Fe₂O₃, less than 4 wt. % in all cases). Agreement factors of the refinement for the 3 at.% Cr (7.5 at.% Cr) particles are: R_B = 1.0 % (1.7 %), R_f = 0.7 % (1.2 %), χ^2 = 5.2 (4.6).

Figure 4.1(d) and (e) show the Rietveld refinement patterns for the 3 at.% Cr and 7.5 at.% Cr NPs, respectively. The top row of vertical bars (in magenta) corresponds to Bragg reflection positions from the *Pna2₁* structure of the epsilon phase, while the bottom vertical bars (in violet) are from hematite

impurity (less than 4 % by weight in both samples). The contribution to the patterns from the minor remaining amorphous silica was treated as background points of the patterns during the refinement. It is interesting to note that we have obtained the best refinement of synchrotron patterns by distributing Cr atoms only between the octahedral Fe sites, without Cr in the tetrahedral site.

On the other hand, with a further increase of Cr content (i.e., for $x \geq 0.15$), several significant changes can be progressively observed in the diffraction patterns: **i)** The intensity of the diffraction peak at $2\theta \sim$ 8.7°, which is the strongest reflection of ε-Fe₂O₃ phase, significantly drops as the Cr-content increases from 10 at.% to 15 at.%, and then it gradually decreases to nearly zero with further Cr-doping increase to 25 at.%; **ii)** For the peak at $\sim$ 8.0° and the two rather broad peaks around $2\theta = 16.0°$ (see Panel (c)), a decline in the diffraction intensity and peak broadening are observed; **iii)** Within the 2θ range of 9.0° to 10.0°, a central diffraction peak (as indicated by the downside arrow in Panel (b)) emerges gradually at the expense of the two consecutive peaks of ε-Fe₂O₃ diffraction intensity. In fact, the intensity enhancement of the valley of the two peaks occurs even for x less than 0.15. These observations strongly suggest the appearance of a new phase upon high Cr-substitution ($x \geq 0.15$) in the parent $Pna2_1$ structure. In particular, the existence in the 25 at.% Cr pattern of well-defined central peaks without the side peaks of ε-Fe₂O₃ phase in the 2θ range of 9.0-10.0° implies this composition may represent the phase-pure new structure. However, due to the low sensitivity of X-ray diffraction to oxygen (see Chapter 2), we are unable to refine the structures of these high Cr-content samples. Further work is ongoing to resolve the structural peculiarities in this system.
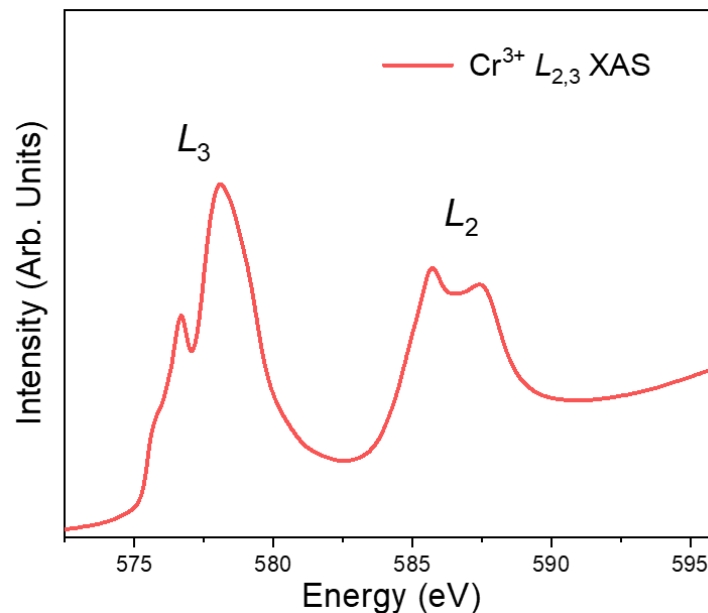
Figure 4.2 XAS spectra of the Cr-$L_{2,3}$ absorption edges acquired at room temperature for the 7.5 at.% Cr sample. The XAS spectra were collected on BOREAS beamline at ALBA synchrotron.

The Cr $L_{2,3}$ edge X-ray absorption spectrum (XAS) shown in Figure 4.2 is found to correlate very well with the experimental XAS $2p_{3/2,1/2}$ spectrum of Cr_2O_3 [7], evidencing the 3+ oxidation state of Cr in the ε-$(Fe_{1-x}Cr_x)_2O_3$. Moreover, the stabilization of the polar structure of ε-Fe_2O_3 phase up to 10 at.% Cr strongly corroborates the isovalent nature of the substitution.

Magnetometry study
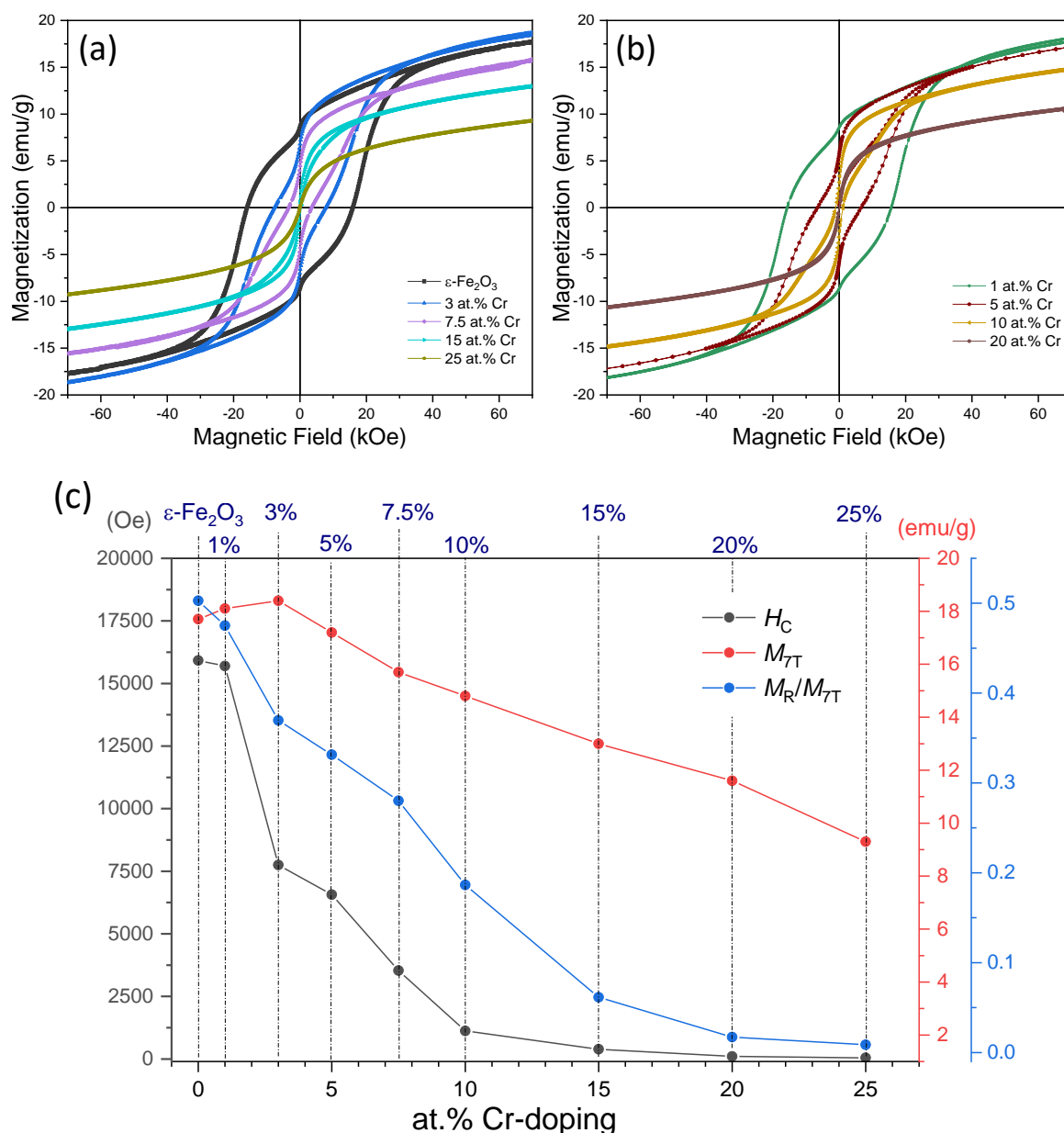
Figure 4.3 (a, b) Room temperature magnetic hysteresis loops recorded using a VSM magnetometer for the parent and Cr-doped ε-$(Fe_{1-x}Cr_x)_2O_3$ NPs (with silica). The measurements were carried out on the non-etched samples. The rounded magnetization loop of ε-Fe_2O_3 gradually disappears upon Cr-substitution. (c) The evolution of coercive field (H_C), the magnetization at 7 T (M_{7T}) and M_R/M_{7T} as a function as Cr-doping rate, showing the gradually softer behavior upon the incorporation of Cr.

Figure 4.3(a-b) presents the room temperature hysteresis loops for the parent ε-Fe₂O₃ NPs and the Cr-doped ones. The M-H loops give evidence of a strong influence of Cr-doping on the hysteresis behaviors of the NPs at room temperature. It is observed that the typical round-shaped magnetization response of ε-Fe₂O₃ progressively becomes sharper and the remanent magnetization (M_R) decreases as the Cr-substitution increases. The hysteretic behavior nearly disappears for the sample with 15 at.% Cr and is almost absent, with M_R<0.2 emu/g, for the highest Cr contents (20 and 25 at.%). The increasingly soft magnetic character developed upon Cr doping is also evidenced in the evolution of the coercive field (H_C) the magnetization at the maximum applied field (M_{7T}) and M_R/M_{7T}, which are presented in Figure 4.3(c) and gathered in Table 4.2, also with M_R. In Figure 4.3(c) we can see that while M_{7T} slightly increases as the Cr content is raised to 3 at. % H_C sharply decreases by more than 50 %. This indicates that the magnetic anisotropy of the system is extremely sensitive to the substitution of Fe^{3+} by Cr^{3+}. Indeed, the pristine giant H_C declines from about 16 kOe for ε-Fe₂O₃ to 1120 Oe for the 10 at.% Cr sample, which is the sample with the highest Cr content that can be refined using the *Pna2₁* model. This tendency continues as x further increases, and an H_C of 50 Oe is found for 25 at.% Cr. After the small initial increase, M_{7T} steadily declines with further Cr-doping. M_R/M_{7T} undergoes a continuous decrease from about 0.5 for undoped nanoparticles to less than 0.01 for 25 at.% Cr-doping.

Table 4.2 Summary of the magnetic measurement results for the parent and Cr-doped ε-Fe₂O₃ nanoparticles under study, including the H_C, M_{7T} and M_R obtained from room temperature (RT) hysteresis measurements, the peak positions of the low-temperature (LT) ZFC dM/dT-T curves, T_{p1} and T_{p2}, together with the high-temperature (HT) transition temperatures (T_{N1} and T_{N2}). The T_{N1} and T_{N2} are determined from the local minima of the dM/dT-T curves collected on the non-etched samples.

Sample	RT Hysteresis Loops			LT M-T		HT M-T	
	H_C (Oe)	M_{7T} (emu/g)	M_R (emu/g)	T_{p2} (K)	T_{p1} (K)	T_{N2} (K)	T_{N1} (K)
ε-Fe₂O₃	15920	17.7	8.9	92	132	492	850
1 at.% Cr	15696	18.1	8.6	73	131	477	843
3 at.% Cr	7751	18.4	6.8	59	128	467	817
5 at.% Cr	6568	17.2	5.7	60	129	450	-
7.5 at.% Cr	3533	15.7	4.4	64	127	438	781
10 at.% Cr	1120	14.8	2.8	77	-	421	-
15 at.% Cr	388	13.0	0.8	-	-	-	-
20 at.% Cr	100	11.6	0.2	-	-	-	-
25 at.% Cr	50	9.3	0.1	-	-	-	-

Figure 4.4 shows ZFC and FC magnetization versus temperature (M-T) curves for all the studied compositions, measured during heating at 2 K/min under an applied field of 100 Oe. As discussed in Chapter 3, the low-filed M-T curve of ε-Fe₂O₃ is featured by an important two-stage magnetization

increase, corresponding to the IM1 incommensurate phase: a sudden increase in 85-100 K (**s2**) and moderate growth in 100-150 K (**s1**). By comparing this *M-T* curve with those shown in Figure 4.4(a), corresponding to doped samples with $x \leq 0.10$, one can notice several differences and some similarities. First, upon cooling, the onset of the sudden magnetization increase (i.e., the **s2**) in the ZFC branch is significantly shifted to lower temperatures as the Cr-doping approaches 5 at.% Cr (from ~100 K for undoped to ~75 K for 5 at.% Cr-doped), accompanied by a rebound to an onset temperature similar to that of the parent sample upon a further Cr-doping increase up to 10 at.%. In contrast, Cr substitution seems to have little influence on the onset of the transition temperature of the **s1** regime under cooling, which for Cr-doped nanoparticles is also very close to 150 K. The local maxima of the derivative of the ZFC magnetization with respect to temperature (*dM/dT*), T_{p1} and T_{p2}, respectively corresponding to the **s1** and **s2** ranges, are listed in Table 4.2. It can be seen that the T_{p1} firstly drops and then increases with increasing Cr-substitution, while the T_{p2} changes marginally around 130 K, in agreement with the tendency of the onset temperatures. Interestingly, this evidences the robustness of the incommensurate magnetic ordering despite the presence of Cr ions up to around 10 at.%. However, both the **s1** and **s2** become progressively less steep with increased Cr-doping. For instance, instead of a steady growth upon heating, **s1** adopts a plateau-like shape for the 7.5 at.% Cr, and becomes basically a broad peak centered at ~120 K for the 10 at.% Cr sample (T_{p2} peak is indistinguishable in *dM-dT* curve).
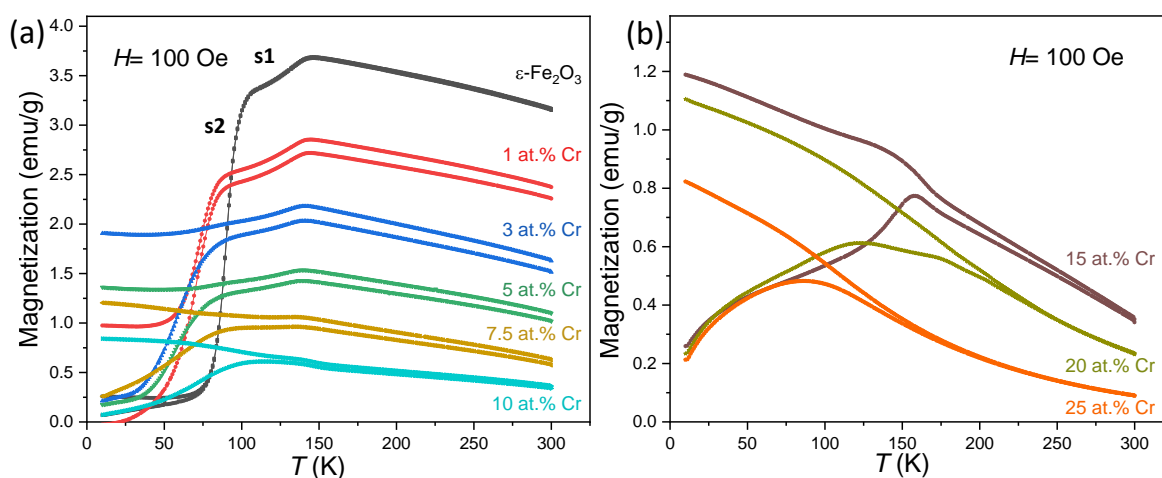
Figure 4.4 Temperature dependence of magnetization under an applied field of 100 Oe in the temperature range of 10-300 K for (a) ε-Fe₂O₃ and 1, 3, 5, 7.5 and 10 at.% Cr-doped and (b) 15, 20, and 25 at.% Cr-doped nanoparticles (without silica). The *M-T* curves were measured in ZFC (the lower branch) and FC (the upper branch) conditions with a 2 K/min heating rate.

For the FC *M-T* curves, the magnetization at 10 K is steadily enhanced with the Cr content compared to its value at 300 K and above 7.5 at. % Cr, the FC magnetization monotonically decreases in all the temperature range. A characteristic of the ZFC-FC measurement for ε-Fe₂O₃ is the reversibility of the FC and ZFC branches from 300 K to about 80 K. In contrast, doping with Cr at only 1 at. % suppresses

this reversibility in the whole temperature range and the FC and ZFC branches diverge at low temperatures.

Another consequence of the substitution of Fe by Cr, is the gradual decrease of the magnetization above 150 K (super-hard FM2 ferrimagnetic phase). The same trend is essentially observed at much larger fields in the hysteresis loops obtained from the NPs embedded in silica at room temperature (see Figure 4.3). Let us now recall that the net magnetization in ε-Fe$_2$O$_3$ results from the difference of the antiparallel Fe^{3+} magnetic moments at the Fe3 regular octahedron and the Fe4 tetrahedral environment, with the latter being smaller. The observed magnetization decrease upon Cr doping, with M_{7T} falling from 17 emu/g for ε-Fe$_2$O$_3$ to 9 emu/g at 25 at. % Cr could be explained by the preferential substitution of Fe3 by Cr. Indeed this would reduce the difference, in contrast to a preferential Cr doping of the Fe4 site which would increase the resulting moment. Since the paramagnetic moment of Cr^{3+} is more than 30% lower than that of Fe^{3+}, the observed magnetization fall of about 50% can be well accounted for by a tendency of Cr^{3+} to go to the Fe3 sites.

As shown in Figure 4.1, significant modifications have been observed in the X-ray diffraction pattern for the 15, 20, and 25 at.% Cr-doped NPs, and dramatic changes have also been found in the *M-T* behavior for these compositions (see Figure 4.4(b)). The ZFC *M-T* curve exhibits a rather sharp bump at ~150 K for the 15 at.% Cr sample, while the 20 at.% Cr one shows a slow magnetization decline in the 125-175 K range, but it has the opposite slope compared to the **s1** of parent ε-Fe$_2$O$_3$. Interestingly, for the 25 at.% Cr, there is a broad peak located at ~80 K in the ZFC *M-T* curve, where the magnetization starts to smoothly decrease as temperature increases and overlaps with the FC *M-T* branch from ~150 K, a temperature dependence of the magnetization that suggests a superparamagnetic behavior.
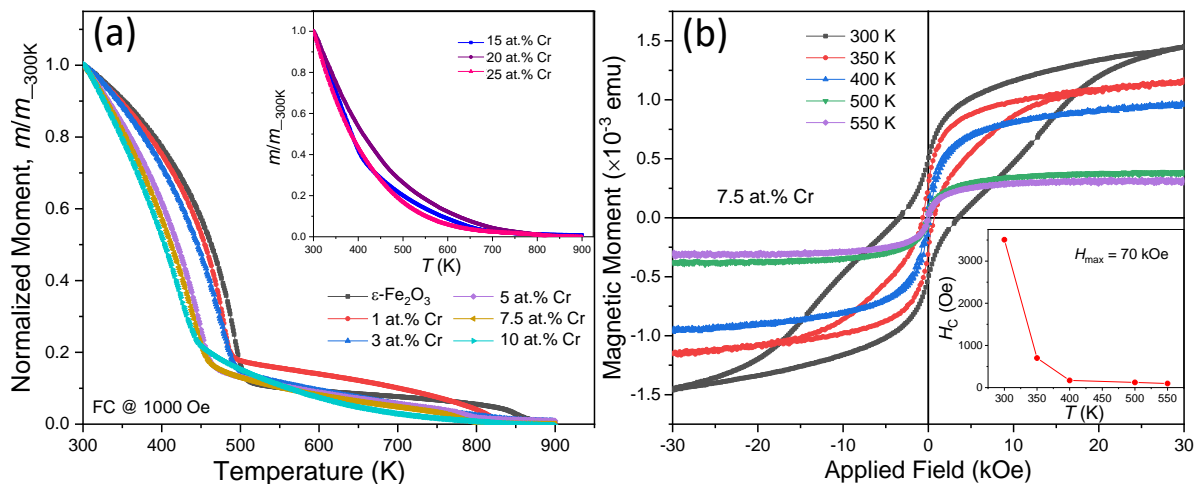
Figure 4.5 (a) Temperature dependence of magnetic moment at high temperatures under a constant field of 1000 Oe for the nanoparticles embedded in silica matrix. The moment has been normalized to the moment at 300 K. For clarity, only the FC branch is shown. (b) High-temperature hysteresis loops recorded at 300, 350, 400, 500, and 550 K for the 7.5 at.% Cr samples. The inset demonstrates the temperature evolution of the coercive field.

We have also investigated the magnetic properties of the particles at high temperatures. Figure 4.5 displays the temperature dependence of FC magnetic moment recorded at a heating rate of 2 K/min in the 300-900 K temperature range, under applied fields of 1000 Oe. In the case of ε-Fe$_2$O$_3$, the FC magnetization presents a Brillouin–type monotonic decrease from 300 K to T_{N2} = 492 K where it is only about one-tenth of its room temperature value. T_{N2} signals the transition from a highly anisotropic collinear magnetic order involving four Fe^{3+} sublattices (super-hard ferrimagnetic FM2 phase) to a high-temperature collinear structure with soft magnetic properties (soft ferrimagnetic FM1 phase) with only two Fe^{3+} ordered magnetic sublattices, and disordered iron moments in tetrahedral and regular octahedral sites [8]. For $x \leq 0.10$, a similar trend is observed, even though the Cr substitution shifts both T_{N2} and T_{N1} to significantly lower temperatures.

The transition temperatures obtained from the minima in *dM/dT* are reported in Table 4.2. The T_{N2} transition temperature declines from 490 K for ε-Fe$_2$O$_3$ to 420 K for the 10 at.% Cr sample. This indicates that the high temperature soft magnetic collinear order is stabilized by Cr doping, in agreement with the fact that the decreased coercive fields of Cr-doped nanoparticles indicate that in ε-Fe$_2$O$_3$ the replacement of Fe^{3+} by Cr^{3+} tends to decrease its magnetic anisotropy.

Neutron Diffraction Study

As discussed in Chapter 2, neutron powder diffraction (NPD) is a powerful tool to characterize transition-metal doped ε-Fe$_2$O$_3$ nanoparticles since the neutron scattering length of neighboring transition metals can be very different from that of Fe. Furthermore, compared to X-ray diffraction method, neutron diffraction allows a precise determination of the polyhedron distortion and the oxygen positions in the unit cell of oxides due to the unique sensitivity of neutrons to oxygen atoms. Rietveld refinement of the neutron patterns acquired at 300 K for the ε-Fe$_2$O$_3$ and 7.5 at.% Cr-doped samples is presented in Figure 4.6. The obtained crystallographic and magnetic information are summarized in Table 4.3. Compared to the parent ε-Fe$_2$O$_3$, the 7.5 at.% Cr has smaller lattice parameters due to the slightly smaller ionic radius of Cr^{3+}, in line with the peak shift observed in the X-ray diffraction patterns (see Figure 4.1). Our refinement considering the occupations of Cr^{3+} among the distinct oxygen polyhedra indeed indicates that Cr^{3+} preferably occupies the Fe3 regular octahedral iron site of the *Pna2$_1$* structure. The refinements show that very little amounts of Cr^{3+} go to the Fe1 and Fe2 distorted octahedra and that no Cr occupying the tetrahedral Fe4 site. This result is consistent with our magnetic measurements, in which the important decrease of the magnetization at high fields pointed to a preferential Cr substitution at the Fe3 site. More analysis of the neutron diffraction data collected on other compositions is currently in progress.
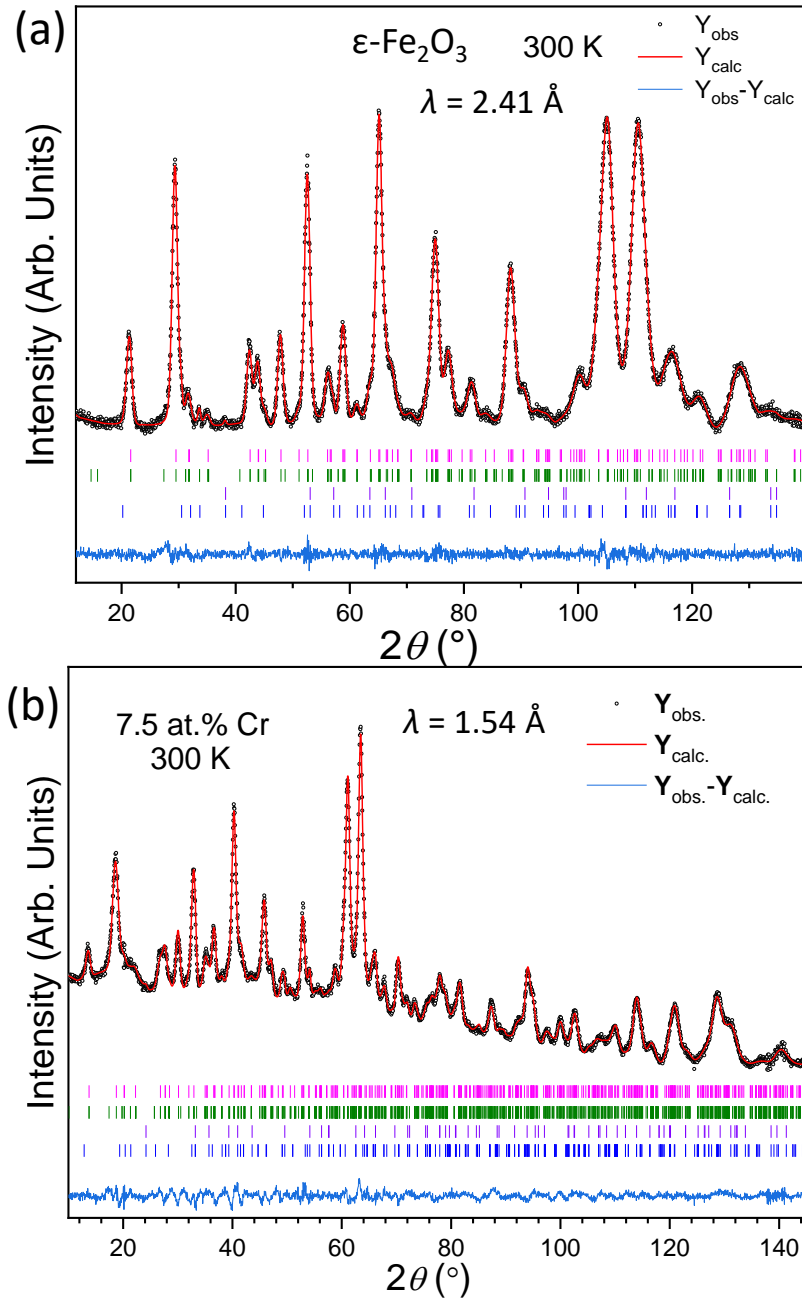
Figure 4.6 Rietveld refinement (red solid line) of the neutron powder diffraction (NPD) patterns collected at 300 K for the undoped (λ= 2.41 Å) and 7.5 at.% Cr-doped (λ= 1.54 Å) ε-Fe₂O₃ particles (black circles, experimental points; bottom blue line, difference). The top row (in magenta) and the second row (in olive) of vertical bars correspond respectively to the nuclear (*Pna2₁*) and magnetic (*Pna'2₁'*) structures of ε-Fe₂O₃. The third row (in violet) and the last row (in blue) of vertical bars indicate the Bragg positions from the nuclear (*R-3c*) and magnetic (*P1*) structures of α-Fe₂O₃. The best fits give 2.8(4) wt.% and 3.7(4) wt.% of hematite in the undoped and 7.5 at.% Cr-doped particles, respectively.

Table 4.3 Refined lattice parameters, distribution of Cr^{3+} ions among the four different Fe sites in the polar *Pna2$_1$* structure of ε-Fe$_2$O$_3$, ordered magnetic moments of the Fe sites (in μ_B/Fe) for the undoped and 7.5 at.% Cr doped samples. Fe sublattices: distorted octahedral Fe1 and Fe2, regular octahedral Fe3 and tetrahedral Fe4. The patterns were collected at 300 K on diffractometer D20 at Institut Laue-Langevin, Grenoble.

	Cell Parameters	Cr^{3+} distributions	Ordered moments (μ_B/Fe)	Goodness factors
ε-Fe$_2$O$_3$	a (Å) = 5.0889(2) b (Å) = 8.7895(8) c (Å) = 9.4704(8) V (Å^3) = 423.61	Fe1: 0 % Fe2: 0 % Fe3: 0 % Fe4: 0 %	m$_x$[Fe1]= 3.6(1) m$_x$[Fe2]= -3.6(1) m$_x$[Fe3]= -2.5(1) m$_x$[Fe4]= 2.7(3)	R_B = 0.4 % R_f = 0.3 % R_{Mag}= 1.9 % χ^2 = 1.5
7.5 at.% Cr	a (Å) = 5.0801(3) b (Å) = 8.7643(5) c (Å) = 9.4428(3) V (Å^3) = 420.43	Fe1: 1 % Fe2: 12 % Fe3: 87 % Fe4: 0 %	m$_x$[Fe1]= 3.8(1) m$_x$[Fe2]= -3.8(1) m$_x$[Fe3]= -2.2(1) m$_x$[Fe4]= 2.2(1)	R_B = 2.7 % R_f = 1.6 % R_{Mag}= 5.1 % χ^2 = 3.4

Mössbauer spectroscopy study

Mössbauer spectroscopy was performed at room temperature for ε-Fe$_2$O$_3$ and the samples doped with 7.5 and 15 at. % Cr using a conventional ^{57}Co/Rh source with velocity calibration based on a 25 m foil of metallic iron. The recorded spectra are presented in Figure 4.7, which also includes the different components (Voigt profile lines or hyperfine field distributions) superposed to fit them using the NORMOS software [9].

The top spectrum of Figure 4.7, corresponding to ε-Fe$_2$O$_3$, has been fit with three sextets, one of which accounts for both Fe1 and Fe2 distorted octahedral environments, and the two remaining to regular octahedral Fe3 and tetrahedral Fe4 environments. The hyperfine parameters obtained from the fitting (see Table 4.4) are in agreement with those previously reported [10]. In the case of the 7.5 at. % Cr (see the middle spectrum in Figure 4.7), out of the three site contributions considered for ε-Fe$_2$O$_3$, only the site corresponding to Fe1+Fe2 could be maintained to fit the spectrum and it was also necessary to include a distribution of hyperfine fields. The distribution shows peaks at the hyperfine fields (B_{hf}) of ~23 T and 38 T, close to the 26.5 T and 39.7 T hyperfine fields of subspectra corresponding to the Fe4 and Fe3 sites of ε-Fe$_2$O$_3$, respectively. A small content of hematite of around 5% has also been found in this sample. It can be also noticed that the distribution also presents some components below 10 T. This can be related to the presence of a small paramagnetic contribution resulting in an increase of the relative intensity of the inner lines of the spectrum closer to zero velocity, even if introducing a doublet did not result in a better fit of the spectrum. In contrast, the presence of a paramagnetic component is very evident for the sample doped with 15 at. % Cr and it accounts for 34 % of the spectrum area. The main contribution to the spectrum is that of a hyperfine field distribution which presents a peak at around 38.5 T. The crystalline site contribution which in the case of 7.5 at. % Cr was assigned to the Fe1+Fe2 subspectrum of ε-Fe$_2$O$_3$ is no longer present. Taking into account that the XRD refinement indicates

that Cr is preferentially going to Fe3 sites, it seems reasonable to assume that the maximum in the hyperfine field distribution at 38.5 T would correspond to iron in the Fe1 and Fe2 sites, now displaying decreased hyperfine fields and disorder due to the presence of some Cr. The distribution also shows a significant shoulder between 20 and 35 T which would respectively correspond to Fe in the Fe4 and Fe3 sites.
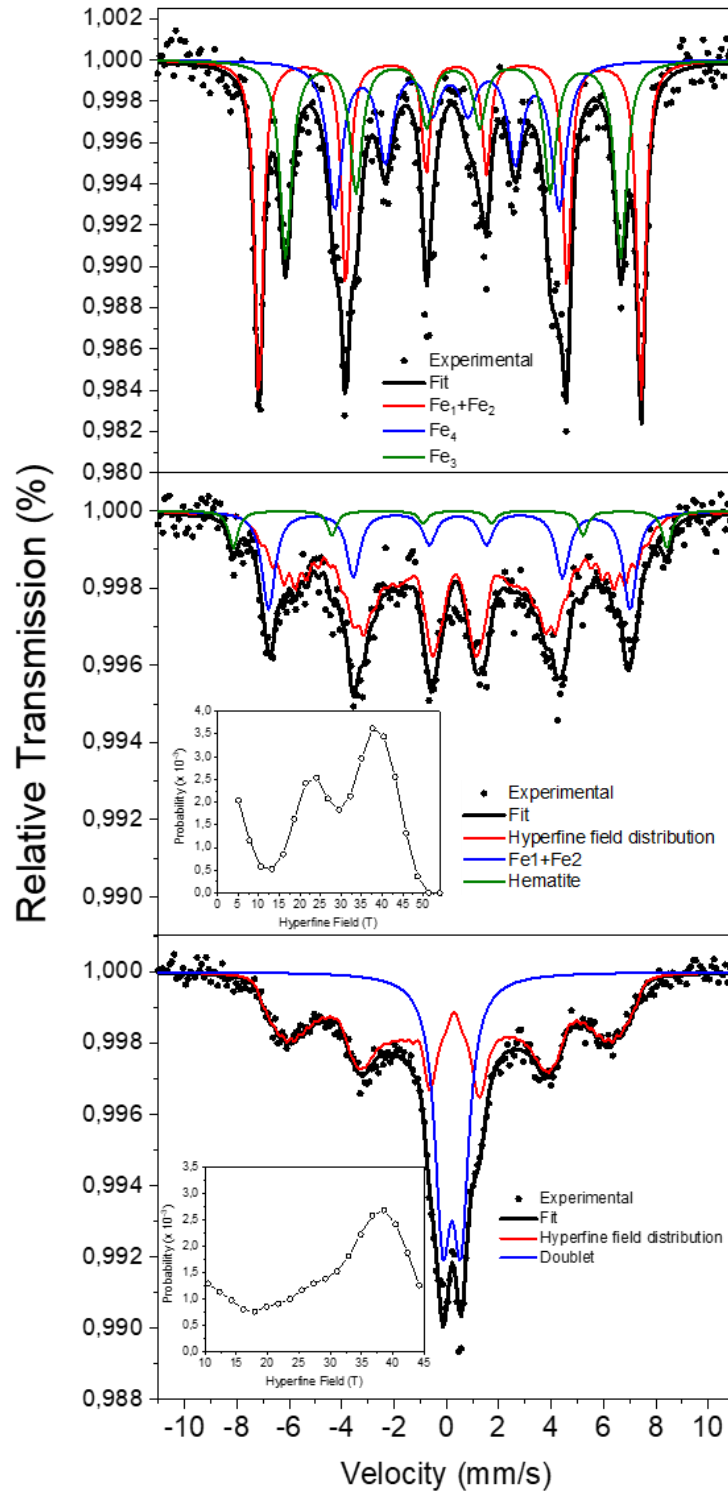
Figure 4.7 Room temperature Mössbauer spectra of ε-Fe₂O₃ (top) and doped samples with 7.5 at. % Cr (middle) and 15 at. % Cr (bottom).

The Mössbauer spectroscopy results confirm the Cr^{3+} reluctance to occupy the Fe1 and Fe2 distorted octahedral positions and its preference for the regular octahedral Fe3 sites. From these results one could also argue that Fe^{3+} is being substituted by Cr^{3+} at the tetrahedral Fe4 sites. However, the neutron diffraction results incontestably show that this is indeed not occurring. The reason why the Fe4 sextet is no longer present in the Mössbauer spectrum corresponding to 7.5 % Cr is most likely a consequence of the disruption of the magnetic order at the Fe3 positions due to Cr substitution.

Indeed, as we have discussed in Chapter 3, on cooling ε-Fe$_2$O$_3$ from high temperatures through FM1→FM2 magnetic transition the Fe3 and Fe4 sublattices which were magnetically disordered will become antiferromagnetically coupled, giving rise to a substantial net magnetic moment and an increasingly larger magnetic anisotropy [8]. Thus, on the basis of this behavior, one can argue that the Fe3 and Fe4 sites are magnetically linked through a strong coupling, which is most likely of magnetoelastic origin, and that the Cr substitution at Fe3 causes a decrease in the strength of this interaction affecting the magnetic order of the Fe4 sites even if no Cr is occupying these positions.

Table 4.4 Summary of the hyperfine parameters of the different components included in the fits Mössbauer spectra of Figure 4.7 corresponding to pure ε-Fe$_2$O$_3$, 7.5% and 15 % Cr-doped ε-Fe$_2$O$_3$ nanoparticles at 300 K. Hyperfine parameters are given relative to metallic iron at room temperature. Except for the areas, the parameters with no associated errors were fixed in the refinement.

at. % Cr	Component	Area (%)	IS (mm/s)	QS (mm/s)	B$_{hf}$ (T)	Width (mm/s)
0	Fe$_{DO1}$+Fe$_{DO2}$	38.4	0.261(4)	-0.238(9)	45.24(3)	0.38(1)
	Fe$_R$	32.1	0.261(9)	0.00(1)	39.66(7)	0.55(3)
	Fe$_T$	29.5	0.09(1)	-0.12(3)	26.54(9)	0.68(4)
7.5	Fe$_{DO1}$+Fe$_{DO2}$	22	0.275(7)	-0.33(2)	42.76(6)	0.61(3)
	B$_{hf}$ distribution	32	0.333(6)	-0.04(1)	Peaks at 23, 38	0.4
	Hematite	6	0.284	-0.28	51.3	0.42
15	B$_{hf}$ distribution	66	0.262(4)	-0.235(9)	Peak at 38.5	0.36(1)
	Doublet	34	0.260(9)	0.01(2)	39.70(7)	0.61(2)

The Mössbauer spectrum for the 15 at. % Cr is also interesting for two reasons. On the one hand, there is an important paramagnetic doublet which, given the preference of Cr^{3+} for occupying the Fe3 positions, is most likely related to the increased relaxation of iron moments at the Fe3 and Fe4 sites as a result of an increasingly lower magnetic anisotropy induced by the presence of Cr. On the other hand, for this composition the robust antiferromagnetic coupling of Fe1 and Fe2 sublattices begins to lose its strong magnetic order as revealed by the hyperfine field distribution which has replaced the Fe1+Fe2 sextet contribution of the ε-Fe$_2$O$_3$ and 7.5 % Cr spectra. Taking into account the magnetoelastic effects

associated with the FM1→FM2 transition which disrupts the magnetic order of the Fe3 and Fe4 sublattices, it is not surprising that the onset of the significant structural changes presented in Figure 4.1 is at 15 at. % Cr.

4.3 Effect of Mn substitutions on the structural and magnetic properties of ε-Fe₂O₃ nanoparticles

A series of Mn-doped ε-$(Fe_{1-x}Mn_x)_2O_3$ (x= 0.01, 0.03, 0.05, 0.075, 0.10, 0.15, and 0.20) nanoparticles were synthesized following similar procedures described in Section 4.2.1. In this case, manganese (III) acetate dihydrate $[(CH_3COO)_3Mn·2H_2O]$ was used as the dopant metal precursor. The weight ratio of metal oxide to silica was 25 %.
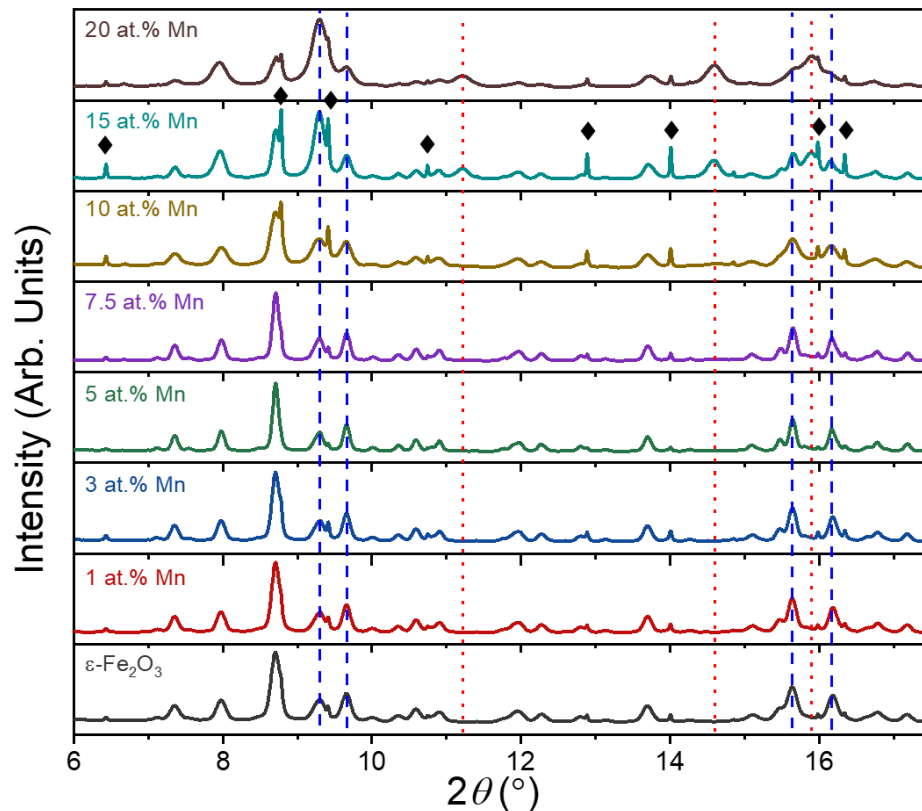
Figure 4.8 Room temperature synchrotron X-ray diffraction patterns for the etched $(Fe_{1-x}Mn_x)_2O_3$ ($0 \le x \le 0.20$) nanoparticles, collected with a wavelength λ= 0.412 84(6) Å. The narrow peaks marked by rhombus in the 15 at.% Mn pattern indicate the main reflections from hematite.

The SXRPD patterns recorded at room temperature for the different synthesized compositions are presented in Figure 4.8. Different amounts of hematite impurities have been detected. No obvious Bragg peak shift has been observed due to the nearly identical ionic radius of Fe^{3+} and Mn^{3+} (0.645 Å). Compared to the pattern of the parent sample, no significant changes are observed in the diffractograms

for $x \leq 0.10$. In other words, the ε-Fe₂O₃ *Pna2₁* structure remains stable under Mn-substitutions of at least 10 at.%.
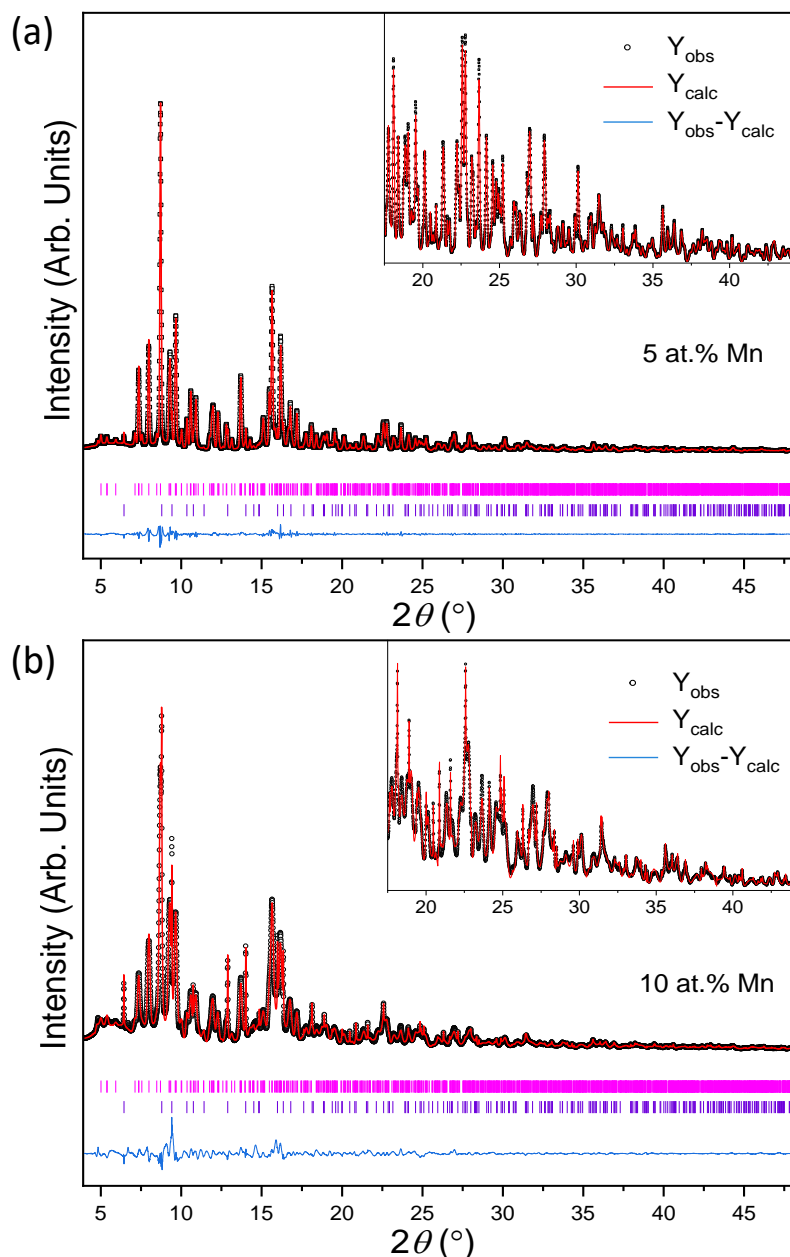
Figure 4.9 Rietveld refinement for the (a) 5 at.% and (b) 10 at.% Mn synchrotron XRD patterns. The bottom blue line is the difference between observed and calculated diffraction patterns. The inset shows an enlarged view of the high-angle region. The top row of vertical bars (in magenta) corresponds to Bragg reflection positions from the *Pna2₁* SG of ε-Fe₂O₃, while the bottom vertical bars (in violet) are from hematite impurity, accounts for 3.9(2) wt. % and 10.0(5) wt. % for the 5 at.% and 10 at.% Mn samples, respectively. Agreement factors of the refinement for the 5 at.% Mn (10 at.% Mn) particles are: R_B = 1.8 % (4.0 %), R_f = 1.2 % (1.5 %), χ^2 = 17.9 (33.7). Note that Mn occupations are not considered during the structural refinement.

On the other hand, for x= 0.15 and 0.20, some interesting modifications of the ε-Fe₂O₃ reflections can be observed. For instance, although most of the ε-Fe₂O₃ reflections get weaker, several new diffraction peaks appear for x= 0.15 and 0.20 (see the red dotted lines). This contrasts with the evolution of the diffractograms upon Cr substitutions above 15 at. % for which in the 2θ range of 9.0-10.0° a central

peak emerged at expenses of the two neighboring ε-Fe$_2$O$_3$ reflections (see Figure 4.1). No sign of appearance of other peaks is found, but the relative intensity of the (130) ε-Fe$_2$O$_3$ reflection 2θ range of 9.0-10.0° increases considerably and becomes the strongest peak for these two compositions. These observations point to the possible existence of additional phase(s) in the 15 at.% and 20 at.% Mn samples. A higher level of Mn-substitution is necessary to provide a better insight into the structural evolution.

Figure 4.9(a) and (b) show the Rietveld refinement patterns of the SXRPD patterns for the 5 at.% and 10 at.% Mn NPs, respectively. We detected 3.9(2) wt.% and 10.0(5) wt.% α-Fe$_2$O$_3$ as an impurity phase for the 5 at.% and 10 at.% Mn, respectively. Unfortunately, due to the comparable scattering power between Mn and Fe atoms, we are not able to refine metal-site occupation parameters on the basis of X-ray diffraction. To probe the distribution of Mn atoms among the different Fe sites in the epsilon-type structure, a detailed examination of the neutron diffraction data collected at 300 K is under way.
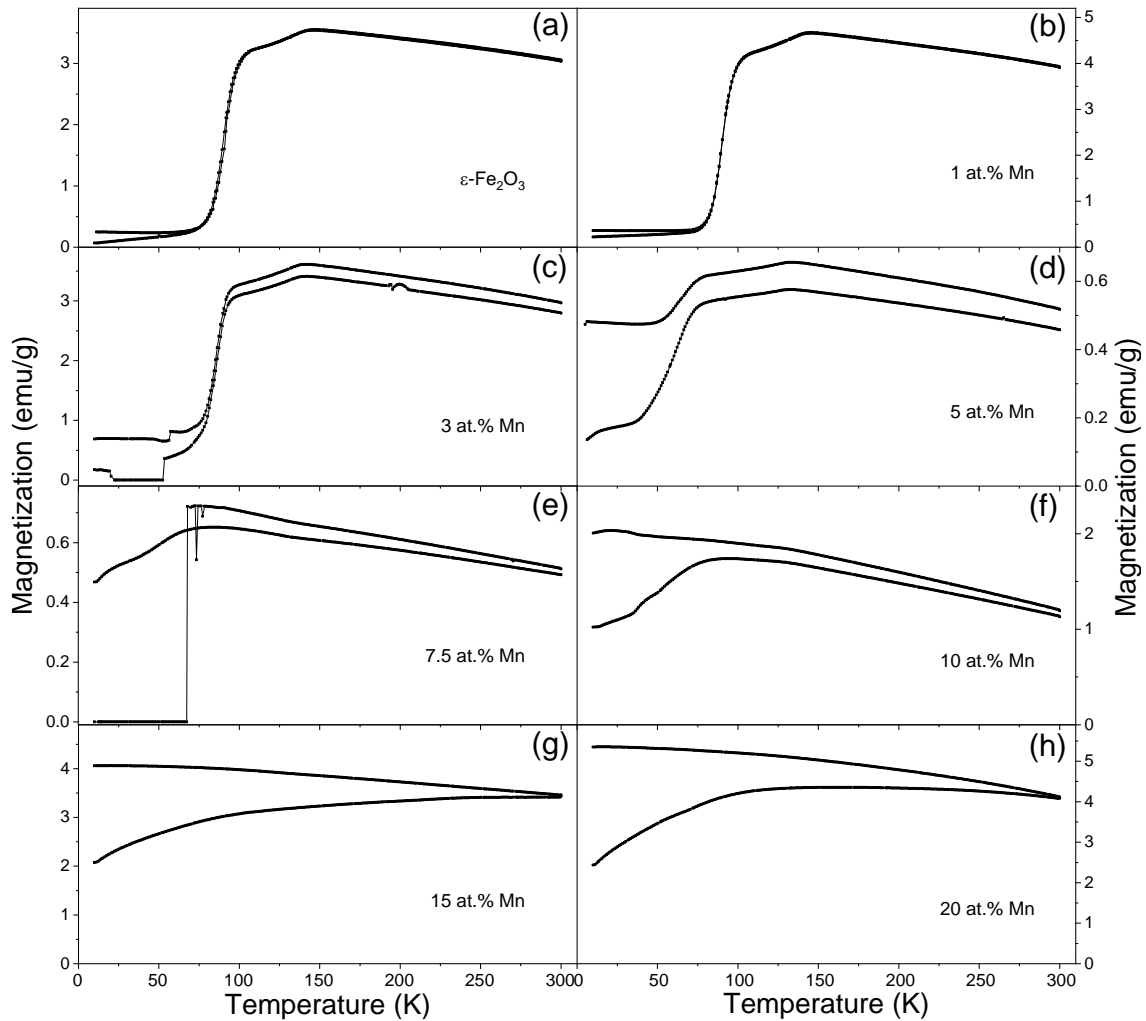
Figure 4.10 (a-h) Temperature dependence of the low-field magnetization (*M-T* curves) acquired under both ZFC (lower branch) and FC (upper branch) conditions for the undoped and Mn-doped nanoparticles (*H*= 100 Oe). The sudden changes of magnetization observed in the low-temperature regions of 3 at.% and 7.5 at.% Mn curves arise from temporary deficiencies in the measurements.

Figure 4.10(a-h) shows the *M-T* curves acquired under both ZFC (lower branch) and FC (upper branch) conditions for the undoped and Mn-doped nanoparticles. The characteristic two-step transition in the *M-T* curve of ε-Fe₂O₃ (**s2** and **s1**), correlated to the low-temperature incommensurate phase, can clearly be seen for the Mn-doping up to 5 at.%. For these samples, the onset temperatures of the **s1** and **s2** (T_{p1} and T_{p2}, respectively) shift to low temperatures with increasing Mn content. For example, the T_{p2} drops to 74 K with $x = 0.05$, and the T_{p1} decreases to 134 K for the same composition (see Table 4.5). A broad bump is observed in the ZFC *M-T* curves of the 7.5 at.% and 10 at.% samples. Upon further increase in Mn content, the peaks associated with the incommensurate phase become indiscernible; moreover, the *M-T* curves manifest behavior that can be associated with that of superparamagnetic nanoparticles with magnetic interactions.

Table 4.5 Summary of the magnetic measurement results for the undoped and Mn-doped ε-Fe₂O₃ nanoparticles under study, including the H_C, M_{7T} and M_R obtained from room temperature (RT) hysteresis measurements, the onset temperatures of the low-temperature (LT) magnetization variations (**s1** and **s2**) in the ZFC *M-T* curves, T_{p1} and T_{p2}.

Sample	RT Hysteresis Loops			LT *M-T*	
	H_C (Oe)	M_{7T} (emu/g)	M_R (emu/g)	T_{p2} (K)	T_{p1} (K)
ε-Fe₂O₃	15920	17.7	8.9	103	146
1 at.% Mn	16820	17.5	8.6	101	145
3 at.% Mn	16120	15.4	7.1	94	143
5 at.% Mn	18290	14.7	7.0	74	134
7.5 at.% Mn	8743	19.0	7.7	-	-
10 at.% Mn	871	18.4	3.8	-	-
15 at.% Mn	95	35.2	3.1	-	-
20 at.% Mn	26	41.5	0.6	-	-

Magnetic hysteresis loops were also measured at room temperature for the particles, and the results are shown in Figure 4.11. The round-shaped hysteresis loops can be observed for $x \leq 0.05$ (see Figure 4.11(a)). As the x further increases, the loops become narrower and narrower. Interestingly, the maximum magnetization for 15 at.% Mn sample is about twice that of the one measured for the sample containing 10 at.% Mn. This may indicate the appearance of additional soft magnetic phase(s) with much larger magnetization than ε-Fe₂O₃, which could be related to the appearance of new peaks marked in red dotted lines in Figure 4.8. Another possibility would be the preferential substitution of Mn in one of the Fe1 or Fe2 distorted octahedral sites which display compensated magnetic moments in the FM2 magnetic structure of ε-Fe₂O₃. The coercive field (H_C), the magnetization at the maximum field (M_{7T}), as well as the remanence (M_R) are gathered in Table 4.5. One can notice that the H_C is enhanced by 15

% with increased Mn-doping up to 5 at.%, which is followed by a dramatic decline as further Mn is incorporated. An opposite trend is found for the M_{7T}.
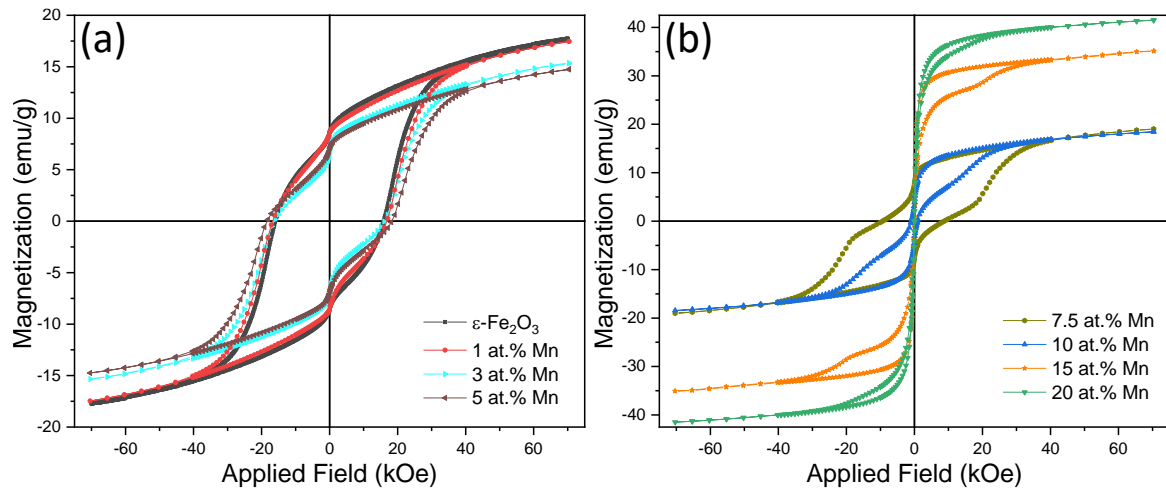
Figure 4.11 Magnetic hysteresis loops recorded at room temperature for the parent and Mn-doped particles (without silica), showing significantly different hysteresis behaviors.

The high-temperature FC magnetization versus temperature curves for the compositions with 1 at.%, 5 at.%, 10 at.% and 20 at.% Mn, are presented in Figure 4.12 (a). Similar to the behavior observed for Cr-doped ε-Fe₂O₃ nanoparticles, the critical temperatures of the FM2-FM1 and FM1-PM transitions are significantly lowered with Mn substitution. The characteristic features of these phase transformations are not observed in this temperature range for the ε-Fe₂O₃ nanoparticles doped with 20 at.% Mn. Hysteresis loops at high temperatures were measured for the sample containing 5 at.% Mn, the one which displays the largest coercive field at room temperature (see Figure 4.12(b)). The giant H_C at room temperature substantially falls off as temperature increases and collapses at around FM2-FM1 transition temperature in a behavior analogous to that reported for pure ε-Fe₂O₃ nanoparticles [8].
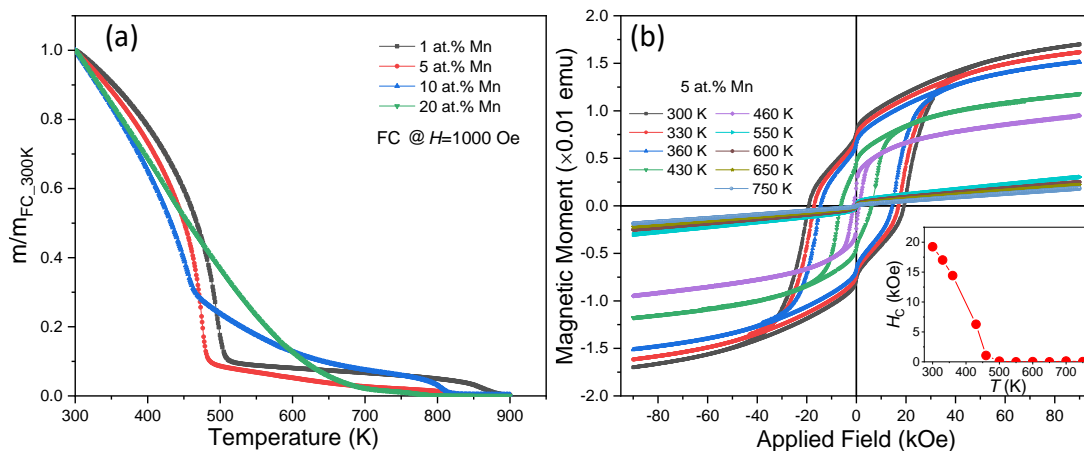
Figure 4.12 (a) Temperature dependence of field cooling magnetic moments in the 300-900 K range for the 1 at.%, 5 at.%, 10 at.% and 20 at.% Mn samples. (b) High-temperature hysteresis behavior of the 5 at.% Mn particles. The inset shows the temperature evolution of the coercive field.

4.4 Effect of Co substitutions on the structural and magnetic properties of ε-Fe$_2$O$_3$ nanoparticles

High-spin Co^{2+} (d^7, $S = {}^3/_2$) ions are interesting because such 3d magnetic ion in octahedral coordination reportedly exhibits a considerable unquenched orbital moment [11][12][13]. In the current work, Co(NO$_3$)$_2$·6H$_2$O was used as the Co precursor, and the weight ratio of metal oxide to silica was 24 % for the sol-gel synthesis of Co-doped ε-Fe$_2$O$_3$ NPs. Below we present the preliminary results on the structural and magnetic properties of (Fe$_{1-x}$Co$_x$)$_2$O$_3$ nanoparticles with x= 0.01, 0.02, 0.03, 0.05, 0.07.

XRD patterns of the 1, 2 and 3 at.% Co-doped NPs (without silica) are shown in Figure 4.13. The removal of silica matrix in 5 and 7 at.% Co samples is undone in the time of writing, the patterns for the unetched ones are thus presented. In addition to the diffraction peaks of ε-Fe$_2$O$_3$ phase, some traces of hematite are also detected but in very low concentrations. The peak at around 2θ= 35° gets stronger in relative intensity with Co-substitution above 3 at.%. Moreover, the appearance additional reflections around 2θ= 43° and 58° is visible for the 5 and 7 at.% Co. This may indicate the crystallization of CoFe$_2$O$_4$ phase (see Figure 4.12(a)), where the Co^{2+} ions occupy the octahedral sites in the inverse spinel structure. The formation of magnetic cobalt ferrite via sol-gel method from its nitride precursors has been reported by several groups [14][15][16]. It is also important to notice that the polar ε-Fe$_2$O$_3$ structure remains stable for Cr- or Mn-substitutions up to at least 10 at.%, while in the present case CoFe$_2$O$_4$ starts to appear at lower substitution levels. Rietveld refinements conducted for the 3 at.% Co sample gives lattice parameters, a, b, c and a cell volume V of 5.092(1) Å, 8.785(2), 9.450(2) Å and 422.7(2) Å^3, respectively. It is interesting to compare these values to the ones of the undoped ε-Fe$_2$O$_3$: a (Å) = 5.0889(2), b (Å) = 8.7895(8), c (Å) = 9.4704(8) and V (Å^3) = 423.61 (see Chapter 3). One can see that upon Co substitution there is a significant stretching along the a, while a compression is found along the b and c, giving a slight shrinkage of the cell volume. This could indicate that the Co in the ε-Fe$_2$O$_3$ lattice is in the +3 valence state due to its smaller ionic radius (Co^{3+}, 0.63 Å and Co^{2+}, 0.74 Å, versus Fe^{3+}: 0.64 Å) but could also be related to magnetoelastic effects associated with the unquenched orbital moment of Co^{2+}. High-intensity synchrotron diffraction measurements and detailed XAS studies near the Co $L_{2,3}$ edge are expected in this regard.
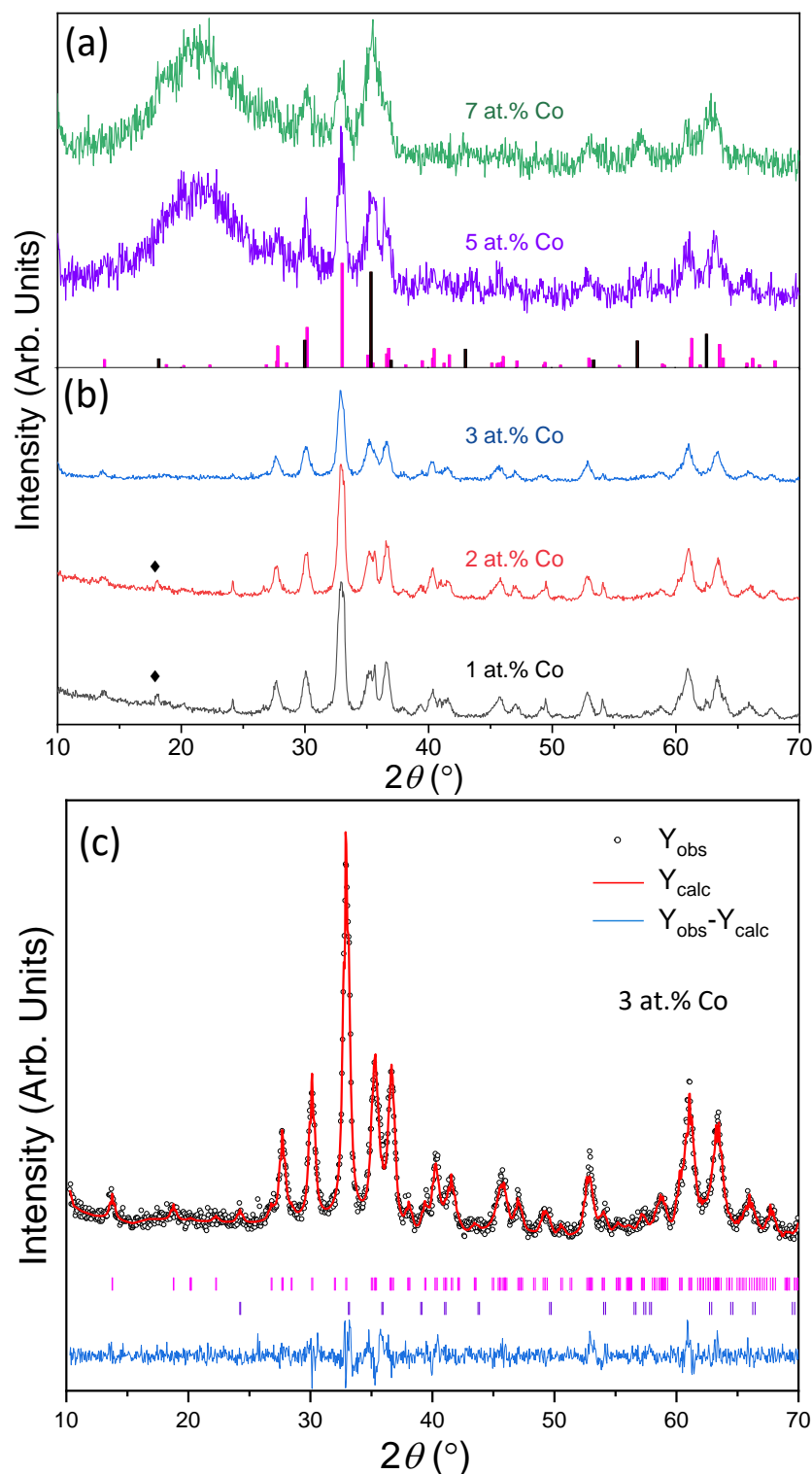
Figure 4.13 XRD patterns collected on a laboratory Siemens D-5000 diffractometer for the (a) 1, 2 and 3 at.% Co-doped NPs (without silica) and (b) 5 and 7 at.% Co NPs (with silica). The peaks marked by rhombus are from the artefact of the instrument. The vertical bars in Panel (a) denote the peak positions of ε-Fe₂O₃ (in pink) and spinel-type CoFe₂O₄ (in black). Note that the 1, 2 and 3 at.% Co patterns are recorded after the removal of silica matrix (collection condition: 0.05°, 16 s/step), whereas the 5 and 7 at.% Co patterns correspond to the non-etched samples (collection condition: 0.05°, 4 s/step). Panel (c) illustrates Rietveld refinement for the 3 at.% Co sample. The top row of vertical bars (in magenta) corresponds to Bragg reflection positions from the $Pna2_1$ SG of ε-Fe₂O₃, while the bottom vertical bars (in violet) are from hematite impurity, accounts for 3.6(6) % in weight. Agreement factors of the refinement are $R_B = 2.3$ %, $R_f = 1.3$ %, $\chi^2 = 1.4$.

Figure 4.14(a) presents the low-file *M-T* curves for the parent and Co-substituted particles, which were measured in a magnetic field of 100 Oe under ZFC and FC modes within the 10-300 K range. The incommensurate magnetic ordering of ε-Fe₂O₃ below 150 K persists for all the three measured compositions. However, significant irreversibility of the ZFC and FC branches is observed. Moreover, there is a moderate shift in the onset temperature towards lower temperatures is observed upon increasing Co content. In addition, the magnetization at room temperature which firstly decreases as a result of rising Co content up to 2 at.%, then increases for the 3 at.% Co particles. It can also be seen that above 150 K (ferrimagnetic FM2 phase) the magnetization variation of the 3 at.% Co adopts a rather different slope in the *M-T* curve when compared with other compositions. The increase of magnetization for the 3 at.% Co sample may be related to the specific substitution of Co atoms at one of the antiferromagnetically couple Fe1 and Fe2 sites which in the ε-Fe₂O₃ have their moments compensated. However, one cannot exclude the possible influence of the minor magnetic CoFe₂O₄ phase. It is known that cobalt ferrite shows a large magnetic anisotropy at room temperature with high saturation magnetization (M_s= 47-85 emu/g at room temperature) (see Ref. [17] and references therein). In our case, the room temperature hysteresis loops presented in Figure 4.14(b) show that the magnetization at the maximum field considerably increases for the NPs doped with 3 at.% Co. This observation could support the hypothesis of preferential substitution of the iron in one of the Fe1 or Fe2 sites, but to rule out the possible influence of traces of CoFe₂O₄ an in-depth structural characterization is needed. Another consequence of increased Co-substitution is that both the coercivity and the remanence of the particles steadily decrease, and as expected, the maximum magnetization increases. Therefore, it is concluded that the substitution of Fe by Co in ε-Fe₂O₃ tends to decrease its magnetic anisotropy.
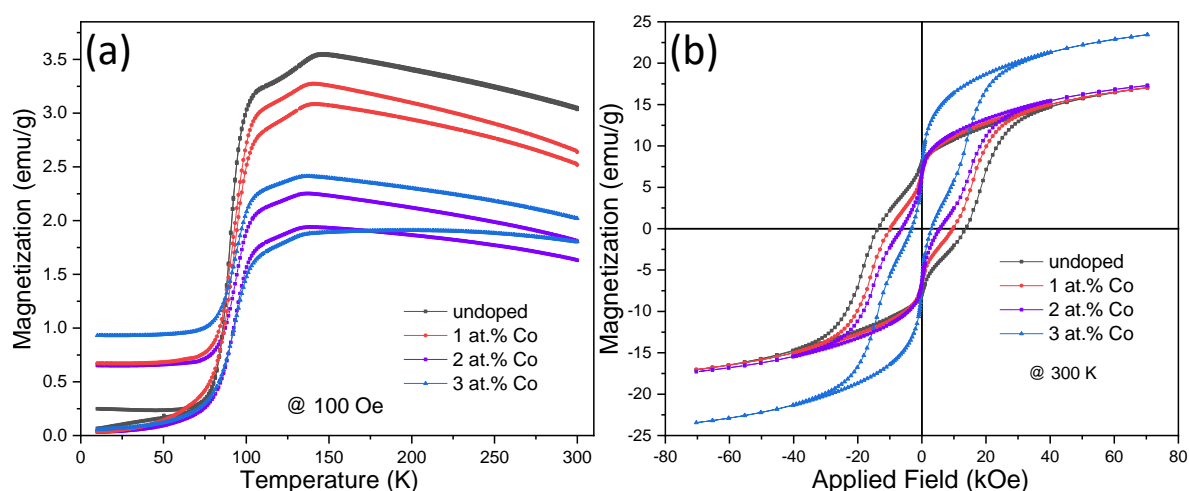
Figure 4.14 (a) Low temperature M-T curves under a constant field of 100 Oe for the undoped, 1, 2 and 3 at.% Co doped samples (without silica). The upper and lower branches correspond to the FC and ZFC magnetization, respectively. (b) Hysteresis loops at 300 K for the particles.

Figure 4.15(a-d) displays the *M-T* curves measured at high temperatures under a field of 1000 Oe in the ZFC and FC conditions for the samples containing 1, 2, 3 and 5 at.% Co. The hard-soft FM2-FM1 and the FM1-PM transitions are evident in the curves. The magnetization transition temperature T_{N1} firstly increases and then decreases as a function of Co-doping (nearly the same value observed for 1 and 5 at.% Co samples), while the T_{N2} essentially decreases. One distinct feature in this series is that the magnetization associated with the soft FM1 ferrimagnetic phase increases with the Co concentration. This indicates that the Co substitution stabilizes the regular octahedral and tetrahedral sublattices of Fe^{3+}, which are known to be disrupted in the case of the pure ε-Fe₂O₃. This also points to the fact that the Co substitution affects the magnetoelastic interactions of the system which play an important role in the hard-soft FM2-FM1 transition and would be an indirect evidence for the divalent state of Co.
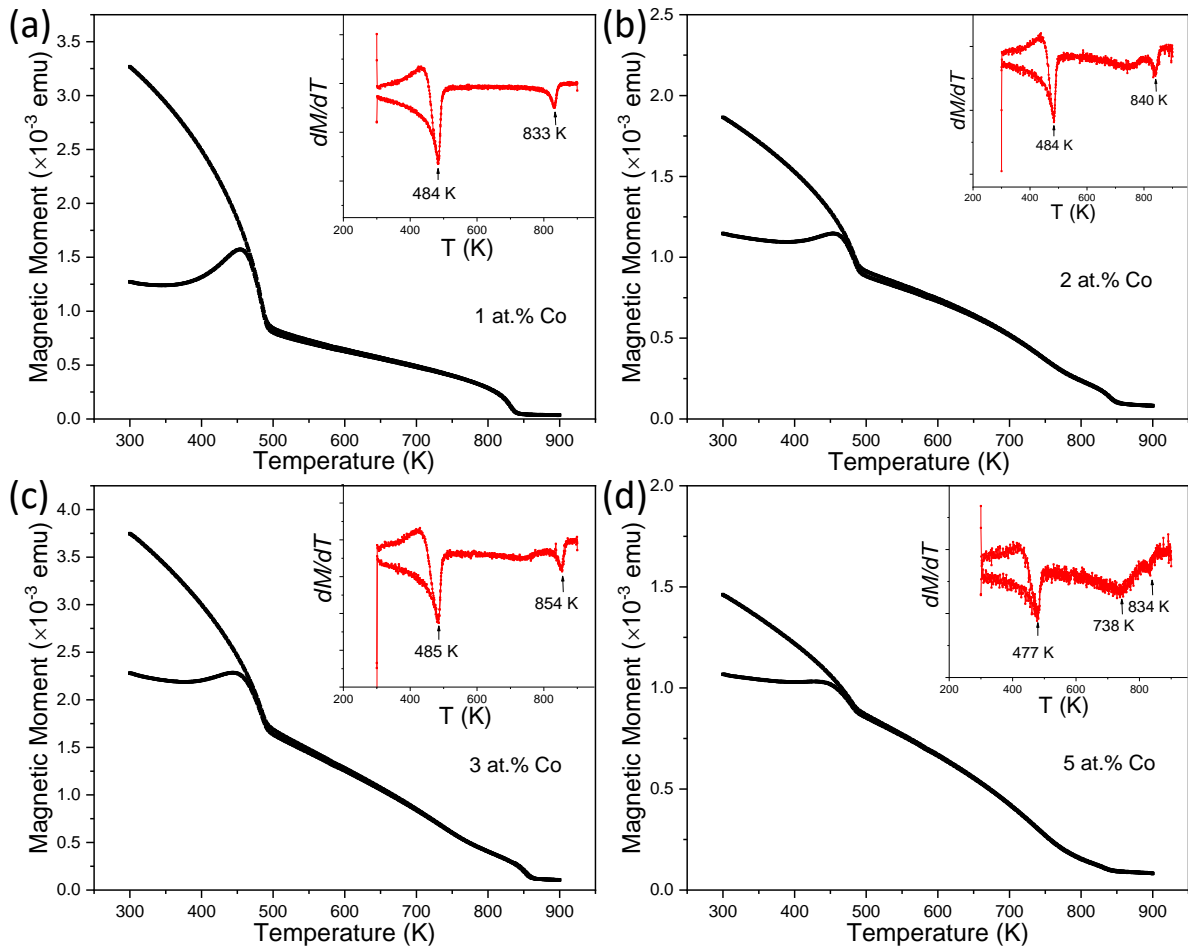
Figure 4.15 High temperature *M-T* curves under a constant field of 1000 Oe for the (a) 1 at.%, (b) 2 at.%, (c), 3 at.%, and (d) 5 at.% Co-doped samples (with silica). The upper and lower branches correspond to the FC and ZFC magnetization, respectively. Their insets display the *dM/dT* versus temperature curves.

In particular, the slope of the *M-T* curve for the FM1 phase is essentially comparable to that of the FM1 phase for the 5 at.% Co sample. Further, in addition to the peaks corresponding to the two above-mentioned transitions, for the 5 at.% Co sample one can notice the broad bump at ~ 740 K in the *dM/dT* versus temperature curve (see the inset of Figure 4.15(d)). These observations might be attributed, at

least partially, to the presence of cobalt ferrite in the oxides. The Curie temperatures of $CoFe_2O_4$ nanoparticles have been reported in 760-820 K depending on their size and the synthesis conditions [18][19].

To summarize, we prepared several Co-substituted ε-Fe_2O_3 nanoparticles by sol-gel chemistry to examine the effect of Co-doping on their structural and magnetic properties. The magnetic measurements show the robustness of both the incommensurate and ferrimagnetic phases with no sign of disappearing for the largest doping rate studied (3 at.% and 5 at.%, respectively). The replacement of Fe by Co tends to reduce the hardness of the parent oxide. Probably due to the non-isovalent substitution nature, the existence of more stable cobalt ferrite is likely for compositions of 5 at. % Co and above according to the magnetic measurements at high temperature.

4.5 Effect of Ru-doping on the structural and magnetic properties of ε-Fe_2O_3 nanoparticles

Among the reported metal dopants, only Rh^{3+} and Ru^{3+} substitutions increase the coercive field (H_C) value of ε-Fe_2O_3 [20][21]. In Reference [21], Ru-doped nanoparticles were produced by sintering iron oxide hydroxide and ruthenium hydroxide in a SiO_2 matrix, and the maximum doping rate reported by the authors is 0.7 at.% Ru (i.e., $x= 0.014$ in ε-$Ru_xFe_{2-x}O_3$ series); however, an increment of 15 % with respect to the parent oxide on H_C is found. This is attributed to the single ion anisotropy of the magnetic spin on Ru^{3+} ($4d^5$, $S = {}^1/_2$) [21]. Rietveld analysis on conventional X-ray diffraction shows that among the four non-equivalent Fe sites Ru ions are selectively substituting Fe^{3+} ions of the regular octahedral Fe3 sites. Motived by this report, we aimed to further explore the effects of high Ru-substitution in ε-Fe_2O_3 on its structural and magnetic properties. In the following note, we present some of the preliminary results in this regard, highlighting the challenges of stabilizing this metastable structure.
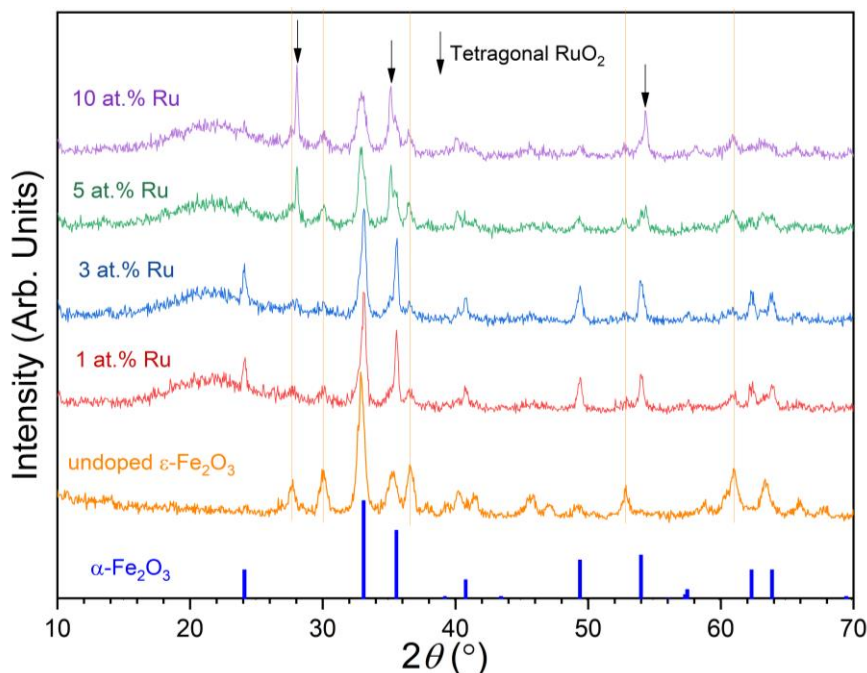
Figure 4.16 XRD patterns of the Ru-doped particles using ruthenium (III) acetylacetonate as the precursor. The pattern of undoped ε-Fe$_2$O$_3$ NPs (in orange) is also shown as a reference. The bottom bars indicate the diffraction peaks of hematite phase. The downside arrows denote the main diffraction peaks of rutile structure oxide (tetragonal, *P4$_2$/mnm*).

In our first trial, we used ruthenium (III) acetylacetonate [Ru(C$_5$H$_7$O$_2$)$_3$, Aldrich] as the Ru ion precursor. The synthesized particles embedded in silica matrix were subjected to 1100 °C annealing for three hours. The XRD patterns of the doped particles after annealing are shown in Figure 4.16. In all cases, ε-Fe$_2$O$_3$ only appears as a minor phase, and a significant amount of hematite is found for the 1 and 3 at.% Ru samples while strong reflections which can be indexed to be rutile RuO$_2$ (S.G, *P4$_2$/mnm*, with Ru^{4+}) are visible in the 5 and 10 at.% Ru patterns. Our attempts to promote the ε-Fe$_2$O$_3$ phase by controlling the synthesis parameters such as the metal oxide/silica ratio and annealing temperature did not significantly improve the yield of ε-Fe$_2$O$_3$.

As the next step, ruthenium (III) chloride hydrate (35-40 % Ru) (Thermo Fisher Scientific) was chosen as the precursor. The weight percentage of metal oxides to silica was 24 %. The XRD characterization of the obtained materials is shown in Figure 4.17. As seen can be seen in Figure 4.17(b), all the strong diffraction peaks correspond to the ε-Fe$_2$O$_3$ phase. However, with increasing Ru content, hematite starts to grow at the expense of ε-Fe$_2$O$_3$ (see Figure 4.17(a)). No traces of rutile structure is found in this case.
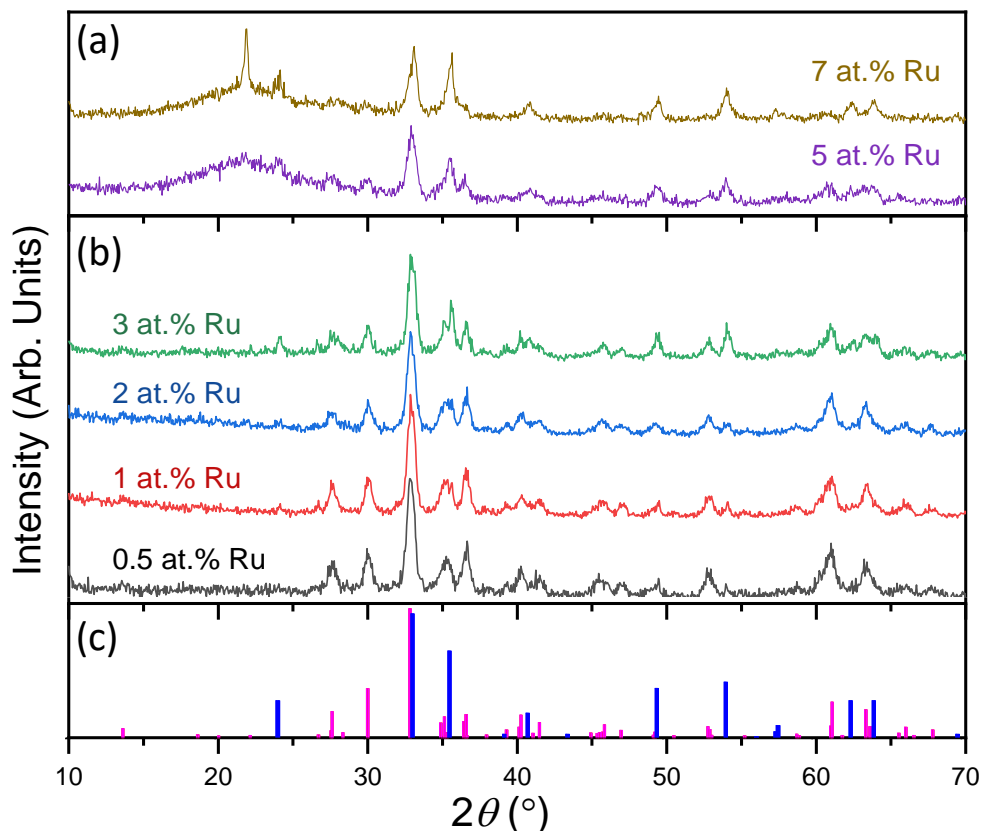
Figure 4.17 XRD patterns of the Ru-doped particles using ruthenium (III) chloride as the precursor. Panel (a) shows the pattern for the 5 and 7 at.% Ru samples (with silica); Panel (b) displays the ones for the etched 0.5, 1, 2 and 3 at.% Ru doped NPs. The bottom panel indicates the peak positions of the epsilon (in pink) and alpha (in blue) phases of iron oxide.

Elemental analyses with inductively coupled plasma mass spectrometry (ICP-MS) indicate that the real Ru compositions for the 1, 2 and 3 at.% samples are 0.28, 0.62, and 1.48 at.%, respectively. For 0.5 at.% Ru sample, the real composition is below 0.20 at.% Ru. These values are consistent with our SEM/EDX analysis. Moreover, the non-etched 3 at.% Ru sample contains 1.54(5) at.% Ru according to SEM/EDX data, excluding the possible loss of Ru during the removal of silica. This Ru deficiency is most likely related to evaporation of Ru, which is known to be volatile, during the heating treatment (1100 °C). Future TG/DTA measurements are necessary to monitor the mass and thermal variation during the process.

To avoid confusion and for consistency, we continue to refer the samples to their theoretical compositions in the following text. The *M-H* hysteresis loops are recorded at room temperature on the annealed particles, and the results are presented in Figure 4.18. The maximum coercive field, $H_C = 15.4$ kOe, is found for the 1 at.% Ru sample. Furthermore, our magnetic measurements reveal notable preparation-dependent magnetic behaviors for this system. For instance, although prepared by nearly the same procedure and subjected to the identical annealing conditions, as seen in Figure 4.18, quite different *M-H* loops are found for different batches: the loops of the 1 and 3 at.% NPs (batch **2**) exhibit

a round-like shape, while a prominent narrowing of the hysteresis loops with much reduced H_C can be observed for 0.5 and 1 at.% Ru (batch **1**). Moreover, in contrast to what is reported in Reference [21], in our case, the doping with Ru did not increase the coercive field of the nanoparticles.
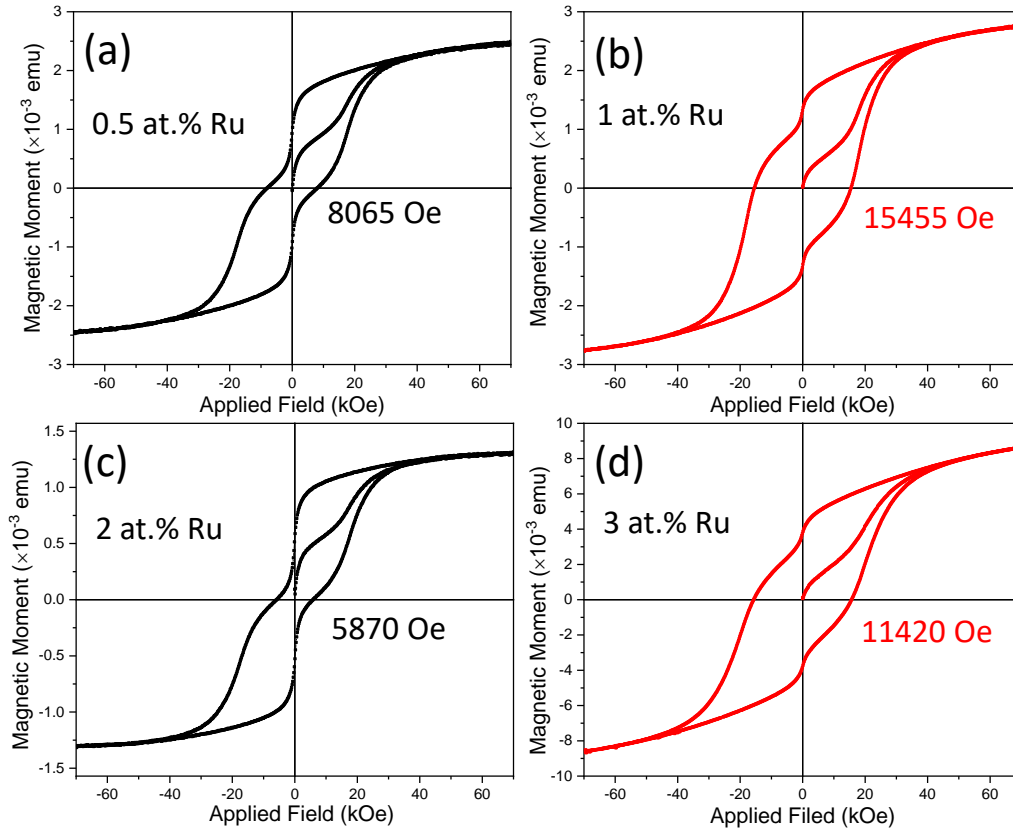
Figure 4.18 Hysteresis loops at 300 K for the Ru-doped particles (with silica). The 0.5 and 2 at.% Ru (in black) were produced from batch **1**, and the 1 and 3 at.% Ru were synthesized from batch **2**.

In summary, we report the preparation of Ru doped ε-Fe$_2$O$_3$ nanoparticles. The successful stabilization of Ru-doped ε-Fe$_2$O$_3$ depends on the choice of the metal precursor, Up to 3 at.% Ru-substitution has been achieved. However, the elemental analysis indicates that the actual Ru concentration is significantly lower than expected most likely due to the volatility OF Ru and the high annealing temperatures that are used for the preparation of these oxides. No clear enhancement of coercive filed is found from the magnetic measurements, which also suggests that the macroscopic magnetic response critically depends on aspects of the synthesis that we have not been able to control so far.

4.6 Summary

In this chapter, we have reported the preparation of different transition-metal substituted ε-Fe$_2$O$_3$ nanoparticles by sol-gel based method. The structural evolution upon the substitution is investigated. The epsilon structure is unexpectedly stable up to 10 at.% of Cr and Mn substitutions. However, only relatively small amounts of Co can be incorporated in ε-Fe$_2$O$_3$ before the formation of Co-containing magnetic phase(s) occurs. The magnetic properties of ε-Fe$_2$O$_3$ are strongly dependent on the doping by transition-metal element. For example, appropriate Mn-substitution is found to promote the hard magnetic behavior, while the Cr and Co substituted oxides present softer magnetic behavior. Moreover, our work suggests that, for a systematic study of the doping effect, a careful selection of metal precursors and fine-tuning synthesis parameters are necessary.

References

[1] T. Arima, D. Higashiyama, Y. Kaneko, J.P. He, T. Goto, S. Miyasaka, T. Kimura, K. Oikawa, T. Kamiyama, R. Kumai, Y. Tokura, Structural and magnetoelectric properties of $Ga_{2-x}Fe_xO_3$ single crystals grown by a floating-zone method, Phys. Rev. B. 70 (2004). https://doi.org/10.1103/PhysRevB.70.064426.

[2] J.Y. Kim, T.Y. Koo, J.H. Park, Orbital and bonding anisotropy in a half-filled $GaFeO_3$ magnetoelectric ferrimagnet, Phys. Rev. Lett. 96 (2006). https://doi.org/10.1103/PhysRevLett.96.047205.

[3] M. Yoshikiyo, A. Namai, M. Nakajima, K. Yamaguchi, T. Suemoto, S.I. Ohkoshi, High-frequency millimeter wave absorption of indium-substituted ε-Fe_2O_3 spherical nanoparticles (invited), in: J. Appl. Phys., American Institute of Physics Inc., 2014: p. 172613. https://doi.org/10.1063/1.4870168.

[4] S.I. Ohkoshi, S. Kuroki, S. Sakurai, K. Matsumoto, K. Sato, S. Sasaki, A millimeter-wave absorber based on gallium-substituted ε-iron oxide nanomagnets, Angew. Chemie - Int. Ed. 46 (2007) 8392–8395. https://doi.org/10.1002/anie.200703010.

[5] A. Namai, S. Sakurai, M. Nakajima, T. Suemoto, K. Matsumoto, M. Goto, S. Sasaki, S. Ohkoshi, Synthesis of an Electromagnetic Wave Absorber for High-Speed Wireless Communication, J. Am. Chem. Soc. 131 (2009) 1170–1173. https://doi.org/10.1021/ja807943v.

[6] R.D. Shannon, Revised effective ionic radii and systematic studies of interatomic distances in halides and chalcogenides, Acta Crystallogr. Sect. A. 32 (1976) 751–767. https://doi.org/10.1107/S0567739476001551.

[7] Y.S. Dedkov, A.S. Vinogradov, M. Fonin, C. König, D. V. Vyalikh, A.B. Preobrajenski, S.A. Krasnikov, E.Y. Kleimenov, M.A. Nesterov, U. Rüdiger, S.L. Molodtsov, G. Güntherodt, Correlations in the electronic structure of half-metallic ferromagnetic CrO_2 films: An x-ray absorption and resonant photoemission spectroscopy study, Phys. Rev. B - Condens. Matter Mater. Phys. 72 (2005) 060401. https://doi.org/10.1103/PhysRevB.72.060401.

[8] J.L. García-Muñoz, A. Romaguera, F. Fauth, J. Nogués, M. Gich, Unveiling a New High-Temperature Ordered Magnetic Phase in ϵ-Fe_2O_3, Chem. Mater. 29 (2017) 9705–9713. https://doi.org/10.1021/acs.chemmater.7b03417.

[9] R.A. Brand, Improving the validity of hyperfine field distributions from magnetic alloys: Part I: Unpolarized source, Nucl. Instruments Methods Phys. Res. Sect. B Beam Interact. with Mater. Atoms. 28 (1987) 398–416. https://doi.org/https://doi.org/10.1016/0168-583X(87)90182-0.

[10] M. Popovici, M. Gich, D. Nižňanský, A. Roig, C. Savii, L. Casas, E. Molins, K. Zaveta, C. Enache, J. Sort, S. De Brion, G. Chouteau, J. Nogués, Optimized synthesis of the elusive $\in$-Fe_2O_3 phase via sol-gel chemistry, Chem. Mater. 16 (2004). https://doi.org/10.1021/cm048628m.

[11] N. Hollmann, Z. Hu, T. Willers, L. Bohatý, P. Becker, A. Tanaka, H.H. Hsieh, H.J. Lin, C.T. Chen, L.H. Tjeng, Local symmetry and magnetic anisotropy in multiferroic $MnWO4$ and antiferromagnetic $CoWO_4$ studied by soft x-ray absorption spectroscopy, Phys. Rev. B - Condens. Matter Mater. Phys. 82 (2010) 184429. https://doi.org/10.1103/PhysRevB.82.184429.

[12] C.F. Smura, D.R. Parker, M. Zbiri, M.R. Johnson, Z.A. Gál, S.J. Clarke, High-Spin cobalt(II) ions in square planar coordination: Structures and magnetism of the oxysulfides $Sr_2CoO_2Cu_2S_2$ and $Ba_2CoO_2Cu_2S_2$ and their solid solution, J. Am. Chem. Soc. 133 (2011) 2691–2705. https://doi.org/10.1021/ja109553u.

[13] H.-J. Koo, R.K. Kremer, M.-H. Whangbo, Orbital Magnetic Moments of the High-Spin $Co2+$ Ions at Axially-Elongated Octahedral Sites: Unquenched as Reported from Experiment or Quenched as Predicted by Theory?, Cite This Inorg. Chem. 59 (2020) 18319–18324. https://doi.org/10.1021/acs.inorgchem.0c02929.

[14] G. Ji, S. Tang, B. Xu, B. Gu, Y. Du, Synthesis of $CoFe_2O_4$ nanowire arrays by sol-gel template method, Chem. Phys. Lett. 379 (2003) 484–489. https://doi.org/10.1016/j.cplett.2003.08.090.

[15] J. Venturini, R.Y.S. Zampiva, S. Arcaro, C.P. Bergmann, Sol-gel synthesis of substoichiometric cobalt ferrite ($CoFe_2O_4$) spinels: Influence of additives on their stoichiometry and magnetic properties, Ceram.

Int. 44 (2018) 12381–12388. https://doi.org/10.1016/j.ceramint.2018.04.026.

[16]   S.R. Naik, A. V. Salker, Change in the magnetostructural properties of rare earth doped cobalt ferrites relative to the magnetic anisotropy, J. Mater. Chem. 22 (2012) 2740–2750. https://doi.org/10.1039/c2jm15228b.

[17]   Y. Kumar, P.M. Shirage, Highest coercivity and considerable saturation magnetization of $CoFe_2O_4$ nanoparticles with tunable band gap prepared by thermal decomposition approach, J. Mater. Sci. 52 (2017) 4840–4851. https://doi.org/10.1007/s10853-016-0719-5.

[18]   A. Franco, F.C. E Silva, High temperature magnetic properties of cobalt ferrite nanoparticles, Appl. Phys. Lett. 96 (2010) 6223. https://doi.org/10.1063/1.3422478.

[19]   A. Sunny, V.R. Akshay, M. Vasundhara, Effect of annealing temperature on the size and magnetic properties of $CoFe_2O_4$ nanoparticle, in: AIP Conf. Proc., American Institute of Physics Inc., 2018: p. 030162. https://doi.org/10.1063/1.5032497.

[20]   A. Namai, M. Yoshikiyo, K. Yamada, S. Sakurai, T. Goto, T. Yoshida, T. Miyazaki, M. Nakajima, T. Suemoto, H. Tokoro, S. Ohkoshi, Hard magnetic ferrite with a gigantic coercivity and high frequency millimetre wave rotation, Nat. Commun. 3 (2012). https://doi.org/10.1038/ncomms2038.

[21]   A. Namai, S. ichi Ohkoshi, Crystal Structure and Magnetic Properties of ϵ-$Ru_xFe_{2-x}O_3$ Nanosize Hard Ferrite, Chem. - A Eur. J. 24 (2018) 11880–11884. https://doi.org/10.1002/chem.201802771.

Part II

Epitaxial ε-Fe₂O₃ Thin Films

The appeal of magnetic and magnetoelectric properties of ε-Fe$_2$O$_3$ nanoparticles for applications in information technologies prompted our group to pursue the stabilization of this polymorph as epitaxial thin films. This was achieved by Pulsed Laser Deposition (PLD), both directly on (111) SrTiO$_3$ (STO) [1] or introducing a buffer layer of the isostructural AlFeO$_3$ (AFO) [2]. The presence of the AFO layer renders the stabilization more robust (i.e. achievable in a broad range of deposition conditions) and reproducible. Indeed, without the AFO layer we were not able to reproduce the ε-Fe$_2$O$_3$ films using the PLD system installed at ICMAB. Interestingly Corbellini et al. [3] and Hamasaki et al.[4] also reported the direct PLD growth of epitaxial ε-Fe$_2$O$_3$, but their works also evidenced the challenge of directly growing epitaxial ε-Fe$_2$O$_3$ films without introducing an isostructural buffer layer. Indeed, Corbellini et al. found that in their films ε-Fe$_2$O$_3$ coexists with about 10 vol. % impurities consisting of magnetite (Fe$_3$O$_4$). On the other hand, Hamasaki et al. managed to stabilize ε-Fe$_2$O$_3$ over α-Fe$_2$O$_3$ only by using a very low laser fluence (0.32 J/cm^2). Interestingly, re-examining the films we had directly grown on STO(111), in different zones of the substrate-film interface it was found a layer of epitaxial magnetite on top of which ε-Fe$_2$O$_3$ was also growing epitaxially (see Figure II.1) [5]. In fact, ε-Fe$_2$O$_3$ growing epitaxially on Fe$_3$O$_4$ or γ-Fe$_2$O$_3$ spinels had been previously observed in nanowires [6] and nanoparticles [7] and more recently on epitaxial thin films grown by PLD [8].
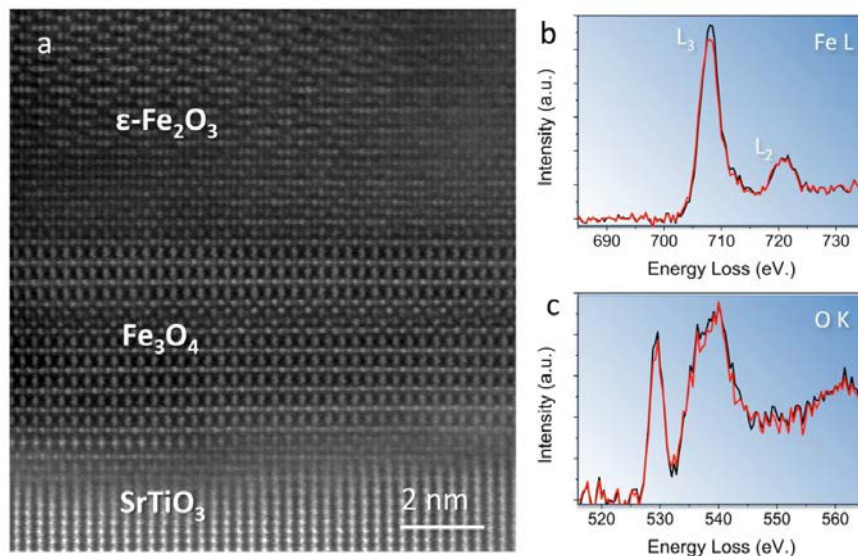
Figure II.1 (a) A Z-contrast image of some specific zones of our first ε-Fe$_2$O$_3$ films directly grown on STO(111) showing the coexistence of ε-Fe$_2$O$_3$ and Fe$_3$O$_4$. Note that Fe$_3$O$_4$ grows epitaxially on the substrate and ε-Fe$_2$O$_3$ grows epitaxially on Fe$_3$O$_4$. (b) and (c) show the Fe $L_{2,3}$ and the O K edges of the two phases, respectively, the ε-Fe$_2$O$_3$ in black and the Fe$_3$O$_4$ in red. The Fe$_3$O$_4$ phase exhibits a smaller $L_{2,3}$ ratio and a lower O K edge pre-peak intensity as well. The figure is taken from reference [9].

On the other hand, despite the challenges of directly stabilizing ε-Fe$_2$O$_3$ on different substrates, there are many reports on epitaxial films of isostructural phases as AFO, with a more straightforward preparation and less stringent growth conditions. More than a decade ago, several teams prepared by PLD epitaxial films of GaFeO$_3$ (GFO), which is considered the prototype of the isostructural ε-Fe$_2$O$_3$

and AlFeO$_3$. The first epitaxial GFO thin films were deposited on (100) yttrium-stabilized zirconia (YSZ) [10–12] and on other substrates such as (111)STO [13], or (100)MgO and (0001)Al$_2$O$_3$ [14]. Since these first works, quite a number of studies reported the epitaxial growth of single metal (e.g., ε-Fe$_2$O$_3$, κ-Ga$_2$O$_3$), binary (e.g., ε-In$_x$Fe$_{2-x}$O$_3$, ε-In$_x$Ga$_{2-x}$O$_3$) or ternary (A$_{0.2}$Ga$_{0.6}$Fe$_{1.4}$O$_3$; A=Al, Sc, In) GFO-type epitaxial films. In most of these publications the stabilization of the metastable GFO-type structures is discussed considering the misfit between the film and the substrate.

Table II.1 gathers the PLD growth conditions of several GFO-type films on different substrates together with the corresponding epitaxial relationships and the calculated % lattice misfit. One can see from the table that in most cases the films would grow under in-plane compression and can sustain a large misfit of up to about 8 %, even though there are also examples of growth under in-plane tensile strain as is the case of films on YSZ. However, some of these works have shown that the films grow relaxed from these substantial strains [2] and it is interesting to note that Sun et al. reported that a poorly crystalline (001)GFO also grows on amorphous quartz films [14], in which the lattice misfit is obviously irrelevant. It is also remarkable that κ-Al$_2$O$_3$ was the only composition from the ε-Al$_x$Fe$_{2-x}$O$_3$ series (0<x<2) which could not be successfully prepared, despite presenting the lowest misfit with STO (111) [4]. Let us finally note that from the point of view of lattice misfit one could expect epitaxial AFO(100) on STO(111) with and the following epitaxial relationships [001]AFO//[11-2]STO (misfit -3.4 %) and [010]AFO//[10-1]STO (misfit 3.2 %). However, this has not been observed by any of the studies reporting AFO films on STO(111) [2,15].

From the above observations it seems reasonable to consider that other aspects, other than lattice misfit, such as the substrate-film chemical interactions or thermodynamics and kinetics favor crystal stabilization. This perspective takes on relevance in the light of several recent publications. On the one hand, Kneiβ et al. were able to stabilize κ-Ga$_2$O$_3$ (doped with 1 at. % Sn) using low oxygen pressures (3·10^{-3} to 2·10^{-2} mbar) in which the increased deposition flux would favor kinetic stabilization of metastable polymorphs [16]. On the other hand, growth conditions which favor the thermodynamic stabilization by the use of high temperatures which enhance the diffusion rate of species have been also exploited. This is, for instance, the case of the study by Viart and co-workers who achieved the growth of ultra-flat (001)GFO on STO(111) by significantly increasing the substrate temperature (900 °C) [17]. Interestingly, this work reports that regardless of their thickness the films are not growing under any substrate-induced in-plane strain, despite the growth mode is 3D for the first few nanometers it then transitions to 2D layer-by-layer growth mode at a film thickness of about 7 nm. Moreover, their detailed characterization of the film close to the substrate interface by Electron Energy Loss Spectroscopy reveals the presence of and Fe^{2+} and Ti, the latter migrated from the substrate. In these regards, Itoh and co-workers deposited, also on STO(111), (001)ε-M$_{0.2}$Ga$_{0.4}$Fe$_{1.4}$O$_3$ films with M=Al, Ga, In, Sc, obtaining remarkably good crystalline quality, namely for Sc and In [18]. As it has been demonstrated

for the case of AlFeO$_3$, it is likely that these isostructural ternary metal oxides are also entropy stabilized [19].

This review of recent literature on GFO-type epitaxial thin films indicates the need for a deeper understanding of the stabilization mechanisms of this material type and may path the way to better control of the microstructure of thin films, particularly relevant for applications that intend exploiting their multiferroic properties. Recent examples of this are the possibility of obtaining out-of-plane magnetic anisotropy in GFO [17] or evidence of ferroelectric switching assisted by domain boundaries in ε-Fe$_2$O$_3$ [20]. In this context, in this thesis we aimed at providing new insights on the stabilization of epitaxial ε-Fe$_2$O$_3$ films.

Building on the work of Itoh's group we investigated the interest of using Sc$_y$Al$_x$Fe$_{2-x-y}$O$_3$ (SAFO) as a buffer layer to improve the crystallinity and decrease the roughness of ε-Fe$_2$O$_3$ films. The growth of epitaxial films of this ternary oxide was studied on a variety of substrates followed by the attempt to use them to stabilize ε-Fe$_2$O$_3$. The results are presented in **Chapter 5**.

Chapter 6 is focused on the stabilization of epitaxial ε-Fe$_2$O$_3$ without making use of buffer layers. Inspired by the different evidences of the tendency of ε-Fe$_2$O$_3$ to grow on magnetite and maghemite, we hypothesized that MgAl$_2$O$_4$ spinel substrates could be good candidates to achieve this goal.

Flexible substrates appear as a convenient platform to investigate strain-dependent magnetic responses in ε-Fe$_2$O$_3$, especially considering that this system is not well adapted for strain engineering using different substrates. Driven by this interest and encouraged by the reported CVD growth of this phase on mica [21], we decided to attempt the PLD growth of ε-Fe$_2$O$_3$ on mica, taking advantage of previously developed SAFO buffer layers. **Chapter 7** reports these studies.

Table II.1 A summary of epitaxial *Pna2₁* thin films and the substrates employed. The in-plane epitaxial relationships and the corresponding misfit are also given, together with some relevant PLD growth conditions including deposition temperature (T_s), laser repetition rate (f), laser fluence, and oxygen pressure (P_{O2}).

(001)-oriented Thin Film	Substrate	T_s (°C)	f (Hz)	Fluence (J/cm²)	P_{O2} (mbar)	% Lattice Misfit (m:n) CSL multiplier	Ref.
GFO	YSZ(100) YSZ(100)/ Si(100)	650		1.8-2	0.53	[100]GFO//[100]YSZ:-0.8 (1:1) [010]GFO//[010]YSZ:-14.4 (1:2)	[10]
GFO	ITO(100)/ YSZ(100)	600-900	10	1	0.5-1	[100]GFO//[100]ITO:0.01 (2:1) [010]GFO//[010]ITO:-13.6 (1:1) [110]GFO//[100]ITO:-0.4 (1:1)	[11]
GFO	MgO(100)	700-750	3	1.5	0.1	[-101]GFO//[1-10]MgO:7.7 (1:1) [010]GFO//[110]MgO:-1.9 (2:3)	[14]
ε-AlFeO₃	Nb:STO (111)	750-900	5	1.5	0.1	[100]AFO//[1-21]STO:4.0 (1:1) [010]AFO//[10-1]STO:3.1 (2:3)	[2]
ε-Fe₂O₃	Nb:STO (111)	800	5	1.5	0.1	[100]AFO//[1-21]STO: 6.3 (1:1) [010]AFO//[10-1]STO:5.9 (2:3)	[1]
ε-In₀.₂₅Fe₁.₇₅O₃ ε-Fe₂O₃	STO(111)	600 800	5	0.96	0.13	[100]IFO//[1-21]STO:7.8 (1:1) [010]IFO//[10-1]STO:7.3 (2:3) [100]ε-Fe₂O₃//[1-21]STO:6.3 (1:1) [010]ε-Fe₂O₃//[10-1]STO:5.9 (2:3)	[22]
Ga₀.₆Fe₁.₄O₃	STO(100) LSAT(100)	700			0.4	[100]GFO//[01-1]STO:-7.9 (1:1) [010]GFO//[011]STO:5.7 (2:3) [110]GFO//[011]STO:-8.3 (1:2) [100]GFO//[01-1]LSAT:-7.2 (1:1) [010]GFO//[011]LSAT:6.6 (2:3) [110]GFO//[011]LSAT:-7.6 (1:2)	[23]
GFO	Al₂O₃(0001) STO(111) YSZ(100)	750	5	1.5	0.4	[100]GFO//[1000]Al₂O₃:6.7 (1:1) [010]GFO//[11-20]Al₂O₃:6.1 (1:2) [100]GFO//[1-21]STO:6.1 (1:1) [010]GFO//[10-1]STO:5.5 (2:3) [100]GFO//[010]YSZ:-0.8 (1:1) [110]GFO//[100]YSZ:-1.2 (1:2)	[24]
ε-Sc₀.₅Fe₁.₅O₃	STO(111)		5	0.32		[100]SFO//[1-21]STO:7.3 (1:1) [010]SFO//[01-1]STO:6.8 (2:3)	[25]
ε-Fe₂O₃	YSZ(100)	800	5	1.8	0.1	[100]ε-Fe₂O₃//[100]YSZ:-0.6 (1:1) [010]ε-Fe₂O₃//[010]YSZ:-14.3 (1:2) [110] ε-Fe₂O₃//[100]YSZ:-0.9 (1:2)	[3]
ε-Fe₂O₃	MgO(111)/ GaN(0001)	800			0.2-0.4	[100]ε-Fe₂O₃//[1-21]MgO:-1.0 (1:1) [010]ε-Fe₂O₃//[10-1]MgO:-1.5 (2:3)	[8]
ε-A₀.₂Ga₀.₄Fe₁.₄O₃ A=Al, Sc, In	STO(111)	700			0.4	Estimated to vary between 5.7 for A=Al and 7.2 for A=In	[18]
κ-In$_x$Ga₂₋ₓO₃ (0<x<0.35)	Al₂O₃(0001)	940			3·10⁻⁴		[26]
κ-Ga₂O₃ (Sn-doped)	STO(111) YSZ(111) MgO(111) Al₂O₃(0001)	670	1..10	2	3·10⁻⁴ 2·10⁻²	[100]κ-Ga₂O₃//[1-21]STO:5.5 (1:1) [010]κ-Ga₂O₃//[10-1]STO:4.9 (2:3) [100]κ-Ga₂O₃//[1-21]YSZ:-19.5 (1:1) [010]κ-Ga₂O₃//[10-1]YSZ:20.2 (1:1) [100]κ-Ga₂O₃//[1-21]MgO:-1.8 (1:1) [010]κ-Ga₂O₃//[10-1]MgO:-2.4 (2:3) [100]κ-Ga₂O₃//[1000]Al₂O₃:6.1 (1:1) [010]κ-Ga₂O₃//[11-20]Al₂O₃:5.5 (1:2)	[16]

Note: Lattice misfit defined as $((m \cdot a_f - n \cdot a_s) / (n \cdot a_s)) \times 100$ %, where a_f is the epilayer and a_s is the substrate lattice constant, and (m:n) the multipliers for coincidence site lattice (CSL).

Table II.2 lists the cell parameters of the orthorhombic ε-Fe$_2$O$_3$-like oxides. All epsilon like materials have very similar lattice parameters. Therefore, in the following discussion we shall only consider the *Pna2$_1$* ε-Fe$_2$O$_3$, however, the epitaxial relation between the epilayer and substrate as well as the general trend are the same for all these compounds.

Table II.2 A summary of the crystal structures and lattice parameters of ε-Fe$_2$O$_3$ and its related oxides. Note that the reported out-of-plane direction is always along the *c*-axis in the *Pna2$_1$* setting (or the *b*-axis in the *Pc2$_1$n* setting) for the oxide epitaxial thin films. Abbreviation: S. G., space group. The lattice constants for ε-Fe$_2$O$_3$ are from the synchrotron X-ray diffraction of the particle sample described in Chapter 3 of the thesis.

Epilayer	Cell Parameters (Å)			Ref.
	a	*b*	*c*	
AlFeO$_3$	4.98	8.55	9.24	[15]
ϰ-Ga$_2$O$_3$	5.05	8.70	9.28	[27]
GaFeO$_3$ *	5.08	8.75	9.40	[28]
Ga$_{0.6}$Fe$_{1.4}$O$_3$	5.07	8.78	9.43	[23]
Sc$_{0.5}$Fe$_{1.5}$O$_3$	5.14	8.86	9.64	[25]
A$_{0.2}$Ga$_{0.4}$Fe$_{1.4}$O$_3$ (A = Al, Ga, Fe, Sc, In)	-	-	9.40-9.55	[18]
ε-Fe$_2$O$_3$	5.09	8.78	9.46	This work NP
	5.06	8.78	9.42	eFO/SAFO//Mica(001)
Sc$_{0.2}$Al$_{0.4}$Fe$_{1.4}$O$_3$	5.04	8.80	9.45	This work SAFO//STO(111)
	5.07	8.77	9.43	SAFO//Mica(001)

* Equivalently, *Pc2$_1$n*.

Figure II.2 depicts the possible in-plane orientations of ε-Fe$_2$O$_3$-like epitaxial thin film on three typical single-crystalline oxide substrates: corundum-type Al$_2$O$_3$ (0001) (Panel (a)), perovskite STO(111) (Panel (b)) and cubic YSZ(100) (Panel (c)). Hereafter the subscripts eFO and S denote ε-Fe$_2$O$_3$ and the substrate. Along the crystallographic *a*-axis of ε-Fe$_2$O$_3$, a very small mismatch is found between its *a* constant and the either side of the equilateral triangles ($a_{eFO} \approx a_S = 4.76$ nm) for Al$_2$O$_3$ (0001), or the heights of the equilateral triangles ($a_{eFO} \approx \sqrt{6}/2\, a_S = 4.79$ nm) for STO(111). On the other hand, small mismatches are also satisfied along the crystallographic *b*-axis of ε-Fe$_2$O$_3$ for Al$_2$O$_3$ (0001) ($b_{eFO} \approx \sqrt{3}a_S = 8.244$ nm) and STO(111) ($2b_{eFO} \approx 3 \times \sqrt{2}a_S = 16.59$ nm), explaining the epitaxy of ε-Fe$_2$O$_3$ on these substrates. Consequently, the following in-plane orientations should be expected: [100]$_{eFO}$//[-1-120]$_S$, [010]$_{eFO}$//[0-110]$_S$, [110]$_{eFO}$//[-12-10]$_S$ for Al$_2$O$_3$ (0001), and [100]$_{eFO}$//[11-2]$_S$, [010]$_{eFO}$//[110]$_S$, [110]$_{eFO}$//[1-21]$_S$ for STO(111).

Furthermore, in the case of cubic YSZ(100) with a four-fold symmetry, the different in-plane orientations of ε-Fe$_2$O$_3$ can be explained considering the different matching possibilities between ε-Fe$_2$O$_3$ and YSZ lattices: $a_{eFO} \approx a_S = 5.12$ nm and $3b_{eFO} \approx 5a_{YSZ} = 25.60$ nm (results in a residual misfit

of +2.9 %), on the one hand, and $\sqrt{a_{eFO}^2 + b_{eFO}^2} \approx 2a_{YSZ}$, on the other hand. The angle between the b

and the diagonal of the ab plane of ε-Fe$_2$O$_3$ cell is $\alpha = \cos^{-1}(b_{eFO}/\sqrt{a_{eFO}^2+b_{eFO}^2}) \approx 30°$. This allows the

existence of the six variants shown in Figure II.2(c), located every 30° [11]. These characteristics give

rise to the in-plane epitaxy of [100]$_{eFO}$//[010]$_S$, [010]$_{eFO}$//[001]$_S$, [110]$_{eFO}$//[010]$_S$.

(d)

					eFO(100)				eFO(010)				eFO(110)	Compressive
substrate	S	S_{11-20}	n_{S11-20}	m_{F100}	5.09	S_{0-110}	n_{S0-110}	m_{F010}	8.78	S_{1-210}	n_{S1-210}	m_{F110}	10.15	
AO(0001)	4.76	4.760	1	1	6.9%	4.122	2	1	6.5%	9.520	2	1	6.6%	
substrate	S	S_{11-2}	n_{S11-2}	m_{F100}	5.09	S_{110}	n_{S110}	m_{F010}	8.78	S_{1-21}	n_{S1-21}	m_{F110}	10.15	
STO(111)	3.91	4.789	1	1	6.3%	5.530	3	2	5.9%	4.789	2	1	6.0%	
substrate	S	S_{001}	n_{S001}	m_{F100}	5.09	S_{010}	n_{S010}	m_{F010}	8.78	S_{010}	n_{S010}	m_{F110}	10.15	
YSZ(100)	5.12	5.120	1	1	-0.6%	5.120	5	3	2.9%	5.120	2	1	-0.9%	Tensile

Figure II.2 Sketches depicting the in-plane epitaxial relationships between ε-Fe$_2$O$_3$-like thin film and different substates (a) Al$_2$O$_3$ (0001), (b) STO (111) and (c) YSZ (100). The eFO and S subscript denote the film and substrate, respectively. Although both exhibit three domain variants with a 120° separation, the a-axes of the film domains are parallel to the in-plane principal axis directions for corundum Al$_2$O$_3$ (0001), whereas they are parallel to the altitudes of the equilateral triangles for the (111) perovskite. For the cubic YSZ(100), one domain is accommodated following the [100]$_{eFO}$//[010]$_S$ relation, while two domains following the [110]$_{eFO}$//[010]$_S$ relation thanks to the [010] and [110] angle of ~ 30° in the ε-Fe$_2$O$_3$ cell. These three kinds of domains together with their 90° rotational variants form six in-plane variants, located every 30°. (d) The in-plane misfit calculated based on the sketched epitaxial relationships.

Chapter 5

Effect of substrate on the epitaxial growth of ε-$Sc_{0.2}Al_{0.4}Fe_{1.4}O_3$ thin films

5.1 Introduction

It is known that the structural, magnetic and ferroelectric properties of ε-Fe_2O_3 can be largely tailored through chemical doping. For example, for the metal-doped ε-$A_xFe_{2-x}O_3$, the crystal stability of ε-Fe_2O_3 is enhanced via the chemical doping of Ga (A= Ga), leading to a thermodynamic stable phase of GFO; moreover, when the dopant A = Ga or Al, the magnetization value at room temperature increases with x ($x\leq 0.6$) [29]. Furthermore, the fine tuning of the magnetic and ferroelectric properties of ε-Fe_2O_3 epitaxial films via a co-substitution method has been recently demonstrated by Katayama et al [18]. The Sc and Ga co-doped $Sc_{0.2}Ga_{0.4}Fe_{1.4}O_3$ thin films were found to not only exhibit an improved crystallinity, but also showed a large room temperature magnetization and a reversible polarization with low leakage current.

In the present work, in order to circumvent the difficulty in obtaining a stoichiometric buffer under the optimized growth conditions for the ε-Fe_2O_3 film due to the rather high volatility of Ga, we replace the Ga to the less volatile Al, and use $Sc_{0.2}Al_{0.4}Fe_{1.4}O_3$ as a PLD target for the stabilization of thin films of metastable ε-Fe_2O_3 phase. We demonstrate the epitaxial stabilization of $Sc_{0.2}Al_{0.4}Fe_{1.4}O_3$ epitaxial thin films with the *Pna2_1* phase (hereafter denoted as ε-SAFO) on different types of substrates, including (111)-oriented STO and $(LaAlO_3)_{0,3}$-$(Sr_2AlTaO_6)_{0,7}$ (LSAT) and (001)-oriented cubic yttria-stabilized zirconia Y:ZrO_2 (YSZ). These substrates are known as suitable substrates for the growth of GFO like phases (see Table II.1). The deposited 60-nm epitaxial films exhibit high crystallinity and very flat

topography. The epitaxial integration of ε-Fe_2O_3 phase with YSZ (001) is of relevance, since the latter has proven to be an effective buffer layer for the growth of oxides on top of (100)-oriented silicon wafers [30][31][32]. Furthermore, we explore the growth of SAFO on (100) $Gd_3Ga_5O_{12}$ (GGG) single-crystalline substrates, firstly because GGG garnet is a well-studied substrate for magneto-optical and microwave applications [33][34][35], and secondly because it may allow for a distinct out-of-plane crystal orientation (note that $\sqrt{2}\,a_{GGG}$= 17.5 Å $\approx 2b_{eFO} \approx 2c_{eFO}$, resulting in potential misfit of +0.3 % and +8.1 % along the b and c axes of the ε-Fe_2O_3 cell, respectively). Recently, the growth of complex oxides on flexible mica (muscovite and fluorophlogopite) substrates could pave the way to novel flexible electronics and hence here we decided to explore the integration of epsilon like iron oxides on fluorophlogopite mica substrates.

5.2 PLD growth of ε-$Sc_{0.2}Al_{0.4}Fe_{1.4}O_3$ epitaxial thin films on various substrates

The quaternary SAFO oxide target used for ε-SAFO deposition was prepared by solid-state reaction method, involving the following steps: First, the stoichiometric commercial Fe_2O_3 (99.9 % purity, Sigma-Aldrich), Al_2O_3 (99.99 % purity, Sigma-Aldrich) and Sc_2O_3 (99.9 % purity, Alfa Aesar) powders were weighed and uniformly mixed via rigorous grinding. The mixture was then pelletized using a manual hydraulic press. The force applied was 2.5 ton and the pressing duration was 30 min. Subsequently, the obtained pressed pellet was subject to sintering in air (annealing at 200 °C and 800°C each for 3 hours, accompanied by final heating at 1000 °C for 24 hours). To decrease the porosity of the target, the sintered pellet was ground into powder and re-pelletized, followed by another sintering process at a maximum temperature of 1200 °C for 12 hours. The calculated porosity of the final 1-inch-diameter target was ~ 30 %. The XRD pattern (not shown) revealed that the sintered target possesses multiple phases of Fe_2O_3 (S.G.: R-$3c$), Al_2O_3 (S.G.: R-$3c$) and Sc_2O_3 (S.G.: $Ia3$). The EDX spectroscopy gave relative Fe, Al and Sc contents of 77(2) wt.%, 14(3) wt.% and 9(1) wt.%, respectively, with the digits in the brackets corresponding to the standard deviations. These values are in excellent agreement with the theoretical chemical composition (i.e., 77 wt.%, 14 wt.% and 9 wt.% for Fe, Al and Sc, respectively). For the film deposition, a KrF excimer laser (248 nm wavelength, 25 ns pulse duration) was employed as a laser source. Single-crystalline Al_2O_3 (0001), LSAT (111), STO (111), MAO (111), YSZ (001), GGG (001) oxide substrates (Crystec GmbH) of a typical size of 5×5 mm^2 were used as-received, whereas the substrates of fluorophlogopite mica [F-mica, $KMg_3(AlSi_3O_{10})F_2$] (Changchun Taiyuan Co., Ltd, China) were freshly exfoliated with a scotch tape prior to its transfer into the vacuum PLD chamber. The substrates were heated to T_s= 825 °C in vacuum, and the oxygen background pressure p_{O2} was then set to be 0.1 mbar. The films were grown with a total number of 8000 laser pulses at 5 Hz laser repetition rate with a fluence of 2 J/cm^2. At the end of the deposition, the films were cooled to room temperature under the same oxygen deposition pressure. The target-substrate distance was 4.7

cm throughout this thesis. The Sc$_{0.2}$Al$_{0.4}$Fe$_{1.4}$O$_3$ (SAFO) films grown on a wide range of commercially available substrates are summarized in Table 5.1.

Table 5.1 A summary of the PLD-deposited SAFO films on varied substrates. Abbreviations: AO (0001), Al$_2$O$_3$ (0001); LSAT (111), (LaAlO$_3$)$_{0.3}$-(Sr$_2$AlTaO$_6$)$_{0.7}$ (111); mica (001), fluorophlogopite mica (KMg$_3$(AlSi$_3$O$_{10}$)F$_2$) with (001) preferred oriented along its basal plane; SAFO, Sc$_{0.2}$Al$_{0.4}$Fe$_{1.4}$O$_3$.

Sample Code	Substrate	Sample Code	Substrate
SAFO//AO(0001)	Al$_2$O$_3$ (0001)	SAFO//Mica(001)	mica (001)
SAFO//LSAT(111)	LSAT (111)	SAFO//YSZ(001)	YSZ (001)
SAFO//STO(111)	SrTiO$_3$ (111)	SAFO//GGG(001)	Gd$_3$Ga$_5$O$_{12}$ (001)
SAFO//MAO(111)	MgAl$_2$O$_4$ (111)		

5.3 Structural characterization of epitaxial ε-Sc$_{0.2}$Al$_{0.4}$Fe$_{1.4}$O$_3$ thin films

5.3.1 XRD characterization: out-of-plane textures

The out-of-plane textures of the SAFO thin films were probed by XRD θ-2θ scans using a Siemens D-5000 diffractometer. As can be seen from Figure 5.1(a), only one diffraction peak associated with the film is identified at $2\theta \sim 39.6°$ for the SAFO//Al$_2$O$_3$(0001) film, which could be attributed to the (0006) reflection of α-Fe$_2$O$_3$ phase. However, highly intense (00l) reflections of ε-Fe$_2$O$_3$ have been observed for the films on LSAT (111), STO (111) and YSZ (001), indicating the crystallization of SAFO with the ε-Fe$_2$O$_3$ structure (hereafter labeled ε-SAFO) with a (00l) out-of-plane texture. The c lattice parameters of the ε-SAFO films on LSAT (111), STO (111) and YSZ (001), estimated using the Nelson Riley method [36], are in the range of 9.43-9.46 Å (see Table 5.2). These values are slightly smaller than the c constant of ε-Fe$_2$O$_3$ nanoparticles (9.46 Å), which can be attributed to the smaller cationic size of Al^{3+} (0.535 Å) compared to that of Fe^{3+} (0.645 Å). The epitaxial ε-SAFO films are about 60 nm thick, according to X-ray reflectivity measurements (see Chapter 2 for an example). These findings indicate that for the chosen growth conditions (T_S= 825 °C, P_{O2}= 0.1 mbar, laser fluence of 2 J/cm^2 and repetition rate of 5 Hz) epitaxial ε-SAFO thin films were grown which are comparable in quality to most epitaxial GaFeO$_3$-type films reported in the literature. Thus, we expand further the exploration of suitable substrates summarized in Table II.1 using a fixed set of deposition parameters.
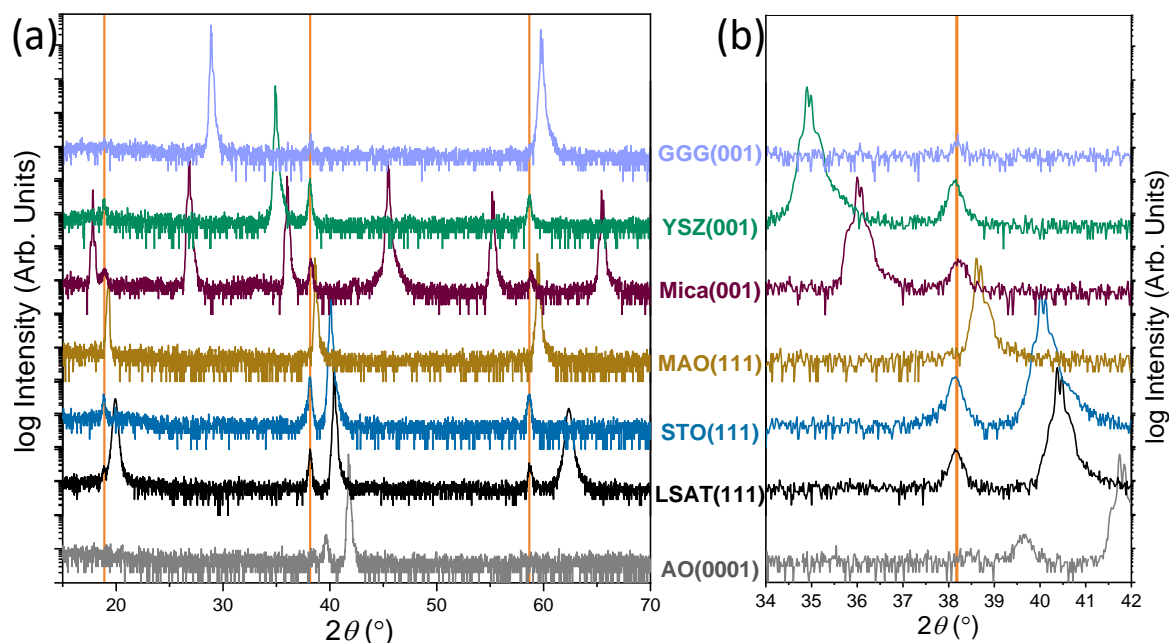
Figure 5.1 (a) XRD θ-2θ scan patterns of the SAFO thin films grown on Al$_2$O$_3$ (0001), LSAT (111), STO (111), MAO (111), mica (001), YSZ (001), and GGG (001) substrates. The vertical orange lines from left to right mark the (002), (004) and (006) diffraction positions of ε-Fe$_2$O$_3$ phase. An enlarged region around the of ε-SAFO (004) peaks (2θ range: 34°- 42°) is shown in Panel (b).

The (00l) reflections of the ε-SAFO films grown on mica (001) are relatively less intense than those of the films grown on the above-mentioned hexagonal symmetric LSAT (111) and STO (111) and four-fold symmetric YSZ (001). Nevertheless, the primary diffraction peaks remain sharp and well-defined. For the SAFO//MAO(111), no traces of diffraction peaks associated with the film are visible in the pattern. However, it is expected that, due to the structural similarities (all possess spinel-type structures and similar lattice parameters), the potential γ-Fe$_2$O$_3$ or Fe$_3$O$_4$ (lll) reflections reside in close proximity of the MAO (lll) reflections and may be screened by the strong substrate peaks in the XRD θ-2θ scans recorded by a point detector. Furthermore, the θ-2θ scan of the SAFO//GGG(001) shows one weak diffraction peak located at $2\theta = 38.2°$, which may correspond to the strongest (004) Bragg peak of ε-Fe$_2$O$_3$ phase. No other out-of-plane textures are observed within the experimental resolution.

Figure 5.2 presents the 2D XRD patterns acquired using a Bruker D8 Advance X-ray diffractometer equipped with a 2D GADDS detector. From the GADDS frames, in addition to the out-of-plane reflections located at $\chi = 0°$, one would expect the {013} diffraction peaks at the position of $\chi \approx \pm 20°$ and $2\theta \approx 30°$ if the films crystalize as ε-Fe$_2$O$_3$ phase (see Figure 5.2(h)). For the SAFO//AO(0001), neither the ε-Fe$_2$O$_3$ (004) reflection nor the (013) side peaks are observed with the 2D detector, so we shall conclude that for this system the main contribution of the grown film is α-Fe$_2$O$_3$ phase. However, this is not the case for the SAFO films grown on other substrates. On MAO (111) and GGG (001) substrates, the characteristic ε-SAFO (004) and (013) reflections are visible, but have rather low intensity. We shall later discuss about these two films in more detail. On the other hand, the presence

of the ε-SAFO (004) and (013) reflections of strong intensity is obvious for the SAFO//LSAT(111), SAFO//STO(111), SAFO//Mica(001) and SAFO//YSZ(001) films, revealing great crystallinity of the epilayer. No other diffraction peaks associated with parasitic phases from the film are found in the patterns. These observations indicate that the stabilization of the GaFeO$_3$ structural type with SAFO is robust.

Table 5.2 XRD results of the SAFO thin films on varied substrates. The c unit cell parameters of the ε-Sc$_{0.2}$Al$_{0.4}$Fe$_{1.4}$O$_3$ (ε-SAFO) and the FWHMs of the rocking curves acquired around the ε-SAFO (004) reflections ($\Delta\omega_{004}$), together with the ε-SAFO in-plane domains, are gathered.

Sample Code	ε-SAFO (001)		Observations
	c (Å)	$\Delta\omega_{004}$ (°)	
SAFO//AO(0001)	–	–	α-Fe$_2$O$_3$ phase
SAFO//LSAT(111)	9.436(5)	0.15	Strong ε-Fe$_2$O$_3$ reflections; three domains
SAFO//STO(111)	9.448(4)	0.12	Strong ε-Fe$_2$O$_3$ reflections; three domains
SAFO//MAO(111)	–	–	Weak ε-Fe$_2$O$_3$ and spinel-like reflections; three domains
SAFO//Mica(001)	9.428(6)	0.58	Strong ε-Fe$_2$O$_3$ reflections; three domains
SAFO//YSZ(001)	9.455(6)	0.11	Strong ε-Fe$_2$O$_3$ reflections; six domains
SAFO//GGG(001)	9.42(2)	–	Weak ε-Fe$_2$O$_3$ reflections; six domains
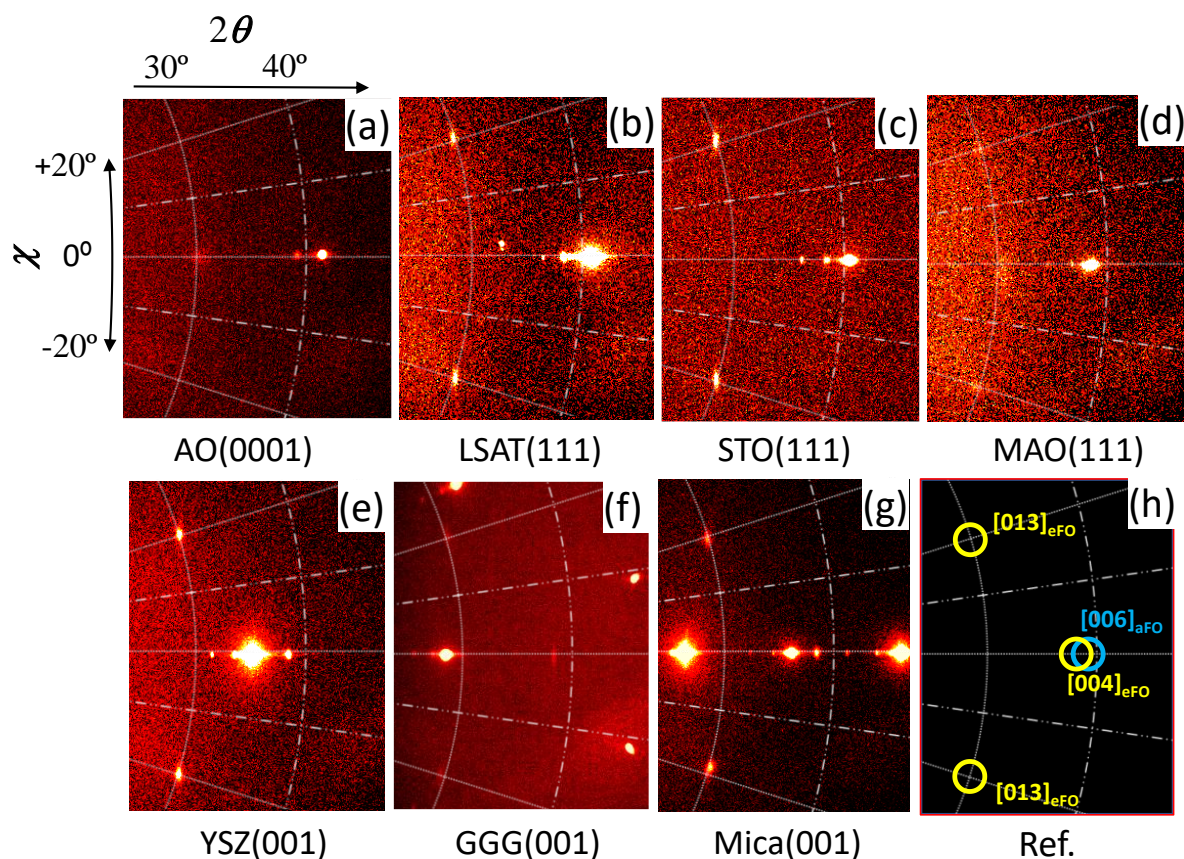
Figure 5.2 (a-h) GADDS 2D XRD patterns from the SAFO thin films grown on various substrates, where the characteristic {013} reflections of ε-Fe$_2$O$_3$ phase, if any, are visible. The χ= 0°, ± 10° and ± 20°, and 2θ = 30° and 40° are indicated by dashed or dash-dotted lines in each frame. The circles in yellow and blue from the last frame denote the reflection positions of ε-Fe$_2$O$_3$ and α-Fe$_2$O$_3$ phases, respectively. The overlayed grid is a guide to the eye.

To evaluate the film quality, we performed high-resolution XRD θ-2θ scan and ϕ-scan (rocking curve) for the ε-SAFO films grown on LSAT (111), STO (111), Mica (001) and YSZ (001) substrates, as shown in Figure 5.3(a) and (b), respectively. While the intrusion of secondary phases such as Fe$_3$O$_4$ or γ-Fe$_2$O$_3$ has been commonly reported in epitaxial ε-Fe$_2$O$_3$ thin films [3][8][18], we did not spot any clear traces of spinel-type iron oxides from Figure 5.3(a). The full width at half maximum (FWHM) of the rocking curve recorded around the (004) peak, $\Delta\omega_{004}$, is 0.58 ° for the ε-SAFO//Mica(001) film. However, $\Delta\omega_{004}$ is as low as 0.11 °, 0.12 ° and 0.15 ° for the films on single-crystalline YSZ, STO and LSAT substrates. These values are comparable with other substituted ternary ε-Fe$_2$O$_3$ epitaxial thin films on STO (111) [18].

It is interesting that the binary Sc$_{0.5}$Fe$_{1.5}$O$_3$ can only grow on STO(111) [25], while we have found that the ternary SAFO is growing on a large diversity of substrates. This can be related to a larger entropy by the introduction of additional element compared to a binary oxide system, which is particularly relevant at the high deposition temperatures that we have been using.
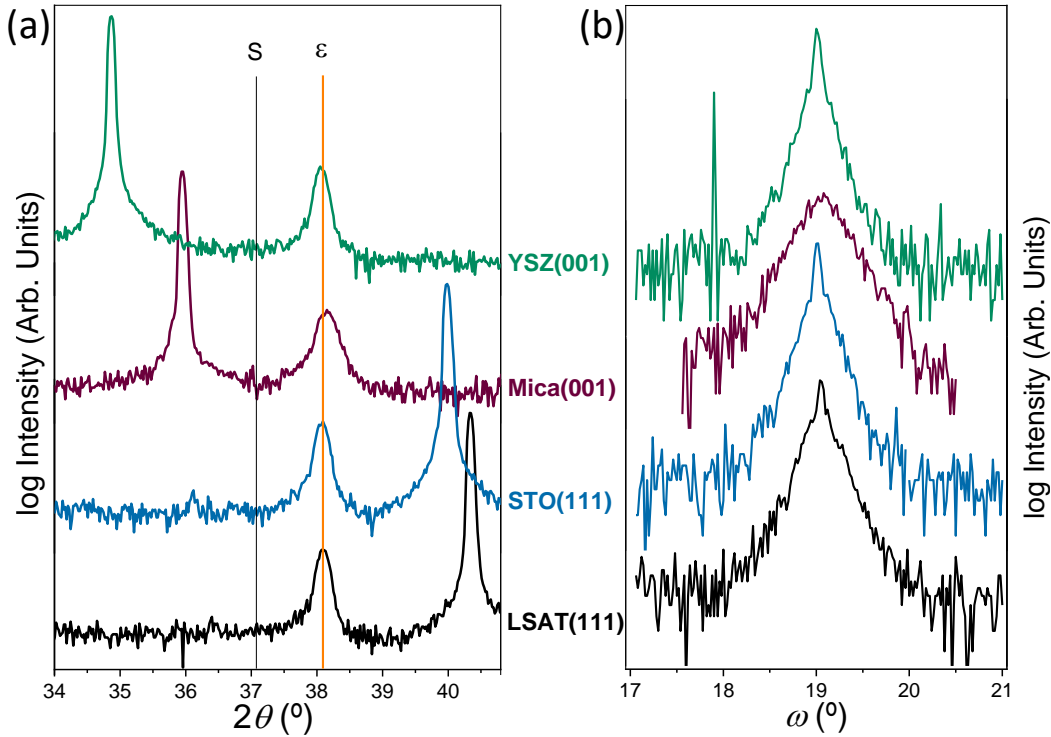
Figure 5.3 High-resolution XRD (a) θ-2θ scan and (b) rocking curve around the (004) of the ε-SAFO films grown on perovskite LSAT(111), STO(111), synthetic mica (001) and cubic YSZ (001) substrates. The vertical straight lines indicate the 2θ positions of spinel Fe$_3$O$_4$ (222) peak (in black) and ε-SAFO (004) peak (in orange). Note that the γ-Fe$_2$O$_3$(222) peak resides at a slightly larger 2θ position than that of spinel Fe$_3$O$_4$ (222). Be aware of the logarithmic scale used here. Reduced relative intensity of the (004) peak in the rocking curve, thus a larger FWHM value (see main text), is found for the SAFO//Mica (001) film in a linear scale.

5.3.2 XRD characterization: in-plane orientations

We next address the in-plane structural characteristic of the epitaxial ε-SAFO films. Figure 5.4(a-c) presents the pole figure scan performed around the {013} plane for the SAFO//STO(111), SAFO//MAO(111) and SAFO//Mica(001) films. Six equivalent ε-SAFO {013} poles separated every 60° in azimuth (ϕ) can be observed from the pole figures of the films on hexagonal symmetric STO (111) and MAO (111). This observation is in agreement with the in-plane relations sketched in Figure II.2 (and for completeness also shown here in Figure 5.4(d-f)), evidencing the presence of three in-plane domain variants in the epilayers. Moreover, for the SAFO//MAO(111) film, one can notice the existence of three relatively weak reflections of the {022} plane of spinel-type phase rotated 60° with respect to the MAO substrate. This is due to the integration conditions used in the pole figure, $2\theta = 29.8\text{-}30.8°$ and the whole observed χ-range of the 2d detector frame. Note that for (111) oriented spinel the (220) reflection has a tilt angle with respect to the normal of about 35° and $2\theta = 30.1°$ for magnetite and $2\theta = 31.3°$ for MAO. This explains the simultaneous observation of the three peak sets in the pole figure image of Figure 5.4(b). Note that the peaks labeled as MAO(022) are thus corresponding to the substrate tail likely overlapping with the spinel SAFO fraction, which manifests by the observed SAFO spinel

(111) twins in the pole figure [37] . Therefore, we can conclude that in SAFO//MAO(111) epitaxial films a competing stabilization of both ε-SAFO (001) and spinel-SAFO (111) phases takes place, while on STO(111) only ε-SAFO (001) stabilizes.
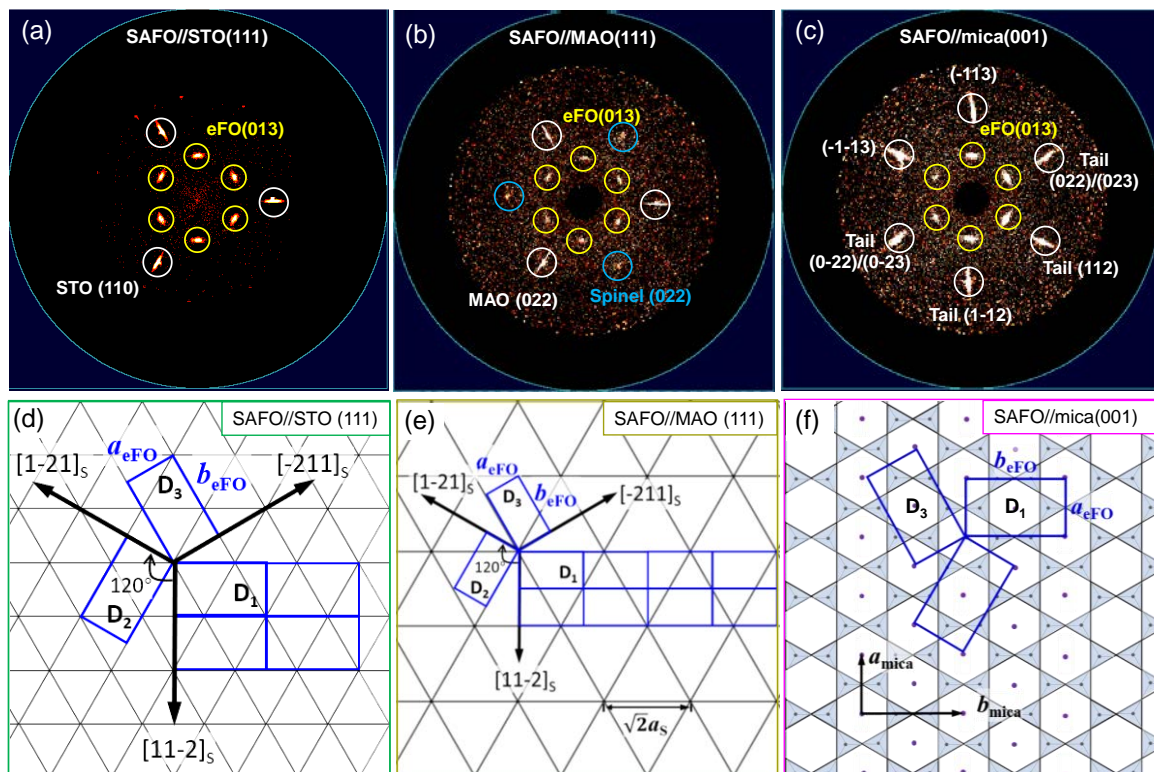
Figure 5.4 Pole figure scan around the ε-SAFO {013} reflections and (a) STO {110}, (b) MAO {022} and (c) Mica {-113} reflections for the epitaxial SAFO//STO(111), SAFO//MAO(111) and SAFO//Mica(001) films, respectively. The different diffraction peaks are represented by circles of distinct colours. (d-f) A schematic representation depicting the in-plane epitaxial relationships between ε-SAFO on mica (001) substrate. The quasi-hexagonal in-plane structure of the mica makes the epitaxial growth of ε-SAFO possible.

For the ε-SAFO//Mica(001) film, also six {013} reflections at 60° intervals are well distinguishable in the pole figure, indicating the three in-plane domain configurations in the system. This is reasonable considering that the top hexagons of corner-sharing (Si, Al)O$_4$ tetrahedra create a quasi-hexagonal in-plane lattice structure of mica. Such structural similarity between the surfaces of mica (001) and (111)-oriented perovskites or spinel (e.g., STO and MAO) makes the lattices of the thin film and mica substrate match well in a periodic way, which reveals an epitaxial relation of [100]$_{eSAFO}$//[100]$_{Mica}$, [100]$_{eSAFO}$//[110]$_{Mica}$, and [100]$_{eSAFO}$//[1-10]$_{Mica}$. Note, that the observed intensity for Mica substrate reflections is rather corresponding to intensity from broad substrate tails (labeled correspondingly in Figure 5.4(c)), and additionally to a certain overlap to an in-plane twinning of the substrate itself. Indeed, in natural mica six in-plane variants have been identified [38], and this will be discussed along with a more detailed description of Mica substrates in Chapter 7. A schematic of the epitaxial relationship between ε-SAFO (001) and mica (001) substrate is shown in Figure 5.4(e).

For the SAFO layers grown on STO(111) and Mica(001) we determined the in-plane lattice parameters from reciprocal space maps (RSM). The *a* parameter was determined from (*h0l*) film reflections, while *b* was obtained by the corresponding (*0kl*) reflections. Since for the film grown on STO the acquisition of the (*0kl*) region was not successful, we alternatively used an approximation combining RSM, pole figure and ω-2θ measurements (see also Section 7.3). We find that, $a = 5.04(1)$ Å, $b = 8.80(5)$ Å and $c = 9.448(4)$ Å for the SAFO//STO(111) film, and $a = 5.07(1)$ Å, $b = 8.77(1)$ Å [8.78(8) Å determined from pole figure data] and $c = 9.428(6)$ Å for the SAFO//Mica(001) film. Within the error bars we can assume that the 60 nm thick films are relaxed. The small differences of the determined lattice parameters might be due to different thermal expansion coefficients of the substrates.
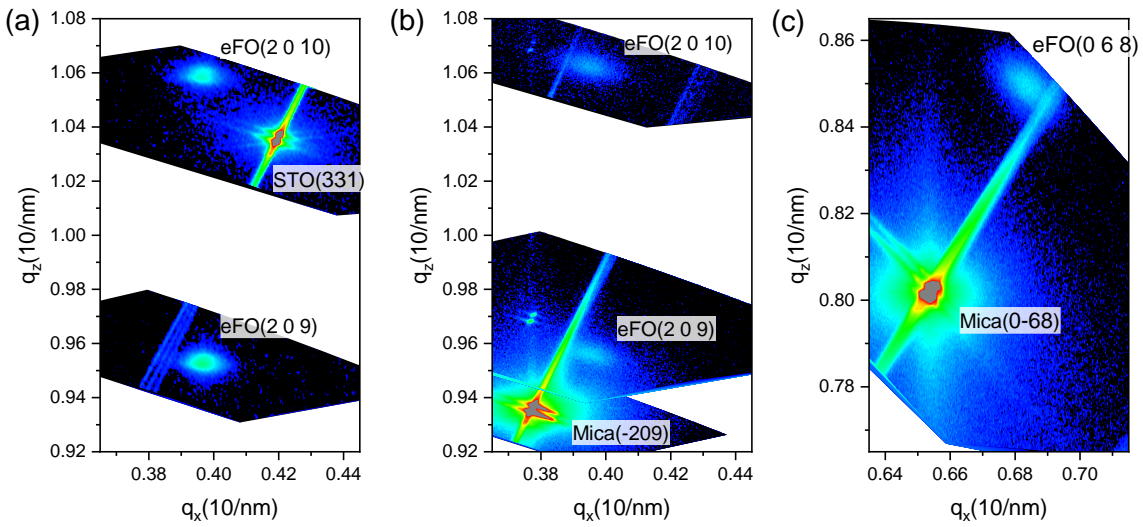
Figure 5.5 XRD reciprocal space maps for the SAFO thin films grown on (a) STO (111) and (b, c) Mica (001) substrates.

The in-plane textures of the SAFO films on (001)-oriented cubic YSZ and GGG substrates were also investigated, and the results are presented in Figure 5.6(a) and (b), respectively. In agreement with the literature (see, for example, reference [11]), twelve {013} poles at a 30° interval can be seen in Figure 5.6(a), indicating six principal ε-SAFO (001) domains (see Figure 5.6(d)). In addition, for the ε-SAFO//GGG(001) film, the {013} reflections are barely distinguishable from the strong diffuse background intensity, but one can appreciate twelve {013} peaks from both the pole figure and the deduced in-plane XRD phi(ϕ)-scan (see Figure 5.6(b)). It is unclear so far why the growth of ε-SAFO film on GGG (001) is of such a poor quality. However, our preliminary results on an ε-Fe$_2$O$_3$(001)/AFO(001)//GGG(001) epitaxial film (see Figure 5.6(c)) reveal better ε-Fe$_2$O$_3$(001) film quality in such AlFeO$_3$-buffered ε-Fe$_2$O$_3$(001) film, which suggests that the effect of epitaxial strain may play a role in stabilization of this polar phase on such substrate.
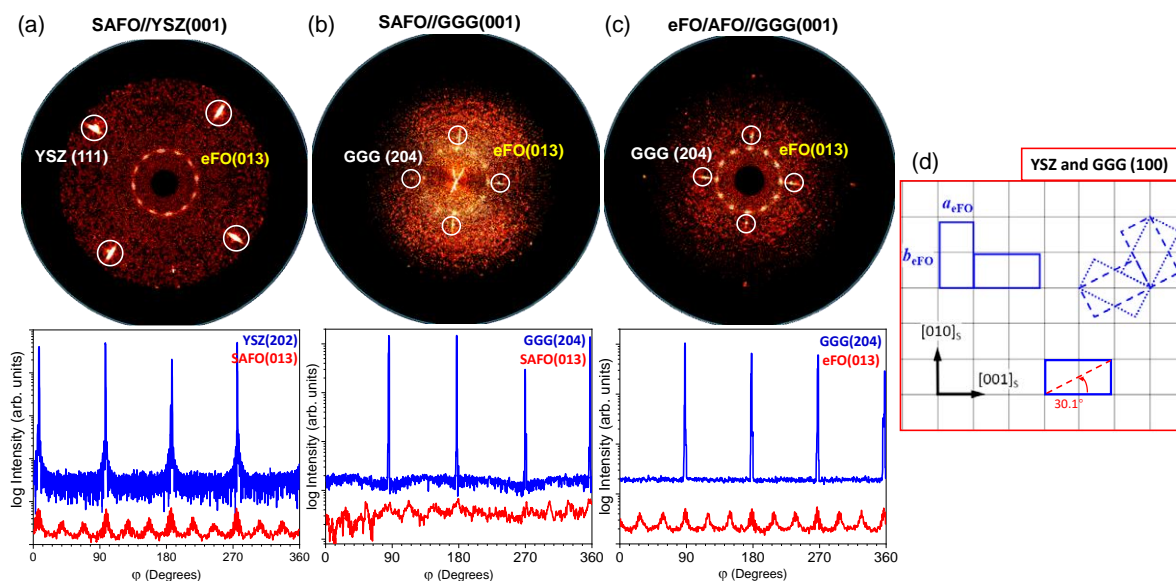
Figure 5.6 Pole figure scan around the ε-SAFO {013} and YSZ {111} and GGG {204} reflections for the (a) ε-SAFO(001)//YSZ(001), (b) ε-SAFO(001)//GGG(001) and (c) a 80-nm ε-Fe$_2$O$_3$(001)/AFO(001)//GGG(001) epitaxial films. The substrate peaks are marked by white circles. The twelve ε-SAFO {013} Bragg peaks forms the inner circle of the reflections. The deduced ϕ-scan patterns are shown in the corresponding lower panels. Note that different acquisition conditions and substrate contribution strongly contribute to a lower S/N ratio in (b). A schematic presentation of the domain orientation is shown in (d).

Nevertheless, as seen in Figure 5.6(b) and (c), both films on GGG show qualitatively similar behaviors. For instance, comparing the ϕ-scan patterns of [013] ε-SAFO with thoso of YSZ (202) and GGG (204) planes, an epitaxial relationship of [100]$_{eSAFO}$//[100]$_S$, [010]$_{eSAFO}$//[100]$_S$ and [110]$_{eSAFO}$//[100]$_S$ can be derived (the subscript S stands for the substrates YSZ or GGG), implying the same in-plane texture of the ε-SAFO films on these (001)-oriented cubic substrates. AFO has a significantly smaller lattice parameter than SAFO. Compared to the GGG substrate with very large lattice parameter (12.38A), considering m:n ratio of (5:2) [100]AFO:[100]GGG a low residual misfit of 0.6% is found, and -0.1% if one considers (5:4) [100]AFO:[100]GGG. For the *b* axis direction one obtains a misfit of 3.6% for (3:2) [010]AFO:[100]GGG. The same calculations considering SAFO lattice parameter results in about 3% for [100]SAFO and [110]SAFO and over 6% for [010]SAFO [100]GGG. Nevertheless, further studies are necessary to confirm the influence of the lattice parameters of the SAFO or AFO layers in the stabilization of ε-Fe$_2$O$_3$ film.

5.3.3 Surface morphology

The morphology of the SAFO thin films was investigated by AFM. Granular surfaces are appreciated in the topographic images (Figure 5.7(a-g)), revealing a 3D growth of the films. Note that the films identified to present a good ε-SAFO(001) epitaxial growth (on STO, LSAT, YSZ and MAO substrates) also show smooth surfaces with RMS roughnesses around 1 nm. In spite of having a smooth background, the presence of sporadic high 3D outgrowth (40 nm) is evident in the SAFO//Mica(001)

film (see Figure 5.7(e)). The low surface roughness at 60 nm thickness should allow the use of SAFO as a thin buffer layer for the stabilization of ε-Fe$_2$O$_3$, which is the desired functional layer. Increased roughness is observed for SAFO films on Al$_2$O$_3$ (~ 3 nm) and GGG (~ 6 nm).
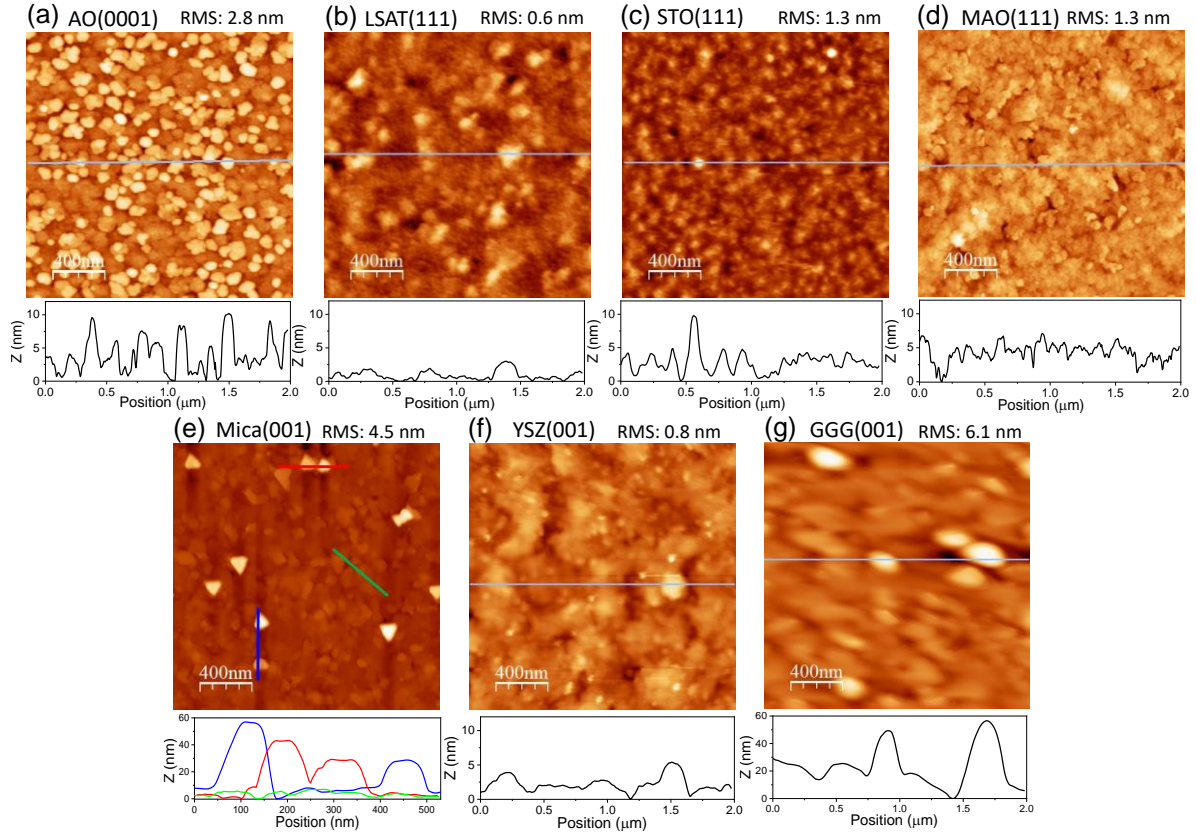
Figure 5.7 (a-g) AFM topographic images of 60 nm thick SAFO layers on a wide variety of substrates. Below each map a line profile is plotted. Note that the maximum height scale is 60 nm for the SAFO//Mica(001) and SAFO//GGG(001) films, and 12 nm for the other films. Sizes of the topographic images: 2×2 μm^2.

5.4 Summary

Epitaxial oxide thin film heterostructures with required characteristic properties are of particular interest for future innovative potential applications. This chapter describes the epitaxial integration of Sc and Al codoped ε-Fe$_2$O$_3$ (i.e., ε-Sc$_{0.2}$Al$_{0.4}$Fe$_{1.4}$O$_3$) thin films with different types of substrates using PLD technique. The effect of different substrates on the structural characteristics of the top SAFO layers was investigated primarily by X-ray based techniques.

For the SAFO//Al$_2$O$_3$(0001) film, only diffraction peaks associated with α-Fe$_2$O$_3$ phase are found, and the grown film exhibits a (0001) texture along the out-of-plane direction. On MAO (111), the ε-SAFO (00l) and the characteristic (013) side peaks appear with moderate intensity in the 2D diffraction. The pole figure results suggest a fraction of the film grows as (lll)-textured spinel phase. The SAFO thin film grown on cubic GGG (001) substrate, presents weak ε-SAFO diffraction peaks. Nevertheless, we can appreciate the twelve (013) poles in the pole figure measurement, analogous to the observation for cubic YSZ (001), indicating the presence of six in-plane domain invariants in these (001) cubic substrates. High-quality ε-SAFO (001) epitaxial films with a thickness of 60 nm have been deposited on LSAT (111), STO (111), Mica (001) and YSZ (001) substrates. They exhibit rather sharp rocking curves with the minimum FWHM as low as 0.11° for the ε-SAFO//YSZ(001) film. From the in-plane X-ray measurement, the existence of three principal ε-SAFO (001) domains is deduced for the films on the hexagonal symmetric substrates, LSAT (111), STO (111) and MAO (111). Moreover, due to its quasi-hexagonal lattice arrangement, a six-fold in-plane symmetry of mica enables the crystallization of ε-Fe$_2$O$_3$ phase in a cubic-on-cubic manner. The possibility to stabilize ε-SAFO films with relatively low roughness on various substrates makes it an appealing candidate buffer layer for the deposition of ε-Fe$_2$O$_3$ epitaxial heterostructures.

Chapter 5 Appendix A

This section is intended to clarify the origin of the intensity of substrate tails in the presented pole figures, in Section 5.3.2. Substrate tails can have diverse origins. Here in the used diffractometer a collimated beam is used and no monochromator or Ni filter are used. Thus, each substrate peak is enlarged by the specific wavelength profile of the copper source, with main lines Cu-K$_{\alpha1}$ (1.5406 Å), Cu-K$_{\alpha2}$ (1.544 Å) and Cu-K$_\beta$ (1.392 Å), but also W-L$_\alpha$ (1.476 Å) line (originated from deposition of the W-filament on the surface of copper source). This generates an elongation of the Bragg spots in 2θ direction. Now, for the integration of the raw data a 2θ-χ region is selected, as marked in Figure 5.A φ0, φ60 and φ120.
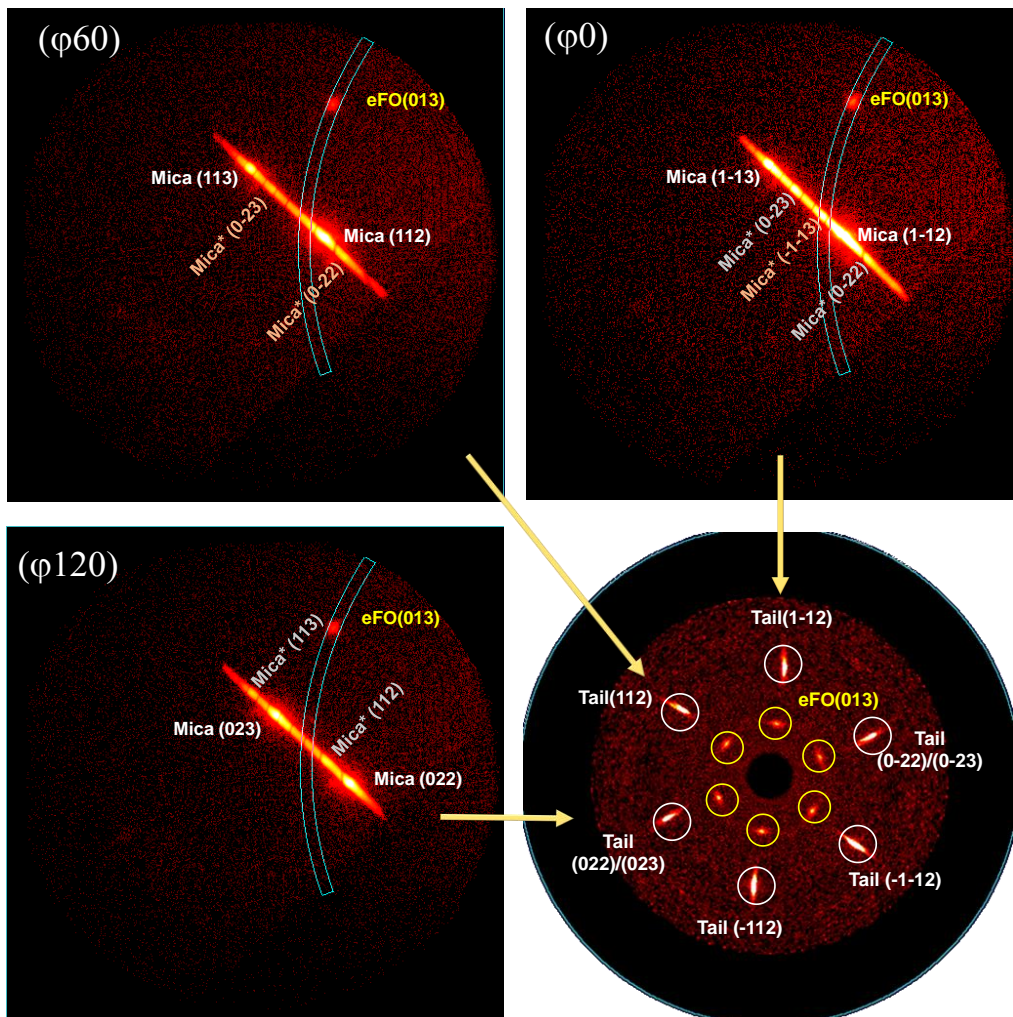
Figure 5.A XRD (013)SAFO pole figure measurement on Mica(001) substrate. $\omega2\theta$-χ integrated frames around specific φ positions. Labelled φ0, φ60 and φ120, respectively. The integrated region used to compute the pole figure (bottom right panel) is marked in a light blue box. Width corresponds to $2\theta = 1°$ around the desired (013) film peaks at $2\theta =30.1°$ (29.6-30.6°) and the height corresponds to the observable χ-range 85 to 23º, with the surface normal $\chi = 90º$.

The shown region corresponds to a 2θ width of 1° around the desired (013) film peaks at $2\theta=30.1$° (29.6-30.6°) and the height corresponds to the observable χ-range 85 to 23° (the sample tilt is 45° is in the detector centre). The integrated intensity is projected to the pole figure plane shown in Figure 5.A (bottom right panel). While the selected region focuses on the position of the film peaks (thickness around 60 nm) also other peaks (substrate, substrate tails or other film phases) may contribute to the intensity at different tilt angles. Mica substrates commonly are not as perfect as many commercial semiconductor or oxide substrates. In addition, the large out-of-plane parameter results in a large number of structurally allowed diffraction planes, as evidenced by ω-2θ scans for the (00l) planes (see e.g., Figure 5.1(a) or Chapter 7), as well as the here shown 2θ-χ regions of the pole figure. The example regions show that the integrated region is in close proximity to substrate reflections (labelled in white) and effectively a fraction of the substrate tails contribute to the pole figure intensity. Due to the monoclinic structure of Mica labelling of the peaks is more complex. Here, the main peaks are labelled white in the example frames (φ0, φ60 and φ120) and the corresponding substrate tails in the pole figure. The used synthetic Mica substrates clearly show features of twinned in-plane domains, corresponding peaks are labeled as Mica* (not shown in the pole figure itself). Nevertheless, the data indicates they are a minor fraction, and do not interfere with the global epitaxial relationship of film and substrate. Reference [38] indicates that up to six (60° rotated) in-plane domains can be possible.

Nevertheless, in most observed samples if not specified in the text the intensity of substrate positions is caused by the substrate tails protruding in the integrated 2θ range.

References

[1]   M. Gich, J. Gazquez, A. Roig, A. Crespi, J. Fontcuberta, J.C. Idrobo, S.J. Pennycook, M. Varela, V. Skumryev, Epitaxial stabilization of epsilon-Fe_2O_3 (00l) thin films on SrTiO3 (111), Appl. Phys. Lett. 96 (2010). https://doi.org/10.1063/1.3360217.

[2]   M. Gich, I. Fina, A. Morelli, F. Sánchez, M. Alexe, J. Gàzquez, J. Fontcuberta, A. Roig, Multiferroic Iron Oxide Thin Films at Room Temperature, Adv. Mater. 26 (2014) 4645–4652. https://doi.org/10.1002/adma.201400990.

[3]   L. Corbellini, C. Lacroix, C. Harnagea, A. Korinek, G.A. Botton, D. Ménard, A. Pignolet, Epitaxially stabilized thin films of ϵ-Fe_2O_3 (001) grown on YSZ (100), Sci. Rep. 7 (2017) 1–9. https://doi.org/10.1038/s41598-017-02742-9.

[4]   Y. Hamasaki, T. Shimizu, S. Yasui, T. Shiraishi, A. Akama, T. Kiguchi, T. Taniyama, M. Itoh, Crystal structure and magnetism in κ-Al_2O_3-type $Al_xFe_{2-x}O_3$ films on SrTiO3(111), J. Appl. Phys. 122 (2017) 15301. https://doi.org/10.1063/1.4990947.

[5]   J. Gázquez, G. Sánchez-Santolino, N. Biškup, M.A. Roldán, M. Cabero, S.J. Pennycook, M. Varela, Applications of STEM-EELS to complex oxides, Mater. Sci. Semicond. Process. 65 (2017) 49–63. https://doi.org/10.1016/j.mssp.2016.06.005.

[6]   Y. Ding, J.R. Morber, R.L. Snyder, Z.L. Wang, Nanowire structural evolution from Fe_3O_4 to epsilon-Fe_2O_3, Adv. Funct. Mater. 17 (2007) 1172–1178. https://doi.org/10.1002/adfm.200601024.

[7]   J.G. Li, G. Fornasieri, A. Bleuzen, M. Gich, A. Gloter, F. Bouquet, M. Impéror-Clerc, Alignment under Magnetic Field of Mixed Fe_2O_3/SiO_2 Colloidal Mesoporous Particles Induced by Shape Anisotropy, Small. 12 (2016) 5981–5988. https://doi.org/10.1002/smll.201602272.

[8]   V. Ukleev, M. Volkov, A. Korovin, T. Saerbeck, N. Sokolov, S. Suturin, Stabilization of ε−Fe_2O_3 epitaxial layer on MgO(111)/GaN via an intermediate γ-phase, Phys. Rev. Mater. 3 (2019). https://doi.org/10.1103/PhysRevMaterials.3.094401.

[9]   J. Gázquez, G. Sánchez-Santolino, N. Biškup, M.A. Roldán, M. Cabero, S.J. Pennycook, M. Varela, Applications of STEM-EELS to complex oxides, Mater. Sci. Semicond. Process. 65 (2017) 49–63. https://doi.org/10.1016/j.mssp.2016.06.005.

[10]   D.C. Kundaliya, S.B. Ogale, S. Dhar, K.F. McDonald, E. Knoesel, T. Osedach, S.E. Lofland, S.R. Shinde, T. Venkatesan, Large second-harmonic kerr rotation in GaFeO3 thin films on YSZ buffered silicon, J. Magn. Magn. Mater. 299 (2006) 307–311. https://doi.org/10.1016/j.jmmm.2005.04.017.

[11]   M. Trassin, N. Viart, G. Versini, J.L. Loison, J.P. Vola, G. Schmerber, O. Cŕgut, S. Barre, G. Pourroy, J.H. Lee, W. Jo, C. Ḿny, Epitaxial thin films of multiferroic $GaFeO_3$ on conducting indium tin oxide (001) buffered yttrium-stabilized zirconia (001) by pulsed laser deposition, Appl. Phys. Lett. 91 (2007) 2–5. https://doi.org/10.1063/1.2813020.

[12]   M. Trassin, N. Viart, G. Versini, S. Barre, G. Pourroy, J. Lee, W. Jo, K. Dumesnil, C. Dufour, S. Robert, Room temperature ferrimagnetic thin films of the magnetoelectric $Ga_{2-x}Fe_xO_3$, J. Mater. Chem. 19 (2009) 8876–8880. https://doi.org/10.1039/b913359c.

[13]   Z.H. Sun, Y.L. Zhou, S.Y. Dai, L.Z. Cao, Z.H. Chen, Preparation and properties of $GaFeO_3$ thin films grown at various oxygen pressures by pulsed laser deposition, Appl. Phys. A. 91 (2007) 97–100. https://doi.org/10.1007/s00339-007-4364-3.

[14]   Z.H. Sun, S. Dai, Y.L. Zhou, L.Z. Cao, Z.H. Chen, Elaboration and optical properties of $GaFeO_3$ thin films, Thin Solid Films. 516 (2008) 7433–7436. https://doi.org/10.1016/j.tsf.2008.02.054.

[15]   Y. Hamasaki, T. Shimizu, H. Taniguchi, T. Taniyama, S. Yasui, M. Itoh, Epitaxial growth of metastable multiferroic $AlFeO_3$ film on SrTiO3 (111) substrate, Appl. Phys. Lett. 104 (2014) 82906. https://doi.org/doi:http://dx.doi.org/10.1063/1.4866798.

[16]   M. Kneiß, A. Hassa, D. Splith, C. Sturm, H. Von Wenckstern, T. Schultz, N. Koch, M. Lorenz, M. Grundmann, Tin-assisted heteroepitaxial PLD-growth of κ-Ga_2O_3 thin films with high crystalline quality,

APL Mater. 7 (2019). https://doi.org/10.1063/1.5054378.

[17]   S. Homkar, D. Preziosi, X. Devaux, C. Bouillet, J. Nordlander, M. Trassin, F. Roulland, C. Lefèvre, G. Versini, S. Barre, C. Leuvrey, M. Lenertz, M. Fiebig, G. Pourroy, N. Viart, Ultrathin regime growth of atomically flat multiferroic gallium ferrite films with perpendicular magnetic anisotropy, Phys. Rev. Mater. 3 (2019) 1–10. https://doi.org/10.1103/PhysRevMaterials.3.124416.

[18]   T. Katayama, S. Yasui, Y. Hamasaki, T. Osakabe, M. Itoh, Chemical tuning of roomerature ferrimagnetism and ferroelectricity in ϵ-Fe$_2$O$_3$-type multiferroic oxide thin films, J. Mater. Chem. C. 5 (2017) 12597–12601. https://doi.org/10.1039/c7tc04363e.

[19]   J. Majzlan, A. Navrotsky, B.J. Evans, Thermodynamics and crystal chemistry of the hematite-corundum solid solution and the FeAlO$_3$ phase, Phys. Chem. Miner. 29 (2002) 515–526. https://doi.org/10.1007/s00269-002-0261-7.

[20]   X. Guan, L. Yao, K.Z. Rushchanskii, S. Inkinen, R. Yu, M. Ležaí, F. Sánchez, M. Gich, S. van Dijken, Unconventional Ferroelectric Switching via Local Domain Wall Motion in Multiferroic ϵ-Fe$_2$O$_3$ Films, Adv. Electron. Mater. (2020). https://doi.org/10.1002/aelm.201901134.

[21]   J. Yuan, A. Balk, H. Guo, Q. Fang, S. Patel, X. Zhao, T. Terlier, D. Natelson, S. Crooker, J. Lou, Room-Temperature Magnetic Order in Air-Stable Ultrathin Iron Oxide, Nano Lett. 19 (2019) 3777–3781. https://doi.org/10.1021/acs.nanolett.9b00905.

[22]   Y. Hamasaki, T. Shimizu, S. Yasui, T. Taniyama, M. Itoh, Evidence of ferroelectricity in ferrimagnetic κ-Al$_2$O$_3$-type In$_{0.25}$Fe$_{1.75}$O$_3$ films, Appl. Phys. Lett. 109 (2016) 162901. https://doi.org/10.1063/1.4964826.

[23]   T. Katayama, S. Yasui, Y. Hamasaki, M. Itoh, Control of crystal-domain orientation in multiferroic Ga0.6Fe1.4O3 epitaxial thin films, Appl. Phys. Lett. 110 (2017) 212905. https://doi.org/10.1063/1.4984211.

[24]   T.M.N. Thai, H.J. Kim, Synthesis of epitaxial GaFeO$_3$ thin films on various substrates, New Phys. Sae Mulli. 65 (2015) 230–233. https://doi.org/10.3938/NPSM.65.230.

[25]   Y. Hamasaki, T. Shimizu, S. Yasui, T. Taniyama, O. Sakata, M. Itoh, Crystal Isomers of ScFeO$_3$, Cryst. Growth Des. 16 (2016) 5214–5222. https://doi.org/10.1021/acs.cgd.6b00770.

[26]   A. Hassa, H. Von Wenckstern, D. Splith, C. Sturm, M. Kneiß, V. Prozheeva, M. Grundmann, Structural, optical, and electrical properties of orthorhombic κ -(In$_x$Ga$_{1-x}$)$_2$O$_3$ thin films, APL Mater. 7 (2019). https://doi.org/10.1063/1.5054394.

[27]   I. Cora, F. Mezzadri, F. Boschi, M. Bosi, M. Čaplovičová, G. Calestani, I. Dódony, B. Pécz, R. Fornari, The real structure of ϵ-Ga$_2$O$_3$ and its relation to κ-phase, CrystEngComm. 19 (2017) 1509–1516. https://doi.org/10.1039/c7ce00123a.

[28]   S.C. Abrahams, J.M. Reddy, J.L. Bernstein, Crystal structure of piezoelectric ferromagnetic gallium iron oxide, J. Chem. Phys. 42 (1965) 3957–3968. https://doi.org/10.1063/1.1695868.

[29]   S.I. Ohkoshi, S. Kuroki, S. Sakurai, K. Matsumoto, K. Sato, S. Sasaki, A millimeter-wave absorber based on gallium-substituted ϵ-iron oxide nanomagnets, Angew. Chemie - Int. Ed. 46 (2007) 8392–8395. https://doi.org/10.1002/anie.200703010.

[30]   H.N. Lee, S. Senz, N.D. Zakharov, C. Harnagea, A. Pignolet, D. Hesse, U. Gösele, Growth and characterization of non-c-oriented epitaxial ferroelectric SrBi$_2$Ta$_2$O$_9$ films on buffered Si(100), Appl. Phys. Lett. 77 (2000) 3260–3262. https://doi.org/10.1063/1.1324982.

[31]   Q.X. Jia, S.G. Song, X.D. Wu, J.H. Cho, S.R. Foltyn, A.T. Findikoglu, J.L. Smith, Epitaxial growth of highly conductive RuO$_2$ thin films on (100) Si, Appl. Phys. Lett. 68 (1996) 1069–1071. https://doi.org/10.1063/1.115715.

[32]   S. Jun, Y.S. Kim, J. Lee, Y.W. Kim, Dielectric properties of strained (Ba, Sr)TiO$_3$ thin films epitaxially grown on Si with thin yttria-stabilized zirconia buffer layer, Appl. Phys. Lett. 78 (2001) 2542–2544. https://doi.org/10.1063/1.1367309.

[33]   B. Bhoi, B. Kim, Y. Kim, M.K. Kim, J.H. Lee, S.K. Kim, Stress-induced magnetic properties of PLD-

grown high-quality ultrathin YIG films, J. Appl. Phys. 123 (2018) 203902. https://doi.org/10.1063/1.5031198.

[34]   S. Shastry, G. Srinivasan, M.I. Bichurin, V.M. Petrov, A.S. Tatarenko, Microwave magnetoelectric effects in single crystal bilayers of yttrium iron garnet and lead magnesium niobate-lead titanate, (n.d.). https://doi.org/10.1103/PhysRevB.70.064416.

[35]   A. Kehlberger, K. Richter, M.C. Onbasli, G. Jakob, D.H. Kim, T. Goto, C.A. Ross, G. Götz, G. Reiss, T. Kuschel, M. Kläui, Enhanced magneto-optic Kerr effect and magnetic properties of $CeY_2Fe_5O_{12}$ epitaxial thin films, Phys. Rev. Appl. 4 (2015) 014008. https://doi.org/10.1103/PhysRevApplied.4.014008.

[36]   J.B. Nelson, D.P. Riley, An experimental investigation of extrapolation methods in the derivation of accurate unit-cell dimensions of crystals, Proc. Phys. Soc. 57 (1945) 160–177. https://doi.org/10.1088/0959-5309/57/3/302.

[37]   L. Yan, Y. Wang, J. Li, A. Pyatakov, D. Viehland, Nanogrowth twins and abnormal magnetic behavior in $CoFe_2O_4$ epitaxial thin films, J. Appl. Phys. 104 (2008) 123910. https://doi.org/10.1063/1.3033371.

[38]   S.R. Zhao, C. Xu, C. Li, Identification of twins in muscovite: An electron backscattered diffraction study, Zeitschrift Fur Krist. - Cryst. Mater. 234 (2019) 329–340. https://doi.org/10.1515/zkri-2018-2139.

Chapter 6

Epitaxial ε-Fe₂O₃ Thin Films on MgAl₂O₄ Spinel

This chapter is focused on the stabilization of epitaxial ε-Fe_2O_3 (eFO) thin films on spinel $MgAl_2O_4$ (MAO) and Fe_3O_4 (FO) buffered heterostructures. In particular we study "eFO//MAO(111)" single layers and Fe_3O_4 buffered "eFO/FO//MAO(111)" heterostructures. We also present a detailed Raman spectroscopy study of the different types of films which can shed more light into the magnetic transitions of ε-Fe_2O_3 above and below room temperature.

6.1 Introduction

The epitaxial growth of metastable ε-Fe$_2$O$_3$ (eFO) thin films was first demonstrated by our group's previous effort by PLD using STO (111) as a substrate [1]. Interestingly, as mentioned in the introduction to Part II, a thin γ-Fe$_2$O$_3$ or Fe$_3$O$_4$ interfacial layer has been observed. The TEM image of Figure II.1(a), shows an atomic resolution Z-contrast STEM image displaying an approximately 7-nm thick magnetite (Fe$_3$O$_4$) interfacial layer located in-between the ε-Fe$_2$O$_3$ film and the STO substrate. Similar findings have been commented by other authors [2].

Also, in the previous chapter SAFO has been partially stabilized on MAO(111) substrates although with a considerable spinel fraction. Within the scope of this chapter we describe the direct growth of eFO on MAO(111) substrates and on Fe$_3$O$_4$ (111) introduced as template layer on MAO(111). The interest of Fe$_3$O$_4$ (111) to promote epitaxial growth of ε-Fe$_2$O$_3$ films is, on the one hand, because it may show a better structural compatibility with eFO (the misfit of -0.9 % and -1.3 % along the a and b axes of eFO, respectively, compare favorably with MAO, see Figure 5.4(e)), and secondly because being a half-metallic oxide it may serve as electrode, too. Fe$_3$O$_4$ is characterized by an inverse-spinel cubic structure (S. G.: *Fd-3m*) and is a well-known half-metal with an MIT transition at ~120 K, known as the Verwey transition. Fe$_3$O$_4$ has been recognized as a promising candidate for spintronic devices due to its high Curie temperature (~ 860 K) and large spin polarization (near 100 % at the Fermi level) [3],[4],[5].

Furthermore, the fact that the implementation of a Fe$_3$O$_4$ buffer could facilitate the stabilization of ε-Fe$_2$O$_3$ films is also appealing because Fe$_3$O$_4$ has already been stabilized on a broad range of suitable substrates or heterostructures, such as semiconductors Si (111) [6], (0001)-oriented sapphire [7], MgO (111) [8] and MgAl$_2$O$_4$ (111) [9]. The latter has the same crystal structure (cubic *Fd-3m* space group) with small lattice mismatch to magnetite ~ 4.0 % (a_{MAO}= 8.08 Å and a_{Fe3O4}= 8.40 Å).

In the following, we show that high quality of ε-Fe$_2$O$_3$ (001) epitaxial films can be grown on half-metallic Fe$_3$O$_4$ (111) and MAO (111) spinels by carefully adjusting the deposition parameters. The epitaxial relations and the impact of the growth condition on the structural properties of the epitaxial films will be discussed in the light of X-ray diffraction and transmission electron microscopy studies. Then Raman spectroscopy measurements will be presented both for ε-Fe$_2$O$_3$ (001) epitaxial films grown Fe$_3$O$_4$ (111)-buffered MAO (111) or directly on MAO (111). For the latter, the magnetic characterization of the films will be also presented.

6.2 Growth and structural characterization of epitaxial ε-Fe₂O₃ thin films on spinel

6.2.1 Growth conditions of the different epitaxial ε-Fe₂O₃ thin films on spinel

In the work described in Chapter 5, we found a suitable growth conditions for eFO: T_S = 825 ºC, P_{O2} = 0.1 mbar for a laser repetition rate of 5 Hz, a laser fluence of 2 J/cm2 and target substrate distance of 47 mm. First, we investigated the influence of the substrate temperature from 750 to 850 ºC on the stabilization of eFO phase, maintaining the other parameters constant. As optimal T_s we find 825 ºC (see Section 6.2.2). Then we grow eFO films *in situ* on top of Fe₃O₄ layers at this optimized temperature.
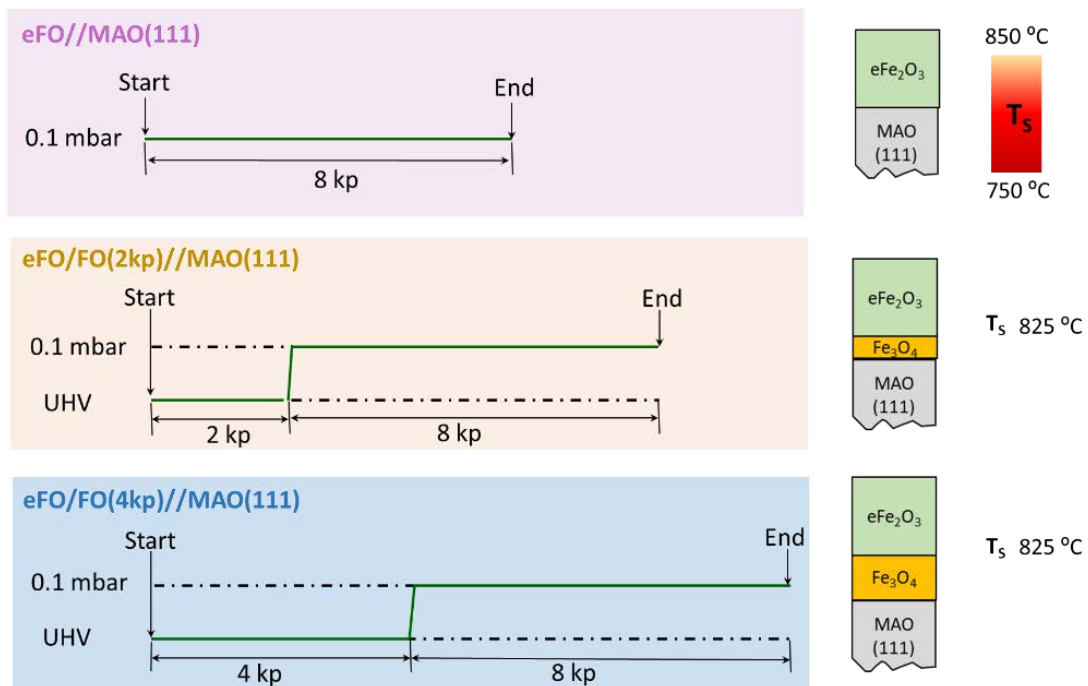
Figure 6.1 The evolution of oxygen partial pressure P_{O2} (mbar) and laser kilopulses (kp) during the PLD processes for the ε-Fe₂O₃ films on Fe₃O₄-buffered spinel MAO (111) substrates. While the dashed lines reflect the oxygen partial pressure, the solid green lines represent the pressure modification during the growth stage. The downward arrows denote the start and end of film depositions. The numbers of pulses are also indicated for the examined films. See the main text for the meaning of the nomenclature of the films. Abbreviation: UHV, ultra-high vacuum (the order of 10^{-6} mbar here). The explored substrate temperature range is shown as label on the right.

To achieve optimal physical properties, Fe₃O₄ has to be prepared in high vacuum condition ($P_{HV} \sim 10^{-6}$ mbar). Although our eFO growth temperature (825 ºC) is high compared to the growth of atomically flat spinel thin films optimal at around 500 ºC [10], using the same T_S for both layers was not detrimental and avoided the slow heating step for the constituent layers. Thus, only by quickly increasing the oxygen pressure from high vacuum to 0.1 mbar after the growth of the Fe₃O₄ layer (15 and 30 nm thickness) we aim to change the growth conditions favoring the stabilization of the eFO phase. The different

epilayers are schematically illustrated in Figure 6.1. For simplicity, in the following discussion these three distinct samples are referred to as "eFO/FO(4kp)//MAO(111)", "eFO/FO(2kp)//MAO(111)" and "eFO//MAO(111)", where "FO" represents Fe_3O_4 buffer layer and the brackets indicate the corresponding number of pluses. The increase of the deposition pressure from high vacuum to 0.1 mbar is stabilized within 1 min (for this period the laser ablation was continued and consequently the transition corresponds to about 300 laser pulses). Finally, the films were cooled to room temperature under the same oxygen pressure. For eFO//MAO(111) films, the oxygen pressure was fixed at 0.1 mbar from the start of the deposition.

6.2.2 Structural characterization by X-ray diffraction

First, we describe the influence of the substrate temperature on the stabilization of the eFO phase directly grown on MAO. In Figure 6.2(a) the corresponding $\omega 2\theta$-χ frames (measured with beam along [11-2] direction are shown for the substrate temperatures in the 750-850 ºC range. For T_S below 800 ºC only the peak corresponding to α-Fe₂O₃(006) (aFO) is distinguishable next to the MAO(222) substrate peak. No other phases are identified within the experimental resolution. Above 800ºC (013) satellite peaks are observed, indicating the stabilization of eFO(00l) phase, with no presence of α-Fe₂O₃(006) or FO (222) peaks. Note that the eFO(004) peak (2θ= 38.1º) is in close proximity of the broad and high intensity (222) substrate peak, and thus is barely distinguishable. Therefore, we measured the sample grown at 825 ºC with ω-2θ in HRXRD, shown in Figure 6.2(b), only eFO(00l) and MAO(lll) reflections are observed. The (004) rocking curve in the figure inset has a narrow FWHM of 1.06º and no spinel nor aFO(006) reflections are observed in the amplified region around the (222) substrate peak. To complete the basic structural analysis, we carried out pole figure measurements. There are six {013} reflections of the ε-Fe₂O₃ layer, which are 30° separated from the closest {220} reflections of MAO. Moreover, since the projections of ε-Fe₂O₃ [013] and MAO [220] on the ε-Fe₂O₃ (001) film and MAO (111) substrate planes are parallel to ε-Fe₂O₃ [010] and MAO [11-2] directions, an epitaxial relationship of 3 possible domain variants D₁, D₂ and D₃ is expected, with [100]$_{eFO}$ ∥ [1-21]$_{MAO}$, [100]$_{eFO}$ ∥ [-211]$_{MAO}$ and [100]$_{eFO}$ ∥ [11-2]$_{MAO}$, respectively. This is also in line with the STEM observations (see Section 6.2.3). Considering these results, we select 825 ºC as optimal growth temperature for the direct stabilization of eFO phase on MAO(111) substrates.
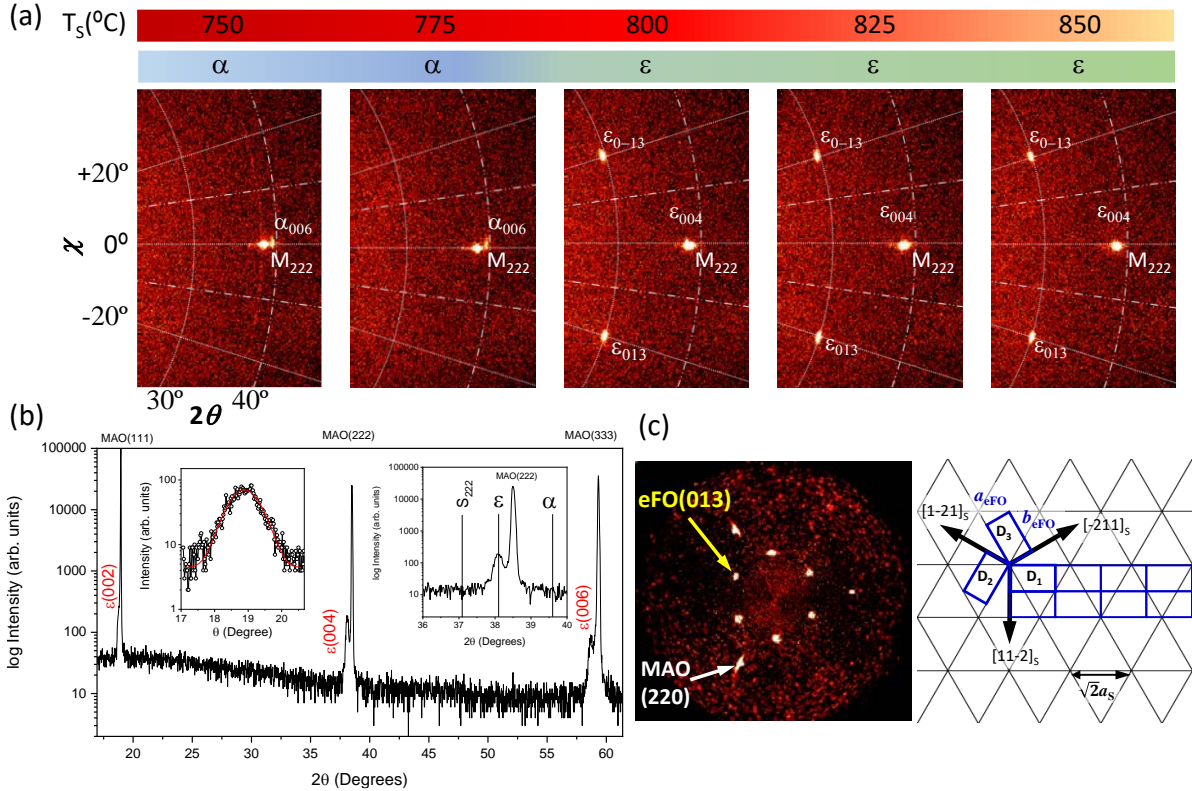
Figure 6.2 (a) XRD $\omega 2\theta$-χ frames for eFO films directly grown on MAO(111) substrates observation direction [11-2] for the indicated temperature range. Dominant Fe$_2$O$_3$ phase is indicated by α and ϵ for the alpha and epsilon phases, respectively. The overlayed grid is a guide to the eye. (b) ω-2θ HRXRD scan (with monochromator) for sample grown at 825 ºC. Left inset shows rocking curve around eFO(004) and right inset the amplified ω-2θ region around the eFO(004) peak. Vertical lines mark bulk single phase positions. (c) XRD eFO (013) pole figure for the same sample as in (b) and corresponding sketch of the epitaxial relationship.

For the implementation of the Fe$_3$O$_4$ interlayer and the stabilization of eFO thin films using Fe$_3$O$_4$/MAO as a model system, the growth temperature of eFO was fixed at 825 ºC. As shown in Figure 6.1 we vary the template layer thickness from 0 to 30 nm (0, 2k and 4k laser pulses). Usually, XRD $\omega 2\theta$-χ frames along the surface normal (χ= 90º) allow an easy assessment of the present phases. Nevertheless, we found that the broad MAO substrate peak $2\theta_{MAO222}$= 38.5º (with additional diffraction spots belonging to W-L$_\alpha$ ($2\theta_{WL-MAO222}$ = 36.8º) and Cu-K_β lines ($2\theta_{CuK\beta-MAO222}$ = 34.7º, see Figure 6.4(a)) hampers the clear identification of FO(222) ($2\theta_{FO222}$= 37.1º) and eFO(004) reflections ($2\theta_{eFO004}$= 38.1º). To overcome this, we measured $\omega 2\theta$-χ frames with the sample normal tilted to χ = 45° with respect a [1-10] substrate direction (beam is along a [11-2]direction). Figure 6.3(a-c) shows the resulting $\omega 2\theta$-χ frames for the eFO//MAO(111), eFO/FO(2kp)//MAO(111) and eFO/FO(4kp)//MAO(111) films, respectively. The eFO film (013) and (113) peaks are labeled in yellow (those corresponding to MAO in white) and an amplified region near the MAO (311) peak at 2θ= 36.8° (marked by the squared box) is presented in the bottom right of each panel. Close to the substrate peak at slightly lower 2θ position (~36°) a broad peak is observed and associated with the Fe$_3$O$_4$ (311). Integrating the intensity profile

(with integration region of 2θ: 31 to 42° and χ_{Frame}: -71.4 to -79.4°) a gradual increase of the magnetite (311) intensity manifests and can be correlated to the increasing thickness of the FO template layer. Within the resolution of the experiment nearly no FO layer is formed for directly grown eFO//MAO sample. The presence of eFO(013) and (113) peaks in the same frame indicate that the epitaxial relationship in the three samples is maintained and this was confirmed by (013) pole figures (not shown) where six eFO(013) poles are present for all the investigated layers. It is noteworthy that for the sample with the thickest FO(30 nm) layer, we observe in addition to the mentioned spinel and epsilon peaks, the clear presence of aFO(104) (see Figure 6.3(c)), i.e., the strongest reflection from aFO phase. The position of the peak suggests a (00l) texture for the aFO fraction. Nevertheless, only a vague intensity might also indicate the presence of the corresponding aFO(006) peak in the $\omega 2\theta$-χ frame in Figure 6.4(a). This may indicate a limitation for the template layer thickness.
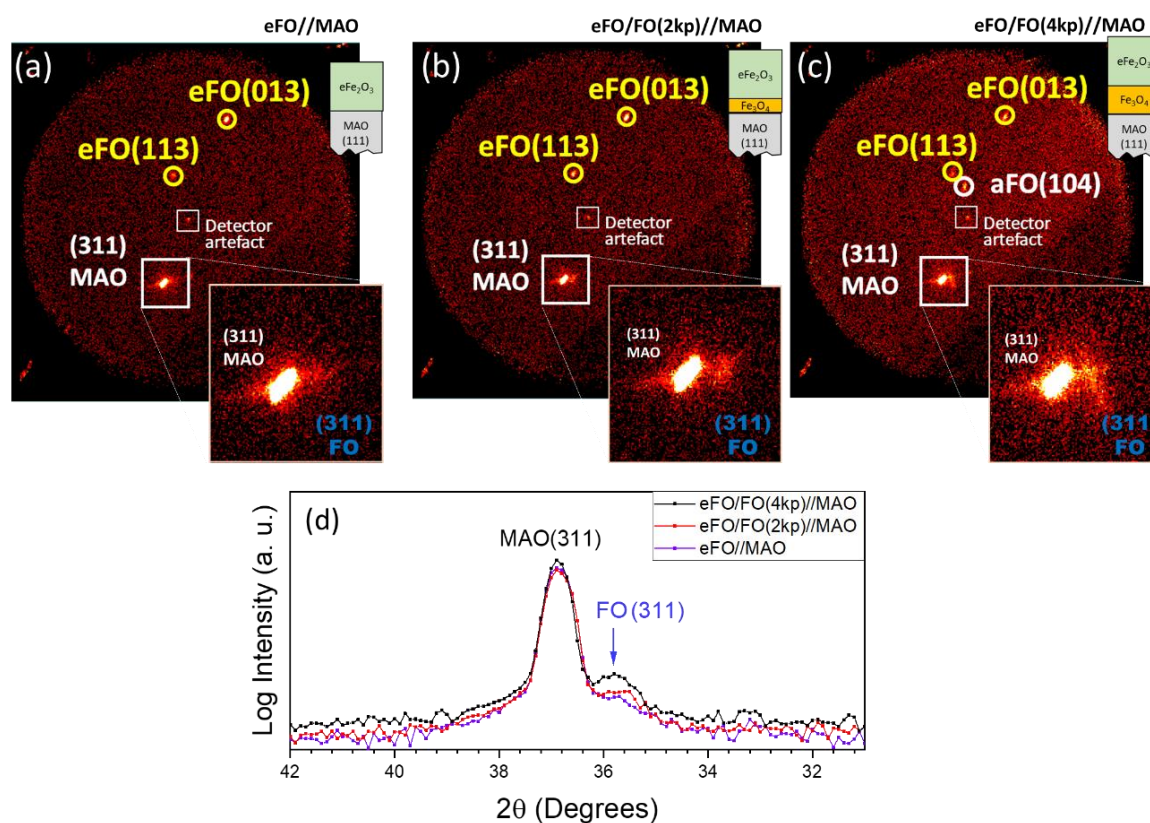
Figure 6.3 $\omega 2\theta$-χ XRD frames taken at tilting angle χ = 45° for the (a) eFO//MAO(111), (b) eFO/FO(2kp)//MAO(111) and (c) eFO/FO(4kp)//MAO(111) heterostructures. The ε-Fe₂O₃ diffraction peaks are highlighted by the closed yellow circles. The small white squares in the center marks a detector artefact. A zoomed region near the MAO (311) spot is amplified on the right bottom of each frame. (d) Integrated intensity profile across (311) reflection, showing the MAO and FO contributions of the samples. The integrations frame region is 2θ: 31-42° and χ_{Frame}: -71.4 to -79.4°.

6.2.3 Structural characterization by transmission electron microscopy

Two of the previously described samples (eFO/FO(4kp)//MAO(111) and eFO//MAO(111)) were studied in more detail by high-resolution TEM (HRTEM) of cross-sections obtained from the films. First, we show the details of the observation of the eFO/FO(4kp)//MAO(111) sample. Figure 6.4(b) represents a cross-sectional TEM image with low magnification showing the 55-nm ε-Fe$_2$O$_3$ film grown on top of a (30 nm) Fe$_3$O$_4$ buffered MAO (111) substrate. The HRTEM image in Figure 6.4(c) indicates the presence of multiple in-plane domains for the ε-Fe$_2$O$_3$ film. The corresponding Fourier transformation results (see the rightmost panel of Figure 6.4(c)) suggest the ε-Fe$_2$O$_3$ in-plane domains have the zone axes of [110] and [100], whereas the Fe$_3$O$_4$ layer has a [11-2] zone axis. This gives the following in-plane relationship for the epilayers: [100]$_{eFO}$ ∥ [11-2]$_{FO}$ and [110]$_{eFO}$ ∥ [11-2]$_{FO}$.
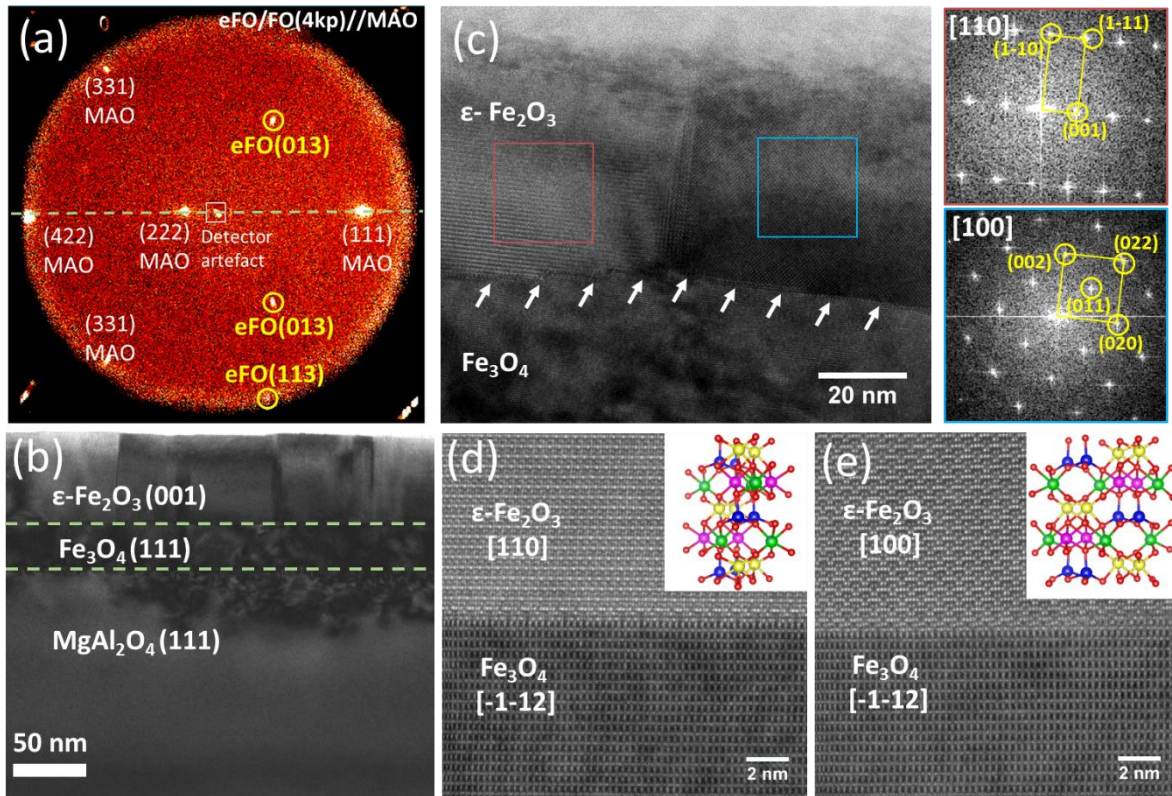
Figure 6.4 (a) 2D XRD patterns obtained with a GADDS detector for the eFO/FO(4kp)//MAO(111) films. For clarity, the light green dashed line refers to the position of χ = 90° for the employed geometry. Closed circles mark the ε-Fe$_2$O$_3$ film XRD peaks. The white spot marked by the white square symbol in the center is from the detector artefact (bad pixels of the detector). (b) Low and (c) High-resolution TEM images from a cross-section of the heterostructure. White arrows indicate the eFO-FO interface. The rightmost panel depicts the Fourier transformation from the areas in the HRTEM image indicated by the red and blue squares. (d-e) depict the high-resolution HAADF-STEM images showing the different in-plane domains and the sharp film-buffer interface where the structure of ε-Fe$_2$O$_3$ has been with the proper orientation has been introduced for reference.

Moreover, the interface between ε-Fe$_2$O$_3$ film and Fe$_3$O$_4$ interlayer (marked by the white arrows in Figure 6.4(c)) is sharp, as can be seen from the high-resolution HAADF images taken along the [110] and [100] ε-Fe$_2$O$_3$ zone axes and the [-1-12] Fe$_3$O$_4$ zone axis (Figure 6.4(d-e)). No defects such as misfit dislocations were observed from the film-buffer interface.

The TEM observations of the eFO//MAO(111) films cross sections are reported in Figures 6.5-6.7. According to the HAADF-STEM micrograph in Figure 6.5(a) and (d), the ε-Fe$_2$O$_3$ film has a very similar thickness of ~ 55 nm compared to the eFO/FO(4kp)//MAO(111) films. The selected-area electron diffraction (SAED) pattern shown in Figure 6.5(b) is indexed by considering the superposition of the diffraction spots along the [100] and [110] zone axes of ε-Fe$_2$O$_3$ film and those along the MAO [-1-12] zone axis. This confirms the epitaxial growth of the ε-Fe$_2$O$_3$ film with the polar axis out of plane and the in-plane relationships which are in agreement with the pole figure results as discussed in Section 6.2.2. Moreover, the splitting of the substrate and film diffraction spots, as indicated by white arrows and circles in Figure 6.5(b) implies that the is relaxed and not subject to epitaxial strain.
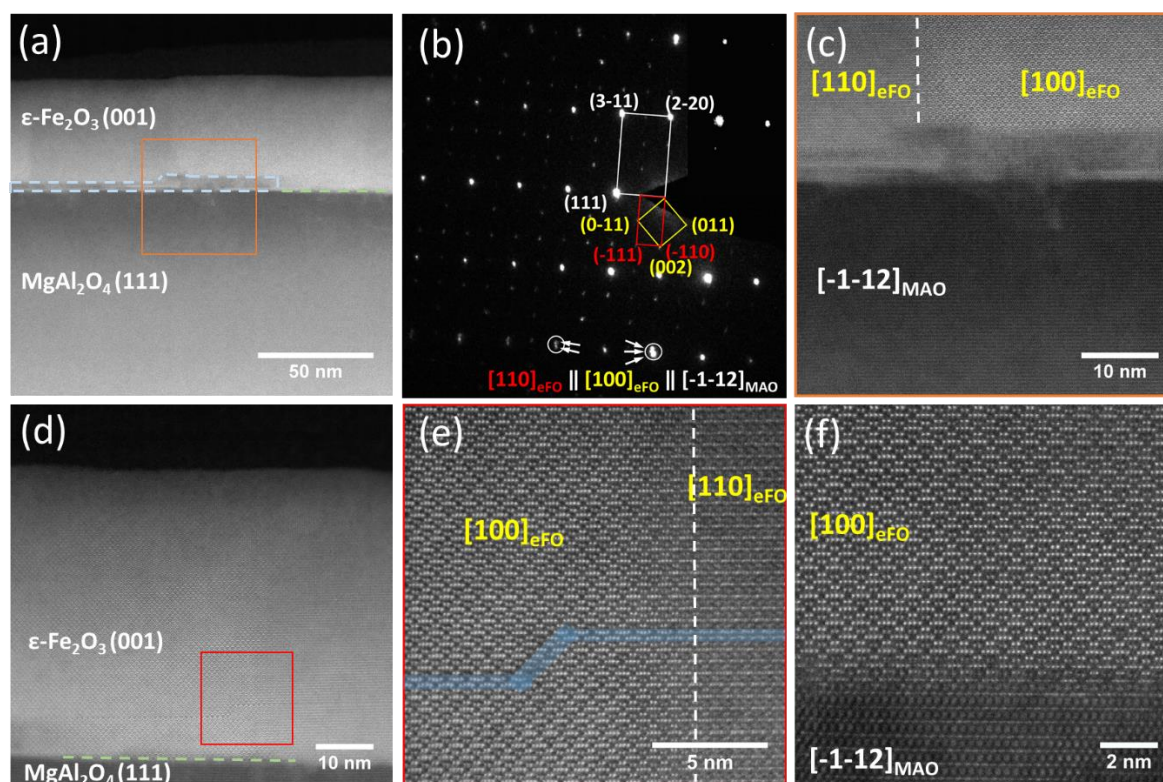
Figure 6.5 Cross-sectional STEM analysis of the eFO//MAO(111) film. Panels (a) and (d) show the low-resolution HAADF-STEM images, where different regions in the interface are evident. The delineated areas in Panels (a) and (d) are shown in Panels (c) and (e), respectively. (b) The SAED pattern of the eFO//MAO(111) taken along the [100] and [110] zone axes of ε-Fe$_2$O$_3$ film and the MAO [-1-12] zone axis (represented by yellow, red, and white rectangle parallelograms, respectively). Panels (e) and (f) display atomic resolution images showing different in-plane domains as well as the stacking fault defect spreading from one domain throughout the boundary to the other.

However, here the ε-Fe$_2$O$_3$ -MAO interface is more complex and contains two distinct regions— the interface looks sharp in one region, while the other region is characterized by a thin intermediate layer of ~ 5 nm (see the light green and blue dashed lines in Figure 6.5(a), respectively). A closer look at the intermediate layer from the high-resolution Z-contrast image shown in Figure 6.5(c) indicates that the transition layer presents a spinel structure which appears with a different contrast than the region of the MAO substrate. The atomic-resolution HAADF-STEM images in Figure 6.5(e) and (f) illustrate the different domains viewed along both the [100] and [110] zone axes of ε-Fe$_2$O$_3$ film. Furthermore, as can be observed in Figure 6.5(e), a stacking fault defect in the film propagates across the domain boundary indicated by a vertical dashed line.

The absence of sharp interface between the MAO substrate and the ε-Fe$_2$O$_3$ film has also been observed in other zones (see Figure 6.6(a)) and also in those cases the spinel structure with a lighter contrast is protruding into the film. This is clearly seen from the high-resolution Z-contrast images in Panels (b) and (c). The former shows a clear discontinuity between the dimmer MAO substrate (containing Al and Mg atoms which with a significantly lower Z nuclear charges than Fe) with the characteristic spinel structure. In Panel (c) this characteristic spinel structure is also found in the film region with a contrast comparable to that of the ε-Fe$_2$O$_3$ structure, growing epitaxially on the MAO substrate. This clearly indicates the formation of an iron-rich spinel, which is not unexpected since both γ-Fe$_2$O$_3$ and Fe$_3$O$_4$ present this structure.
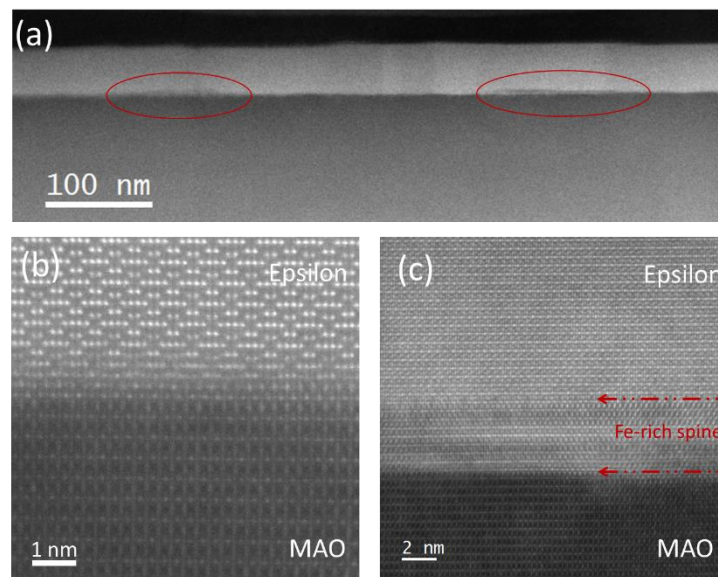
Figure 6.6 (a) Low magnification TEM image of the eFO//MAO(111) sample. The red ellipses show regions with spinel protruding into the film region. High-resolution Z-contrast images for the direct eFO on MAO in zones (b) without and (c) with a Fe-rich spinel structure localized at the interface, respectively. In (c) the arrows mark the position of the interface between the spinel interlayer and the eFO film or substrate, respectively.

In contrast one can think about why the spinel structure remains relatively marginal (i.e., not detected by X-ray diffraction) and does not favor the growth γ-Fe_2O_3 or Fe_3O_4. A more detailed analysis by electron energy loss spectroscopy (EELS) of a zone comprising this iron-rich spinel zone and the border MAO and ε-Fe_2O_3 areas (see Figure 6.7(a)) can give an answer. The elemental maps of Fe, Al and Mg indicate that the Fe-rich spinel area contains certain amounts of Al and specially Mg, while the Fe content is less than in the ε-Fe_2O_3 zone. The Fe L edge spectra of the Fe-rich spinel with that of the ε-Fe_2O_3, cannot be distinguished, which indicates that the iron atoms in the Fe-rich spinel and ε-Fe_2O_3 are quite similar. In particular, the intensity ratio between L_3 and L_2 of Fe L edge, depends on the Fe's oxidation state [11]. In this case, it implies that both the epsilon and the spinel contain Fe with the same oxidation state, this is, Fe ions are in form of Fe^{3+}, which could explain the relatively fewer presence of Al^{3+} compared to Mg^{2+}. It is interesting to note that the Fe map also reveals a diffusion of Fe into the MAO substrate. The fact that this occurs at specific points of the substrate surface could indicate that this is related to the presence of certain defects that make the interdiffusion of Fe into the substrate and Al^{3+}, Mg^{2+} into the film. We can now understand that the presence of spinel in the film is limited to the zone where Mg(Al, Fe)₂O₃ has been formed thanks to the diffusion of Al^{3+} and Mg^{2+}, and stops as soon as those elements are absent since film growth conditions of high temperature and oxygen pressure are respectively incompatible with the growth of γ-Fe_2O_3 and Fe_3O_4.
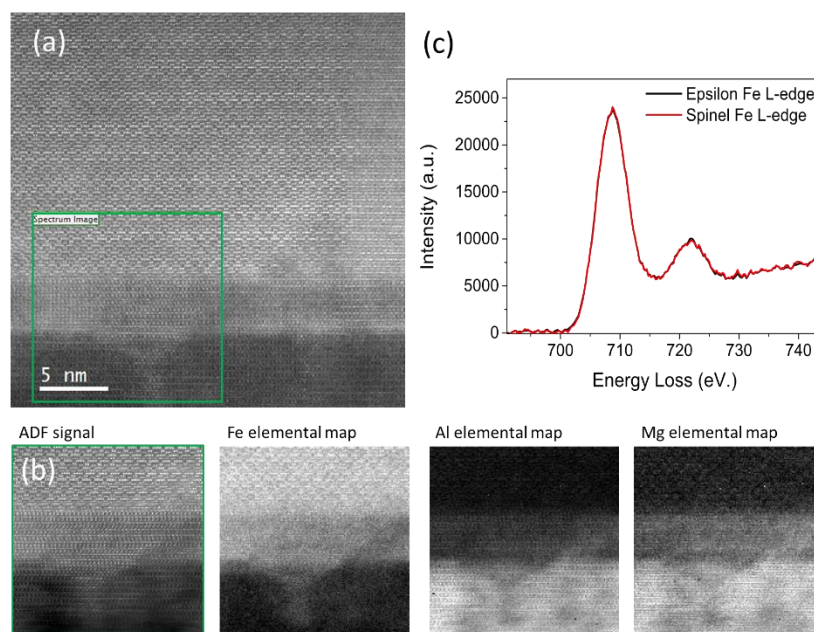
Figure 6.7 (a) High magnification TEM image of the the eFO/spinel//MAO interface of the eFO//MAO(111) sample. The green box in (a) shows the limits of a region selected for an element wise EELS map. The maps for the corresponding elements are labeled (b). (c) The EELS spectrum around the Fe L-edge comparing eFO and iron rich spinel interlayer.

In the light of the above results, let's focus again on the films with a spinel oxide layer deliberately introduced. There are in principle two reasons which can explain that it was possible to stabilize this layer. One is the relatively weak strain energy due to the well-matched symmetry and lattice between Fe_3O_4 and the MAO substrate, which is favorable to the formation of Fe_3O_4. On the other hand, under the very reducing conditions used in our PLD process, Fe_3O_4 is believed to be the thermodynamically stable phase in the Fe-O system. In the PLD experiments carried out by Takahashi et al. [12], it was shown that the Fe_3O_4 films could be stabilized by self-templating in the temperature range of 400-1100 °C and under a similar partial oxygen pressure $p(O_2) \sim 10^{-6}$ mbar. The observed interdiffusion of Fe^{3+}, Al^{3+} and Mg^{2+} between film and substrate in the eFO//MAO(111) film can also play a relevant role in stabilization of the spinel phase in eFO/FO(4kp)//MAO(111) film. Moreover, this casts reasonable doubts on our initial assumption that the layer grown at ultrahigh vacuum between MAO and the ε-Fe_2O_3 is Fe_3O_4. Since the growth of this layer is followed by another growth stage at higher $p(O_2)$ and at high temperature, Fe_3O_4 that has been eventually form could have been oxidized. Two indirect evidences seem to point to this possibility. On the one hand, our tests to try to see if the bottom layer is conducting electricity by contacting test probes to the opposite lateral sides of the films with the help of some silver paint were negative. Preliminary EELS measurements on the eFO/FO(4kp)//MAO(111) film which are not shown here indicated, even if with a relatively low signal to noise ratio, that the intensity ratio between L_3 and L_2 of Fe L edge is closer to that of Fe^{3+} than to Fe^{2+} [11,13].

In summary, in Section 6.2 we have presented the PLD growth of ε-Fe_2O_3 epitaxial thin films on spinel-type structures. By careful tuning of the growth parameters, the introduction of both ε-Fe_2O_3 and spinel iron oxide epilayers from a single target is possible and the thickness of the latter can be modified at will, but it is still not clear if it consists of Fe_3O_4, γ-Fe_2O_3 or a Fe rich spinel also containing Al^{3+} and Mg^{2+}. Interestingly, a ε-Fe_2O_3 epilayer can be deposited on MAO (111) directly. The 55-nm ε-Fe_2O_3 epitaxial films present a c-axis orientation along the out-of-plane direction and three types of in-plane domains rotated 120° to each other, which is typical for the epitaxial ε-Fe_2O_3 films grown cubic (111) perovskites with hexagonal in-plane symmetry. In the next Section 6.3 we present the results of a detailed Raman spectroscopy study of eFO/FO(4kp)//MAO(111) and eFO//MAO(111)films

.

6.3 Raman characterization of epitaxial ε-Fe₂O₃ films on MAO(111)

Dejoie et al. reported the first Raman spectra of ε-Fe_2O_3 (presumably with minor α-Fe_2O_3 impurities), which was considered as one of the indications of the existence of ε-Fe_2O_3 on the glaze surfaces of ancient Jian wares [14]. Later on, the vibrational modes of ε-Fe_2O_3 phase have been experimentally identified by López-Sánchez et al. [15]. Twenty-four active Raman modes and several modes related to

overtones or second order scattering processes are probed on the ε-Fe₂O₃ microparticles embedded in a SiO₂ matrix using confocal Raman microscopy (CRM) study. The assigned two-magnon excitation appears above the Néel temperature $T_{N2} \sim 480$ K, where the magnetostructural anomaly happens and which is also the onset temperature of the antiferromagnetic ordering between the regular octahedral and the tetrahedral Fe sublattices. Shortly, Mendili et al. used Raman spectroscopy to monitor the appearance of ε-Fe₂O₃ as an intermediate phase between the transition of γ-Fe₂O₃ nanocrystals to α-Fe₂O₃ [16]. In recent Yuan et al.'s work, Raman spectroscopy was also used as an effective tool for the phase identification of their ε-Fe₂O₃ nanoflakes [17]. However, neither of these works present systematic Raman spectroscopy studies of this intriguing Fe₂O₃ phase.

It is known that Raman spectroscopy can probe lattice excitations (i.e., phonons) and magnetic excitations (i.e., magnon) as well as their interactions. Raman spectroscopy study can thus give valuable information on their structures and spin dynamics on the one hand, and on the other hand, it could be of relevance to understand the coupling between the spin degree of freedom and phonons expected in magnetoelectric ε-Fe₂O₃ thin films. In addition, in the case of thin film property study, micro-Raman study has several advantages over diffraction methods such as its superb sensitivity to noncrystalline phases, its ability to detect low-concentration impurity phases and to monitor subtle structural changes that are generally missed by x-ray diffraction. Nevertheless, the Raman examination on epitaxial ε-Fe₂O₃ thin films has never, to our knowledge, been reported in the literature. Within this work, detailed micro-Raman characterizations of the ε-Fe₂O₃/spinel film system has been carried out thanks to the collaboration with Dr. J. López-Sánchez from Universidad Complutense de Madrid. We next present Raman micro-spectroscopy as a powerful tool for identifying the iron oxide phases and probing the phonon behavior in the ε-Fe₂O₃ epitaxial films.

6.3.1 Micro-Raman study of ε-Fe₂O₃/Fe₃O₄//MAO(111) heterostructure

The eFO/FO(4kp)//MAO(111) heterostructure was examined by CRM. A typical Raman spectrum of the ε-Fe₂O₃ epilayer is shown in Figure 6.8 (see the green line). For comparison, the spectra of ε-Fe₂O₃ microparticle and ε-Fe₂O₃ nanoparticle aggregates (with minor hematite impurities) both embedded in SiO₂ matrices are also presented (see the blue and red spectra, respectively) [18]. It can be seen that the Raman spectra of ε-Fe₂O₃ phase depend on the shape of the sample, as well as the size and orientation of the crystals. The micro- and nanoparticles represent polycrystalline samples and a shift of the spectrum towards lower frequencies and better-defined band peaks were observed as the particle size increases. The Raman spectrum of the film resembles that acquired from nanoparticles; nonetheless visible variations can be found below 400 cm⁻¹. In comparison to the red spectrum, where three characteristic ε-Fe₂O₃ Raman bands are visible in the yellow rectangular region in Figure 6.8, only two ε-Fe₂O₃ Raman bands are appreciated for the eFO thin film in this region. The differences also occur in the area marked with the orange rectangle, where there is only one Raman band for the eFO thin film

instead of two bands as observed in the blue spectrum. The extra bands are unlikely from the residual hematite in the particles considering the relatively narrow and sharp Raman bands; rather, this behavior could be attributed to the orientation of the ε-Fe_2O_3 crystals in the thin film, for which some specific Raman vibration modes are not activated.
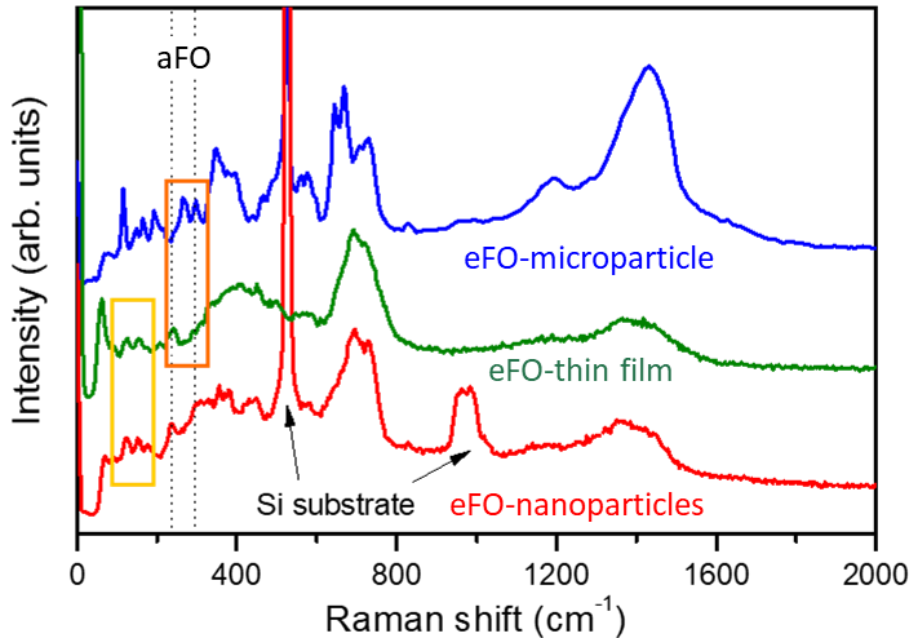
Figure 6.8 Comparison of the Raman spectra collected from ε-Fe_2O_3 thin film (green, this work), microparticle (blue, Ref [18]) and nanoparticle aggregates (red, Ref [18]).

Figure 6.9(a) shows an optical micrograph obtained with the CRM system, and a zoomed area is shown in Panel (b). A flat continuous region and several rounded regions with different colour tonalities are manifested. In the area marked with a yellow square in Panel (b), a Raman mapping is carried out with an integration time of 0.5 seconds at an irradiation laser power of 4 mW. The average of the Raman spectra obtained in different zones and the in-plane Raman intensity image are represented in Figures 6.9(c) and Figures 6.9(d), respectively. To obtain the Raman intensity images in the XY plane, the region of the Raman spectra ranging from 660 to 750 cm^{-1} is integrated for ε-Fe_2O_3, and spectral ranges of 202-237 cm^{-1} (pink colour), 240-262 cm^{-1} (purple colour) and 385-412 cm^{-1} (red colour) were integrated for the α-Fe_2O_3 phase. The observed Raman spectra are related to the hematite phase with different orientations depending on the area studied (pink, red and purple colour) and to the epsilon phase (green colour). By correlating the Raman intensity mapping with the different regions observed by optical microscopy in panel (b), it is concluded that the continuous layer is composed of ε-Fe_2O_3 and the lamellar and rounded shape regions are associated with α-Fe_2O_3 (see Figure 6.9(c)).
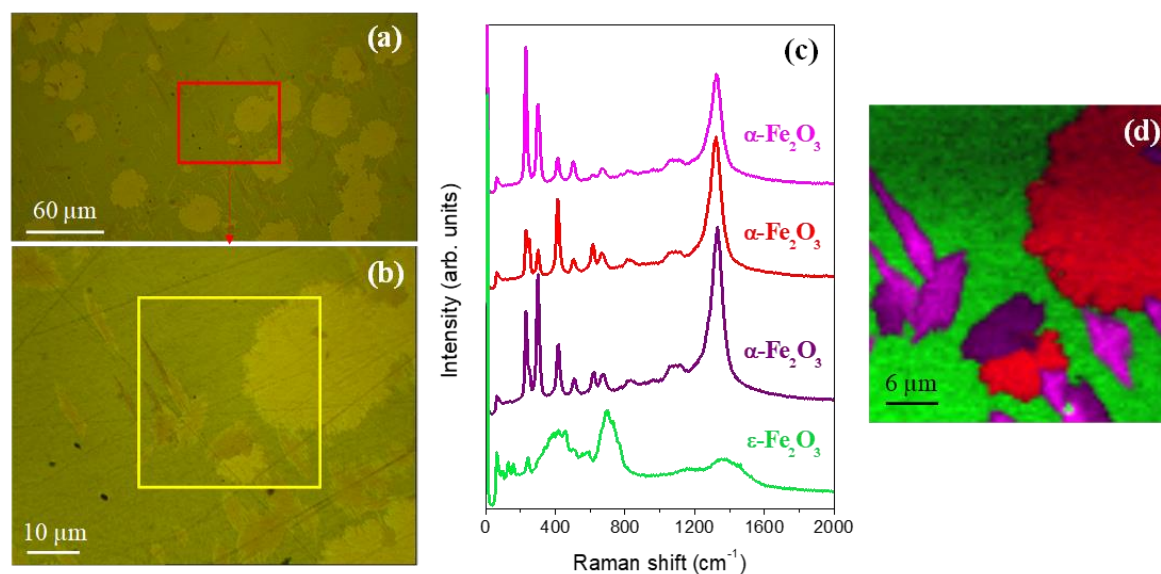
Figure 6.9 (a) Optical micrographs of the α- and ε-Fe$_2$O$_3$ films grown on Fe$_3$O$_4$ (30 nm) buffered MAO (111) substrate. Panel (b) represents a magnification of the area indicated with a red rectangle in panel (a) and the yellow square delimits the selected scanning region for CRM analysis. (c) Average Raman spectra of the iron oxides observed in panel (d); (d) Raman intensity images in the XY plane obtained on the marked region in panel (b). The integration window chosen to obtain the intensity image ranges from 660 cm^{-1} to 750 cm^{-1} for the ε-Fe$_2$O$_3$ phase (green colour), whereas the integration windows employed for the intensity images for α-Fe$_2$O$_3$ phase are 1310-1340 cm^{-1} (red colour), 209-241 cm^{-1} (pink colour), and 272-332 cm^{-1} (purple colour).

Thus far, we have confirmed the presence of oriented ε-Fe$_2$O$_3$ film in the eFO/FO(4kp)//MAO(111) heterostructure. This is consistent with what we have derived from the discussion in Section 6.2. The existence of hematite impurity phase revealed here by CRM, confirms what has been detected using XRD (see Figure 6.3(c)).

Let's now discuss the origin of these α-Fe$_2$O$_3$ impurities detected in the eFO/FO(4kp)//MAO(111) heterostructure by CRM experiment. Before we proceed, it is important to stress that iron oxides (α-Fe$_2$O$_3$, β-Fe$_2$O$_3$, γ-Fe$_2$O$_3$, ε-Fe$_2$O$_3$ and Fe$_3$O$_4$), especially in nanometric form, have very complex growth mechanisms and kinetics of polymorphous transformations. Great effort has been devoted to identifying and understanding the growth thermodynamic and kinetic properties by controlling different parameters, including the intrinsic properties such as particle size and morphology, surface structure and chemical states, as well as synthetic/growth parameters such as temperature, pressure and atmosphere. Here, two possible reasons for the intrusion of hematite in the heterostructure are described below.

In recent works by Kim and co-workers [19,20], it has been argued that the specific in-plane domain pattern of the ε-Fe$_2$O$_3$ film creates nucleation sites for α-Fe$_2$O$_3$ growth. These works have shown that, for film thickness above a certain threshold value, such in-plane domain pattern of ε-Fe$_2$O$_3$ (001) could become a nucleation site for α-Fe$_2$O$_3$ phase [19,20]. The resulting α-Fe$_2$O$_3$ layer tends to crystallize with the (006) direction out of plane in order to reduce the surface energy, leading to three in-plane domain

variants, as schematically illustrated in Figure 6.10(a). Therefore, one cannot exclude that the formation of α-Fe$_2$O$_3$ (006) epilayer also happened in our case, and nevertheless the diffraction peak associated with the α-Fe$_2$O$_3$ {006} planes are too weak to be appreciated (e.g., the intensity of α-Fe$_2$O$_3$ (006) only accounts for 3 % of the strongest (104) diffraction peak, according to the JCPDS Card No. PDF #00-033-0664).
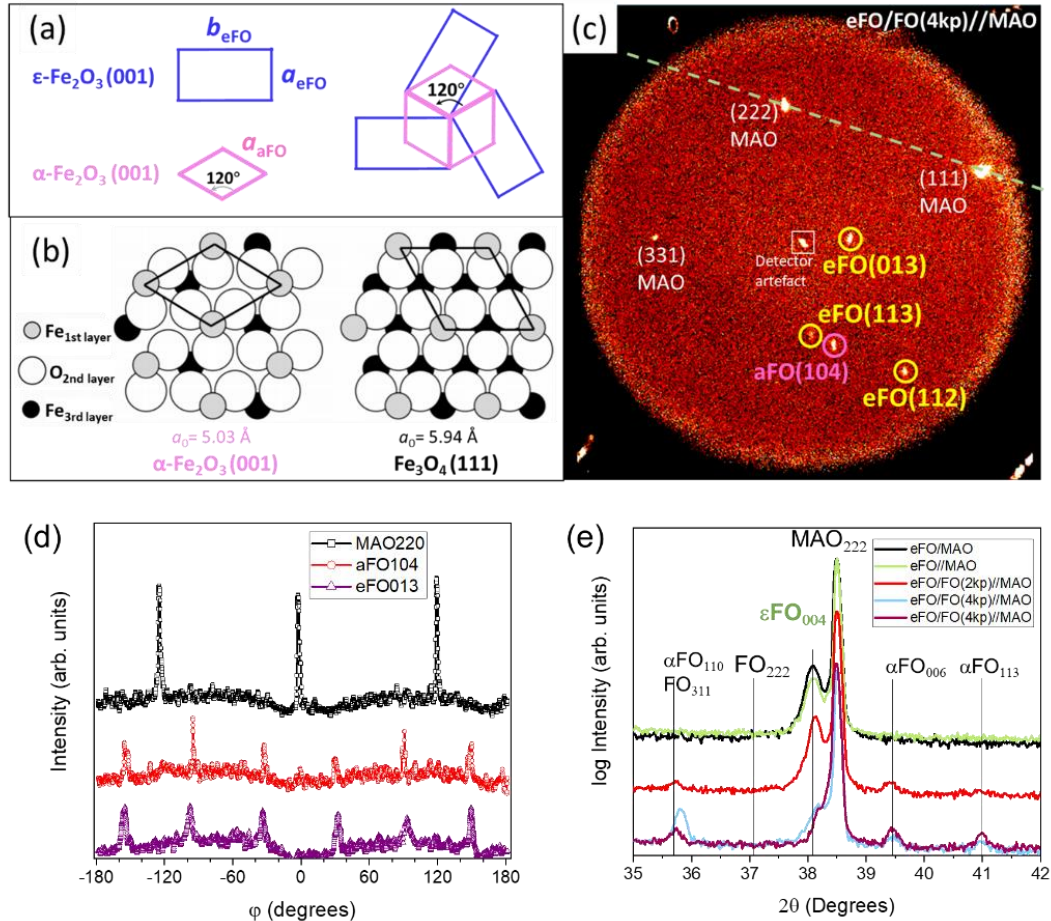
Figure 6.10 (a) Schematic illustration of the possible α-Fe$_2$O$_3$ domain structure on top of ε-Fe$_2$O$_3$, showing the three 120° domain pattern of ε-Fe$_2$O$_3$ as an effective nucleation site for rhombohedral α-Fe$_2$O$_3$. Note that the lattice parameter a_{eFO}= 5.09 Å ≈ a_{aFO}=b_{aFO}= 5.04 Å. (b) Top views of α-Fe$_2$O$_3$ (001) and Fe$_3$O$_4$ (111) surfaces. The surface unit cells are indicated. Figure adapted from Reference [21]. (c) 2D XRD frame obtained with χ= 70° for the eFO/FO(4kp)//MAO(111) films showing the appearance of the (104) peak of hematite (yellow circle) at 2θ= 33°. For clarity, the light green dashed line marks the χ = 90° position. Closed circles mark the ε-Fe$_2$O$_3$ film XRD peaks. The white spot marked by the white square symbol in the center is from the detector artefact. (d) ϕ-scans extracted from pole figure measurement for the labeled reflections. (e) HRXRD ω-2θ scans with monochromator (only λ[Cu-K$_{\alpha1}$]) and long (20 s/step) acquisition time. Vertical lines and labels mark bulk positions for aFO, eFO and FO-spinel phases.

The other reason for the appearance of α-Fe$_2$O$_3$ may be related to the oxidation of Fe$_3$O$_4$ (111) surface, yielding an α-Fe$_2$O$_3$ (001) structure during the deposition. We note that the transition of Fe$_3$O$_4$ (111) epilayer to α-Fe$_2$O$_3$ (001) reportedly happens when the background O$_2$ pressure increases at high temperature and/or when the Fe$_3$O$_4$ (111) epilayer above certain critical thickness [21–24]. Therefore,

the intrusion of minor α-Fe$_2$O$_3$ phase may be attributed to the structural transition of Fe$_3$O$_4$ layer caused by at least one of these two factors — the p(O$_2$) pressure change (UHV-0.1 mbar) and the thickness of the Fe$_3$O$_4$ (111) layer. Furthermore, from a crystallographic point of view, the Fe-terminated surfaces of α-Fe$_2$O$_3$ (001) and Fe$_3$O$_4$ (111) are both of hexagonal symmetry, nevertheless their surface lattice constants are quite different (a_0= 5.04 and 5.94 Å, respectively), as given in Figure 6.10(b). However, the close-packed oxygen planes are almost coincident along the α-Fe$_2$O$_3$ [001] and Fe$_3$O$_4$ [111] directions, which may be the reason for the epitaxial relation.

Thus by the observation of the above mentioned aFO(104) peak we may identify even a minor fraction of α-Fe$_2$O$_3$ (006) that grows along the film normal direction. This diffraction peak is not observed in our previously shown 2D GADDS frame with tilt angle χ= 90° (Figure 6.4(a)), due to their insufficient intensity. As the GADDS detector employed in this work allows simultaneous collection of diffraction data over a tilt angle (χ) range of no more than 70°, i.e. in the range of χ= 90° ± 35° for the commonly used geometry. Considering (00l) texture of aFO, the strongest α-Fe$_2$O$_3$ (104) peak is out of the frame range as the angle between {104} and {006} planes is ~ 38°. Therefore, in order to capture the α-Fe$_2$O$_3$ (104) diffraction peak we acquired additional GADDS frames with χ = 70° for the ε-Fe$_2$O$_3$/spinel film system, and the result for the eFO/FO(4kp)//MAO(111) films is shown in Figure 6.10(c). A peak at $2\theta = 33$° and $\chi = 62$°, that neither belongs to ε-Fe$_2$O$_3$ nor to FO/MAO coincides well with the (104) peak of hematite. Moreover, the χ difference between this peak and χ= 90° is in agreement with α-Fe$_2$O$_3$ {104} and {006} plane angle, confirming the α-Fe$_2$O$_3$ (006) epitaxy along the out-of-plane direction. A pole figure was acquired using the same tilt conditions. Both eFO(013) and aFO(104) show six poles indicating domain formation for both phases. The FO spinel {311} and {220} reflections were too weak and in too close proximity of the MAO substrate. This hampered a precise extraction from the pole figure data, nevertheless other XRD data and TEM indicate 'cube-on-cube' growth of FO and MAO(111). Typical twinning for the FO spinel may lead to a second set of three (311) or (220) peaks rotated by 60º with respect to the MAO substrate peaks [25], but are not observed within the experimental resolution, see the extracted φ-scans in Figure 6.10(d). The epitaxial relationship for eFO is not altered by the FO buffer layer, three domains with two poles each and aligned [100]eFO‖[11-2]FO‖[11-2]MAO. The six aFO(104) poles indicate twinning, thus [100]aFO‖[-100]aFO‖[11-2]FO‖[11-2]MAO. By observing much larger amounts of aFO related region the Raman measurements in Figure 6.9 we revised the sample series by HRXRD with monochromator and long acquisition time, see Figure 6.10(e). Indeed, the acquired ω-2θ scans reveal that for the eFO/FO(4k)//MAO sample traces of polytextured aFO phases can be identified, also in much less account in the thinner buffer layer sample eFO/FO(2k)//MAO. On the other hand, it is also evident that the eFO fraction is reduced for the eFO/FO(4k)//MAO, as evidenced from the much smaller eFO(004) peak intensity compared to these of the other two samples. No spurious traces of neither aFO nor FO (apart of small mixed spinel interface regions observed in HRTEM) are found in the eFO//MAO film. Therefore, we directly stabilized pure

eFO epilayer on MAO(111) films. This may indicate a critical thickness for FO buffer layers and may leave some improvement to tune the growth transition from FO to eFO.

Next, we put our focus on the regions where only epsilon phase is present and explore the temperature dependence of its structural peculiarities. The sample was firstly placed in a temperature chamber (open to air) and Raman spectra were acquired at different temperatures, starting from 30 ºC, and then from 50 ºC to 150 ºC with a steps of 50 ºC, and then every 25 ºC up to 200 ºC, and finally every 5 ºC up to 270 ºC. The red cross in Figure 6.11(a) indicates one of the points where the temperature dependent experiment was performed, and some of the Raman spectra are presented in Figure 6.10(b). In general, the frequency of all examined Raman peaks softens with increasing temperature (anharmonic effects). Besides, the bandwidths (FWHM) of the modes increase when the sample is heated, and meanwhile their intensities tend to decrease. This behavior is expected due to lattice expansion and an increase in the phonon population as a result of increasing temperature. In order to illustrate the temperature dependence of the Raman bands, Lorentzian fits have been made for all temperatures for several characteristic modes, and the deduced Raman shift evolution for the M1, M6 and M20-M23 modes (taking the same labels as in [18]) are depicted in Figure 6.11(c-e). The M20-M23 modes composing of four distinct modes near 700 cm^{-1} cannot be distinguished from one another due to the nanometric scale of ε-Fe₂O₃ phase (see, for instance, the Raman spectrum of ε-Fe₂O₃ microparticle in Figure 6.8 for comparison). Therefore, we have made the fit considering them as a single band in this case. As shown in Figure 6.11(c-e), in contrast to the above-mentioned general tendency in Raman frequency with increasing temperatures, some anomalies are detected at around 200 ºC (473 K), where the frequencies undergo a sudden increase prior to a gradual decrease with rising temperatures. This anomaly is more obvious for the low-frequency M1 and M6 modes. It is important to note that the onset temperature of the anomaly is relatively close to the Néel transition temperature ($T_{N2}\sim$ 480 K) between the FM1 and FM2 ferrimagnetic orders of ε-Fe₂O₃ nanoparticles which has been discussed in Chapter 3. A magnetic transition from the fully ordered FM2 magnetic phase to the FM1 phase in which two of the four magnetic sublattices become disordered and which is accompanied by a significant magnetostructural anomaly ($\Delta V/V \approx -0.1\%$) occurs at this temperature [26]. Thus, the observed Raman mode anomalies are indicative of the possible presence of the exchange-striction effects in ε-Fe₂O₃ thin films. Another interesting observation is that, in contrast to the two-magnon enhancement above T_{N2} reported in microparticle samples [18], we did not detect such variations in our films.
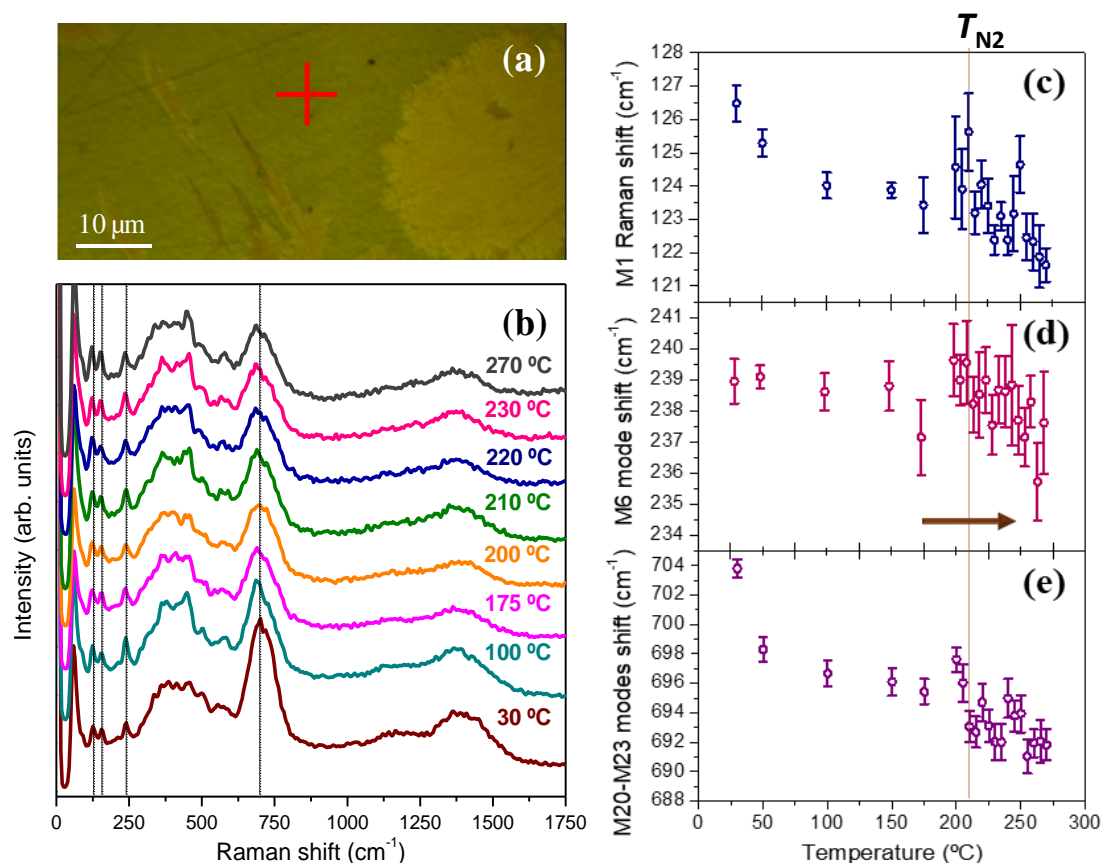
Figure 6.11 (a) Optical micrograph of the eFO/FO(4kp)//MAO(111) heterostructure. The red cross in an area where only epsilon phase exists indicates the point where the temperature evolution experiment was carried out. (b) Evolution of the Raman spectra as a function of temperature. Panels (c-e) the Raman shift vs. temperature for M1, M6 and M20-M23 modes, respectively. The dashed line near 200 ℃ indicates the Néel transition temperature T_{N2}.

6.3.2 Raman spectroscopy studies of epitaxial ε-Fe₂O₃//MAO(111) thin film

A detailed Raman spectroscopy investigation at low temperatures was done on the eFO//MAO(111) films. The motivation to undertake this study came on the one hand from the encouraging results obtained by monitoring the evolution of Raman mode anomalies along the FM2-FM1 transition above room temperature (Figure 6.11) in eFO/FO(4kp)//MAO(111) films and the differences observed between these films and ε-Fe₂O₃ nanoparticles. On the other hand, the magnetic characterization of those films (see Section 6.4) reveals anomalies at low temperature which remind those observed in nanoparticles along the FM2-IM1 transition [27]. Several times in the past, the Raman study of this low temperature transition was attempted without success in our group, both using ε-Fe₂O₃ nanoparticles and ε-Fe₂O₃ thin films on STO(111) but this substrate gives a very broad background which masks the modes of the film.

From the optical micrograph shown in Figure 6.12(a), one can see that the appearance of the film is quite homogeneous, unlike what happened in the eFO/FO(4kp)//MAO(111) sample, which presented a series of rounded and elongated islands of several to tens of microns. In the Raman mapping in the XZ

plane thanks to the use of the confocal microscopic system which allows collect selective signal from different focal positions only ε-Fe$_2$O$_3$ phase is detected in the film region, with no signature of hematite (see Figure 6.12(b)). The average Raman spectra of ε-Fe$_2$O$_3$ film (in green) and MAO substrate (in gray) acquired in different areas are shown in Figure 6.12(d). Next, an XY Raman mapping was performed on the region marked by the blue square in Figure 6.12(a), and the resulting intensity image (Figure 6.12(c)) further corroborates the presence of ε-Fe$_2$O$_3$ phase without intrusion of secondary phase. Figure 6.12(e) depicts the average Raman spectrum of the film from the XY Raman mapping. Comparing it to the spectra acquired from the eFO/FO(4kp)//MAO(111) sample (represented in blue and green in Figure 6.12(e)), which present an enhancement of the Raman band located at 725 cm^{-1} (the shoulder close to the Raman band at 695 cm^{-1}), here we see a slightly different spectrum in which such shoulder becomes almost invisible.
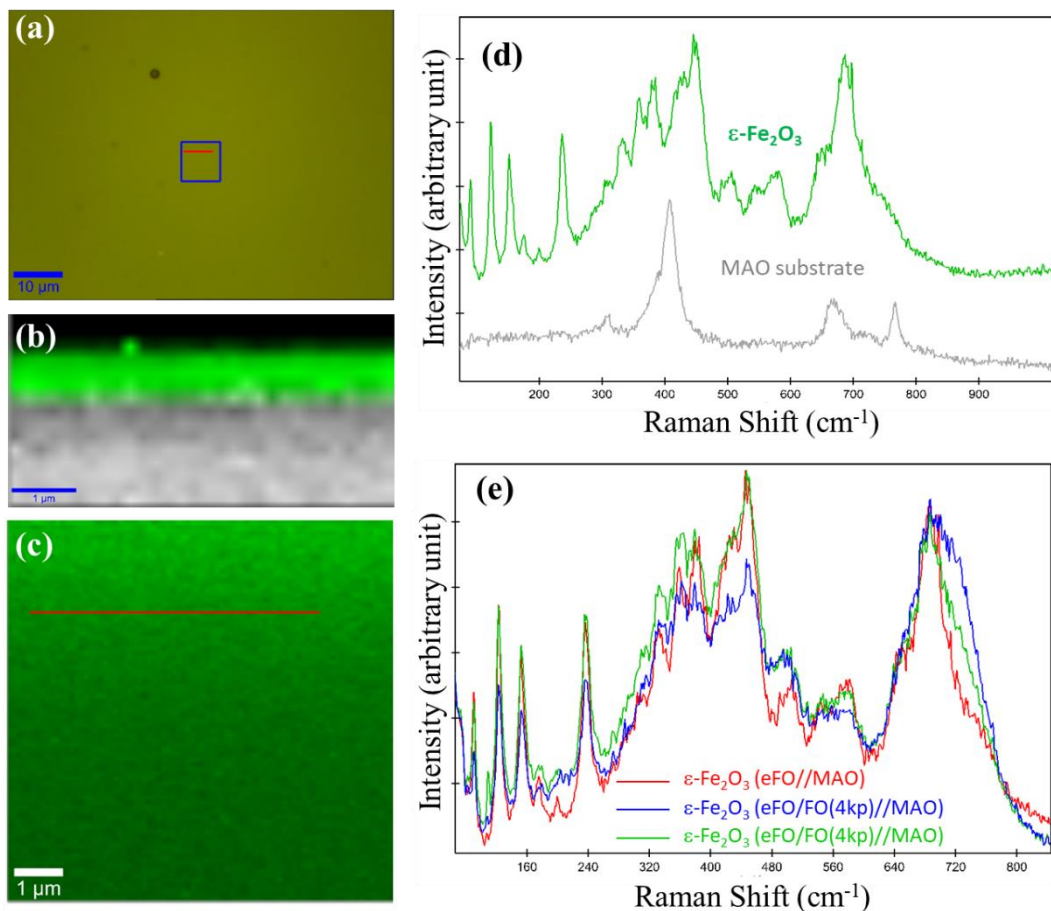
Figure 6.12 (a) Optical micrograph of the eFO//MAO(111) film. The red line and the blue squared region represent, respectively, where the XZ and XY plane Raman intensity images are obtained. Panels (b) and (c) present the Raman mapping results acquired with an integration time of 1 s at 8 mW in the XZ (6×3 μm^2) and XY (8×8 μm^2) planes, respectively. Their corresponding average Raman spectra acquired in different areas are shown in Panel (d) and (e). The gray spectrum in Panel (d) belongs to MAO substrate. For comparison, the Raman spectra from the eFO/FO(4kp)//MAO(111) sample and which can be ascribed to diferent domains are also shown respectively in blue and green in Panel (e).

Temperature dependent Raman spectra were collected to obtain further insights on the FM2-IM1 transition. In particular it is expected that information about the effect of spin-phonon interactions on the Raman modes will be valuable to understand the microscopic details of this magnetic and structural phase transformation. Figure 6.13(a) shows the temperature evolution of the Raman spectra of eFO//MAO(111) film between 80 and 300 K. Neither the disappearance of existing modes nor the appearance of any new modes is detected, indicating that the *Pna2$_1$* space group is maintained down to 80 K as it has indeed observed for ε-Fe$_2$O$_3$ nanoparticles [27,28]. Moreover, one would expect the Raman modes exhibit sharper peaks at low temperatures due to the increase in the phonon lifetime. This is essentially true above 200 K. Below 200 K, however, the peak intensities decrease upon reducing temperature (see Figure 6.13(b-d)). This anomalous Raman mode behavior is most likely related to the spin-phonon interactions at low temperatures.
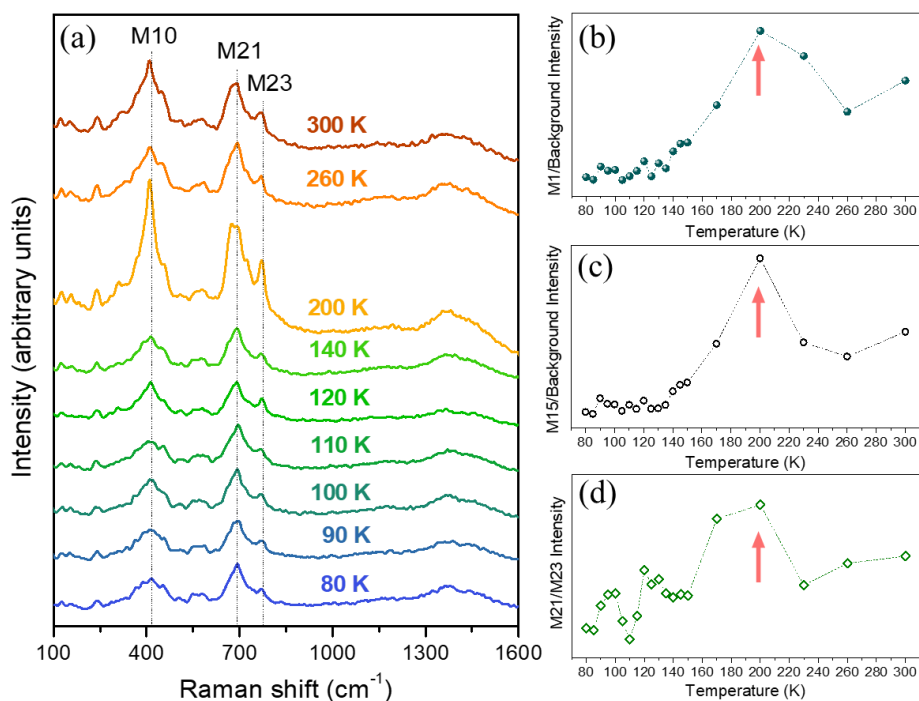
Figure 6.13 (a) Temperature-dependent Raman spectra of the eFO//MAO(111) film obtained between 80 and 300 K. (b) The derived temperature dependence of the intensity of M1 and M15 Raman modes, and the relative intensity between the M21/M23 modes. The dashed lines connecting the points are guides to the eye.

For a dielectric, the temperature induced variation in the mode frequency $\omega(T)$ is a consequence of lattice anharmonicity and spin-phonon coupling. The shift in the mode frequency governed by an anharmonic phonon decay can be analyzed approximately using [29],[30]

$$\omega_{anh}(T) = \omega_0 - C\left(1 + \frac{2}{e^x - 1}\right) \tag{7.1}$$

where ω_0 is the phonon frequency in harmonic approximation, C is the anharmonic correction to the frequency at $T = 0$ K, and $x = \hbar\omega_0/2k_B T$.

154

A deviation of the temperature evolution of phonon spectra from the anharmonic phonon effects, $\delta\omega = \omega(T) - \omega_{anh}(T)$, is generally attributed to the spin ordering contribution. To put it into perspective, the anomalous phonon softening in the manganese-based oxides [31],[32] , as revealed by temperature-dependent Raman spectra, was interpreted in terms of a spin-phonon coupling caused by a phonon modulation of the superexchange integral (J_{ij}). It has been demonstrated that the frequency deviation from the anharmonicity formalism is proportional to the second derivative of the superexchange integral, J_{ij}'', and the scalar spin-spin correlation function, $<\vec{S_i} \cdot \vec{S_j}>$, showcasing that the phonon frequency behavior can be related to the sublattice magnetic ordering in oxides.
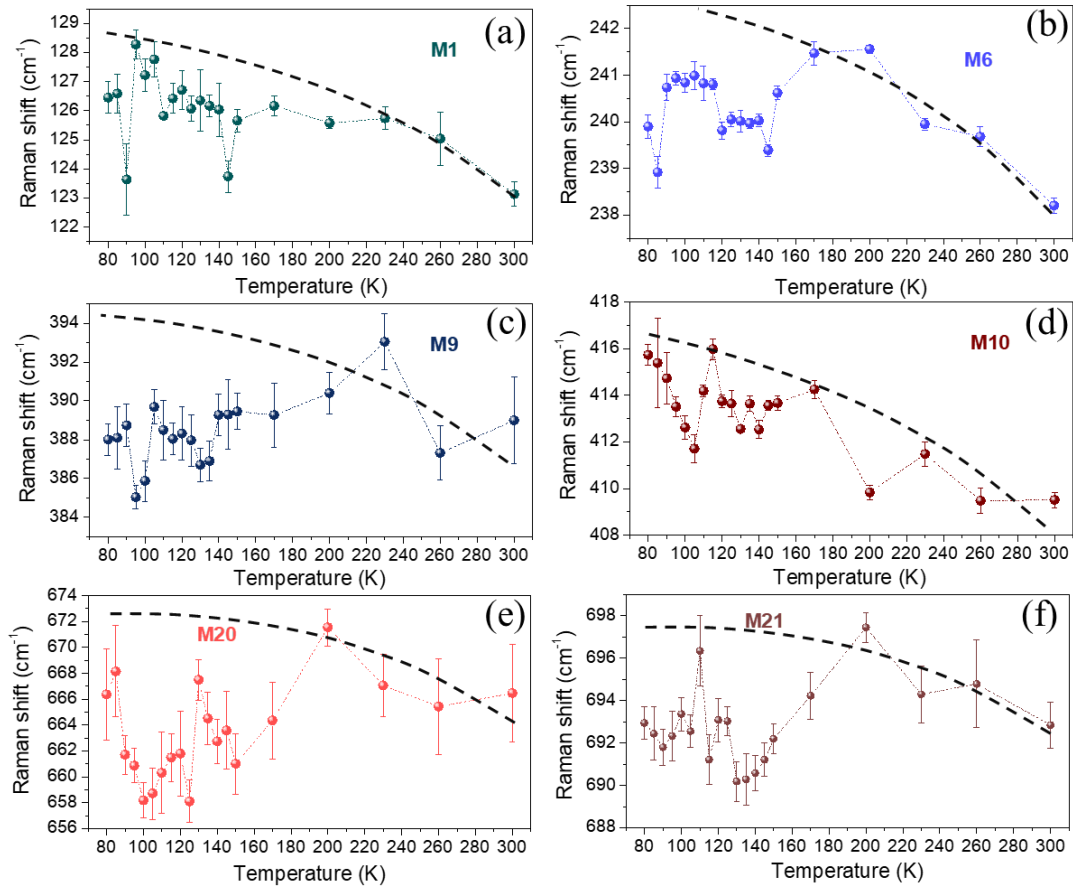
Figure 6.14 Temperature dependence of the frequency shift of several characteristic Raman modes (a) M1, (b) M6, (c) M9, (d) M10, (e) M20, and (f) M21. The spheres indicate the experimental data points at different temperatures whereas the dashed lines connecting the points are guides to the eye. The black dashed lines indicate the temperature dependence in agreement with the anharmonic model.

The temperature dependence of the frequency shift of some characteristic Raman modes for the eFO//MAO(111) film, together with the temperature dependence given by the anharmonic model is shown in Figure 6.14. It becomes clear that the trend of Raman shift primarily agrees with the anharmonic model at temperatures above ~ 200 K, whereas a marked phonon softening can be observed below this temperature for most of the modes shown in Figure 6.14. This shift in mode frequency could be attributed to spin-phonon effect in this oxide. Another interesting feature of the Raman shift

evolution is that the frequency variation $\delta\omega$ for the studied phonons is non-monotonous, but an oscillatory-like function of temperature. Therefore, one could speculate that the $\delta\omega(T)$ dependence directly follows some temperature changes of the propagation vector of an incommensurate structure or a spin reorientation between different pairs of Fe sites in ε-Fe₂O₃. A theoretical interpretation of the findings involving the phonon and lattice dynamics calculations by density functional calculations is ongoing in collaboration with Victor Ivanov (University of Sofia) and Rohan Mishra (Washington Univesity in Saint Louis), in order to shed some light on the nature of the low-temperature magnetic phase transition(s).

6.4 Magnetic properties of epitaxial ε-Fe₂O₃//MAO(111) thin film

As one of the less well understood of its properties, the magnetism of ε-Fe₂O₃ has been widely explored. Nonetheless, the majority of the studies thus far mainly focused on the nanoparticles of ε-Fe₂O₃, albeit the thin film structures with well-oriented crystallographic directions are expected to have a greater impact in different application domains. This is partially due to the fact that, thanks to the ease of producing in large amounts from chemical routes, ε-Fe₂O₃ nanoparticles generally give large enough magnetic signal that can be probed by macroscopic magnetic measurements and neutron scattering. This can be relevant considering the relatively small magnetization of this oxide (less than 20 emu/g with an applied field of 70 kOe at room temperature, more than three times smaller compared to magnetically soft maghemite or magnetite). As for epitaxial ε-Fe₂O₃ thin films, aside from the challenge in obtaining films o thickness above 100 nm without the intrusion of parasitic phase(s), buffer layers such as AlFeO₃ or GaFeO₃ employed to promote the ε-Fe₂O₃ epitaxial growth are generally magnetic and could have a non-negligible influence on the measurement magnetic properties of the top epilayer, and thus hindering a precise understanding of the intrinsic magnetic properties of the ε-Fe₂O₃ thin films. For these reasons, the exploration of the magnetic structures and phase transitions is lagging far behind that of its nanoparticle counterparts. In the following text, we discuss the magnetic characteristics of the ε-Fe₂O₃//MAO(111) epitaxial film, which have the advantage of being directly grown on the MAO substrate without the need of introducing any buffer layer.

Let us start with the magnetic moment measurements using an MPMS-XL superconducting quantum interference magnetometer device (SQUID, Quantum Design Inc.) magnetometer. Figure 6.15(a) depicts the temperature (T) dependence of the zero-field-cooling (ZFC) and field-cooling (FC) magnetic moment (m) under an in-plane magnetic field H= 100 Oe for the ε-Fe₂O₃//MAO(111) film. The surface area of the film used in the SQUID measurements is around 2.4×5 mm². The experiment was carried out according to the following procedures: (1) the film was demagnetized at room temperature and cooled down to 10 K without magnetic field applied; (2) A 100 Oe field was applied, and the magnetic

moment was recorded while the film was being heated to 300 K with a rate of 2 K/min (ZFC curve, represented in black in Figure 6.15(a)); (3) Then, the film was cooled down to 10 K at 10 K/min under the same field; (4) Finally, the magnetic moment was recorded as the temperature was increases to 300 K at 2 K/min (FC curve, represented in red in Figure 6.15(a)). From the ZFC-FC m-T curves, one can see that m presents a gradual increase upon heating up to ~ 100 K, which is accompanied by a continuous decrease until 300 K. This broad peak coincides well with the low-temperature magnetic transition(s) that were reported in ε-Fe₂O₃ nanoparticles, indicating that a low-temperature magnetic transition is also present in the 55-nm ε-Fe₂O₃ epitaxial film. Although much effort has been placed on investigating the intriguing low-temperature magnetic incommensurate phase(s) in ε-Fe₂O₃ nanoparticles, this is, to our knowledge, the first evidence which could point to the existence of this phase in ε-Fe₂O₃ thin films. However, taking into account that as we have seen in Chapter 3, these incommensurate magnetic orders are very sensitive to strain, neutron diffraction experiments would be needed get more information about the nature of the low temperature magnetic order in the thin films. It is worth noting that the m-T curves show visible upturn at temperatures near 10 K. This upturn is due to the relevance at low temperatures of paramagnetic impurities of the MAO (111) substrate which strongly decrease its intrinsic diamagnetic signal, as can be seen in a measurement of the in-plane magnetic moment vs temperature of a MAO substrate presented in Figure 6.15(b).
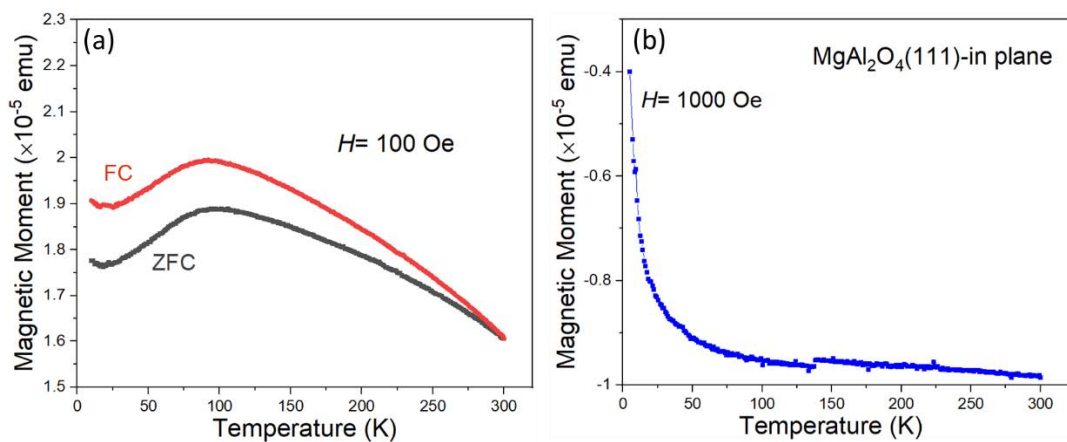
Figure 6.15 (a) In-plane magnetic moment as a function of temperature collected under ZFC and FC conditions (H= 100 Oe) for the 55-nm ε-Fe₂O₃//MAO(111) film. The low-temperature transition of the film is obvious. Note that the magnetic moment variation between the maximum moment at ~ 100 K and that at 10 K is in the order of 10^{-6} emu. (b) In-plane magnetic moment as a function of temperature recorded at H= 1000 Oe for the MAO(111) substrate, showing a paramagnetic response due to impurities which strongly decreases its intrinsic diamagnetic signal. The step at around 140 K is due to the measurement and is not physical.

Figure 6.16(a) shows the in-plane isothermal magnetic moment versus magnetic field (m-H) curves up to a maximum field of 70 kOe. This measurement was performed in RSO (Reciprocating Sample Option) operating mode. RSO centering was carried out manually at several temperatures to correct the specimen position during the measurement. The "no overshoot" mode was adopted for most of the data points (this is especially true for the low-field regions with low magnetic moment) in order to stabilize

the magnetic field, minimizing the effect of field noise. The dominating effect of the diamagnetic MAO substrate can be seen at high magnetic fields. At the low field region, however, the magnetic moment does not cross the origin at $H= 0$ for all the temperatures, indicating the presence of hard magnetic ε-Fe₂O₃ phase. The diamagnetic response can be subtracted from the linear fitting of the m-T curves at high fields, and the hysteresis loops of the thin film are obtained (see Figure 6.16(b)). The hard magnetic nature of the film is evident from the wide loops. Moreover, the low-field region of the hysteresis loop curves (see Figure 6.16(c)) shows quite well-defined shapes, and no obvious step-like behavior related to the presence of any secondary phase(s) is found at $H= 0$. The temperature variations of the coercive field (H_C) and remanence (M_R) derived from the hysteresis loops are shown in Figure 6.16(d). From the M_R versus temperature (M_R-T) curve, M_R slowly increases upon decreasing temperatures up to around 80 K, where it then starts to drop with a further temperature decrease. The room temperature H_C and M_R are approximately 5170 Oe and 44 emu/cm³, respectively. Moreover, it can be seen from the H_C versus temperature (H_C-T) curve that the H_C increases on cooling, reaching a maximum value of 5700 Oe at 200 K. It then gradually decreases when subject to a further cooling down to 80 K, where a minimum value of 4415 Oe is achieved. Finally, a sharp increase of H_C to 6230 Oe is observed from 80 K to 10 K. Such behaviors are reminiscent of the H_C-T and M_R-T curves observed in the ε-Fe₂O₃ nanoparticles [27]. As for the ε-Fe₂O₃ nanoparticles, the coercivity collapse (from a maximum H_C of ~ 22 kOe at 200 K to a minimum of ~ 0.8 kOe at 100 K) has been ascribed to the reduction of spin-orbit coupling connected to a large drop of the Fe orbital moment m_{orb} [33]. The coercivity collapse is indicative of the transition from the commensurate to incommensurate magnetic state. However, it is interesting to note that, in comparison to the H_C-T curve of the polycrystalline samples (nanoparticles), here the variation of H_C is much smaller (the H_C within the range of 4400-5700 Oe between 80-300 K), but the sharp enhancement of H_C at low temperatures is relatively large for the thin films.
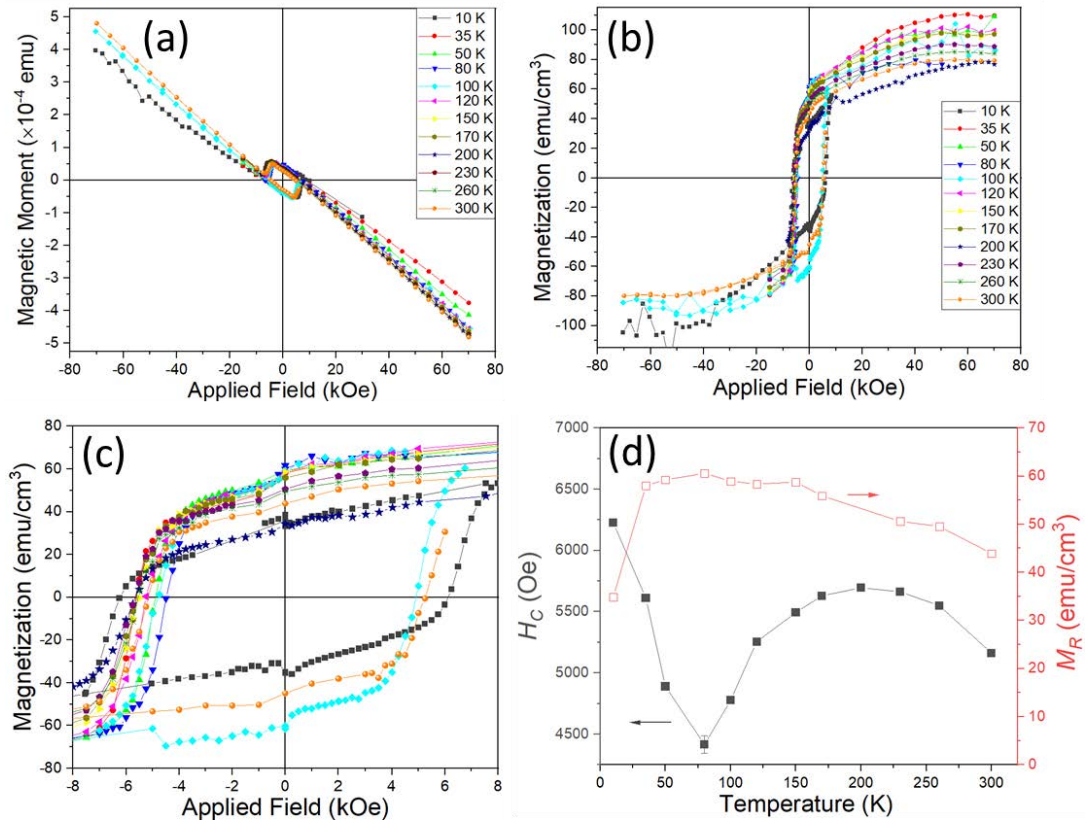
Figure 6.16 (a) Magnetic field dependence of the in-plane magnetic moment recorded with a maximum field of 70 kOe at different temperatures for the eFO//MAO(111) film (raw data). (b) In-plane magnetization vs magnetic field for various temperatures (after subtracting the substrate diamagnetic contribution). A zoom-in of the low-field region of the hysteresis loops is shown in Panel (c). (d) In-plane coercive field H_C and remanence M_R as a function of temperature derived from the hysteresis loops. The lines connecting the points are guides to the eye.

It is important to point out that the observed decrease of H_C below 200 K coincides with the onset of the deviations of the typical anharmonic dependence with temperature in Raman measurements (Figure 6.14). Let us finally point out that this film has also been studied in a temperature dependent XAS XMCD experiments at BOREAS beamline of ALBA synchrotron in collaboration with Javier Herrero. This experiment has revealed that from 300 K to 200 K the ratio of the Fe L_3 pre-peak intensity to the main L_3 peak intensity increases and then strongly decreases below 200 K becoming stable below 100 K. A similar trend is observed for the ratios of the 1st and 2nd minima of the XMCD signal. The analysis of the data of this experiments is ongoing and we expect it can also contribute to understand the low temperature magnetic transition in ε-Fe₂O₃//MAO(111) films.

6.5 Summary

In this chapter, we presented more detailed structural and magnetic properties of the ε-Fe₂O₃ thin films grown on MAO (111) spinel. Temperature dependent Raman spectra collected both above and below

room temperature successfully probed the signatures of the high-temperature FM1-FM2 magnetic transition and of the low-temperature transition in the same range of temperatures as the FM2-IM1 transition of nanoparticles. Magnetization measurements show that the film exhibits a room temperature in-plane coercivity of H_C= 5170 Oe. Temperature dependent measurements have also confirmed the existence of a low temperature magnetic transition displaying $H_C(T)$ and $M_R(T)$ trends which are similar to those found in nanoparticles.

References

[1]   M. Gich, J. Gazquez, A. Roig, A. Crespi, J. Fontcuberta, J.C. Idrobo, S.J. Pennycook, M. Varela, V. Skumryev, M. Varela, Epitaxial stabilization of ϵ -Fe$_2$O$_3$ (00l) thin films on SrTiO3 (111), Appl. Phys. Lett. 96 (2010) 112508. https://doi.org/10.1063/1.3360217.

[2]   L. Corbellini, C. Lacroix, C. Harnagea, A. Korinek, G.A. Botton, D. Ménard, A. Pignolet, Epitaxially stabilized thin films of ϵ-Fe$_2$O$_3$ (001) grown on YSZ (100), Sci. Rep. 7 (2017) 1–9. https://doi.org/10.1038/s41598-017-02742-9.

[3]   Z. Zhang, S. Satpathy, Electron states, magnetism, and the Verwey transition in magnetite, Phys. Rev. B. 44 (1991) 13319–13331. https://doi.org/10.1103/PhysRevB.44.13319.

[4]   M.S. Ansari, M.H.D. Othman, M.O. Ansari, S. Ansari, M.Z.M. Yusop, Room temperature growth of half-metallic Fe$_3$O$_4$ thin films on polycarbonate by reactive sputtering: Heterostructures for flexible spintronics, J. Alloys Compd. 816 (2020) 152532. https://doi.org/10.1016/j.jallcom.2019.152532.

[5]   S. Soeya, J. Hayakawa, H. Takahashi, K. Ito, C. Yamamoto, A. Kida, H. Asano, M. Matsui, Development of half-metallic ultrathin Fe3O4 films for spin-transport devices, Appl. Phys. Lett. 80 (2002) 823–825. https://doi.org/10.1063/1.1446995.

[6]   N. Takahashi, T. Huminiuc, Y. Yamamoto, T. Yanase, T. Shimada, A. Hirohata, T. Nagahama, Fabrication of Epitaxial Fe$_3$O$_4$ Film on a Si(111) Substrate, Sci. Rep. 7 (2017) 1–8. https://doi.org/10.1038/s41598-017-07104-z.

[7]   X. Liu, H. Lu, M. He, L. Wang, H. Shi, K. Jin, C. Wang, G. Yang, Room-temperature layer-by-layer epitaxial growth and characteristics of Fe$_3$O$_4$ ultrathin films, J. Phys. D. Appl. Phys. 47 (2014) 105004. https://doi.org/10.1088/0022-3727/47/10/105004.

[8]   O. Chich Arina, T.S. Herng, W. Xiao, X. Hong, J. Ding, Magnetic anisotropy modulation of epitaxial Fe$_3$O$_4$ films on MgO substrates, J. Appl. Phys. 117 (2015) 17D722. https://doi.org/10.1063/1.4918695.

[9]   D. Gilks, L. Lari, Z. Cai, O. Cespedes, A. Gerber, S. Thompson, K. Ziemer, V.K. Lazarov, Magnetism and magnetotransport in symmetry matched spinels: Fe$_3$O$_4$/MgAl$_2$O$_4$, in: J. Appl. Phys., American Institute of PhysicsAIP, 2013: p. 17B107. https://doi.org/10.1063/1.4800690.

[10]   N. Dix, I. Fina, R. Bachelet, L. Fàbrega, C. Kanamadi, J. Fontcuberta, F. Sánchez, Large out-of-plane ferroelectric polarization in flat epitaxial BaTiO$_3$ on CoFe$_2$O$_4$ heterostructures, Appl. Phys. Lett. 102 (2013) 172907. https://doi.org/10.1063/1.4803943.

[11]   C. Colliex, T. Manoubi, C. Ortiz, Electron-energy-loss-spectroscopy near-edge fine structures in the iron-oxygen system, Phys. Rev. B. 44 (1991) 11402–11411. https://doi.org/10.1103/PhysRevB.44.11402.

[12]   R. Takahashi, H. Misumi, M. Lippmaa, Growth temperature effect on the structural and magnetic properties of Fe$_3$O$_4$ films grown by the self-template method, J. Appl. Phys. 116 (2014). https://doi.org/10.1063/1.4890510.

[13]   J. Gázquez, G. Sánchez-Santolino, N. Biškup, M.A. Roldán, M. Cabero, S.J. Pennycook, M. Varela, Applications of STEM-EELS to complex oxides, Mater. Sci. Semicond. Process. 65 (2017) 49–63. https://doi.org/10.1016/j.mssp.2016.06.005.

[14]   C. Dejoie, P. Sciau, W. Li, L. Noé, A. Mehta, K. Chen, H. Luo, M. Kunz, N. Tamura, Z. Liu, Learning from the past: Rare ϵ-Fe$_2$O$_3$ in the ancient black-glazed Jian (Tenmoku) wares, Sci. Rep. 4 (2014) 1–9. https://doi.org/10.1038/srep04941.

[15]   J. López-Sánchez, A. Serrano, A. Del Campo, M. Abuín, O. Rodríguez De La Fuente, N. Carmona, Sol-gel synthesis and micro-raman characterization of ϵ-Fe$_2$O$_3$ micro- and nanoparticles, Chem. Mater. 28 (2016) 511–518. https://doi.org/10.1021/acs.chemmater.5b03566.

[16]   Y. El Mendili, J.F. Bardeau, N. Randrianantoandro, J.M. Greneche, F. Grasset, Structural behavior of laser-irradiated γ-Fe$_2$O$_3$ nanocrystals dispersed in porous silica matrix : γ-Fe$_2$O$_3$ to α-Fe$_2$O$_3$ phase transition and formation of ϵ-Fe$_2$O$_3$, Sci. Technol. Adv. Mater. 17 (2016) 597–609. https://doi.org/10.1080/14686996.2016.1222494.

[17]   J. Yuan, A. Balk, H. Guo, Q. Fang, S. Patel, X. Zhao, T. Terlier, D. Natelson, S. Crooker, J. Lou, Room-Temperature Magnetic Order in Air-Stable Ultrathin Iron Oxide, Nano Lett. 19 (2019) 3777–3781. https://doi.org/10.1021/acs.nanolett.9b00905.

[18]   J. López-Sánchez, A. Serrano, A. Del Campo, M. Abuín, O. Rodríguez de la Fuente, N. Carmona, Sol–Gel Synthesis and Micro-Raman Characterization of ε-Fe_2O_3 Micro- and Nanoparticles, Chem. Mater. 28 (2016) 511–518. https://doi.org/10.1021/acs.chemmater.5b03566.

[19]   V.Q. Viet, S.Y. Adeyemi, W.H. Son, J.-S. Rhyee, N.-S. Lee, H.-J. Kim, Specific Domain Pattern of ε-Fe_2O_3 Thin Films Grown on Yttrium-Stabilized Zirconia (100) as a Nucleation Site for α-Fe_2O_3, Cryst. Growth Des. 18 (2018) 3544–3548. https://doi.org/10.1021/acs.cgd.8b00338.

[20]   Y.A. Salawu, N.S. Lee, H.J. Kim, Bi-Stability and Orientation Change of a Thin α-Fe_2O_3 Layer on a ϵ-Fe_2O_3 (004) Surface, ACS Omega. 4 (2019) 13330–13337. https://doi.org/10.1021/acsomega.9b01497.

[21]   M. Xue, S. Wang, K. Wu, J. Guo, Q. Guo, Surface Structural Evolution in Iron Oxide Thin Films, Langmuir. 27 (2011) 11–14. https://doi.org/10.1021/la103732r.

[22]   X. Zhang, S. Yang, Z. Yang, X. Xu, Kinetics and intermediate phases in epitaxial growth of Fe_3O_4 films from deposition and thermal reduction, J. Appl. Phys. 120 (2016). https://doi.org/10.1063/1.4961607.

[23]   H. Hong, J. Kim, X. Fang, S. Hong, T.C. Chiang, Interfacial stability of ultrathin films of magnetite Fe_3O_4 (111) on Al_2O_3(001) grown by ozone-assisted molecular-beam epitaxy, Appl. Phys. Lett. 110 (2017) 3–8. https://doi.org/10.1063/1.4973808.

[24]   K. Freindl, J. Wojas, N. Kwiatek, J. Korecki, N. Spiridis, Reversible oxidation-reduction of epitaxial iron oxide films on Pt(111): Magnetite-hematite interconversion, J. Chem. Phys. 152 (2020). https://doi.org/10.1063/1.5136322.

[25]   L. Yan, Y. Wang, J. Li, A. Pyatakov, D. Viehland, Nanogrowth twins and abnormal magnetic behavior in $CoFe_2O_4$ epitaxial thin films, J. Appl. Phys. 104 (2008) 123910. https://doi.org/10.1063/1.3033371.

[26]   J.L. García-Muñoz, A. Romaguera, F. Fauth, J. Nogués, M. Gich, Unveiling a New High-Temperature Ordered Magnetic Phase in ϵ-Fe_2O_3, Chem. Mater. 29 (2017) 9705–9713. https://doi.org/10.1021/acs.chemmater.7b03417.

[27]   M. Gich, A. Roig, C. Frontera, E. Molins, J. Sort, M. Popovici, G. Chouteau, D. Martín y Marero, J. Nogús, Large coercivity and low-temperature magnetic reorientation in ε-Fe_2O_3 nanoparticles, J. Appl. Phys. 98 (2005) 044307. https://doi.org/10.1063/1.1997297.

[28]   M. Gich, C. Frontera, A. Roig, E. Taboada, E. Molins, H.R. Rechenberg, J.D. Ardisson, W.A.A. Macedo, C. Ritter, V. Hardy, J. Sort, V. Skumryev, J. Nogués, High- and low-temperature crystal and magnetic structures of ε-Fe_2O_3 and their correlation to its magnetic properties, Chem. Mater. 18 (2006) 3889–3897. https://doi.org/10.1021/cm060993l.

[29]   I.P. Ipatova, A.A. Maradudin, R.F. Wallis, Temperature dependence of the width of the fundamental lattice-vibration absorption peak in ionic crystals. II. Approximate numerical results, Phys. Rev. 155 (1967) 882–895. https://doi.org/10.1103/PhysRev.155.882.

[30]   M. Balkanski, R.F. Wallis, E. Haro, Anharmonic effects in light scattering due to optical phonons in silicon, Phys. Rev. B. 28 (1983) 1928–1934. https://doi.org/10.1103/PhysRevB.28.1928.

[31]   V.G. Ivanov, V.G. Hadjiev, A.P. Litvinchuk, D.Z. Dimitrov, B.L. Shivachev, M. V. Abrashev, B. Lorenz, M.N. Iliev, Lattice dynamics and spin-phonon coupling in $CaMn_2O_4$: A Raman study, Phys. Rev. B - Condens. Matter Mater. Phys. 89 (2014) 184307. https://doi.org/10.1103/PhysRevB.89.184307.

[32]   E. Granado, A. García, J.A. Sanjurjo, C. Rettori, I. Torriani, F. Prado, R.D. Sánchez, A. Caneiro, S.B. Oseroff, Magnetic ordering effects in the Raman spectra of $La_{1-x}Mn_{1-x}O_3$, Phys. Rev. B - Condens. Matter Mater. Phys. 60 (1999) 11879–11882. https://doi.org/10.1103/physrevb.60.11879.

[33]   Y.C. Tseng, N.M. Souza-Neto, D. Haskel, M. Gich, C. Frontera, A. Roig, M. van Veenendaal, J. Nogues, Nonzero orbital moment in high coercivity epsilon-Fe_2O_3 and low-temperature collapse of the magnetocrystalline anisotropy, Phys. Rev. B. 79 (2009). https://doi.org/10.1103/PhysRevB.79.094404.

Chapter 7

Characterization of Epitaxial ε-Fe$_2$O$_3$ Thin Films on Flexible Mica

This chapter is devoted to the characterizations of commercial fluorophlogopite mica and the epitaxial ε-Fe$_2$O$_3$ thin films grown on this flexible substrate, with the main emphasis on their structural characteristics, as well as their magnetic properties as a function of magnetic field and temperature.

7.1 Introduction

Mica, one of the most common phyllosilicates, has been widely recognized as an appealing playground for surface science studies on gases, liquids [1],[2], and also as a substrate for the deposition of thin films [3],[4],[5],[6],[7]. One of the advantages of utilizing 2D mica as growth substrates is its clean and atomically flat surface, which is ideal for high-quality crystal growth. Among the members of the mica group, phlogopite [(KMg$_3$(AlSi$_3$O$_{10}$)(OH)$_2$] is one of the most common rock-forming minerals. In synthetic fluorophlogopite (fluoromica or F-mica), the apical hydroxyl groups of phlogopite are substituted by fluorine ions (F$^-$), resulting in an ideal formula KMg$_3$(AlSi$_3$O$_{10}$)F$_2$. Compared to natural micas, synthetic F-mica has enhanced crystallinity and higher purity [8]. Thanks to the presence of F$^-$, this mica has an improved thermal stability and a marked endurance for larger stresses in tension and compression. Besides, due to its well-controlled chemistry, it features a highly ordered atomically smooth surface, high transparency and chemical durability. F-mica is characterized by layered structure (see Figure 7.1a). It is made up of negatively charged aluminosilicate layers consisting of two tetrahedral sheets with their apical oxygen atoms sandwiching an internal octahedral sheet and their basal oxygens defining six-membered rings of corner sharing tetrahedra on the layer surfaces (see Figure 7.1b) [9].
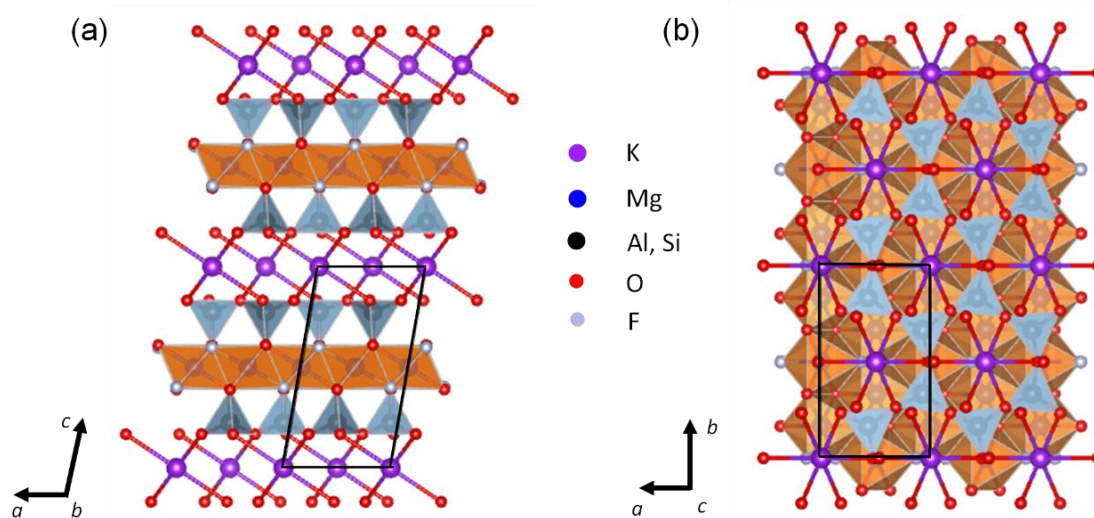
Figure 7.1 Crystal structure of fluorophlogopite (F-mica) projected along the (a) [010] and (b) [001] crystaographic directions. One representative unit cell is outlined by black solid lines. The crystal consists of a magnesium coordinated octahedral (MgO$_6$) sheet sandwiched between two sheets of tetrahedra coordinated by silicon or aluminium [(Si, Al)O$_4$], where (Si, Al)O$_4$ represents that some of the silicon cations (1/4) in the tetrahedral sheets are partially replaced by aluminium cations. Two adjacent unit layers are weakly bonded though potassium cations (K$^+$). When projected along the basal plane normal, the top tetrahedral sheet of the unit cell can be perceived as honeycomb arrangement of hexagons of six corner sharing (Si, Al)O$_4$ tetrahedra. The apical oxygens of the tetrahedra are connected to the three MgO$_6$ octahedra from the central sheet. Each of the basal F^{-1} anion is shared between three MgO$_6$ in the octahedral sheet.

Neighbouring layers are held together by a weak bonding through 12-coordinated potassium ions accommodated at these ring cavities and which is responsible for an easy cleavage parallel to the {001} basal plane, resulting in atomically flat surfaces [10]. It possesses a monoclinic space group C2/m symmetry, with a= 5.308(2) Å, b= 9.183(3) Å, c= 10.139(l) Å, β= 100.07(2)°, and two formula units per unit cell [11].

The growth of functional oxides on flexible substrates, a long sought-after goal in the era of flexible electronics, is often deterred by their high crystallization temperatures. The operating temperatures of most of the proposed flexible substrates are disappointingly low. For example, most plastic substrates degrade or deform at over 300 °C, and polyimide (PI), one of the most widely used flexible substrate, degrades at temperatures around 375 °C. Moreover, the amorphous or partially crystalline character of plastics prevents the epitaxial growth. On the other hand, F-mica possesses excellent thermal stability. Its high working temperature (up to 1100 °C) is compatible with the high crystallization temperatures of most oxides. This, together with its advantageous mechanical properties, high optical transparency, remarkable chemical inertness and high dielectric strength, make layered mica particularly desirable for the potential applications in the next-generation flexible electronics. As a result, layered F-mica has become an increasingly popular substrate for 3D oxide thin film growth (see, for example, references [12],[13],[14]).

Recently, Yuan el al. reported air-stable ultrathin crystals of ε-Fe$_2$O$_3$ chemical vapor deposition (CVD) on F-mica substrates [15]. They found that the epsilon phase remains free of hematite impurities for crystals thinner than 100 nm. Robust magnetic order, irrespective of the crystal thickness, was probed in thin ε-Fe$_2$O$_3$ flakes at room temperature by magneto-optical Kerr effect magnetometry. The bonding between the CVD-grown ε-Fe$_2$O$_3$ and its growth substrate is reportedly van der Waals-like, enabling to integrate it with other 2D materials such as graphene. Motivated by this work, we undertook the epitaxial PLD growth of ε-Fe$_2$O$_3$ thin films on F-mica substrates and the exploration of their functional properties.

We have briefly described in Chapter 5 the epitaxial growth and the structural characterization of ε-Fe$_2$O$_3$/SAFO heterostructure grown on F-mica substrate. In order to achieve a better understanding of the properties of the ε-Fe$_2$O$_3$ thin films, an in-depth investigation of F-mica crystals has been carried out, and the relevant findings are presented in the first part (Section 7.2). Special focus is placed on quantifying the paramagnetic response, which has been neglected in most of the previous reports. We will then proceed with a description of the works in progress, containing more structural characterizations of the ε-Fe$_2$O$_3$/mica system (Section 7.3), together with their magnetic properties (Section 7.4). Finally, the main conclusions of the work are formulated in Section 7.5.

7.2 Characterization of fluorophlogopite mica crystals

It is particularly important for using mica as a support substrate for thin film epitaxy that mica is readily cleaved down to a thickness of several micrometers, so that the interference of bulk substrate properties with subsequent measurements could be significantly lowered, which is otherwise impossible for single-crystalline ceramic oxide substrates. So, in the case of the integration of mica with magnetic nanostructures (especially, for nanometer-sized thin layers with weak magnetic moment like ε-Fe$_2$O$_3$ thin films), one may argue that such nanomagnet/mica system could be ideal for the assessment of the intrinsic magnetic properties of the nanostructures. This conjecture is essentially correct provided that the mica substrate utilized is diamagnetic (non-magnetic).

On the other hand, despite mica substrate is gaining importance for growing various magnetic nanostructures in the wake of the growing interest for flexible electronics [7],[16],[17],[18], surprisingly, not enough attention has been paid to the magnetic properties of mica itself. We can find in the recent literature examples in which the magnetic contribution of mica substrates is simply ignored [7,19] or others in which the issue of the substrate contribution to the overall magnetic response is bypassed by transferring it to another substrate that is easier to deal with from the magnetic point of view [20]. Prior knowledge of the magnetic characteristics of mica substrate appears as imperative and convenient before undertaking the magnetic characterization of the nanostructures grown on top of it. In principle, pure mica should be diamagnetic as most commercially available oxide substrates. This means that, for the conventional diamagnetic substrates, their magnetic responses are weak (with susceptibilities in the order of -10^{-6}), independent of temperature and vary linearly with an applied field. Thus, to obtain the magnetic response of a film, one can readily offset the contribution of a diamagnetic substrate. This is done by compensating the signal obtained from the linear fitting of the magnetization versus magnetic field curve at high enough fields so that the ferri-/ferromagnetic film is already saturated, and the diamagnetic substrate signal dominates the magnetic response.

However, it has been shown that impurities of iron, the most abundant magnetic element in the Earth's crust, are responsible for paramagnetic and/or ferromagnetic contributions in the measured minerals [21,22]. Coey et al. investigated the magnetic anomalies of natural micas at various temperatures and at high magnetic fields [23],[24]. The observed magnetic anisotropy of trioctahedral micas was ascribed to iron incorporation in their crystal structures [23]. It is worth noting that unlike the diamagnetic contribution the paramagnetic one is both temperature and field dependent, which makes the above-mentioned correction method inappropriate for iron-bearing mica substrates. Thus, the correction of the magnetic response of iron- or other elements with unpaired spins contained in mica becomes crucial, since it can potentially screen intrinsic magnetic response of the nanoscale objects with small magnetic moments grown on it. In this case, the method by Schmidt et al. [25] to separate diamagnetic and paramagnetic components, which based on high field torque measurements, is not convenient because

it is not sensitive at low fields and requires samples with oblate or prolate shapes and subtracting the measuring holder contribution.

Among the different members of mica family, F-mica has increasingly been the substrate of choice for the development of new functional materials [18],[26],[15],[27]. Yet, the fundamental understanding of this fluorine-rich silicate is far from complete. This is particularly true concerning the magnetic properties which, to our knowledge, were only qualitatively studied by Tsui et al. [28] on the fluoromica samples prepared in their laboratory to be used as substrates to grow rare earth films. Their work reports the magnetic response of the mica as that of a paramagnet and diamagnet mixture and speculates that can be due to the presence of ferromagnetic clusters.

In this section, I will give an account of the recent work on synthetic fluorophlogopite mica crystals (see Reference [29], DOI: 10.1039/d0ma00317d), where we explored the physical properties of F-mica with special emphasis on their magnetic responses to both temperature and magnetic field. Our study shows that the magnetic response of mica comprises diamagnetic and paramagnetic components. The latter is quite significant at low temperatures and can be analyzed within the framework of Curie's law and the Langevin theory. Hence, special cautions must be taken to address properly the magnetic properties of mica-supported nanostructures. Moreover, our study reveals that the paramagnetic signal of F-mica under study originates from isolated magnetic cations rather than from superparamagnetic clusters. We propose a protocol to correct the magnetic contributions of mica substrates which can be useful in future developments of flexible magnetic devices.

7.2.1 Characterization of fluorophlogopite mica crystals

The (001)-cut synthetic F-mica sheets (Changchun Taiyuan Co., LTD., China) of 5 by 5 mm in lateral size and 0.2 μm in thickness were used in this study. The top and bottom surfaces of the mica were freshly exfoliated with a scotch tape prior to all the measurements. Firstly, the preferred (00l) out-of-plane orientation of the crystal and the crystallographic configurations in the basal plane were analyzed by XRD θ-2θ scan and XRD ϕ scan in a Bruker D8 Discover X-ray diffractometer using Cu-K_α radiation. Figure 7.2(a) shows the out-of-plane XRD θ-2θ scan of the tape-exfoliated mica plate. The observation of only the strong (00l) diffraction peaks indicates a highly textured structure with this orientation perpendicular to the out-of-plane direction of the sheets. Six (202) reflection peaks found at 60 ° intervals are observed in the in-plane XRD ϕ scan pattern (see Figure 7.2(b)). This implies the presence of twinning in the mica crystals. Due to the monoclinic tilt angle between a and c axes ($\beta \sim 100°$) the multiplicity of the (202) reflection is only two, with the (-20-2) parallel planes also contributing to it, one must conclude that the six observed peaks in ϕ scan result from six in-plane twins. This type of twinning is not unexpected considering the pseudohexagonal symmetry of the (001) planes and has been recently reported in Muscovite mica [30].
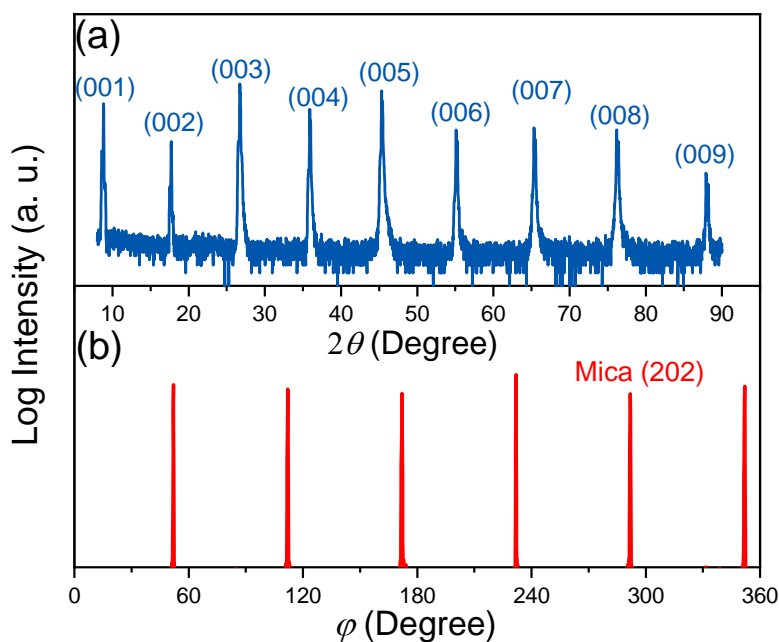
Figure 7.2 (a) XRD θ-2θ scan indicating (001) out-of-plane texture of the mica plate, and (b) in-plane φ scan of the mica crystals, showing six (202) reflections at 60 ° intervals.

Next, the elemental composition of F-mica was determined via inductively coupled plasma mass spectrometry (ICP-MS) analysis. Prior to this, the specimen was digested in a concentrated acid mixture of 4 mL HNO_3 (Aldrich), 2 mL HCl (Aldrich), 4 mL H_3PO_4 (Aldrich), and 0.5 mL HF (Aldrich) at 260 °C using a Milestone UltraWAVE microwave digestion system. The results presented in Table 7.1 show that the relative molar fractions of the mica cations are in agreement with the ideal composition (12.5 % K, 37.5 % Mg, 12.5 % Al, and 37.5 % Si) except for a significant substitution of Si by Al in the tetrahedral sites. It is worth noting that in 2:1 layered phyllosilicates both the tetrahedrally and octahedrally coordinated cations are prone to considerable substitution by other metal ions. In particular, this concerns the interchangeable Al^{3+} and Si^{4+} cations in the tetrahedral sites and the substitutions of Fe^{2+} and Ti^{4+} of octahedral Mg^{2+} [22],[31],[32],[33], and the resulting charges can be eventually balanced by the cations in the interlayer positions (see Figure 7.1). Therefore, the above-observed non-stoichiometry in F-mica is reasonable. In addition, as shown in Table 7.1, the ICP-MS analysis reveals traces of Ti [0.5(1)×10⁻³ wt.%], Fe [0.30(6)×10⁻³ wt.%], and Ni [0.40(8)×10⁻⁴ wt.%], accounting for less than 0.1 wt.% of the sample. It has been reported that in Ti-rich trioctahedral mica the incorporated Ti cation mostly adopts the 4+ oxidation state [34],[35], which does not carry any magnetic moment. In contrast, iron and nickel cations have large magnetic moments (Fe^{2+}: 5.4 μB, Fe^{3+}: 5.9 μB, and Ni^{2+}: 3.2 μB), which can dominate the magnetic properties even when only present in small amounts. Considering that the magnetic moments of iron cations are about two times that of nickel and that iron content in our sample is nearly one order of magnitude higher than that of nickel, we can anticipate the significant impact of iron impurities on the magnetic properties of our mica crystals.

Table 7.1 Analytical results obtained from ICP-MS for the major and trace elements in F-mica. The relative molar fractions of the major elements and mass fractions of the trace elements are also listed.

Major elements	Concentration (mg/g)	Molar fraction (mol.%)	Trace elements	Concentration (mg/g)	Mass fraction (wt.%)
K	79±16	16±3	Ti	0.5(1)	0.05(1)
Mg	122±24	39±8	Fe	0.30(6)	0.030(6)
Al	68±14	19±4	Ni	0.040(8)	0.0040(8)
Si	96±19	26±5	Total	0.8(1)	< 0.1%

The transmittance spectrum of F-mica collected using a Jasco V-570 spectrometer in the region of 200-1000 nm is shown in Figure 7.3(a). Firstly, in the UV region, mica displays a strong absorbance from 200 to 320 nm and as wavelength increases up to ~ 400 nm a sharp increase of the transmittance occurs in two steps to reach 90 %. Further, it is evident that the mica has an excellent optical transmittance throughout the total visible range (from 400 to 800 nm) with ~ 90% transmittance, which is maintained in the infrared region of the spectrum with no sign of decreasing at 1000 nm wavelength (the maximum wavelength examined). The high optical transmittance confirms the high quality of the mica crystals. This high visible transmittance is also indicative of the low iron content of synthetic mica compared to natural micas [36],[37]. Indeed, the presence of iron decreases both the transmittance in the visible and the UV cut-off frequency and the absorption coefficient was reported to be proportional to the concentration of iron [36]. Thus, the measurement of the UV-Vis spectra is a simple and fast technique to assess the level of iron impurities in mica. The images presented in the inset of Figure 8.3(a) show both high optical transparency and good mechanical flexibility of the exfoliated mica sheets. The topographic images of the freshly exfoliated sheet of mica were acquired with an Agilent 5100 atomic force microscope (AFM) in tapping mode using FORT Si tips (Applied NanoStructures Inc.), and one representative topographic image is shown in Figure 7.3(b). The height profile, as depicted in the inset, shows a small height variability within the range of ~ 2 Å. The measured average root mean square (RMS) roughness is 3.5 Å, which is much smaller than the thickness of a single unit cell layer (~ 10 Å). The atomically flat surface of the crystals is thus confirmed.
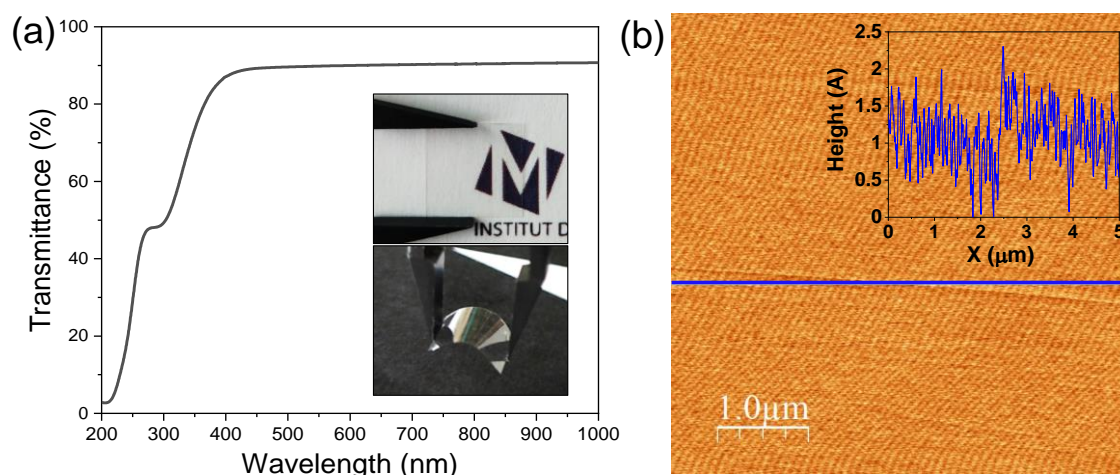
Figure 7.3 (a) Transmittance spectrum showing the high transparency of fluorophlogopite mica. This is also illustrated by the upper inset which displays an optical image of an exfoliated mica sheet clamped by a black plastic tweezer on top of an image, demonstrating the high transparency of the crystals. The lower inset is an optical image of the bent mica sheets which reveals their superb mechanical flexibility. (b) A representative topographic AFM image (5 × 5 μm) of the crystals. Inset represents the height profile along the blue line marked in the AFM image.

7.2.2 Magnetic properties of fluorophlogopite mica crystals

In the following, we report the magnetic characterization of the mica crystals. Some experimental details are provided here. The magnetic measurements were collected on a freshly exfoliated fluorophlogopite sheet with mass of 13.81 mg using Quantum Design MPMS-XL SQUID magnetometer. The applied dc magnetic fields either parallel or perpendicular to the mica sheets. For the in-plane magnetic field geometry, the mica was well centred in a clear drinking straw by clamping it in-between the walls of the straw without using any additional supporting pieces. The mounting of the sample perpendicular to the magnetic field was made thanks to two transversal cuts on each side of the straw, slightly shorter than the straw diameter, through which the sample was inserted to be placed perpendicular to the straw axis. In order to avoid damaging the sample by the tight contact with the slots cut in the straw, it was covered with a clear commercial PVC film. All the precautions to avoid magnetic contaminations (such as using nonmagnetic tweezers and avoiding textmarker labelling) were taken throughout the sample handling process. Measurements were performed in RSO (Reciprocating Sample Option) operating mode to achieve better sensitivity by eliminating low-frequency noise. RSO centering was carried out manually at several temperatures to adjust the specimen position during the temperature dependent measurements. Throughout the isothermal magnetic moment versus magnetic field curve measurements, the "no overshoot" mode was adopted to stabilize the magnetic field, minimizing the effect of field noise.

Magnetic measurements as a function of temperature (T) were carried out with the magnetic field (H) applied along the out-of-plane direction. The obtained evolution of the magnetic moment m as a function of temperature (m-T) curve is presented in Figure 7.4(a). It is seen that, after an initial sharp

decrease with increasing T to about 20 K, the moment m continues to decrease less and less steeply with further heating, then changes sign, finally tends to level-off at negative moment values at the high-temperature end. A magnetic moment with very small negative values and almost no temperature dependence is the typical diamagnetic response to external magnetic field. In contrast, the paramagnetic response is positive, and the paramagnetic susceptibility is typically inversely proportional to temperature. Therefore, the observed rapid increase of m at the low-temperature end unambiguously evidences the existence of a paramagnetic contribution, which dominates the magnetic response at low temperatures. On the other hand, the levelling off at the high-temperature end is a manifestation of the mica intrinsic diamagnetism, as the contribution to m coming from the paramagnetic component tends to become negligibly small. The observed paramagnetic behaviour is not unexpected taking into account the presence of traces of magnetic elements (iron and nickel) revealed by the elemental analysis of our fluoromica. In fact, other research groups have ascribed the paramagnetic behaviour of natural micas to the random incorporation of iron into the parent mica lattice [21],[22],[23]. Unlike diamagnetism, the paramagnetic response is typically a function of both, temperature and applied field. Consequently, the prevailing paramagnetic contribution at low temperatures poses an extra challenge for accurate magnetic characterizations of nanometre-sized objects of interest grown on top of mica.
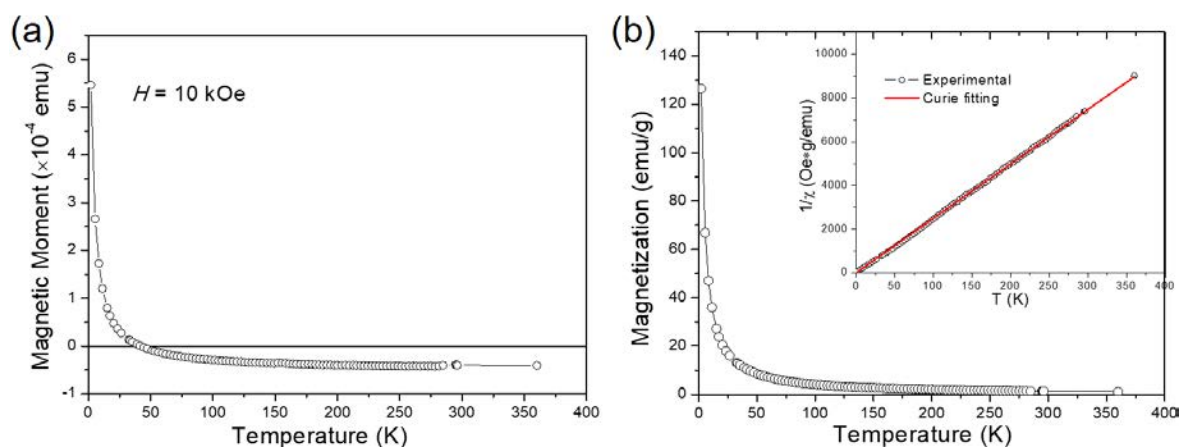
Figure 7.4 (a) Out-of-plane magnetic moments as a function of temperature recorded with external fields of 10 kOe for the mica crystals (raw data). Panels (b) depicts the out-of-plane M-T curves for the paramagnetic phase derived by subtracting the diamagnetic component of mica. The inset shows the inverse mass susceptibilities as a function of temperature.

In the next step, we explored the paramagnetic contribution of magnetic impurities by separating it from the diamagnetic one. The subtraction of the diamagnetic signal was achieved by proper vertical translations of the raw m-T curve above the horizontal axis of zero magnetic moment, i.e., by subtracting the value measured at the high-temperature end. Figure 7.4(b) presents the resulting magnetization M as a function of temperature (M-T) curve. Note that the magnetic moments have been normalized to the weight of the magnetic cations (namely, Fe and Ni) based on the mass fraction from the ICP-MS

elemental analysis. Then, the inverse mass susceptibility versus temperature (χ^{-1}-T) curve can be constructed, as illustrated in the inset of Figure 7.4(b), where magnetic susceptibility is defined as $\chi = M/H$. According to the Curie's law, the susceptibility of a paramagnet should obey the relation:

$$\chi = \frac{C}{T} \tag{7.1}$$

with the Curie constant C given by

$$C = \frac{N_A \mu_{eff}^2}{3k_B A} \tag{7.2}$$

where μ_{eff} is effective paramagnetic moment, A is atomic weight, N_A is the Avogadro's constant, and k_B the Boltzmann constant. Thus, the obtained χ^{-1}-T curve was fitted to Equation (7.1), and the result is plotted in red solid line together with the experimental data (open symbols) in the inset panel of Figure 7.4(b). It can be observed that the Curie law fitting is closely coincident with the experimental points over nearly the entire temperature range studied. In other words, χ^{-1} linearly depends on T with an intercept very close to zero. According to Equation (7.1), the Curie constant C was derived from the slope of the fitted curve in the inset of Figure 7.4(b), resulting in a $C = 0.04(1)$ emu·K/g·Oe. When more than one magnetic ion is present, the total Curie constant is given by the sum of the constants of the different species as given by Equation (7.2), and each multiplied by the relative concentration of the corresponding ion. In the present case, considering Fe^{2+} and Ni^{2+} in respective relative fractions of 0.88 and 0.12, the calculated total Curie constant is 0.06 emu·K/g·Oe, in reasonably good agreement with the value obtained experimentally. This experimental value slightly lower than expected could be due, at least partly, to the presence, in concentrations below the limit of detection of our ICP-MS measurements (0.025 mg/g), of other magnetic ions with moments lower than that of Fe^{2+} (e.g., Cr^{2+}, Cr^{3+}, V^{3+}, V^{2+}, Co^{2+}, Mn^{2+} or Cu^{2+}) or to the fact that a fraction of the titanium impurities is in form of magnetic Ti^{3+} [34]. We also performed the in-plane temperature dependent magnetic measurements obtaining, within the experimental error, the same value of the Curie constant.

To shed more light on the characteristics of the mica crystals, we present the measured magnetic moment versus applied field (m-H) curves recorded under isothermal condition with the in-plane (Figure 7.5(a)) and out-of-plane (Figure 7.5(b)) applied fields. No direction was specified for the in-plane geometry due to the multiple in-plane configurations in the crystals. From the in-plane m-H curves (see Figure 7.5(a)), one can make the following observations. Firstly, for the isothermal scan acquired at 2 K, m undergoes a steep increase with the field H increasing to about 1 kOe, where it slows down its increase until a maximum moment is reached at $H \sim$ 30 kOe. This is accompanied by a final almost linear decrease of m as the H further increases. A similar tendency can be observed for the isothermal curve recorded at 5 K, but m peaks at a much larger $H \sim$ 50 kOe and the linear variation in the high-field region becomes less obvious. Secondly, a typical paramagnetic-like behavior is presented for the curves obtained in the 10-30 K temperature interval. Finally, a linear relationship between m and H is evident

for the curves acquired at temperatures above 30 K, for which the m becomes negative. In this temperature regime, the curves tend to converge toward the curve measured at 360 K, which is the highest temperature in this study. These observations and those made above from the thermomagnetic curves allow us concluding that a competition exists between the intrinsic diamagnetic (negative) response of mica and the paramagnetic (positive) response from the impurities to the applied field, which becomes dominant at temperatures below 30 K. It is important to point out that all the $M(H)$ isotherms go through the origin at $H= 0$ and thereby no magnetic hysteresis is observed. This is in line with what is expected for diamagnetic and/or paramagnetic phases in the absence of applied field. The above observation also rules out the possible existence of ferro- or ferri-magnetic phases.

Further insights into the paramagnetic phase can be made by separating the diamagnetic-paramagnetic components from the m-H curves. To this end, the m-H curve at 360 K was used as the baseline of the diamagnetic background, since the paramagnetic component has a negligibly small contribution to it. This baseline curve was subtracted from the isothermal m-H curves, which were subsequently normalized to the weight of the magnetic elements contained in the mica. The resulting magnetic field dependence of magnetization (M-H) curves of the paramagnetic phase are presented in Figure 7.5(c) and Figure 7.5(d), for the H along the in-plane and out-of-plane directions, respectively. According to the Langevin theory of paramagnetism, magnetization M can be expressed by the Langevin function

$$M = n\mu \cdot (coth\, a - \frac{1}{a}) \tag{7.3}$$

where $a= \mu H/k_B T$, k_B is the Boltzmann constant, μ represents magnetic moment, and n is the number of magnetic moments per gram of sample, so that $n\mu$ is maximum magnetization achieved when all the magnetic moments are aligned. The fits of the M-H curves to the Langevin function using n and μ as fitting parameters are displayed by the dashed lines in Figure 7.5(c) and Figure 7.5(d) for the H along the in-plane and out-of-plane directions, respectively. A good agreement between the fitted curves and experimental data (symbols) has been found irrespective of the measurement geometries. The fittings of the curves between 2 and 30 K gave us values of μ around 6 Bohr magnetons (μ_B) and n of the order of $5 \cdot 10^{21}$. The obtained value of the magnetic moment is in the order of that of Fe^{3+} (5.9 μ_B) and Fe^{2+} (5.4 μ_B) indicating that the paramagnetic signal within the mica crystals comes from isolated magnetic cations rather than from magnetic clusters. This is further confirmed by estimating [38], from n and the mass of Fe contained in the substrate, that the volume of bcc Fe or Fe_3O_4 hypothetical clusters would be of the order of 100 pm^3 which is less than the volume of an atom.
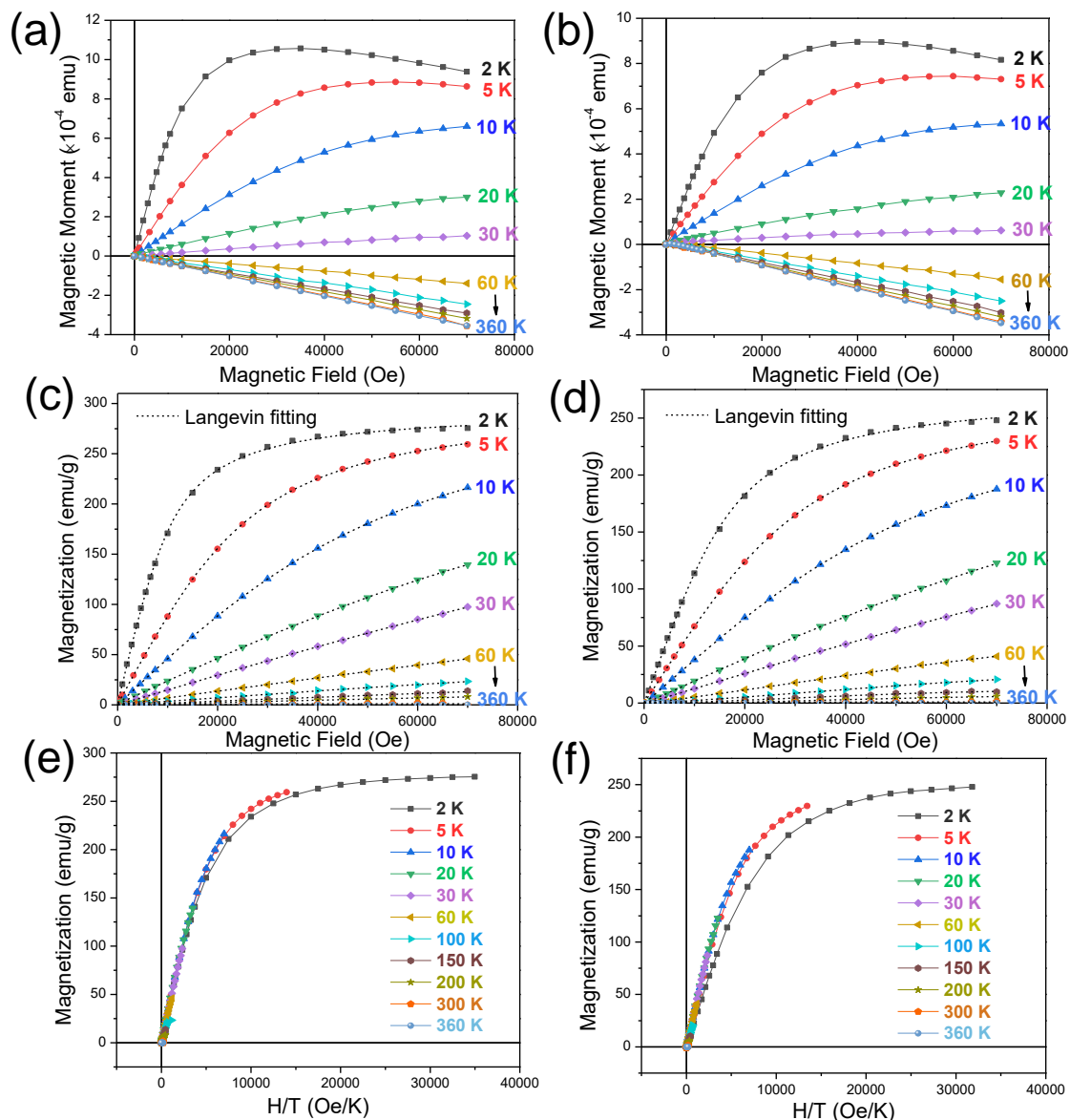
Figure 7.5 (a) In-plane and (b) out-of-plane magnetic moment as a function of magnetic field recorded under isothermal condition for the mica crystals (raw data), where the lines connecting the points are guides to the eye. (c) In-plane and (d) out-of-plane isothermal magnetization curves for the paramagnetic phase. The dashed lines are the fits to the Langevin function. (e) and (f) panels depict the corresponding M-H/T curves showing the curves collapse into a universal curve.

Finally, it is well-known that, from the Langevin theory, when the magnetization of a (super)paramagnet is plotted against *H/T* for different temperatures, all the curves overlap. The panels (e) and (f) of Figure 8.5 show the *M* versus *H/T* plots, corresponding to the in-plane and out-of-plane applied field geometries, respectively. The expected overlapping is observed for all the temperatures except for the curve at the lowest temperature (2 K), for which the deviation is might be related to some magnetic interactions at such low temperature. It is tempting to suggest appearing of dipole-dipole type of interactions and/or onset of long-range order at 2 K. However, since the concentration of the paramagnetic entities and their size are rather small any suggestion would be too speculative.

To summarize, we reported an in-depth study of the magnetic properties of commercial fluorophlogopite mica crystals as a function of magnetic field and temperature. Our study shows that the magnetic response of mica comprises diamagnetic and paramagnetic components. The latter is quite significant at low temperatures and can be analyzed within the framework of Curie's law and the Langevin theory. Hence, special care must be taken to study the magnetic properties of mica-supported nanostructures.

Furthermore, the effective moment μ_{eff} determined from the temperature dependence of magnetic susceptibility and magnetization curves, the size of the hypothetic clusters, the absence of coercivity and the fact that no difference between thermomagnetic curves measured after field- and zero-field cooling was observed at any field value, they all strongly support that the magnetic response of impurities in our mica crystals originates from isolated paramagnetic atoms. No evidence of blocked/unblocked superparamagnetic clusters or simply from magnetically ordered contaminations was found.

The way to separate and analyze the competing diamagnetic and paramagnetic responses to temperature and external magnetic field in fluorophlogopite mica has been demonstrated. It should be applicable to other diamagnetic materials containing paramagnetic impurities and could be useful when assessing the magnetic properties of nanoobjects grown on substrates of such materials.

7.3 Structural characterization of epitaxial ε-Fe₂O₃ thin films grown on mica

7.3.1 Stabilization of ε-Fe₂O₃ thin films on mica substrates

We studied two scenarios for the stabilization ε-Fe$_2$O$_3$ (eFO) on mica. First, we explored the possibility of direct stabilizing of epsilon iron oxide on exfoliated Mica and then the use of buffer layers which can promote the eFO growth. Spinel phase iron oxide films have been grown directly on mica substrate and achieved an excellent surface roughness and high crystalline (111) texture [39]. We selected the substrate growth temperature as principal growth parameter, which was varied from 750 to 850 °C. XRD θ-2θ measurements, shown in Figure 7.6(a) indicate that in the whole temperature range only α-Fe$_2$O$_3$ oxide with (00L) texture was stabilized. At the highest tested temperature (850ºC) additional peaks appear close to α-Fe$_2$O$_3$ (006) reflection and spinel (004), but both present a large offset with respect to the bulk parameters of the spinel phase. Thus it may be related to a degeneration of the mica substrates at elevated growth temperatures. Further investigation of structural stability of mica substrates might be necessary and for this work the highest growth temperature was set to 825ºC. As previously discussed in Chapter 6, Fe$_3$O$_4$ (111) layers are structurally compatible with (00L) texture of eFO and thus could be a suitable candidate for integrating eFO on mica substrates. The Fe$_3$O$_4$ layer (FO) has to be deposited in high vacuum conditions ($p<10^{-6}$ mbar) and then the oxygen background pressure has to be increased to 0.1 mbar to promote eFO growth. While we achieved high quality (111) oriented single layer Fe$_3$O$_4$ films (see XRD ω-2θ diffraction pattern in Figure 7.6(b) red curve), the consecutive deposition at high oxygen pressure (0.1 mbar) results in the full transformation of the film into α-Fe$_2$O$_3$. No evidence of film peaks for Fe$_3$O$_4$ (111) and eFO (00l) texture can be observed in Figure 7.6(b) black curve) within the experimental resolution. The introduction of buffer layers isostructural to ε-Fe$_2$O$_3$ is expected to favor the stabilization of this phase. In spite of the fact that AlFeO$_3$ (AFO) layers have enabled the stabilization of eFO on STO(111) substrates [40], AlFeO$_3$ did not properly grow with the expected (00L) orientation on mica, displaying a very low intensity (004) Bragg peak in Figure 7.6(c) for a 60 nm thick AFO film on mica. Indeed, this was one reason to develop the isostructural quaternary SAFO thin films reported in Chapter 5. Comparing 60 nm thick AFO and SAFO thin films (the blue and red curves in Figure 7.6(c), respectively), a much stronger (00L) out-of-plane orientation is found for SAFO. By growing a 15 nm (2kp) thick SAFO buffer layer followed by the deposition of iron oxide allows stabilizing eFO with (00L) out of plane texture as can be observed in the black curve in Figure 7.6(c). Since SAFO has been identified as a suitable buffer layer for eFO growth mica substrates, we explore the critical thickness of the eFO films. Films with eFO thickness 60, 75 and 90 nm were prepared on 15 nm SAFO buffer and the XRD ω-2θ diffraction pattern are plotted in Figure 7.6(d). The thicker films (75 and 90 nm) show both a high-intensity peak close to the α-Fe$_2$O$_3$ and a low-intensity peak close to eFO bulk position, the latter partly originated by the 15 nm SAFO buffer layer. This intensity

distribution indicates that after about 60-65 nm the metastable eFO film transforms into the more stable α-Fe₂O₃. Due to these findings we will concentrate on films with approximately 60 nm eFO on 15 nm SAFO buffer layer.
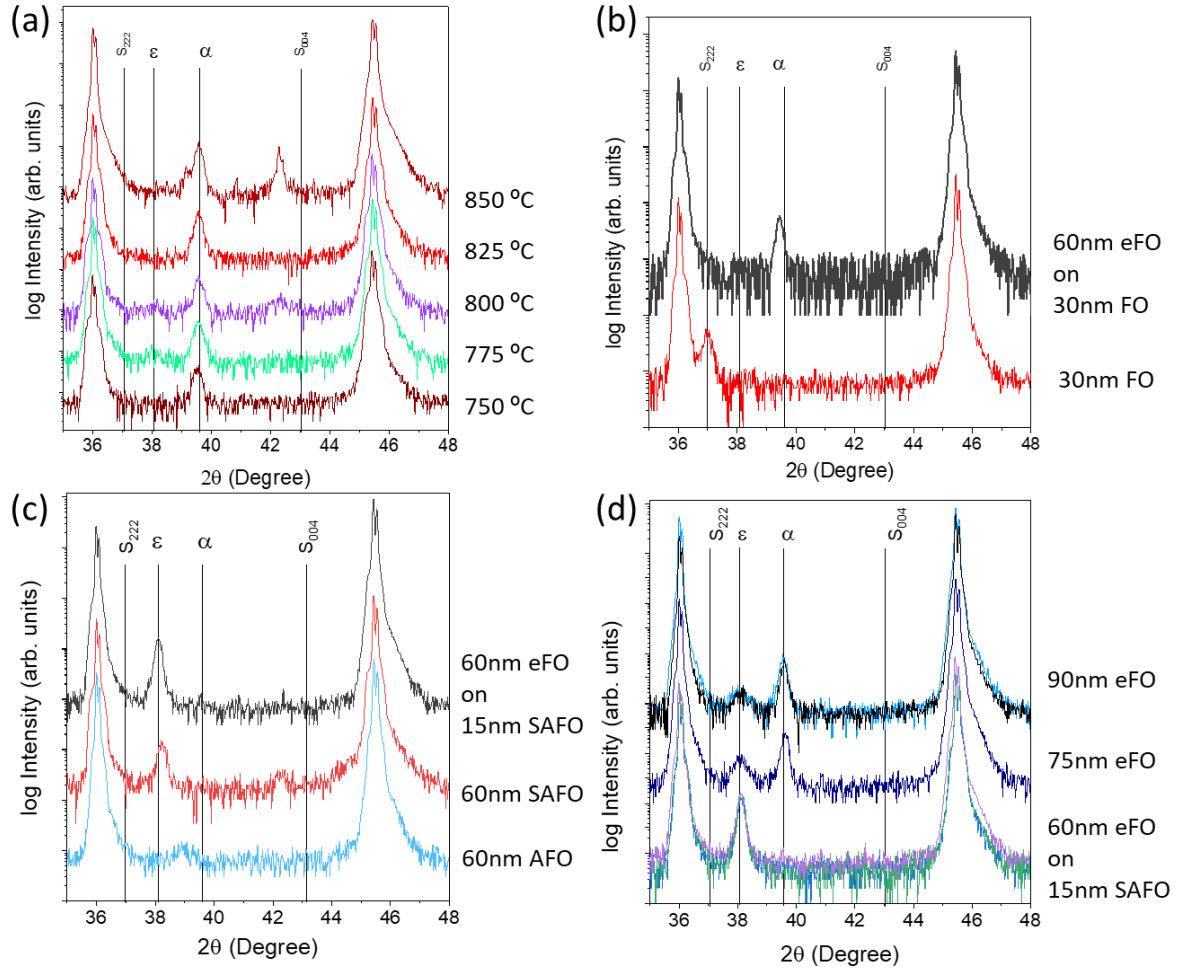
Figure 7.6. XRD θ-2θ diffraction patterns of ε-Fe₂O₃ films grown (a) directly on exfoliated Mica substrate vs. substrate temperature and (b-d) on buffer layers grown in situ. (b) Fe₃O₄ (4kp, 30 nm) single layer (red curve) and eFO (8kp, 60 nm) on Fe₃O₄ buffer layer (black curve). (c) 60 nm single layer AFO (blue) and SAFO (red) and 60 nm eFO on 15 nm SAFO (black). (d) Thickness dependence of eFO thin films on SAFO buffer. The highest intensity diffraction peaks correspond to mica (00L) substrate planes. The vertical lines indicate the peak positions for bulk spinel (S), epsilon (ε) and alpha (α) iron oxide phases.

7.3.2 Characterization of ε-Fe₂O₃ thin films on SAFO buffered mica substrates

The structural analysis of the ε-Fe₂O₃/SAFO//mica heterostructure is revisited in more detail using a Bruker D8 Discover high-resolution X-ray diffractometer. Figure 7.7(a) shows a high-resolution θ-2θ scan of the heterostructure, where the (004), (006) and (008) diffraction peaks of epsilon phase are observed. These sharp diffraction peaks indicate a high crystallinity of the 75-nm-thick ε-Fe₂O₃/SAFO films and likely a large eFO grain size.
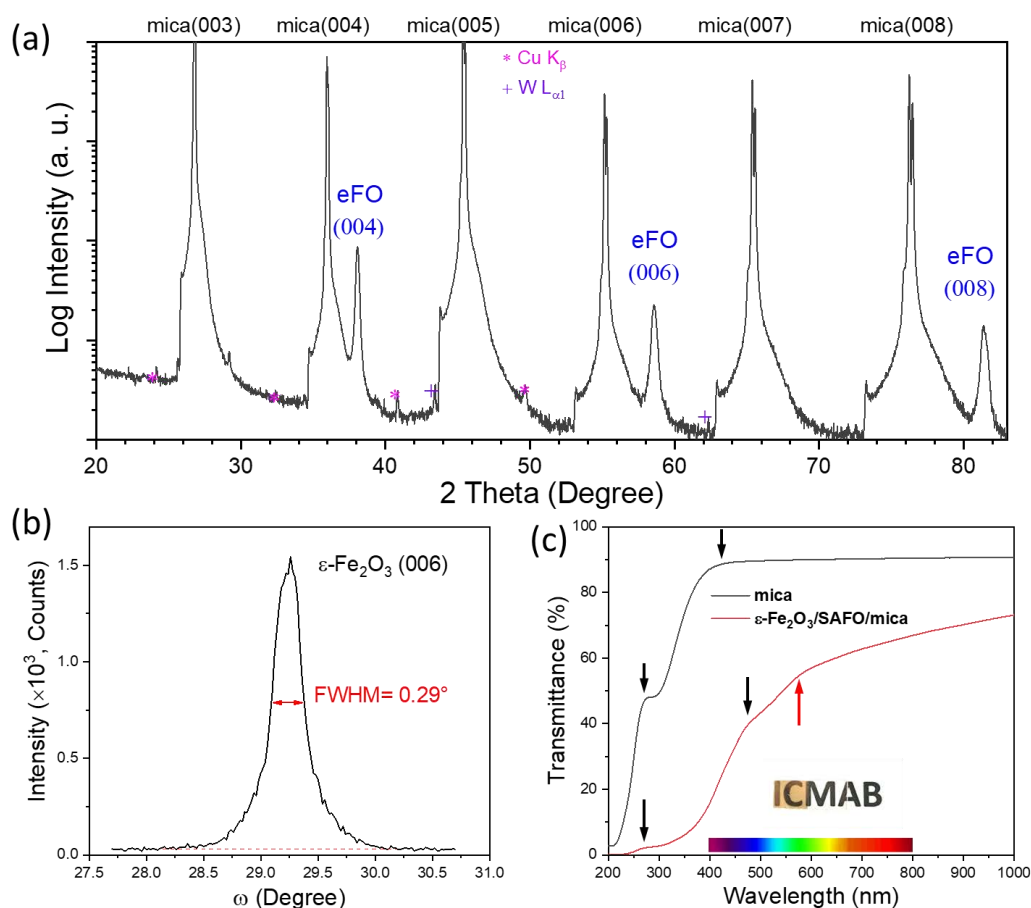

Figure 7.7 (a) High-resolution XRD θ-2θ scan of the eFO/SAFO//mica heterostructure, where the sharp (00l) peaks of the films are obvious. The peaks marked with an asterisk and cross symbols are the reflections due to Cu-K_β and W-L_α radiations of the X-ray source, respectively. (b) XRD rocking curve for the ε-Fe₂O₃ (006) diffraction peak. (d) The transmittance spectrum showing the semitransparent nature of the heterostructure. The spectrum from the mica substrate is also shown for comparison. The transmittance cutoffs due to the mica substrate and the thin films are respectively indicated by the black downward arrows and the red upward arrow. A photo of the heterostructure is displayed in the inset.

The full width at half maximum (FWHM) of the rocking curve of the (006) peak presented in Figure 7.7(b) is 0.29°, which is much smaller than the value reported by Knížek et al. (FWHM 0.8° on YSZ 001)[41] and significantly smaller than the FWHM values obtained for analogous rocking curves of 60 nm thick SAFO on mica (0.62°). The narrow rocking curve indicates that the films have high crystalline

quality with low mosaicity. Figure 7.7(c) presents the transmittance spectra of the heterostructure and a bare mica substrate. It can be appreciated that the absorption of the heterostructure is enhanced at all the wavelengths. The transmittance enhancement of the mica substrate at the wavelength of ∼400 nm is shifted to larger wavelengths and the visible transmittance lies between ∼30% at 400 nm and ∼70% at 800 nm. Moreover, a transmittance cutoff due to the films was observed at approximately 575 nm, which gives a bandgap of 2.16 eV for the epilayers. This value is consistent with the band gap reported by Quynh et al. (2.1 eV) [42].

The in-plane orientation was evaluated using XRD ϕ scans of ε-Fe$_2$O$_3$ (202) and mica (202) reflections (Figure 7.8(a)). The six peaks with a rotation of 60° indicate a six-fold in-plane symmetry of substrate and film. Two scenarios are possible due to monoclinic symmetry of mica. First, six in-plane domains could be present rotated each by 60°, and alternatively it may be explained by the hexagonal pseudosymmetry of mica with six-fold diffraction pattern around c^*. Due to the large substrate tails and proximity in $\omega 2\theta$-χ of (202), (132), (-133), (-201), (1-33), (1-32) these six peaks may contribute to the observed six peaks in the ϕ scan (performed with open slit). Although, here we used synthetic mica and thus twinning shall be reduced to some amount. So most likely a combination of both scenarios is present.

The reciprocal space mapping (RSM) in Figure 7.8(c)) shows mica (-207) and (206) reflection simultaneously, pointing to the presence of a 180° domain (or the spot does not correspond to (206) with $q_x = 3.762$ 1/nm / $q_z = 6.332$ 1/nm, but to (136) or (1-36) peaks with very similar $q_x = 3.761$ 1/nm and $q_z = 0.6338$ 1/nm). Thus, the interpretation for the film layer is similar. The top aluminosilicate layers in the mica consist of a hexagonal arrangement of corner-sharing (Si, Al)O$_4$ tetrahedra, creating a quasi-hexagonal in-plane lattice structure (3 nearly identical a, b lattice parameters rotated by 120°) and consequently the alignment of mica {202} and ε-Fe$_2$O$_3$ {202} peaks suggests the in-plane relationship as [100]$_{eFO}$ ∥ [100]$_{mica}$, as well as, [100]$_{eFO}$ ∥ [110]$_{mica}$ and [100]$_{eFO}$ ∥ [-110]$_{mica}$ considering 6 peaks in the phi scan (note that the scenario with 6 mica in-plane domains may not be distinct within the performed experiments). A schematic representation of the domain structure viewed along the [001] films direction is depicted in Figure 7.8(b). The RSM around the asymmetric ε-Fe$_2$O$_3$ (206) and mica (-207) Bragg peaks, also reveals that the film is fully relaxed along a. Due to the lack of a RSM map along b, we estimate it by the relation between the lattice spacings d_{hkl} and the lattice parameters (a, b and c) of orthorhombic lattices:

$$\frac{1}{d_{hkl}} = \sqrt{\frac{h^2}{a^2} + \frac{k^2}{b^2} + \frac{l^2}{c^2}} \qquad (7.4)$$

where the lattice spacing d_{hkl} of the {hkl} planes can be derived from the Bragg's law. The c parameter estimated by Nelson-Riley function from ω-2θ scans (see Chapter 5), a is fixed by the RSM around (206) and d_{hkl} from the 2θ position of (013), (022), (122) and (123) observed by low resolution pole

figure in an area detector system. The resulting ε-Fe$_2$O$_3$ lattice constants are a = 5.085(8) Å, b = 8.801(18) Å and c = 9.440(8) Å. These values are in good agreement with bulk values of ε-Fe$_2$O$_3$ a = 5.09 Å and b = 8.78 Å and c = 9.46 Å and we can conclude the films are fully relaxed.
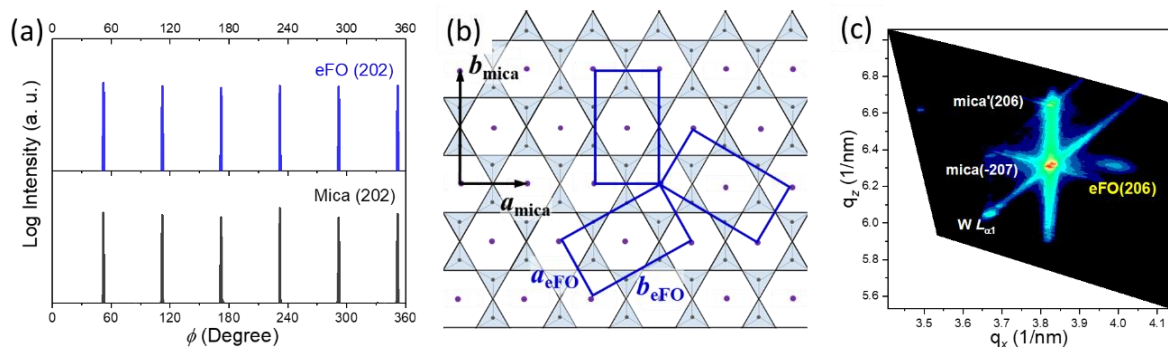

Figure 7.8 (a) XRD ϕ scans of the ε-Fe$_2$O$_3$ (202) and mica (202) reflections for the eFO/SAFO films deposited on mica substrate. (b) A schematic illustration of the domain structure viewed along the [001] direction of the films. The top hexagons of corner sharing (Si, Al)O$_4$ tetrahedra create a quasi-hexagonal in-plane lattice structure of mica, compatible with the 3 different domains of ε-Fe$_2$O$_3$. (c) High-resolution XRD asymmetry RSM around mica (-207) and ε-Fe$_2$O$_3$ (206) reflections.

The surface topography of SAFO 15 nm buffer layer and the eFO/SAFO heterostructure, along with the height profiles, are presented in Figure 7.9(a) and (b), respectively. While the buffer layer shows a smooth (but granular) surface with root mean square (RMS) roughness around 4.5 nm, the eFO/SAFO heterostructure shows a high density of 3D islands, which suggests a columnar growth of the films. The 3D islands mostly feature regular hexagonal/truncated triangle shapes, often displaying flat-top surfaces as can be seen in the height profiles of Figure 7.9(b). The lateral dimensions of the islands are about 100 nm and about 25 nm in height. Nevertheless, some can reach heights up to 40 nm (the relative area of the grains with sizes below 40 nm account for more than 95 % from the 5×5 μm^2 image). Similar crystal shapes have been observed in ε-Fe$_2$O$_3$ grown by CVD unit cell [15]. In this work, a TEM study of a truncated triangular flake that could be removed from the mica and transferred directly onto a TEM grid revealed that it consists of arrangements of the three types of domains as the ones displayed in Figure 7.8(b) which are found in ε-Fe$_2$O$_3$ epitaxial films grown by PLD on hexagonal or pseudohexagonal surfaces such as (111) cubic substrates or (001) mica.
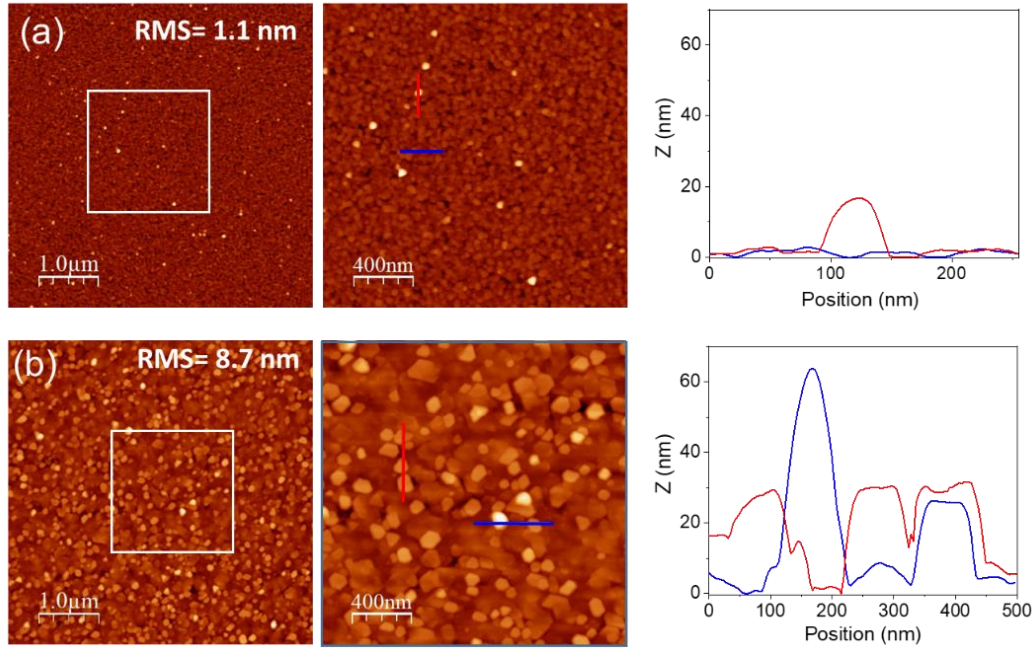
Figure 7.9 AFM analysis of the (a) 15nm SAFO buffer layer and (b) the thin film heterostructure 60 nm eFO on SAFO. A topographic image from a 5×5 μm^2 scanned area is shown in the left. The delineated area (2×2 μm^2) topographic image is shown in the middle penal, along with the line profiles along the marked lines in the right panel.

Figure 7.10 presents TEM images of a cross section of eFO/SAFO heterostructure on mica. Panel (a) shows a low magnification Z-contrast overview of the columnar structures, where the different density of the iron oxide film and the mica substrate is clearly appreciated. In the higher magnification image of Panel (b) we can see the flat surface of the islands and the presence of lateral facets. A red square centered in one of these lateral facets has been imaged in atomic resolution and is presented in panel (c). The image is characteristic of a crystal oriented along the zone axis as previously observed in [43]. Panels (d) and (e) correspond to bright-field images in which fringes stemming from atomic planes can be observed for the film and the substrate indicating that there is a good epitaxy. This is confirmed by the fast Fourier transform of all the image of Figure 7.10(e) included as an inset and which is in agreement with an orientation along the zone axes [100] of mica and [-1-10] of the ε-Fe₂O₃ film. The Mica substrate got very damaged under the electron beam during the image acquisition and this explains why there are regions of the substrate without fringes.
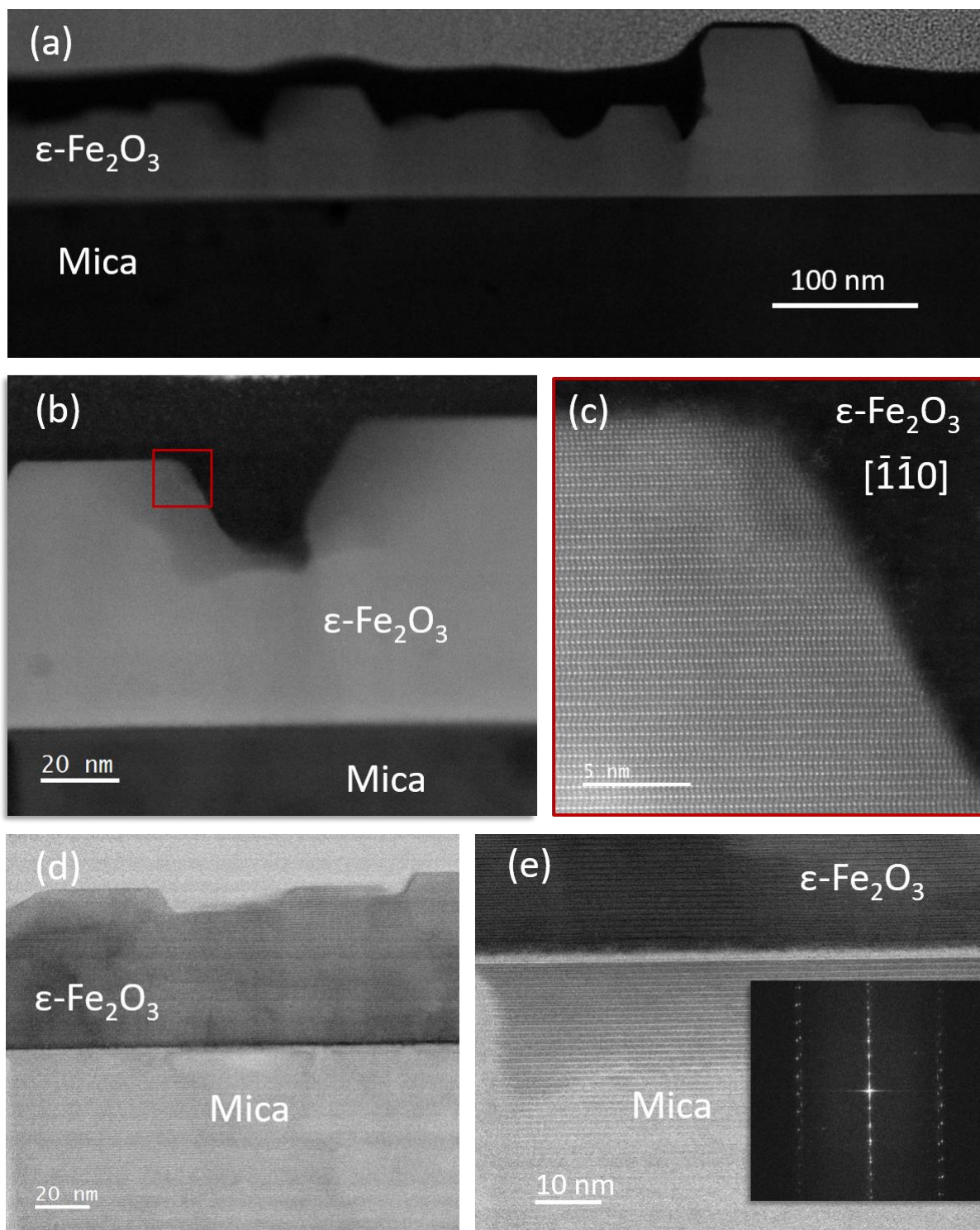
Figure 7.10. TEM images of a cross-section of eFO/SAFO heterostructure on mica. Z-contrast images: (a) Low magnification overview of the heterostructure showing 3D islands with flat surface, (b) Higher magnification of the islands in which the red square corresponds to the area of (c) atomic resolution image of one of the islands which can be assigned to ε-Fe$_2$O$_3$ oriented along the [-1-10] zone axis. (d) Bright field image of film and substrate in which where fringes of the atomic planes are visible, but in some zones of mica these are lost due to beam amorphisation.(e) Higher magnification bright field image around the interface where fringes are clearly visible for the substrate and the film except at the interface, probably due to beam amorphisation. The inset shows the fast Fourier transform of the whole image which is in agreement with an orientation along the zone axes [100] of mica and [-1-10] of the ε-Fe$_2$O$_3$ film.

7.4 Magnetic properties of epitaxial ε-Fe₂O₃ thin films grown on mica

Having addressed the structural features of the ε-Fe$_2$O$_3$/SAFO//mica heterostructure, the next step is to characterize its magnetic response with respect to temperature and external magnetic field. We first consider the temperature-dependent magnetic properties. Figure 7.11 shows the magnetic moment *m* as a function of temperature *T* (*m-T* curve) measured in the virgin demagnetized state under a magnetic field of 10 kOe applied in-plane. It can be seen that *m* firstly decreases rapidly as the *T* increases up to ~50 K and then it starts to increase reaching a maximum value at about 100 K, accompanied by a final gradual decrease until 300 K. On the basis of our previous discussion (Section 7.2), three magnetic responses are expected in this heterostructure: the magnetic signal from the film and the paramagnetic and diamagnetic contributions from the F-mica substrate. The initial drop of *m* is due to the paramagnetic response from the substrate, whereas the local maximum can be related to the onset of a low-temperature transition similar to the one discussed in Chapter 6 for the ε-Fe$_2$O$_3$ films grown on MAO(111). Such feature is also observed in the low-field ZFC-FC *m-T* curves measured on a demagnetized ε-Fe$_2$O$_3$/SAFO//mica heterostructure (Figure 7.11).
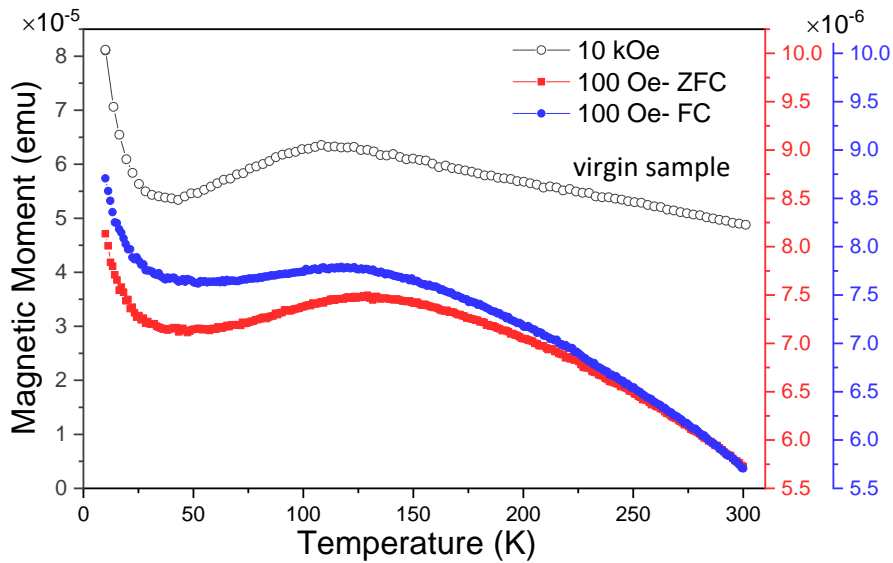
Figure 7.11 Temperature dependence of the in-plane magnetic moments (*m-T* curves) for the eFO/SAFO//mica heterostructure (raw data). The *m-T* curve at *H*= 10 kOe (empty circles) was taken on the sample initially in its virgin state. The in-plane *m-T* curve recorded with a low-field *H*= 100 Oe at ZFC (filled red squares) and FC (filled blue circles) conditions. The solid lines connecting the symbols are guides to the eye. Note the different scale on the left and right axis. Note the different scales between the two Y-axes (left and right).

Figure 7.12(a) presents the isothermal magnetic moment versus magnetic field (*m-H*) curves up to a maximum in-plane magnetic field of 70 kOe. For the curves measured at 5 K and 10 K we observe a magnetic signal which is significantly larger than for measurements at higher temperatures. This can be attributed to the paramagnetic impurities of the mica substrate discussed in Section 7.2, which become dominant at very low temperatures (below 30 K). The complete hysteresis and are characteristic

183

a hard magnetic response and at all the temperatures there is a remanent magnetic moment at $H= 0$ (Figure 7.12(b)).
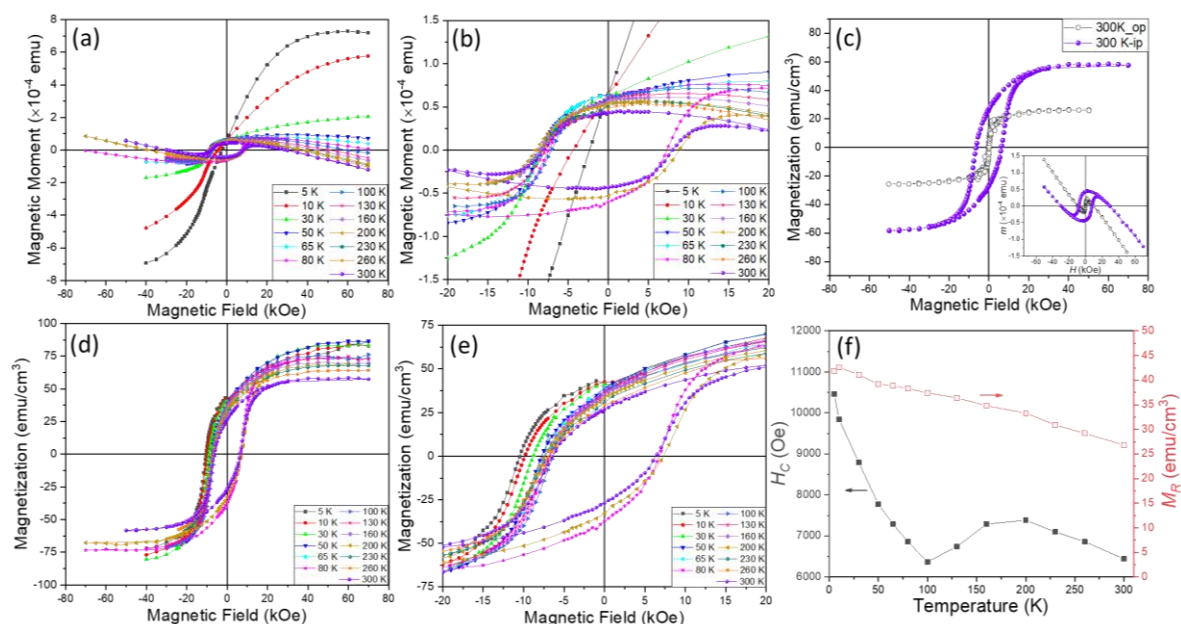

Figure 7.12 (a) Magnetic field dependence of the in-plane magnetic moment (*m-H* curves) recorded with a maximum magnetic field of 70 kOe for the eFO/SAFO//mica heterostructure (raw data). For temperatures below 50 K only half of the loop has been measured. (b) The enlarged low-field regions of the hysteresis loops. (c) The room temperature hysteresis loops acquired under the magnetic field along the in-plane or out-of-plane directions. The inset shows the raw data. (d) The corrected hysteresis loops after removing the substrate contributions. An enlarged image of the low-field region is presented in Panel (e). The coercivity (H_C) and remanent magnetization (M_R) as a function of temperature are summarized in Panel (f).

It is also interesting to note that the hysteresis loops do not present step-like behaviors at $H= 0$, which is generally ascribed to the presence of other secondary magnetic soft phases. For comparison, the in-plane and out-of-plane room temperature hysteresis loops are shown in Figure 7.12(c). In contrast to the round-shaped in-plane loop with a quite large coercivity $H_C= 6450$ Oe, the out-of-plane hysteresis presents a much smaller H_C of less than 200 Oe, which may correlated with a misplacement of the sample on the sample holder. This observation is in agreement with the fact that the magnetic easy axis of ε-Fe₂O₃, which coincides with the crystallographic *a*-axis, lies within the film basal plane. The maximum magnetization observed for the out-of-plane measurement is significantly lower than that of the in-plane measurement. This is an intriguing behavior has been observed previously by us and other groups studying thin films of ε-Fe₂O₃ and related compounds but never properly discussed [43–45]. Comparing the out-of-plane magnetizations up to 40 kOe reported by Itoh and coworkers of films in which iron has been partially substituted by ε-$A_{0.2}Ga_{0.4}Fe_{1.4}$, with A=Sc, Ga, Fe one can see the out-of-plane magnetization at saturation tends to approach that of the in-plane measurement as the coercive field decreases [45]. Thus, the significantly lower out-of-plane magnetization of ε-Fe₂O₃ films as compared to the in-plane value is a consequence of their large magnetic anisotropy.

Next, we subtract the F-mica substrate contribution from the obtained loops. This is done, for loops measured at $T > 10$ K, by compensating the signal obtained from the linear fitting of the curves at the high-field end. This is reasonable considering that both the paramagnetic and the diamagnetic responses of mica show a linear dependence on magnetic fields (see Section 7.2.2). On the other hand, for correcting the M-H curves at 5 K and 10 K, we have utilized the m-H curves of F-mica substrate acquired at the same temperatures (see Figure 7.5(a)). More precisely, we first extrapolated the whole hysteresis loops using the Langevin function. Then, the hysteresis loops with the magnetization were obtained from the known mass of the F-mica (13.81 mg). Finally, assuming that the mass of the mica substrate is the same as the eFO/SAFO//mica heterostructure (9.64 mg), the magnetic moment from the mica can be estimated, and then subtracted from the raw m-H hysteresis loops. The resulting hysteresis loops of the films are shown in Figure 7.12(d) and (e). The H_C and M_R values obtained from the loops are represented as a function of temperature in Figure 7.12(f). The evolution of the H_C and M_R is quite similar to the one measured for ε-Fe$_2$O$_3$//MAO(111) films, pointing to the existence of a similar a low-temperature transition as the one discussed in Chapter 6.

7.5 Summary

We reported an in-depth study of the magnetic properties of commercial fluorophlogopite mica crystals as a function of magnetic field and temperature. The magnetic response of mica comprises diamagnetic and paramagnetic components. The latter is quite significant at low temperatures and can be analyzed within the framework of Curie's law and the Langevin theory, which indicate that it originates from isolated magnetic cations. We propose a protocol to correct the magnetic contributions of mica substrates. Then, we discussed the structural properties of ε-Fe$_2$O$_3$/SAFO//mica films. The magnetic characterization of the films provides evidence of the presence of the low-temperature magnetic transition. The coercivity H_C evolution obtained from the magnetic hysteresis loops has some resemblance with that of its nanoparticle counterpart. The H_C is as large as 10 kOe (1 T) at low temperatures. The ε-Fe$_2$O$_3$/SAFO//mica films will allow future exploration of the functional properties of epitaxial ε-Fe$_2$O$_3$ thin films on flexible 2D substrates.

References

[1]   I. Langmuir, The adsorption of gases on plane surfaces of glass, mica and platinum, J. Am. Chem. Soc. 40 (1918) 1361–1403. https://doi.org/10.1021/ja02242a004.

[2]   B. Drake, C. Prater, A. Weisenhorn, S. Gould, T. Albrecht, C. Quate, D. Cannell, H. Hansma, P. Hansma, Imaging crystals, polymers, and processes in water with the atomic force microscope, Science (80-.). 243 (1989) 1586–1589. https://doi.org/10.1126/science.2928794.

[3]   J.W. Matthews, Defects in silver films prepared by evaporation of the metal onto mica, Philos. Mag. 7 (1962) 915–932. https://doi.org/10.1080/14786436208212889.

[4]   C.E.D. Chidsey, D.N. Loiacono, T. Sleator, S. Nakahara, STM study of the surface morphology of gold on mica, Surf. Sci. 200 (1988) 45–66. https://doi.org/10.1016/0039-6028(88)90432-3.

[5]   K. Ueno, K. Saiki, T. Shimada, A. Koma, Epitaxial growth of transition metal dichalcogenides on cleaved faces of mica, J. Vac. Sci. Technol. A Vacuum, Surfaces, Film. 8 (1990) 68–72. https://doi.org/10.1116/1.576983.

[6]   J. Jiang, Y. Bitla, C.W. Huang, T.H. Do, H.J. Liu, Y.H. Hsieh, C.H. Ma, C.Y. Jang, Y.H. Lai, P.W. Chiu, W.W. Wu, Y.C. Chen, Y.C. Zhou, Y.H. Chu, Flexible ferroelectric element based on van der Waals heteroepitaxy, Sci. Adv. 3 (2017) e1700121. https://doi.org/10.1126/sciadv.1700121.

[7]   J. Liu, Y. Feng, R. Tang, R. Zhao, J. Gao, D. Shi, H. Yang, Mechanically Tunable Magnetic Properties of Flexible $SrRuO_3$ Epitaxial Thin Films on Mica Substrates, Adv. Electron. Mater. 4 (2018) 1700522. https://doi.org/10.1002/aelm.201700522.

[8]   H.R. Shelll, K.H. Ivey, Fluorine Micas, Washington D. C., 1969.

[9]   S.W. Bailey, Structures of Layer Silicates, in: Cryst. Struct. Clay Miner. Their X-Ray Identif., Mineralogical Society of Great Britain and Ireland, 2015: pp. 1–124. https://doi.org/10.1180/mono-5.1.

[10]   W. De Poel, S. Pintea, J. Drnec, F. Carla, R. Felici, P. Mulder, J.A.A.W. Elemans, W.J.P. Van Enckevort, A.E. Rowan, E. Vlieg, Muscovite mica: Flatter than a pancake, Surf. Sci. 619 (2014) 19–24. https://doi.org/10.1016/j.susc.2013.10.008.

[11]   James W. McCauley ; R. E. Newnham ; G. V. Gibbs, Crystal Structure Analysis of Synthetic Fluorophlogopite, Am. Mineral. 58 (1973) 249–254. https://doi.org/https://doi.org/.

[12]   Z. Liang, C. Ma, L. Shen, L. Lu, X. Lu, X. Lou, M. Liu, C.L. Jia, Flexible lead-free oxide film capacitors with ultrahigh energy storage performances in extremely wide operating temperature, Nano Energy. 57 (2019) 519–527. https://doi.org/10.1016/j.nanoen.2018.12.056.

[13]   C. Yang, P. Lv, J. Qian, Y. Han, J. Ouyang, X. Lin, S. Huang, Z. Cheng, Fatigue-Free and Bending-Endurable Flexible Mn-Doped Na 0.5 Bi 0.5 TiO 3 -BaTiO 3 -BiFeO 3 Film Capacitor with an Ultrahigh Energy Storage Performance, Adv. Energy Mater. 9 (2019) 1803949. https://doi.org/10.1002/aenm.201803949.

[14]   T. Amrillah, Y. Bitla, K. Shin, T. Yang, Y.-H. Hsieh, Y.-Y. Chiou, H.-J. Liu, T.H. Do, D. Su, Y.-C. Chen, S.-U. Jen, L.-Q. Chen, K.H. Kim, J.-Y. Juang, Y.-H. Chu, Flexible Multiferroic Bulk Heterojunction with Giant Magnetoelectric Coupling via van der Waals Epitaxy, ACS Nano. 11 (2017) 6122–6130. https://doi.org/10.1021/acsnano.7b02102.

[15]   J. Yuan, A. Balk, H. Guo, Q. Fang, S. Patel, X. Zhao, T. Terlier, D. Natelson, S. Crooker, J. Lou, Room-Temperature Magnetic Order in Air-Stable Ultrathin Iron Oxide, Nano Lett. 19 (2019) 3777–3781. https://doi.org/10.1021/acs.nanolett.9b00905.

[16]   H.J. Liu, C.K. Wang, D. Su, T. Amrillah, Y.H. Hsieh, K.H. Wu, Y.C. Chen, J.Y. Juang, L.M. Eng, S.U. Jen, Y.H. Chu, Flexible Heteroepitaxy of CoFe2O4/Muscovite Bimorph with Large Magnetostriction, ACS Appl. Mater. Interfaces. 9 (2017) 7297–7304. https://doi.org/10.1021/acsami.6b16485.

[17]   G. Lan, L. Shen, L. Lu, C. Cao, C. Jiang, H. Fu, C. You, X. Lu, C. Ma, M. Liu, C.L. Jia, Flexible Lithium Ferrite Nanopillar Arrays for Bending Stable Microwave Magnetism, ACS Appl. Mater. Interfaces. 10 (2018) 39422–39427. https://doi.org/10.1021/acsami.8b12954.

[18]   W. Liu, M. Liu, R. Ma, R. Zhang, W. Zhang, D. Yu, Q. Wang, J. Wang, H. Wang, Mechanical Strain-Tunable Microwave Magnetism in Flexible $CuFe_2O_4$ Epitaxial Thin Film for Wearable Sensors, Adv. Funct. Mater. 28 (2018) 1705928. https://doi.org/10.1002/adfm.201705928.

[19]   J. Huang, H. Wang, X. Sun, X. Zhang, H. Wang, Multifunctional $La_{0.67}Sr_{0.33}MnO_3$ (LSMO) Thin Films Integrated on Mica Substrates toward Flexible Spintronics and Electronics, ACS Appl. Mater. Interfaces. 10 (2018) 42698–42705. https://doi.org/10.1021/acsami.8b16626.

[20]   M.T. Dau, C. Vergnaud, M. Gay, C.J. Alvarez, A. Marty, C. Beigné, D. Jalabert, J.F. Jacquot, O. Renault, H. Okuno, M. Jamet, Van der Waals epitaxy of Mn-doped $MoSe_2$ on mica, APL Mater. 7 (2019). https://doi.org/10.1063/1.5093384.

[21]   J.T. Kendall, D. Yeo, Magnetic Susceptibility and Anisotropy of Mica, Proc. Phys. Soc. Sect. B. 64 (1951) 135–142. https://doi.org/10.1088/0370-1301/64/2/306.

[22]   A.R. Biedermann, C. Bender Koch, W.E.A. Lorenz, A.M. Hirt, Low-temperature magnetic anisotropy in micas and chlorite, Tectonophysics. 629 (2014) 63–74. https://doi.org/10.1016/j.tecto.2014.01.015.

[23]   O. Ballet, J.M.D. Coey, Magnetic properties of sheet silicates; 2:1 layer minerals, Phys. Chem. Miner. 8 (1982) 218–229. https://doi.org/10.1007/BF00309481.

[24]   J.M.D. Coey, S. Ghose, Magnetic Ordering and Thermodynamics in Silicates, in: Phys. Prop. Thermodyn. Behav. Miner., Springer Netherlands, 1988: pp. 459–499. https://doi.org/10.1007/978-94-009-2891-6_14.

[25]   V. Schmidt, A.M. Hirt, P. Rosselli, F. Martín-Hernández, Separation of diamagnetic and paramagnetic anisotropy by high-field, low-temperature torque measurements, Geophys. J. Int. 168 (2007) 40–47. https://doi.org/10.1111/j.1365-246X.2006.03202.x.

[26]   M. Zheng, H. Sun, K.W. Kwok, Mechanically controlled reversible photoluminescence response in all-inorganic flexible transparent ferroelectric/mica heterostructures, NPG Asia Mater. 11 (2019) 1–8. https://doi.org/10.1038/s41427-019-0153-7.

[27]   M. Zheng, X.Y. Li, H. Ni, X.M. Li, J. Gao, Van der Waals epitaxy for highly tunable all-inorganic transparent flexible ferroelectric luminescent films, J. Mater. Chem. C. 7 (2019) 8310–8315. https://doi.org/10.1039/c9tc01684h.

[28]   F. Tsui, P.D. Han, C.P. Flynn, Growth of rare-earth monolayers on synthetic fluorine mica, Phys. Rev. B. 47 (1993) 13648–13652. https://doi.org/10.1103/PhysRevB.47.13648.

[29]   Z. Ma, V. Skumryev, M. Gich, Magnetic properties of synthetic fluorophlogopite mica crystals, Mater. Adv. 1 (2020) 1464–1471. https://doi.org/10.1039/d0ma00317d.

[30]   S.R. Zhao, C. Xu, C. Li, Identification of twins in muscovite: An electron backscattered diffraction study, Zeitschrift Fur Krist. - Cryst. Mater. 234 (2019) 329–340. https://doi.org/10.1515/zkri-2018-2139.

[31]   S. Pini, M.F. Brigatti, M. Affronte, D. Malferrari, A. Marcelli, Magnetic behavior of trioctahedral micas with different octahedral Fe ordering, Phys. Chem. Miner. 39 (2012) 665–674. https://doi.org/10.1007/s00269-012-0520-1.

[32]   Q. Wang, C. Zhu, J. Yun, G. Yang, Isomorphic Substitutions in Clay Materials and Adsorption of Metal Ions onto External Surfaces: A DFT Investigation, J. Phys. Chem. C. 121 (2017) 26722–26732. https://doi.org/10.1021/acs.jpcc.7b03488.

[33]   A. Ibhi, H. Nachitand, H. El Abia, Titanium and barium incorporation into the phyllosilicate phases: The example of phlogopite-kinoshitalite solid solution, J. Phys. IV JP. 123 (2004) 331–335. https://doi.org/10.1051/jp4:2005123060.

[34]   E. Schingaro, F. Scordari, E. Mesto, M.F. Brigatti, G. Pedrazzi, Cation-site partitioning in Ti-rich micas from Black Hill (Australia): A multi-techical approach, Clays Clay Miner. 53 (2005) 179–189. https://doi.org/10.1346/CCMN.2005.0530208.

[35]   A. Gianfagna, F. Scordari, S. Mazziotti-Tagliani, G. Ventruti, L. Ottolini, Fluorophlogopite from Biancavilla (Mt. Etna, Sicily, Italy): Crystal structure and crystal chemistry of a new F-dominant analog of phlogopite, Am. Mineral. 92 (2007) 1601–1609. https://doi.org/10.2138/am.2007.2502.

[36]   P. Popper, Transmission of natural and synthetic mica in the ultra-violet, Nature. 168 (1951) 1119–1120.

https://doi.org/10.1038/1681119b0.

[37] R.N. Dhar, S.R. Das, Transmission of Inidan mica between 300 and 1,000 mµ and its visual classification [4], Nature. 209 (1966) 185–186. https://doi.org/10.1038/209185a0.

[38] A. Lawska-Waniewska, M. Gutowski, H.K. Lachowicz, T. Kulik, H. Matyja, Superparamagnetism in a nanocrystalline Fe-based metallic glass, Phys. Rev. B. 46 (1992) 14594–14597. https://doi.org/10.1103/PhysRevB.46.14594.

[39] P.C. Wu, P.F. Chen, T.H. Do, Y.H. Hsieh, C.H. Ma, T.D. Ha, K.H. Wu, Y.J. Wang, H.B. Li, Y.C. Chen, J.Y. Juang, P. Yu, L.M. Eng, C.F. Chang, P.W. Chiu, L.H. Tjeng, Y.H. Chu, Heteroepitaxy of Fe3O4/Muscovite: A New Perspective for Flexible Spintronics, ACS Appl. Mater. Interfaces. 8 (2016) 33794–33801. https://doi.org/10.1021/acsami.6b11610.

[40] M. Gich, I. Fina, A. Morelli, F. Sánchez, M. Alexe, J. Gàzquez, J. Fontcuberta, A. Roig, Multiferroic Iron Oxide Thin Films at Room Temperature, Adv. Mater. 26 (2014) 4645–4652. https://doi.org/10.1002/adma.201400990.

[41] K. Knížek, M. Pashchenko, P. Levinský, O. Kaman, J. Houdková, P. Jiříček, J. Hejtmánek, M. Soroka, J. Buršík, Spin Seebeck effect in ϵ-Fe2O3 thin films with high coercive field, J. Appl. Phys. 124 (2018) 213904. https://doi.org/10.1063/1.5045304.

[42] L.T. Quynh, C.N. Van, Y. Bitla, J.W. Chen, T.H. Do, W.Y. Tzeng, S.C. Liao, K.A. Tsai, Y.C. Chen, C.L. Wu, C.H. Lai, C.W. Luo, Y.J. Hsu, Y.H. Chu, Self-Assembled BiFeO3-ε-Fe2O3 Vertical Heteroepitaxy for Visible Light Photoelectrochemistry, Adv. Energy Mater. 6 (2016) 1–8. https://doi.org/10.1002/aenm.201600686.

[43] M. Gich, J. Gazquez, A. Roig, A. Crespi, J. Fontcuberta, J.C. Idrobo, S.J. Pennycook, M. Varela, V. Skumryev, M. Varela, Epitaxial stabilization of ε-Fe$_2$O$_3$ (00l) thin films on SrTiO3 (111), Appl. Phys. Lett. 96 (2010) 112508. https://doi.org/10.1063/1.3360217.

[44] Y. Hamasaki, T. Shimizu, S. Yasui, T. Taniyama, M. Itoh, Evidence of ferroelectricity in ferrimagnetic κ-Al$_2$O$_3$-type In0.25Fe1.75O3 films, Appl. Phys. Lett. 109 (2016) 162901. https://doi.org/10.1063/1.4964826.

[45] T. Katayama, S. Yasui, Y. Hamasaki, T. Osakabe, M. Itoh, Chemical tuning of roomerature ferrimagnetism and ferroelectricity in ε-Fe$_2$O$_3$-type multiferroic oxide thin films, J. Mater. Chem. C. 5 (2017) 12597–12601. https://doi.org/10.1039/c7tc04363e.

Chapter 8

General Conclusions and Outlook

8.1 General conclusions

In this thesis, we have presented the synthesis of ε-Fe_2O_3 and its related oxides in the forms of nanoparticle and thin film, as well as a series of experimental investigations of their properties. Results were discussed in two parts: ε-Fe_2O_3 nanoparticles (**Part I**) and epitaxial ε-Fe_2O_3 thin films (**Part II**).

In **Part I**, we have provided further insights into the structural and magnetic properties of ε-Fe_2O_3 (Chapter 3) as well as transition-metal doped ε-Fe_2O_3 (Chapter 4) nanoparticles synthesized by sol-gel chemistry. The main conclusions are summarized below:

i) High-quality ε-Fe_2O_3 nanoparticles of 20 nm in diameter have been synthesized by sol-gel chemistry. A coercive field (H_C) of around 14 kOe was found at room temperature for the particles. Above 300 K, a magnetic transition FM2-FM1 takes place at $T_{N2} \sim 490$ K and meanwhile the H_C collapse near T_{N2}. The magnetocaloric properties associated with this magnetostructural transition have been evaluated. Preliminary high-pressure synchrotron X-ray diffraction experiments reveal the existence of anomalous thermal expansion under pressure near this phase transition. Below 300 K, the presence of incommensurate IM1 phase was evidenced by both magnetometry and neutron diffraction studies in our particles. The research on nanoparticles has brought new insights on the high and low-temperature phase transitions of pure ε-Fe_2O_3, revealing its sensitivity to magnetic fields and strain state.

ii) It has been found that Cr^{3+} preferentially substitutes Fe^{3+} in the regular octahedral environment of ε-$(Fe_{1-x}Cr_x)_2O_3$, drastically reducing the magnetic anisotropy and saturation magnetization of the

nanoparticles. The Fe^{3+} replacement by Cr^{3+} was studied up x=0.25 without the appearance of other secondary phases but strong evidence of structural evolution was observed for x>0.10. The Mn substitution was studied up to x=0.20 and did not induce the appearance of additional secondary phases but above x=0.10 a structural change was also observed. In connection with this, low Mn substitution has the effect of enhancing the magnetic anisotropy which rapidly falls for x>0.05 while the magnetization is strongly increased. In contrast to Cr and Mn, the Co substitution was found to be limited to 3 at. % with secondary phases appearing above this limit. Even such small substitutions resulted in significant changes of the lattice parameters with the effect of stretching a and compressing b and c, most likely as a consequence of magnetoelastic effects related to the unquenched orbital moment of Co^{2+}. The latter seems to strongly influence the high-temperature magnetic transition of ε-Fe_2O_3 by magnetically stabilizing the regular octahedral and tetrahedral sublattices of Fe^{3+}. The synthesis of stoichiometric Ru substituted ε-Fe_2O_3 was challenging due to the volatility of this metal and the magnetic characteristics of the Ru-doped nanoparticles presented reproducibility issues among different batches, indicating that experimental improvements are still needed.

In **Part II** of this thesis, we explored the stabilization mechanisms of ε-Fe_2O_3 epitaxial thin films grown by pulsed laser deposition, and the characterization of their structural and magnetic properties. The main results are:

i) We investigated the effect of different substrates on the structural characteristics of the top $Sc_{0.2}Al_{0.4}Fe_{1.4}O_3$ layers primarily by X-ray diffraction. ε-Fe_2O_3 structure was successfully stabilized on substrates of perovskite-type, spinel-type and some (001)-oriented cubic oxides (e.g., YSZ (001) and GGG (001)), as well as fluorophlogopite mica. In particular, high-quality epitaxial films have been deposited on LSAT (111), STO (111), Mica (001) and YSZ (001) substrates.

ii) The above work has allowed us to stabilize epitaxial ε-Fe_2O_3 films on flexible Mica substrates using $Sc_{0.2}Al_{0.4}Fe_{1.4}O_3$ films as a buffer layer. A careful examination of the magnetic properties of mica crystals, which reveals the presence of paramagnetic response in the substrate, promises an accurate evaluation of the intrinsic properties of the ε-Fe_2O_3 films. The magnetic characterization of the ε-Fe_2O_3 films on Mica revealed the existence of a low-temperature magnetic transition which reminds that of ε-Fe_2O_3 nanoparticles, but which had not been previously reported in films.

iii) We also stabilized epitaxial ε-Fe_2O_3 (001) films on Fe_3O_4 (111) spinel buffer layers or directly on $MgAl_2O_4$ (111) (MAO (111)) substrates. It was found that impurities are prone to appear when Fe_3O_4 (111) layers are used due to the structural compatibility between different iron oxide polymorphs. The low-temperature magnetic transition was also found on the ε-Fe_2O_3 films directly grown on MAO (111). Not only does Raman spectroscopy provide an effective way for fast phase identification, but it also is a powerful tool to probe both the high and low-temperature magnetostructural transformations in this system.

8.2 Outlook and future work

ε-Fe$_2$O$_3$ has attracted considerable attention in the scientific community in the last two decades, by virtue of its exotic and fascinating properties, including a giant magnetic coercivity at room temperature, strong magneto-optical effect, magnetoelectric coupling as well as multiferroicity at room temperature, all of which hold exciting promise for exploitation in emerging nano-electronic or spin-electronic devices. Furthermore, from a fundamental point of view, the unusual complex entwining of different physical properties in such a simple transition-metal oxide may render ε-Fe$_2$O$_3$ an attractive playground for exploring novel phenomena in strongly correlated systems. These attributes make the author believe that "there is always light at the end of the tunnel". I hope the knowledge obtained in this thesis can be such a ray of light.

While several specific future research focuses have been indicated in the discussion of the main text, some interesting research directions to a broader extend are presented below:

i) The development of new strategies for the synthesis of ε-Fe$_2$O$_3$

Despite sustained research, the study of ε-Fe$_2$O$_3$ has substantial concerns in terms of obtaining phase pure ε-Fe$_2$O$_3$ due to its thermodynamical metastability. Hitherto most of the investigation subjects were synthesized in laboratory with nanometer-size dimension. Bulk single crystals have not been synthesized, nor single-crystalline thin films.

Developing new approaches towards ε-Fe$_2$O$_3$ phase with larger domains and further expanding the suitable substrate list for ε-Fe$_2$O$_3$ phase stabilization is also highly desirable. It is reported that ε-Fe$_2$O$_3$ thin film can be stabilized by industrially-compatible atomic layer deposition (ALD) technique [1], but the reported films are of polycrystalline nature. Our endeavor to grow epitaxial ε-Fe$_2$O$_3$ via ALD points out the important roles of types of precursors and the substrates employed in its formation. Further effort is necessary to fully address this issue. On the other hand, it is worth to mention that, single-domain κ-Ga$_2$O$_3$, which is isostructural to ε-Fe$_2$O$_3$, has recently been grown on FZ-grown ε-GaFeO$_3$ substrates by Yoshimoto and coworkers [2]. This is the first report of *Pna2$_1$* thin films of single-domain.

ii) Further understanding of the physics of ε-Fe$_2$O$_3$

To fully understand the delicate coupling between various degrees of freedom in this system, advanced experimental techniques, such as synchrotron X-ray-based diffraction and spectroscopy, microscopic techniques, and neutron scattering, have to be exploited more extensively. Our results obtained on Mn and Co substituted ε-Fe$_2$O$_3$ are relevant enough to study them in more detail in this regard.

Furthermore, the intriguing magnetic properties of ε-Fe$_2$O$_3$ have been mainly revealed on the particles, we expect an increase in importance of related studies in thin films over the next years. For exploring magnetism in ε-Fe$_2$O$_3$ epitaxial films, the newly established ε-Fe$_2$O$_3$ epilayer grown on mica substrate

may allow us to modulate the magnetic features of the top film due to the change of its strain state achieved by mechanically bending the flexible mica (as revealed by this thesis work, the magnetic orders near the magnetostructural transitions are strain sensitive). Moreover, 2D layered mica can be fully or largely peeled off from the top film, thus free-standing epilayers may be fabricated and further transfer onto an electrode for electrical characterization is possible. Our preliminary attempts to remove the bottom mica layers have shown some promises.

iii) Exploration of its multifunctionality for IT and energy related applications

Application-driven research based on ε-Fe$_2$O$_3$ is also gaining importance. One important example is its tunable high-frequency ferromagnetic resonance (in the millimeter-wave and terahertz frequency bands), which makes ε-Fe$_2$O$_3$ appealing for the next-generation communication application. Investigations into other research themes, including resistive memory, solar cell and photoelectrochemical water splitting, may also gain importance.

Reference

[1]   A. Tanskanen, O. Mustonen, M. Karppinen, Simple ALD process for ε-Fe2O3 thin films, APL Mater. 5 (2017) 056104. https://doi.org/10.1063/1.4983038.

[2]   H. Nishinaka, O. Ueda, D. Tahara, Y. Ito, N. Ikenaga, N. Hasuike, M. Yoshimoto, Single-Domain and Atomically Flat Surface of κ-Ga 2 O 3 Thin Films on FZ-Grown ε-GaFeO 3 Substrates via Step-Flow Growth Mode, ACS Omega. 5 (2020) 29585–29592. https://doi.org/10.1021/acsomega.0c04634.